

**RELATIVISTIC DFT CALCULATIONS OF MAGNETIC SHIELDING
TENSORS FOR SPIN $\frac{1}{2}$ HEAVY NUCLEI**

by

Fahri Alkan

A dissertation submitted to the Faculty of the University of Delaware in partial fulfillment of the requirements for the degree of Doctor of Philosophy in Chemistry and Biochemistry

Summer 2016

© 2016 Fahri Alkan
All Rights Reserved

RELATIVISTIC DFT CALCULATIONS OF MAGNETIC SHIELDING

TENSORS FOR SPIN $\frac{1}{2}$ HEAVY NUCLEI

by

Fahri Alkan

Approved: _____
Murray V. Johnston, Ph.D.
Chair of the Department of Chemistry and Biochemistry

Approved: _____
George H. Watson, Ph.D.
Dean of the College of Arts and Sciences

Approved: _____
Ann L. Ardis, Ph.D.
Senior Vice Provost for Graduate and Professional Education

I certify that I have read this dissertation and that in my opinion it meets the academic and professional standard required by the University as a dissertation for the degree of Doctor of Philosophy.

Signed:

Cecil Dybowski, Ph.D.
Professor in charge of dissertation

I certify that I have read this dissertation and that in my opinion it meets the academic and professional standard required by the University as a dissertation for the degree of Doctor of Philosophy.

Signed:

Tatyana Polenova, Ph.D.
Member of dissertation committee

I certify that I have read this dissertation and that in my opinion it meets the academic and professional standard required by the University as a dissertation for the degree of Doctor of Philosophy.

Signed:

Svilen Bobev, Ph.D.
Member of dissertation committee

I certify that I have read this dissertation and that in my opinion it meets the academic and professional standard required by the University as a dissertation for the degree of Doctor of Philosophy.

Signed:

Robert W. Schurko, Ph.D.
Member of dissertation committee

ACKNOWLEDGMENTS

My sincere thanks goes to my advisor, Prof. Cecil Dybowski, for his continuous support, encouragement and patience. His mentoring, kindness and positive attitude have helped me greatly over the course of my studies at University of Delaware. I would also like to thank my lab members, Yao, Sean, and Anna, for their friendship and helpful discussions during my PhD years. I am also grateful to Dr. Olga Dimitrenko and Dr. Steve Bai for their help and guidance.

I would like to thank my committee members, Prof. Schurko, Prof. Polenova, and Prof. Bobev, for their valuable suggestions. I should also acknowledge our early discussions about this project and the theory of magnetic-shielding tensors with Prof. Jochen Autschbach and Prof. Cynthia Jameson.

I would also like to thank the University of Delaware and National Science Foundation for their financial assistance during my graduate studies.

I am very grateful to my family, especially my father Huseyin and my mother Ummuhan, whose supports and encouragements have been invaluable for me. My deepest gratitude is reserved for my wife, Ozlem, who not only has encouraged me with her love and understanding during my PhD years, but also helped me greatly with the Matlab codes that are employed in this work.

The results in this dissertation include portions of my previously published work. Chapter 4 is based on the article ‘Calculation of chemical-shift tensors of heavy nuclei: a DFT/ZORA investigation of ^{199}Hg chemical-shift tensors in solids, and the effects of cluster size and electronic-state approximations’, which is published in

Physical Chemistry Chemical Physics (volume 16, pages 14298-14308). Chapter 5 is based on ‘Chemical-shift tensors of heavy nuclei in network solids: a DFT/ZORA investigation of Pb-207 chemical-shift tensors using the bond-valence method’ (*Physical Chemistry Chemical Physics*, volume 17, pages 25014-25026) and ‘Analysis of the bond-valence method for calculating ^{29}Si and ^{31}P magnetic shielding in covalent network solids’ (*Journal of Computational Chemistry*, DOI: 10.1002/jcc.24389). Chapter 6 is based on the article ‘Effect of coordination chemistry and oxidation state on the Pb-207 magnetic-shielding tensor: A DFT/ZORA investigation’ (*Journal of Physical Chemistry A*, volume 120, pages 161-168).

Dedicated to my wife, Ozlem and my son, Yekta

‘The underlying physical laws necessary for the mathematical theory of a large part of physics and the whole of chemistry are thus completely known, and the difficulty is only that the exact application of these laws leads to equations much too complicated to be soluble. It therefore becomes desirable that approximate methods of applying quantum mechanics should be developed, which can lead to an explanation of the main features of complex atomic systems without too much computation’

P.A.M. Dirac, *Proc. R. Soc. Lond. Ser. A-Contain. Pap. Math. Phys. Character*, 1929, 123, 714-733

TABLE OF CONTENTS

LIST OF TABLES	xii
LIST OF FIGURES	xv
ABSTRACT	xxiii
Chapter	
1 INTRODUCTION	1
1.1 Motivation of the Study	1
1.2 Overview	2
1.3 Basic Principles of Solid-State Nuclear Magnetic Resonance	4
1.3.1 Nuclear Interactions in External Magnetic Field	4
1.3.2 Magnetic Shielding	7
1.3.3 Magnetic-Shielding Anisotropy	8
1.3.4 Conventions for Reporting the Magnetic-Shielding Tensor	10
1.4 SSNMR of Spin- $\frac{1}{2}$ Heavy Nuclei	13
1.4.1 General Aspects of the SSNMR Experiment for Spin- $\frac{1}{2}$ Heavy Nuclei	13
1.4.2 High Resolution SSNMR Techniques for Spin- $\frac{1}{2}$ Heavy Nuclei	14
1.4.2.1 Magic Angle Spinning	14
1.4.2.2 Variable Offset Cumulative Spectroscopy	16
1.4.2.3 CPMG-type SSNMR Techniques	16
1.4.3 Correlation of Electronic and Solid-State Structure with NMR Parameters	17
REFERENCES	21
2 QUANTUM CHEMICAL CALCULATIONS OF NMR PARAMETERS	27
2.1 Theoretical Framework of Density Functional Theory	27

2.1.1	Kohn-Sham Formalism of Density Functional Theory	28
2.1.2	Exchange-Correlation Functionals	31
2.1.2.1	Local Density Approximation (LDA)	32
2.1.2.2	Generalized Gradient Approximation (GGA)	32
2.1.2.3	Hybrid Functionals	33
2.1.3	On the Accuracy of DFT	34
2.2	Introducing Relativity in Quantum Chemistry Methods	35
2.2.1	Dirac Equation	36
2.2.2	Four-Component and Two-Component Relativistic Methods	37
2.2.3	Zeroth Order Regular Approximation	39
2.3	Theory of Magnetic Shielding	40
2.3.1	Formulation of Magnetic Shielding from Double Perturbation Theory	41
2.3.2	Gauge Origin Dependence	44
2.3.3	Magnetic Shielding Calculations for Many-Electron Systems ...	45
2.4	Literature Review of Magnetic Shielding Calculations for Spin- $\frac{1}{2}$ Heavy Nuclei	46
	REFERENCES	49
3	COMPUTATIONAL METHODS	54
3.1	Magnetic Shielding Calculations in Solid State	54
3.2	Periodic Boundary Calculations and the GIPAW Approach	54
3.2.1	Approximate Cluster Models	56
3.2.2	Comparison of GIPAW and Cluster Models for Magnetic Shielding Calculations in Solids	57
3.3	Definition of Cluster Models for Solids	58
3.3.1	Definition of the Cluster Models for Molecular Solids	59
3.3.2	Definition of Cluster Models for Ionic or Covalent Network Solids	62
3.3.2.1	Termination of the Cluster for a Network Solid	64
3.3.2.2	Bond Valence Model Approach in Cluster Models	65

3.4	Computational Protocols	69
REFERENCES		71
4	MAGNETIC SHIELDING CALCULATIONS FOR MOLECULAR SOLIDS CONTAINING ^{199}Hg NUCLEI.....	76
4.1	Introduction	76
4.2	The Effect of Cluster Size and Charge on Magnetic Shielding.....	77
4.2.1	Model Clusters of Hg_2Cl_2	77
4.2.2	Isolated Molecule versus Large Cluster	81
4.3	The Effect of Basis Set and Frozen Core Approximation	89
4.3.1	Correlation of Experimental and Calculated ^{199}Hg principal components.....	89
4.3.2	Comparison of Computational Time; All Electron vs. Frozen Core	94
4.3.3	Convergence of Magnetic Shielding with Cluster Size.....	95
4.4	Relativistic Effects on ^{199}Hg Magnetic Shielding	97
REFERENCES		101
5	MAGNETIC SHIELDING CALCULATIONS FOR NETWORK SOLIDS EMPLOYING CLUSTERS ADAPTED FROM BOND VALENCE THEORY	103
5.1	Introduction	103
5.2	Magnetic Shielding Calculations on $\alpha\text{-PbO}$ and $\beta\text{-PbO}$	105
5.2.1	Effect of Termination Method and Cluster Size on the ^{207}Pb Magnetic Shielding Tensor.....	106
5.2.2	Symmetry Requirements for Calculated Principal Components.....	109
5.2.3	Effects of the Charge on the Terminal Atoms.....	111
5.3	VMTA/BV Model for ^{207}Pb Magnetic Shielding Calculations for Various Lead-Containing Solids	114
5.3.1	Effect of Cluster Size.....	116
5.3.2	Relativistic Effects.....	118
5.3.3	Accuracy of Calculated Principal Components of the ^{207}Pb Shielding Tensor.....	122

5.3.3.1	Clusters and the VMTA/BV Model	122
5.3.3.2	Relativistic Effects at the ZORA/Spin-Orbit Level....	124
5.3.3.3	Effect of the Density Functional by Introducing Exact Exchange	124
5.3.3.4	Experimental Uncertainty.....	127
5.4	Performance of PBC and VMTA/BV Models on Magnetic Shielding Calculations for Non-Relativistic Systems: the Case of ^{29}Si and ^{31}P	129
5.4.1	Cluster Size and Magnetic Shielding in ^{29}Si - and ^{31}P - Containing Solids	130
5.4.2	Effect of Basis Set in Cluster-based and Period Boundary Calculations	132
5.4.3	Comparison of Periodic and Cluster Models for ^{29}Si and ^{31}P - Containing Solids	134
	REFERENCES	139
6	EFFECT OF COORDINATION CHEMISTRY AND OXIDATION STATE ON MAGNETIC SHIELDING TENSOR	143
6.1	Introduction	143
6.2	The Relation between Coordination Chemistry and Magnetic Shielding of ^{207}Pb nuclei	143
6.2.1	Relativistic Effects on Principal Components: ZORA/Scalar vs. ZORA/Spin-Orbit	148
6.2.2	The Effect of Density Functional on Calculated ^{207}Pb Principal Components: BP86 vs. B3LYP.....	155
6.3	The Relation between Coordination Chemistry, Oxidation State and Magnetic Shielding of ^{119}Sn nuclei	162
6.3.1	Relativistic Effects on Principal Components of ^{119}Sn : ZORA/Scalar vs. ZORA/Spin-Orbit	165
6.3.2	The Performance of Hybrid DFT Methods for the Calculated ^{119}Sn Magnetic-Shielding Tensor	177
6.4	Effects of Relativistic Spin-Orbit Coupling and Hartree-Fock Exchange on Calculated Principal Components of Magnetic-Shielding Tensor for ^{125}Te Nuclei	180
6.4.1	Relativistic Effects on Principal Components of ^{125}Te : ZORA/Scalar vs. ZORA/Spin-Orbit	182

6.4.2	The Performance of Hybrid DFT Methods for the Calculated ¹²⁵ Te Magnetic-Shielding Tensor	186
	REFERENCES	188
7	CONCLUSION	194
	REFERENCES	200
Appendix		
A	CARTESIAN COORDINATES USED IN CLUSTER MODELS.....	201
B	ADDITIONAL TABLES AND FIGURES	210
C	PERMISSION AND COPYRIGHT	216

LIST OF TABLES

Table 1.1 NMR Properties of Spin- $\frac{1}{2}$ Heavy Nuclei.....	14
Table 4.1 Reference Codes and Space Groups for the Investigated Mercury-containing Solids.	77
Table 4.2 Calculated ^{199}Hg NMR Chemical Shifts for Model Clusters of Hg_2Cl_2	79
Table 4.3 NMR Chemical-Shift Parameters for Small and Large Model Clusters of ^{199}Hg -Containing Solids.	83
Table 4.4 Comparison of Calculated ^{199}Hg NMR Parameters Using the Frozen Core Approximation (FCA) for Remote Regions with Calculations Using the All-Electron (AE) Method for All Regions of the Cluster.	90
Table 4.5 Computational Time (CT) and Number of Cartesian Functions (cf) for Selected AE and FCA Large Cluster Calculations.	94
Table 4.6 Comparison of ^{199}Hg NMR Parameters of Large Clusters and Extended Clusters of $\text{Hg}(\text{SCN})_2$ and Hg_2Cl_2 Using the Frozen Core Approximation.	97
Table 5.1 Reference Codes and Crystallographic Data for Lead-Containing Solids .	104
Table 5.2 Reference Codes and Crystallographic Data for Silicon-Containing Solids	104
Table 5.3 Reference Codes and Crystallographic Data for Phosphorus-Containing Solids	105
Table 5.4 Principal Components of the ^{207}Pb Magnetic-Shielding Tensor, Reduced Chemical Shifts and Residuals (R) for Various Cluster Models of α - PbO and β - PbO	107
Table 5.5 Principal Components of the ^{207}Pb Magnetic-shielding Tensors of Symmetric and Perturbed Clusters of α - PbO	110
Table 5.6 Dependence of the Predicted Magnetic-shielding Tensor of α - PbO on the Total Charge on a Cluster Extending to the Fifth Coordination Shell ..	112

Table 5.7 Predicted Principal Components of ^{207}Pb Magnetic-Shielding Tensors, Determined at Either the ZORA/BP86 Level of Theory or the ZORA/B3LYP Level of Theory on a Cluster Extending to the Third Coordination Shell.....	125
Table 5.8 Experimental ^{207}Pb Chemical-Shift Tensors of the Two Forms of PbO....	128
Table 5.9 Principal Components of Experimental and Computed Magnetic-Shielding Tensors, Isotropic Magnetic Shielding, and Span for First, Third, and Fifth Coordination-Shell Clusters of α -quartz, Na_2SiO_3 , $\text{Mg}_2\text{P}_4\text{O}_{12}$, and $\text{Mg}_3(\text{PO}_4)_2$ Determined with VMTA/BV Model.	131
Table 5.10 Calculated ^{29}Si and ^{31}P Principal Components of Magnetic-Shielding Tensors for Various All-Electron Slater-Type and Pseudopotential Plane-Wave Basis Sets.	133
Table 6.1 Experimental Crystallographic Data and ^{207}Pb Chemical Shifts of Lead-Containing Materials	146
Table 6.2 Linear Regression Correlations of Experimental ^{207}Pb Chemical-Shift Tensor Principal Components with Calculated ^{207}Pb Magnetic-Shielding Tensor Principal Components, Using the BP86 Functional and the ZORA/Scalar Relativistic Hamiltonian or the ZORA/Spin-Orbit Relativistic Hamiltonian.	151
Table 6.3 Linear Regression Correlations of Experimental ^{207}Pb Chemical-Shift Tensor Principal Components with Calculated ^{207}Pb Magnetic-Shielding Tensor Principal Components, Using the BP86 and B3LYP Functionals and the ZORA/Spin- Orbit Hamiltonian.....	157
Table 6.4 Effect of HF Exchange on ^{207}Pb Magnetic-Shielding Tensors in α -PbO and Lead(IV) Acetate, Determined at the B3LYP Level of Theory.	159
Table 6.5 Experimental Crystallographic Data and ^{119}Sn Chemical Shifts of Tin-Containing Materials.	164
Table 6.6 Linear-Regression Parameters for the Linear Relations Between Calculated Magnetic Shieldings and Experimental Chemical Shifts of ^{119}Sn -Containing Solids.....	169
Table 6.7 Calculated and Experimental NMR Parameters of ^{119}Sn -Containing Solids Determined with Various DFT Methods.....	170

Table 6.8	Comparison of Calculated Magnetic Shieldings (σ_{iso}) for Tin-Containing Molecules using GIPAW ^a and ZORA/scalar Methods.	176
Table 6.9	Experimental and Calculated NMR Parameters of ¹¹⁹ Sn-Containing Solids using Model Clusters and PBE0/ZORA/Spin-Orbit Level of Theory.	179
Table 6.10	Experimental Crystallographic Data and ¹²⁵ Te Chemical Shifts of Tellurium-Containing Materials.	181
Table B1	Frozen Inner Shells in FCA(TZP)/AE and FCA(DZ)/AE Basis Sets for the Elements in Large Clusters of ¹⁹⁹ Hg-Containing Solids	210
Table B2	R ₀ and b Parameters Used in the Bond Valence Modelling of the Clusters of Investigated Systems	210
Table B3	Calculated NMR Chemical Shielding Parameters of First and Third Coordination Shell Clusters of Lead-Containing Systems Determined at ZORA-SO/BP86 Level of Theory	212

LIST OF FIGURES

Figure 1.1 The orientation of the PAS for the ^{13}C chemical-shift tensor in CO_2 and the simulated powder pattern from the experimentally obtained principal components from ref. [39].....	10
Figure 1.2 Schematic representations of powder patterns due to the chemical-shift dispersion, where $\kappa = 1.0, 0.0$ and -1.0 . Ω is defined as the maximum width of the spectrum.	12
Figure 1.3 a) Schematic representation of MAS and b) the effect of MAS on the observed spectrum under conditions of slow spinning.	15
Figure 3.1 Extended solid state structures of a) HgCl_2 and b) lead(IV) acetate, which are illustrated in the ball-and-stick model.	59
Figure 3.2 Comparison of a) small, b) large, and c) extended clusters of HgCl_2 . The small cluster consists of the NMR-active nucleus and the nearest neighbors to the NMR-active nucleus. A large cluster consists of the central molecule with its NMR-active nuclei and its nearest neighbors, as well as next-nearest neighbors to NMR nuclei (blue) and the ligands (red), and the atoms to complete the molecules (orange). An extended cluster includes the next-nearest neighbors of the large cluster and atoms to complete the molecules.	61
Figure 3.3 Cluster models for NaF that contains a) the first coordination shell, $[\text{NaF}_6]^{5-}$ b) the third coordination shell, $[\text{Na}_{19}\text{F}_{44}]^{25-}$ and c) the fifth coordination shell, $[\text{Na}_{85}\text{F}_{146}]^{61-}$	63
Figure 3.4 Different terminal oxygen sites according to the bond valence model in a) $\alpha\text{-PbO}$ and b) $\beta\text{-PbO}$	67
Figure 3.5 Energy levels for the third coordination cluster of $\alpha\text{-PbO}$. The occupied levels are shown in black whereas unoccupied levels are shown in red. These qualitative calculations are carried out with BP86 functionals and the ZORA/spin-orbit Hamiltonian.....	68

Figure 3.6 Graphical illustration of convergence versus number of SCF cycles for a DFT calculation that employs the α -PbO cluster without VMTA/BV modification (shown by the blue line) and for a DFT calculation using a cluster where the terminal atoms are modified by the VMTA/BV method (shown by the red line).....	69
Figure 4.1 Various molecular clusters of Hg ₂ Cl ₂ , as discussed in the text.	78
Figure 4.2 Small (left) and large (right) cluster models for the mercury-containing molecular solids.....	82
Figure 4.3 Correlation diagram for the calculated principal components of the magnetic-shielding tensor and the principal components of the experimental chemical-shift tensor for the ¹⁹⁹ Hg-containing systems modelled using small clusters . The blue line is the best-fit linear correlation. For the small clusters, $\sigma_{\text{calc}} = -1.3518 \delta_{\text{exp}} + 7854$ and the R ² value of the correlation is 0.934. The dashed line shows the ideal behavior. ($\sigma_{\text{calc}} = -\delta_{\text{exp}} + 7854$).....	86
Figure 4.4 Correlation diagram for the calculated principal components of the magnetic-shielding tensor and the principal components of the experimental chemical-shift tensor for the ¹⁹⁹ Hg-containing systems modelled using large clusters . The red line is the best-fit linear correlation. For the large clusters, $\sigma_{\text{calc}} = -1.0352 \delta_{\text{exp}} + 8042$ and the R ² value of the correlation is 0.981. The dashed line shows the ideal behavior. ($\sigma_{\text{calc}} = -\delta_{\text{exp}} + 8042$).....	87
Figure 4.5 Correlation diagram for the calculated principal components of the magnetic-shielding tensor determined with the FCA(DZ)/AE basis set, and the principal components of the experimental chemical-shift tensor for the ¹⁹⁹ Hg-containing molecular solids. For this correlation, $\sigma_{\text{calc}} = -1.0354 \delta_{\text{exp}} + 8085$ and the R ² value of the correlation is 0.980. The dashed line shows the ideal behavior. ($\sigma_{\text{calc}} = -\delta_{\text{exp}} + 8085$).....	92
Figure 4.6 Correlation diagram for the calculated principal components of the magnetic-shielding tensor determined with the FCA(TZP)/AE basis set, and the principal components of the experimental chemical-shift tensor for the ¹⁹⁹ Hg-containing molecular solids. For this correlation, $\sigma_{\text{calc}} = -1.0316 \delta_{\text{exp}} + 8055$ and the R ² value of the correlation is 0.980. The dashed line shows the ideal behavior. ($\sigma_{\text{calc}} = -\delta_{\text{exp}} + 8055$).....	93
Figure 4.7 Extended cluster models for Hg(SCN) ₂ and Hg ₂ Cl ₂	96

- Figure 4.8 Correlation diagram for the calculated principal components of the magnetic-shielding tensor at the **nonrelativistic** level of theory (BP86/AE), and the principal components of the experimental chemical-shift tensor for the ^{199}Hg -containing molecular solids. For this correlation, $\sigma_{\text{calc}} = -0.667\delta_{\text{exp}} + 6221$ and R^2 is 0.841. The dashed line shows the ideal behavior. 98
- Figure 4.9 Correlation diagram for the calculated principal components of the magnetic-shielding tensor at **ZORA/scalar level of theory**, and the principal components of the experimental chemical-shift tensor for the ^{199}Hg -containing molecular solids. For this correlation, $\sigma_{\text{calc}} = -0.695\delta_{\text{exp}} + 5965$ and the R^2 value of the correlation is 0.806. The dashed line shows the ideal behavior. 99
- Figure 5.1 First, third and fifth coordination shell geometries of α -PbO. The terminal oxygen atoms are shown in red circles. The corresponding β -PbO clusters have the same bonding network with differences in bond lengths and angles. 106
- Figure 5.2 Distorted fifth coordination-shell cluster of α -PbO. The added coordination in the x-direction is shown in red circles, and the central ^{207}Pb nucleus is highlighted in green. 109
- Figure 5.3 The effect of Z_{mod} on isotropic shielding for models that extend through the first (blue), third (red), and fifth (black) coordination shells for α -PbO. ΔZ_{mod} is the deviation of Z_{mod} from the optimal values determined by the VMTA/BV method. 113
- Figure 5.4 The effect of Z_{mod} on calculated span for models that extend through the first (blue), third (red), and fifth (black) coordination shell for α -PbO. ΔZ_{mod} is the deviation of Z_{mod} from the optimal values determined by the VMTA/BV method. 114
- Figure 5.5 First and third coordination-shell clusters for selected systems investigated in this work. The TZ2P/AE (all-electron) region is shown in the ball-and-stick model, whereas the region where FCA/DZ is used is shown by a stick model. 115
- Figure 5.6 The correlation between experimental and calculated principal components for the first coordination-shell model (●). The equation of the linear correlation line for the first-coordination-shell model is: $\sigma_{\text{cal}} = -0.541\delta_{\text{exp}} + 9990$ with $R^2 = 0.608$. The dotted line shows ideal behavior (with a slope of -1). 117

- Figure 5.7 The correlation between experimental and calculated principal components for the third coordination-shell model (\blacklozenge). The equation of the linear correlation line for the first-coordination-shell model is: $\sigma_{\text{cal}} = -0.869\delta_{\text{exp}} + 8643$ with $R^2 = 0.983$. The dotted line shows ideal behavior (with a slope of -1). 118
- Figure 5.8 The correlation between principal components of the magnetic shielding and experimental chemical shift of various lead-containing solids: (\bullet) with inclusion of only scalar relativistic terms; (\blacklozenge) with inclusion of all relativistic corrections through spin-orbit effects. The calculations were carried out on a third-coordination-shell model at the ZORA/DFT level. The equation of the correlation line for the principal components is: $\sigma_{\text{cal}} = -0.365\delta_{\text{exp}} + 7060$ with $R^2 = 0.887$ for ZORA/scalar calculations, and $\sigma_{\text{cal}} = -0.869\delta_{\text{exp}} + 8643$ with $R^2 = 0.983$ for ZORA/spin-orbit calculations. The dotted line shows ideal behavior. 119
- Figure 5.9 The correlation of magnetic-shielding span with experimental span of the various lead-containing solids: (\bullet) with inclusion of only scalar relativistic terms; (\blacklozenge) with inclusion of all relativistic corrections through spin-orbit effects. For the span, the correlation is: $\Omega_{\text{cal}} = 0.281\Omega_{\text{exp}}$ with $R^2 = 0.871$ for ZORA/scalar calculations and $\Omega_{\text{cal}} = 0.866\Omega_{\text{exp}}$ with $R^2 = 0.962$ for ZORA/spin-orbit calculations. The dotted line shows ideal behavior. 120
- Figure 5.10 The correlation of the principal components of the experimental chemical-shift tensor and the predicted shielding tensor for α -PbO, β -PbO, Pb_2SnO_4 , Pb_3O_4 and PbSiO_3 using fifth-coordination-shell cluster models. For the fifth-coordination-shell model, the correlation line is $\sigma_{\text{cal}} = -0.910\delta_{\text{exp}} + 8690$ with $R^2 = 0.986$. The dotted line shows ideal behavior. The equation of the correlation line for the third-coordination-shell model for the same data set is: $\sigma_{\text{cal}} = -0.891\delta_{\text{exp}} + 8689$ with $R^2 = 0.983$ 123
- Figure 5.11 The effect of B3LYP on the calculated principal components of sites in α -PbO, β -PbO and PbSiO_3 for the third-coordination-shell model. The equation of the correlation line is: $\sigma_{\text{cal}} = -0.985\delta_{\text{exp}} + 8781$ with $R^2 = 0.987$. The equation of the correlation line for the model using BP86 for the same data set is: $\sigma_{\text{cal}} = -0.898\delta_{\text{exp}} + 8605$ with $R^2 = 0.987$. The dotted line shows ideal behavior. The values of the slope show how use of B3LYP approaches the ideal behavior. 127

Figure 5.12	Illustration of third-coordination-shell clusters for Mg_2SiO_4 and $\text{Mg}_3(\text{PO}_4)_2$. The TZ2P region is shown in ball-and-stick model and the TZP region is shown as a wireframe model.	130
Figure 5.13	Correlation between calculated and experimental principal components of magnetic-shielding tensors for ^{29}Si -containing materials. Values obtained using the GIPAW approach are shown in blue, and results obtained using the VMTA/BV cluster approach are shown in red. Results were computed at the PBE level of theory. The best-fit correlations are given as solid lines.	135
Figure 5.14	Correlation between calculated and experimental principal components of magnetic-shielding tensors for ^{31}P -containing materials. Values obtained using the GIPAW approach are shown in blue, and results obtained using the VMTA/BV cluster approach are shown in red. Results were computed at the PBE level of theory. The best-fit correlations are given as solid lines.....	136
Figure 6.1	(a) Classification scheme of lead coordination in the solid state; (b) schematic structures of hemidirected and holodirected Pb centers. The orange ball represents the lead atom and red balls represent, bonding ligands. In the holodirected geometry, ligands are approximately uniformly distributed about the lead center, whereas in the hemidirected geometry, ligands tend to be non-uniformly distributed.....	144
Figure 6.2	Cluster models for (a) Ca_2PbO_4 and (b) $\text{Pb}(\text{BB})_4$. The highlighted regions (shown in ball-and-stick models) represent the first coordination shell for the lead center. These atoms are treated with the TZ2P basis set. The higher coordination shells (shown with stick models) are treated with the DZ basis set.....	147
Figure 6.3	The correlation between experimental and calculated principal components for calculations at the BP86/ZORA/scalar relativistic level of theory. Data for hemidirected geometries are indicated by blue symbols, whereas data for holodirected lead centers are indicated by red symbols. The dotted line in each graph shows the ideal behavior (a relation with a slope of -1). The best-fit linear correlations are given in Table 6.2.	149
Figure 6.4	The correlation between experimental and calculated principal components for at the BP86/ZORA/spin-orbit relativistic level of theory. The dotted line in each graph shows the ideal behavior. The best-fit linear correlations are given in Table 6.2.....	150

Figure 6.5	The difference ($\Delta\sigma$) between ^{207}Pb components calculated using the full ZORA/spin-orbit Hamiltonian and components calculated using the ZORA/scalar Hamiltonian. The numbering scheme for labeling lead-containing compounds is given in Table 6.1.	153
Figure 6.6	The orientation of shielding tensors and the MOs with significant 6s (Pb-centered) contributions are shown for (a) $\alpha\text{-PbO}$ and (b) $\text{Pb}(\text{OAc})_4$. The σ_{22} component is perpendicular to the page for both systems.	154
Figure 6.7	The correlation between principal components of the experimental ^{207}Pb chemical-shift tensor and the principal components of the calculated ^{207}Pb magnetic-shielding tensor determined at the B3LYP(20% XC)/ZORA/spin-orbit level of theory. Holodirected lead centers are represented by blue symbols; hemidirected lead centers are represented by red symbols. The dotted lines show the expected ideal behavior.	156
Figure 6.8	The difference between ^{207}Pb components ($\Delta\sigma_{ii}$) calculated using the B3LYP, and BP86 density functionals. Both sets of calculations are carried out using the ZORA/spin-orbit Hamiltonian.	158
Figure 6.9	The correlation between calculated span and fraction of HF exchange in the B3LYP functional for $\alpha\text{-PbO}$	161
Figure 6.10	The correlation between calculated span and fraction of HF exchange in the B3LYP functional for lead(IV) acetate.	162
Figure 6.11	Cluster models for a) SnO and b) SnO_2 . The central ball-and-stick region, representing the NMR-active ^{119}Sn center and the first-coordination shell, are treated with the TZ2P basis set. The outer coordination shells are treated with the smaller TZP basis set.	165
Figure 6.12	Correlations between calculated principal components of ^{119}Sn magnetic-shielding tensors and experimental ^{119}Sn chemical-shift tensors for twelve tin-containing solids, as determined with the PBE/GIPAW method. Sn(II) sites are shown in red; Sn(IV) sites are shown in blue.	166
Figure 6.13	Correlations between calculated principal components of ^{119}Sn magnetic-shielding tensors and experimental ^{119}Sn chemical-shift tensors for twelve tin-containing solids, as determined with the PBE/ZORA/scalar and cluster method. Sn(II) sites are shown in red; Sn(IV) sites are shown in blue.	167

Figure 6.14	Correlations between calculated principal components of ^{119}Sn magnetic-shielding tensors and experimental ^{119}Sn chemical-shift tensors for twelve tin-containing solids, as determined with the PBE/ZORA/spin-orbit and cluster method. Sn(II) sites are shown in red; Sn(IV) sites are shown in blue.	168
Figure 6.15	The differences ($\Delta\sigma_{ii}$) in principal components of ^{119}Sn magnetic-shielding tensors calculated with the PBE/ZORA/spin-orbit method and the PBE/ZORA/scalar method. All calculations modeled the solid-state environment with the cluster-based VM TA/BV approach. .	173
Figure 6.16	Correlation between calculated principal components of ^{119}Sn magnetic-shielding tensors and experimental ^{119}Sn chemical-shift tensors for twelve tin-containing solids. Calculations were performed at the PBE0/ZORA/spin-orbit level of theory. Sn(II) sites are shown in red; Sn(IV) sites are shown in blue.	178
Figure 6.17	Correlations between calculated principal components of ^{125}Te magnetic-shielding tensors at PBE/ZORA/scalar level of theory and experimental ^{125}Te chemical-shift tensors for the tellurium-containing solids tabulated in Table 6.10. The dotted line represents the best-fit line.	183
Figure 6.18	Correlations between calculated principal components of ^{125}Te magnetic-shielding tensors at PBE/ZORA/spin-orbit level of theory and experimental ^{125}Te chemical-shift tensors for the tellurium-containing solids. The dotted line represents the best-fit line.	184
Figure 6.19	The differences ($\Delta\sigma_{ii}$) in principal components of ^{125}Te magnetic-shielding tensors calculated with the ZORA/spin-orbit method and the ZORA/scalar method. All calculations modeled the solid-state environment with the cluster-based VM TA/BV approach. Magnetic-shielding calculations used the PBE functional.	185
Figure 6.20	Correlation between calculated principal components of ^{125}Te magnetic-shielding tensors at PBE0/ZORA/spin-orbit level of theory and experimental ^{125}Te chemical-shift tensors for the tellurium-containing solids. The dotted line represents the best-fit line.	187
Figure B1	Correlation between calculated and experimental principal components of magnetic-shielding tensors for ^{29}Si -containing materials. Results were computed at the PBE0 level of theory. The best-fit correlation is given as solid line.	214

Figure B2 Correlation between calculated and experimental principal components of magnetic-shielding tensors for ^{31}P -containing materials. Results were computed at the PBE0 level of theory. The best-fit correlation is given as solid line. 215

ABSTRACT

A computational study of magnetic-shielding tensors of spin- $\frac{1}{2}$ heavy nuclei in solids has been carried out by employing relativistic DFT and cluster models. The performance of various theoretical treatments and cluster models has been investigated by comparing the agreement between theory and experiment as a metric of the goodness of the calculation.

A significant amount of effort in this study has been dedicated to the development of cluster models for accurate calculation of magnetic-shielding tensors in the solid state. The performance of cluster models of various sizes, symmetries, as well as clusters with different net charges and with preparation by different truncation methods have been studied. The convergence of calculated principal components with cluster size is monitored in benchmark calculations. The results suggest that inclusion of higher coordination shells in the molecular cluster is generally necessary for quantitative predictions of magnetic-shielding tensors. However, it has been found possible to reduce the size of these computationally expensive molecular-cluster calculations with limited effect on the calculated NMR parameters by carefully introducing the frozen core approximation and locally dense basis sets.

For network solids, a new formalism, which employs pseudo-atoms with altered nuclear charges and parameters obtained from bond-valence theory, is proposed for the truncation of clusters. This model has been applied to a large selection of systems with success. The performance of the cluster models in network

solids is also compared to models that account for the full translational symmetry of the extended system (periodic boundary conditions with GIPAW) for lighter nuclei such as ^{29}Si and ^{31}P .

The importance of treating a system with the relativistic Hamiltonian for accurate prediction of principal components of the magnetic-shielding tensor of heavy nuclei (^{207}Pb , ^{199}Hg , ^{125}Te and ^{119}Sn) is demonstrated within the cluster approach. The results demonstrate that inclusion of the spin-orbit component in the ZORA Hamiltonian is essential to obtain good agreement with experimental results. It is shown that spin-orbit effects on the principal components are strongly dependent on the oxidation state and coordination geometry about the NMR nuclei.

Finally, the performance of hybrid functionals (B3LYP and PBE0) is examined for the prediction of magnetic-shielding tensors of ^{207}Pb , ^{125}Te and ^{119}Sn . The results show that employing hybrid functionals improves agreement between theory and experiment, compared to GGA functionals. This improvement is more noticeable in the case of ^{207}Pb than it is for ^{125}Te and ^{119}Sn .

Chapter 1

INTRODUCTION

1.1 Motivation of the Study

Calculation of magnetic resonance properties with quantum chemistry methods has become an important research tool in the last two decades.[1-3] Accurate predictions of nuclear magnetic resonance (NMR) parameters from first principles can predict the correlations between the experimental NMR data, and the electronic structure and connectivity of a system, giving rationalizations of empirical relations and providing explanations when empirical relations do not suffice. In general, such calculations have reached a certain maturity for the light nuclei such as ^{13}C or ^1H , and they are often employed for enhanced interpretations of experimental spectra.[4-6] For heavy nuclei such as ^{199}Hg or ^{207}Pb , however, calculations of magnetic resonance properties still remain challenging for otherwise established quantum chemical methods. [1, 7, 8] This situation is due to the large number of electrons present in the heavy nuclei and to the relativistic effects associated with the high nuclear charge.[9, 10] For this reason, careful methodological optimizations are needed for reliable and accurate calculations that can be performed using reasonable computational resources.

In the solid state, the full tensor interaction for magnetic shielding or quadrupolar coupling gives a description of a three-dimensional structure.[11, 12] The theoretical treatment of these tensor quantities often requires a model for the crystalline nature of the material.[3, 13] Two methods have been proposed for the calculation of magnetic properties in solids: (1) use of periodic boundary conditions

(PBC) based on the full crystal symmetry,[5, 14-16] and (2) use of model clusters that define the local environment.[17-22] Unfortunately, PBC-based quantum chemistry methods are not suitable for systems containing heavy nuclei, because the required relativistic methods and higher level ab-initio methods have not been implemented in the currently-available PBC formalisms. For cluster modelling, there is, of course, a larger selection of program packages and methodologies available. However, this approach requires the optimization of various parameters such as cluster size, cluster charge, and local symmetry around nuclei.[22]

The aim of this study is to establish a framework for the cluster modelling, which allows accurate predictions of the magnetic-shielding tensor for heavy nuclei. To do this, we shall test the performance of different types of cluster models with respect to size, symmetry, charge, and termination methods for well-characterized solids containing heavy nuclei. The convergence of the magnetic shielding components will be investigated for different cluster sizes, as an indicator of the quality of the cluster modelling.

Another motivation for our study is to understand the effects of various theoretical treatments on the magnetic shielding tensor of heavy nuclei in solids. In solids, comparison between theory and experiment for all principal components of the shielding tensor, instead of the single isotropic value, provides a more stringent test for the performance of the current quantum chemistry methods in benchmarking magnetic shielding calculations.

1.2 Overview

This dissertation is organized as follows: The first chapter briefly introduces some of the basic principles of solid-state NMR (SSNMR). This chapter also covers

the existing literature on the SSNMR of spin $\frac{1}{2}$ heavy nuclei such as ^{207}Pb and ^{199}Hg . Chapter two deals with the theoretical concepts of quantum chemistry that are important for understanding the remainder of this study. This chapter includes general background information on density functional theory (DFT), relativistic quantum chemistry methods, and the calculation of magnetic-shielding tensor from first principles. Chapter three describes specific computational methodologies employed in this work. The main focus of this chapter is the formulation of cluster models for different types of solids. Chapter four introduces magnetic shielding calculations for molecular solids using cluster models. In this chapter, calculated principal components of the shielding tensor using various cluster models are compared to experimental data for ^{199}Hg -containing materials. The performance of different approximations in the theoretical treatment of clusters is investigated. In chapter five, we introduce magnetic shielding calculations for network solids using cluster models. Different termination schemes for clusters are investigated with respect to convergence of principal components. Additionally, benchmark calculations of the cluster models for network solids are compared with PBC methods for non-relativistic systems containing ^{31}P and ^{29}Si nuclei. In chapter six, the effect of coordination chemistry and electronic structure on the magnetic shielding tensor are investigated for ^{207}Pb and ^{119}Sn containing solids. Our focus in this chapter is to provide a link between the performance of different theoretical treatments and the coordination chemistry of the heavy nuclei-containing solids. Finally, in chapter seven, the results of these investigations are summarized, with some prediction of the subsequent developments that may enhance this methodology.

1.3 Basic Principles of Solid-State Nuclear Magnetic Resonance

SSNMR spectroscopy is a powerful technique that is applied in various fields of chemistry, materials science, engineering, and geology. The applications of SSNMR include, but are not limited to, catalysis and zeolite systems,[12, 23, 24] structure elucidation of amorphous solids and proteins,[25, 26] and dynamics of chemical processes.[27-32] The theory of SSNMR spectroscopy and its applications have been reviewed and can be found in ref. [5, 12, 33-36]. In the following sections, we introduce some of the specific concepts in SSNMR related to the present theoretical work.

1.3.1 Nuclear Interactions in External Magnetic Field

NMR spectroscopy is based on the interaction of nuclear spins with the external magnetic field. For a non-isolated spin, the energy levels of the spin states are perturbed by the interactions with surrounding nuclei and electrons. These perturbations can yield important information about the chemical environment of the NMR-active nucleus. For a spin ($I \geq \frac{1}{2}$), the interactions are expressed by the Hamiltonian [34]

$$H_{\text{spin}} = H_Z + H_{\text{RF}} + H_{\text{DC}} + H_{\text{CS}} + H_J + H_{\text{QC}} \quad (1.1)$$

The components of the Hamiltonian in Eq. 1.1 are summarized as follows: The Zeeman Hamiltonian (H_Z) describes the interaction between each spin and the applied external magnetic field. This interaction is responsible for the energy splitting of spin states that occurs when a spin is placed in a magnetic field. It is often assumed that the coupling described by the Zeeman Hamiltonian is the strongest interaction felt by a spin. H_Z for a spin in an external magnetic field B_0 and having a spin operator I_z is

$$H_Z = -\hbar\gamma B_0 I_z \quad (1.2)$$

where the z axis is assumed to be parallel to the direction of the external magnetic field, γ is the gyromagnetic ratio of the spin, and \hbar is Planck's constant divided by 2π

The radio frequency Hamiltonian (H_{RF}) characterizes the interaction of the spin with an applied radio frequency field in the NMR experiment. The radio frequency field may be pulsed or continuous, it may be weak or it may be strong, but usually its amplitude makes it a perturbation on the interaction with the applied external field. Like the static Zeeman interaction, H_{RF} is also a Zeeman coupling to the time-dependent radio frequency field, B_1 .

The dipolar-coupling Hamiltonian, H_{DC} , reflects the direct pairwise interaction of two spins. The dipolar interaction between two unlike spins, \mathbf{I} and \mathbf{S} , with spin operators for the components along the magnetic field direction I_z and S_z , is given, in a strong external applied field, by

$$H_{DC} = \frac{\mu_0}{4\pi} \left(\frac{\gamma_I \gamma_S}{r^3} \right) [1 - 3\cos^2\theta] I_z S_z \quad (1.3)$$

where r is the distance between the nuclei and θ is the angle between the external magnetic field and the vector \mathbf{r} . μ_0 is the permeability of free space.

The magnetic shielding interaction describes the effects of the electrons on the local magnetic field in the vicinity of a nucleus induced by their interaction with the external applied field. The effect is usually defined as the difference between the resonance position of the nucleus and some reference material, called the chemical shift. The effective Hamiltonian, H_{CS} , for this shielding effect is given by

$$H_{CS} = \gamma \hbar \mathbf{B}_{\text{ext}} \cdot (1 - \boldsymbol{\sigma}) \cdot \mathbf{I} \quad (1.4)$$

where σ is the magnetic shielding tensor and σ_{zz} is the diagonal component of the magnetic shielding tensor in the frame in which the external applied magnetic field is parallel to the z axis.

The through-bond indirect spin-spin coupling between a pair of spins is given by the so-called J coupling Hamiltonian, H_J , between two spins \mathbf{I} and \mathbf{S} defined by the following expression

$$H_J = \mathbf{I} \cdot \mathbf{J}_{IS} \cdot \mathbf{S} \quad (1.5)$$

where \mathbf{J}_{IS} is the indirect spin-spin coupling tensor for the interaction between the spins.

The quadrupolar coupling with an applied electric field gradient is an interaction unique to nuclei with $\mathbf{I} > 1/2$. It is characterized by a contribution to the Hamiltonian of the form

$$H_Q = \mathbf{I} \cdot \mathbf{Q} \cdot \mathbf{I} \quad (1.6)$$

where \mathbf{Q} is the quadrupole interaction tensor for the nucleus. It depends on the strength of the electric-field gradient at the nuclear site and on a fundamental constant for the nucleus, the quadrupole moment. Depending on the site and the nucleus, the quadrupole interaction may be the strongest interaction that a spin experiences, in which case it cannot be treated as a perturbation on the Zeeman coupling to the interaction with the applied external magnetic field.

These interactions furnish information about the connectivity, coordination, and electronic structure of a molecular system. In principle, NMR interactions may depend on the relative orientation of the external field and the molecular system.[11, 12, 33-35] They are formally defined as rank-2 tensors. In the solution state, the effects of the dipolar coupling and the quadrupolar coupling vanish through first and

the second order, due to the rapid motion of the molecules, whereas the magnetic shielding and the J coupling interactions are reduced to the isotropic values of the full tensor. Hence, NMR spectra in solution state generally consist of sharp lines. For solids, however, the molecular motion is relatively limited compared to the solution state. As a result, NMR spectra of solids are affected by the orientation-dependent interactions which may make the spectra broader and complicated, particularly when the sample is powder containing multiple orientations of the principal axes of these interactions relative to the magnetic field.[11, 12, 34]

1.3.2 Magnetic Shielding

Among the interactions described in the previous section, magnetic shielding is by far the most investigated interaction through NMR spectroscopy. The magnetic shielding Hamiltonian is detected through the effects on the spins; however, it is explicitly a function only of the electronic structure of the system. Therefore, it provides information about the chemical bonding and structure in molecular systems.[11, 34]

As mentioned, the magnetic shielding is formally a rank-2 tensor with nine independent components.[3, 37, 38] The generic form of the tensor may be written as

$$\boldsymbol{\sigma} = \begin{bmatrix} \sigma_{xx} & \sigma_{xy} & \sigma_{xz} \\ \sigma_{yx} & \sigma_{yy} & \sigma_{yz} \\ \sigma_{zx} & \sigma_{zy} & \sigma_{zz} \end{bmatrix} \quad (1.7)$$

The tensor in Eq. 1.7 can be divided to symmetric and antisymmetric parts. In general, only the symmetric part of the tensor, which has six independent components ($\sigma_{\alpha\beta} = \sigma_{\beta\alpha}$), affects the NMR spectra because the antisymmetric contribution is either very small or zero.[3] In the principal-axis system (PAS), the magnetic shielding

tensor is diagonal. The three non-vanishing components of the tensor (the symmetric part) in its PAS are called principal components: $\sigma_{11} \leq \sigma_{22} \leq \sigma_{33}$. [11, 34] The remaining three determinants of the tensor are the Euler angles that relate the PAS to the experimental co-ordinate system. From studies of powdered samples, it is not generally possible to determine these orientation parameters except under conditions of high point symmetry at the nuclear center.

In the SSNMR experiment, the components of the magnetic-shielding tensor are not the measured quantity. Instead, the chemical shift (δ), the magnetic shielding relative to some reference material, is reported. The principal components of the magnetic-shielding tensor and the principal components of the experimentally observed chemical-shift tensor are related by the following expression

$$\delta_{ii} = \frac{\sigma_{ref} - \sigma_{ii}}{1 - \sigma_{ref}} \approx \sigma_{ref} - \sigma_{ii} \quad (1.8)$$

In Eq. 1.8, the approximate expression can be used when $\sigma_{ref} \ll 1$. This situation is usually true for light nuclei such as ^1H and ^{13}C . However, for heavy nuclei such as ^{199}Hg or ^{207}Pb , the reference shielding is usually in the order of thousands of ppm. For this reason, one needs to include the factor $1/(1 - \sigma_{ref})$, in experimental or theoretical calculations of chemical shifts for such nuclei.

1.3.3 Magnetic-Shielding Anisotropy

The NMR spectra of polycrystalline samples display frequencies resulting from different tensor orientations with respect to the magnetic field, due to random geometric distributions of crystallites, whose principal axes are randomly oriented relative to the frame of the applied magnetic field. [34] For each crystallite, the measurable magnetic shielding varies according to the orientation of the principal axes

of the magnetic-shielding tensor with respect to the magnetic field. If the electronic environment is spherical or tetrahedral, symmetry requires that all different orientations of the crystallite axes yield the same magnetic shielding constant ($\sigma_{11} = \sigma_{22} = \sigma_{33}$); [3, 38] and all resonances for the various crystallites occur at one unique position in the spectrum. For nuclear sites for which the electronic environment has lower symmetries, at least one of the principal components on the magnetic-shielding tensor is required to be different from the others. For such systems, the SSNMR spectrum consists of a band which represents the distribution of magnetic shieldings. The resulting spectrum is called a powder pattern. In Figure 1.1, the orientations of the principal axes of chemical-shift tensor for CO₂ is shown in the molecular frame. The powder pattern for ¹³C nuclei in solid CO₂ are indicated in Figure 1.1. [39] For CO₂, the δ_{11} and δ_{22} components are degenerate due to the axial symmetry of the molecule, and they are in the plane perpendicular to the principal axis (C_{∞}) of the molecule. Because these two components are not unique, there is technically an infinite number of pairs of orthogonal axes that could be defined as the 11 and 22 axes. The δ_{33} component corresponds to the most shielded component and the 33 axis is along the C-O bond.

The magnetic shielding anisotropy can be detected directly in the SSNMR experiment without any referencing. For this reason, comparison of calculated and experimental values of the magnetic-shielding anisotropy for a particular system can be used as a gauge for the performance of the theoretical methods, especially in benchmark calculations.

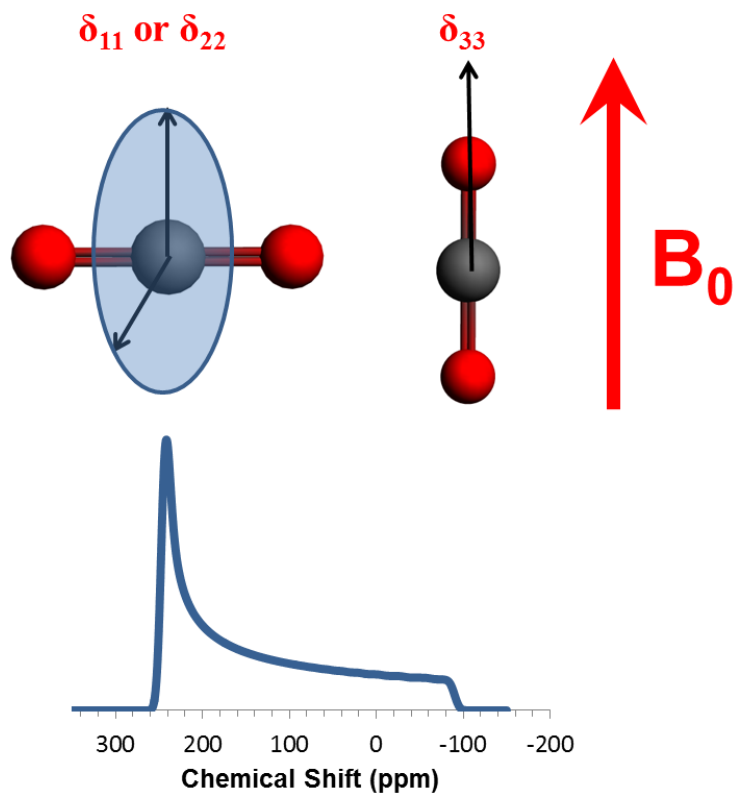


Figure 1.1 The orientation of the PAS for the ^{13}C chemical-shift tensor in CO_2 and the simulated powder pattern from the experimentally obtained principal components from ref. [39]

1.3.4 Conventions for Reporting the Magnetic-Shielding Tensor

The magnetic-shielding tensor (or the chemical-shift tensor) is defined by the three principal components, σ_{11} , σ_{22} , and σ_{33} . The full tensor is also described by the orientations of the principal axes relative to some fixed axes in the sample. Such a description, in the general sense, requires the specification of three angles, and the full tensor requires 6 independent variables for complete specification. The principal components $\sigma_{11} \leq \sigma_{22} \leq \sigma_{33}$ are usually assigned in the frequency-ordered convention.[40] At least two other conventions are commonly used to report a magnetic-shielding tensor.

In Haeberlen's convention,[11] the tensor is described by three parameters, the spherical components of the tensor, and the ordering convention discussed above is not necessarily followed. The isotropic shielding, σ_{iso} , refers to the center of gravity of the magnetic-shielding tensor relative to the resonance position of the bare nucleus. The shielding anisotropy, Δ (or sometimes $\Delta\sigma$), describes the largest separation of a component (in this case, called σ_{33}) from the isotropic shielding. The asymmetry, η , is a measure of the deviation from axial symmetry. The relationship between these parameters and the principal components is given in Equations 1.9.

$$\sigma_{\text{iso}} = \frac{\sigma_{11} + \sigma_{22} + \sigma_{33}}{3} \quad (1.9a)$$

$$\Delta = \frac{3}{2} (\sigma_{33} - \sigma_{\text{iso}}) \quad (1.9b)$$

$$\eta = \frac{\sigma_{22} - \sigma_{11}}{\sigma_{33} - \sigma_{\text{iso}}} \quad (1.9c)$$

Another convenient description of the magnetic-shielding tensor is the Maryland convention.[40] In this description, in addition to the isotropic shielding (Eq. 1.9a), two parameters describe the powder pattern. The span, Ω , describes the maximum width of the spectral powder pattern. The skew, κ , defines the relative position of σ_{22} to σ_{iso} . Figure 1.2 schematically shows powder patterns with axial symmetry ($\kappa = +1.0$ or -1.0) and nonaxial symmetry ($\kappa = 0.0$) The relations between these parameters and the principal components are given in equations 1.10.

$$\Omega = \sigma_{33} - \sigma_{11} \quad (1.10a)$$

$$\kappa = \frac{3(\sigma_{\text{iso}} - \sigma_{22})}{\Omega} \quad (1.10b)$$

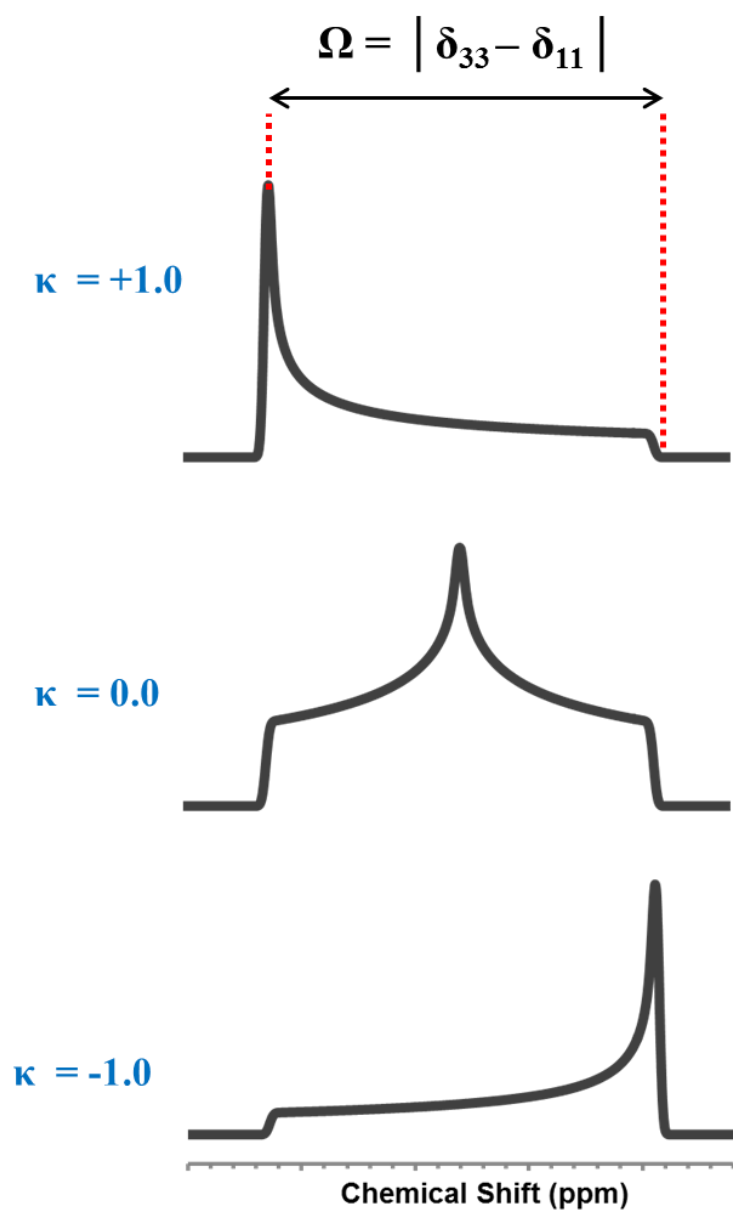


Figure 1.2 Schematic representations of powder patterns due to the chemical-shift dispersion, where $\kappa = 1.0, 0.0$ and -1.0 . Ω is defined as the maximum width of the spectrum.

In the previous discussion, the conventions for the magnetic-shielding tensor have been indicated. The conventions for the chemical-shift tensor are similar, but

one should always be careful about the definitions of axes, particularly the 11 and 33 axes.

In this dissertation, calculated magnetic-shielding tensors and chemical-shift tensors are reported in the frequency-ordered convention or in the Maryland convention. Equations 1.9 and 1.10 may be used to convert the information to other conventions. Where known or calculated, the geometric information is reported, generally as Euler angles between the principal axis system and some fixed coordinate system.

1.4 SSNMR of Spin- $1/2$ Heavy Nuclei

1.4.1 General Aspects of the SSNMR Experiment for Spin- $1/2$ Heavy Nuclei

In general, experimental SSNMR of heavy metal nuclei such as ^{199}Hg or ^{207}Pb involves extra difficulties, as compared to SSNMR of nuclei like ^{13}C , due to the large chemical-shift ranges and the long T_1 relaxation times.[41-43] Additionally, broad powder patterns (with spans of thousands of ppm), arising from the significant chemical shift anisotropy, are often observed for powdered samples containing heavy nuclei. For samples having such powder patterns, uniform excitation of the entire range of the absorption spectrum is an experimental challenge. Despite these difficulties, SSNMR investigations of heavy nuclei are appealing because the magnetic shielding of these nuclei is usually very sensitive to local chemical environment. Some characteristic NMR properties of selected spin- $1/2$ heavy nuclei are provided in Table 1.1.

Table 1.1 NMR Properties of Spin- $1/2$ Heavy Nuclei.

Nucleus	Natural Abundance (%)	ν_0 at 7.0459 T (MHz)	Chemical Shift Range (ppm)
^{119}Sn	8.59	111.872	~5000
^{195}Pt	33.7	64.497	~15000
^{199}Hg	16.9	53.7325	~5000
^{205}Tl	70.48	173.052	~7000
^{207}Pb	22.1	62.7622	~10000

1.4.2 High Resolution SSNMR Techniques for Spin- $1/2$ Heavy Nuclei

To obtain well-resolved and usable SSNMR spectra of heavy-nuclei-containing materials, specialized techniques beyond single-pulse excitation are often required. In this section, I briefly discuss some of these techniques.

1.4.2.1 Magic Angle Spinning

Magic angle spinning (MAS) techniques involve rapid rotation of the sample around an axis inclined at 54.74° with respect to the external field, an angle referred as the “magic angle”. This special angle is chosen because interactions such as the dipole-dipole coupling and the first-order quadrupole coupling vary as $(3\cos^2\theta - 1)$, where θ is the angle between the unique principal axis of the tensor and the magnetic field. The expansion of these interactions in terms of the orientation of the axis of spinning also contains this same factor of the angle between the spinning axis and the magnetic field. Thus, the time average of these first-order nuclear interactions vanishes when the frequency of spinning is greater than the magnitude of anisotropy, about an axis inclined at this “magic” angle. As a result, spinning of the sample at the magic angle causes at least partial suppression of these interactions’ effects, which

enhances the resolution of SSNMR spectra acquired with rapid magic-angle spinning.[34] When the spinning is “slow”, the result is a manifold of spinning sidebands caused by the frequency modulation of the interaction. An illustration of MAS and its effect on the powder pattern under slow spinning is illustrated in Figure 1.3.

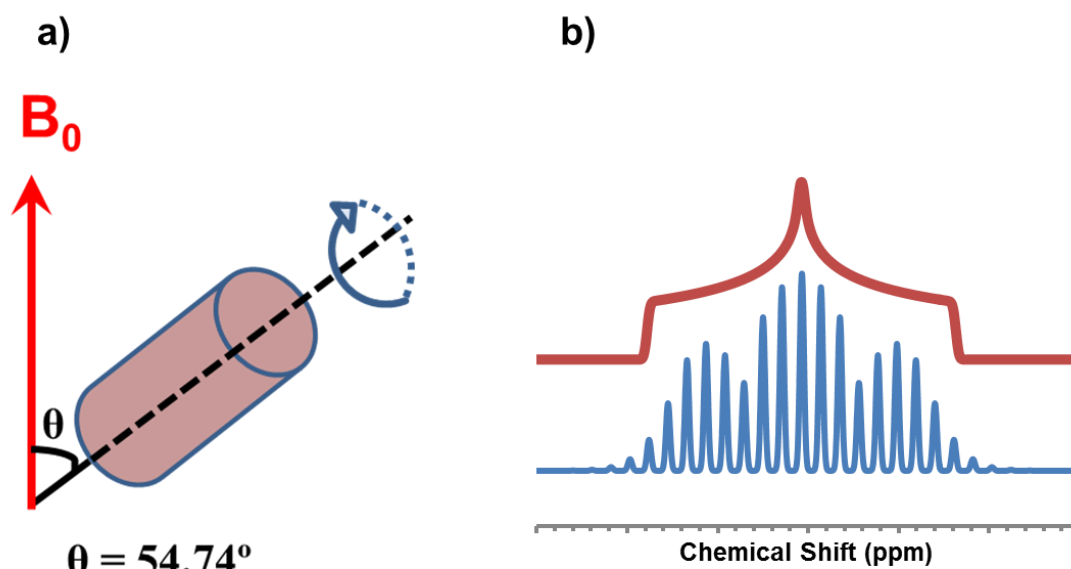


Figure 1.3 a) Schematic representation of MAS and b) the effect of MAS on the observed spectrum under conditions of slow spinning.

MAS suppresses the effects of orientation-dependent terms in the magnetic shielding Hamiltonian completely when the spinning frequency is substantially higher than the anisotropy. For lower spinning frequencies, the resulting spectra is composed of spinning sidebands, which appear on either side of the isotropic peak with integer multiples of spinning rate. (Figure 1.3b.) A careful analysis of the relative intensities

of the sidebands in this slow-spinning version of the spectrum allows one to retrieve information about the anisotropic components of the chemical-shift tensor, thereby giving access to the principal components.[44]

1.4.2.2 Variable Offset Cumulative Spectroscopy

For wide SSNMR powder patterns, the failure to excite the powder pattern uniformly over the entire resonance range results in distortions in the spectrum that directly affect the ability to determine the principal components of the chemical-shift tensor. In such situations, one may use variable offset cumulative spectroscopy (VOCS) to determine a minimally distorted band from a static sample. In this procedure, a set of SSNMR spectra is recorded with systematic variation of the transmitter frequency from spectrum to spectrum. Each spectrum is collected using identical experimental parameters other than the transmitter frequency. These spectra are added in the frequency domain, to yield the VOCS spectrum. The VOCS technique has been shown to reproduce the broad powder patterns of heavy-metal nuclei such as ^{207}Pb and ^{199}Hg successfully.[43, 45-47]

1.4.2.3 CPMG-type SSNMR Techniques

Another useful technique to acquire high resolution SSNMR spectra of heavy nuclei involves application of sequences of pulses to manipulate the spin system in desired way. One particular example of this sort of technique is the application of multi-pulse techniques such as the Carr-Purcell-Meiboom-Gill (CPMG) pulse sequence.[48-50] The CPMG sequence produces a series of spin echoes by the pulse sequence, $[90^\circ_x-\tau-(180^\circ_y-2\tau)_n]$. The spectrum resulting from the use of the CPMG experiment is called a spikelet spectrum, in which the band is frequency modulated to

produce a series of sidebands, the relative intensities of which can be used to determine the principal components of the tensor. This method typically improves the signal-to-noise ratio significantly by concentrating the response into the sidebands. For broad powder patterns, this substantially improves the detectability in a reasonable experimental time. Some applications of the CPMG pulse sequence to determining the chemical-shift tensors of heavy nuclei are given in ref. [51-54]

Although the CPMG technique increases signal-to-noise ratio and spreads the power out across a somewhat wider band efficiently, for very wide bands there is still a substantial power drop-off at frequencies far from the transmitter frequency. In an attempt to spread the power across the wider band, another technique is employed. This is the wideband uniform-rate smooth truncation (WURST) multi-pulse technique. [55-57] A WURST pulse is a phase- and amplitude-modulated pulse, the net effect of which is to spread the power over a range determined by the rate of slew of the frequencies and phases. If the WURST pulse is an inversion pulse (effectively a π pulse), one may use it in the CPMG sequence to excite a spikelet spectrum more uniformly over a wider range (often up to 500 kHz). This is the so-called WURST-CPMG sequence, resulting in significant reduction in experimental time to obtain the spikelet spectrum. WURST-CPMG techniques have been shown to be quite useful for the acquisition of broad NMR patterns of heavy-nuclei, which may have spans of hundreds of kHz.[58-62]

1.4.3 Correlation of Electronic and Solid-State Structure with NMR Parameters

Establishing the connection between the NMR parameters and the electronic structure of heavy-nuclei-containing solids is difficult. Various empirical

correlations of the chemical-shift tensors with structural and electronic properties of such systems have been proposed in the literature.[42, 63-65]

Among the spin-1/2 heavy nuclei in Table 1.1, ^{207}Pb has received the most attention by chemists attempting to establish a structure-shift relation. For example, Fayon et al.[63] showed there is a linear correlation between mean Pb-O bond length or coordination number (C.N.) of ^{207}Pb and the isotropic chemical shift. However, this linear relation does not hold for more covalent compounds such as $\alpha\text{-PbO}$ or Pb_3O_4 . In yet another example, ^{207}Pb nuclei in solid lead halides becomes less shielded with the decreasing electronegativity of the halide.[66] The trend of ^{207}Pb chemical shifts for the lead halides and lead hydroxyhalides has been correlated with the inverse ionization potential of these compounds.[67] Van Bramer et al.[68] have shown that the isotropic chemical shift of lead in materials containing lead(II) and oxyanions depends on the electronegativity of the central atom of the anion.

The solid-state NMR studies of certain lead compounds have provided correlations between the chemical-shift tensor of and the lone-pair activity.[69] In general, the chemical-shift tensor of ^{207}Pb with stereochemically active lone pair (hemidirected lead sites) exhibits large anisotropies (2000-4000 ppm) due to the asymmetry in the electron density distribution around the lead site.[43, 45, 53, 62-64, 70-74] For these systems, the skew (κ) of the chemical-shift tensor is positive and close to 1.00, which indicates the existence of a significantly shielded principal component. For lead sites without a stereochemically active lone pair, the chemical-shift tensor is more symmetric.[43, 63, 68] The reported investigations of lead(IV) sites show that the range of isotropic chemical shifts for these sites is smaller than the range of chemical shifts of lead(II) sites. The lead(IV) sites also generally have

smaller anisotropies, similar to anisotropies reported for a lead(II) site with a stereochemically inactive lone pair.[75, 76]

A similar trend can be observed for reported ^{119}Sn chemical-shift tensors and lone-pair activity of tin site. In general, the reported spans of tin(II) sites are in the range of 700-1000 ppm[65, 77-81] whereas the spans of tin(IV) sites are 100-300 ppm. In analogy to the hemidirected lead(II) sites, the ^{119}Sn chemical-shift tensor for the +2 oxidation state exhibits skews close to 1.00.

For ^{199}Hg -containing compounds, Bowmaker and his collaborators have shown an empirical relationship between the anisotropy of the ^{199}Hg chemical-shift tensor and the C.N. of mercury.[42, 82, 83] A relation between the symmetry of the mercury site and the asymmetry parameter, η , has been proposed for linear HgX_2 and tetragonal planar HgX_3 coordination geometries. For mercury compounds where C.N. = 2, the ^{199}Hg chemical-shift tensor may exhibit slight deviation from axial symmetry ($\delta_{11} = \delta_{22} > \delta_{33}$) due to small distortions from linearity.[42] Nevertheless, κ is larger than 0.8 for most cases. The anisotropies of the chemical-shift tensors for such systems are in the range of 3000-4000 ppm. When C.N. = 3, the reported anisotropies of the chemical-shift tensors are smaller (1500-2000 ppm).[42]

As an example of correlations for other nuclei, authors have proposed relationships between the chemical-shift tensors of ^{195}Pt and $^{203/205}\text{Tl}$ sites and electronic and solid-state structure of the materials. Some selected examples are given in the ref. [41, 60, 61, 84].

Currently, the trend is to NMR interaction tensors and their relationship to molecular structure using quantum chemical calculations. It is this type of connection between NMR parameters and electronic and solid-state structure that is the topic of

this dissertation, specifically for heavy nuclei like ^{207}Pb , ^{199}Hg , and ^{119}Sn . Our hypothesis is that it is possible, with modern quantum chemical computations, to calculate NMR magnetic-shielding tensors with sufficient accuracy that comparison of predicted NMR parameters with experiment allows one to corroborate structure.

REFERENCES

1. Kaupp, M., M. Buhl, and V.G. Malkin, *Calculation of NMR and EPR Parameters: Theory and Applications*. 2004, Weinheim: WILEY-VCH Verlag GmbH & Co. KGaA.
2. Vaara, J., *Theory and computation of nuclear magnetic resonance parameters*. Physical Chemistry Chemical Physics, 2007. **9**(40): p. 5399-5418.
3. Facelli, J.C., *Chemical shift tensors: Theory and application to molecular structural problems*. Progress in Nuclear Magnetic Resonance Spectroscopy, 2010. **58**(3-4): p. 176-201.
4. deDios, A.C., *Ab initio calculations of the NMR chemical shift*. Progress in Nuclear Magnetic Resonance Spectroscopy, 1996. **29**: p. 229-278.
5. Bonhomme, C., et al., *First-Principles Calculation of NMR Parameters Using the Gauge Including Projector Augmented Wave Method: A Chemist's Point of View*. Chemical Reviews, 2012. **112**(11): p. 5733-5779.
6. Holmes, S.T., et al., *Density functional investigation of intermolecular effects on C-13 NMR chemical-shielding tensors modeled with molecular clusters*. Journal of Chemical Physics, 2014. **141**(16): p. 164121.
7. Autschbach, J., *The calculation of NMR parameters in transition metal complexes*, in *Principles and Applications of Density Functional Theory in Inorganic Chemistry I*. 2004. p. 1-48.
8. Autschbach, J., *Relativistic calculations of magnetic resonance parameters: background and some recent developments*. Philosophical Transactions of the Royal Society a-Mathematical Physical and Engineering Sciences, 2014. **372**(2011): p. 20120489.
9. Pyykko, P., *Relativistic Effects in Structural Chemistry*. Chemical Reviews, 1988. **88**(3): p. 563-594.
10. Autschbach, J., *Perspective: Relativistic effects*. Journal of Chemical Physics, 2012. **136**(15): p. 15.
11. Haeberlen, U., *High Resolution NMR in Solids*. 1976, New York: Academic Press.
12. MacKenzie, K.J.D. and M.E. Smith, *Multinuclear Solid-State NMR of Inorganic Materials*. Pergamon Materials Series ed. R.W. Cahn. 2002, Amsterdam: Pergamon.
13. Orendt, A.M. and J.C. Facelli, *Solid-state effects on NMR chemical shifts*. Annual Reports on Nmr Spectroscopy, 2007. **62**: p. 115-178.

14. Pickard, C.J. and F. Mauri, *All-electron magnetic response with pseudopotentials: NMR chemical shifts*. Physical Review B, 2001. **63**(24): p. 13.
15. Sebastiani, D. and M. Parrinello, *A new ab-initio approach for NMR chemical shifts in periodic systems*. Journal of Physical Chemistry A, 2001. **105**(10): p. 1951-1958.
16. Sebastiani, D., et al., *NMR chemical shifts in periodic systems from first principles*. Computer Physics Communications, 2002. **147**(1-2): p. 707-710.
17. Tossell, J.A., *Second-nearest-neighbor effects upon N NMR shieldings in models for solid Si₃N₄ and C₃N₄*. Journal of Magnetic Resonance, 1997. **127**(1): p. 49-53.
18. Valerio, G., et al., *Calculation of Si-29 and Al-27 MAS NMR chemical shifts in zeolite-beta using density functional theory: Correlation with lattice structure*. Journal of the American Chemical Society, 1998. **120**(44): p. 11426-11431.
19. Tossell, J.A., *Second-nearest-neighbor effects on the NMR shielding of N in P(3)N(5) and hexagonal BN*. Chemical Physics Letters, 1999. **303**(3-4): p. 435-440.
20. Zhang, Y. and E. Oldfield, *Solid-state P-31 NMR chemical shielding tensors in phosphonates and bisphosphonates: A quantum chemical investigation*. Journal of Physical Chemistry B, 2004. **108**(50): p. 19533-19540.
21. Stueber, D., *The embedded ion method: A new approach to the electrostatic description of crystal lattice effects in chemical shielding calculations*. Concepts in Magnetic Resonance Part A, 2006. **28A**(5): p. 347-368.
22. Weber, J. and J. Gunne, *Calculation of NMR parameters in ionic solids by an improved self-consistent embedded cluster method*. Physical Chemistry Chemical Physics, 2010. **12**(3): p. 583-603.
23. Pavlovskaya, G.E., et al., *Metallic clusters and color changes in silver-exchanged zeolites: Ag-109 solid state NMR and optical studies*. Journal of Physical Chemistry B, 2004. **108**(5): p. 1584-1589.
24. Brouwer, D.H. and G.D. Enright, *Probing local structure in zeolite frameworks: Ultrahigh-field NMR measurements and accurate first-principles calculations of zeolite (29)Si magnetic shielding tensors*. Journal of the American Chemical Society, 2008. **130**(10): p. 3095-3105.
25. Wang, S., et al., *Solid-state NMR spectroscopy structure determination of a lipid-embedded heptahelical membrane protein*. Nature Methods. **10**(10): p. 1007-+.
26. Castellani, F., et al., *Structure of a protein determined by solid-state magic-angle-spinning NMR spectroscopy*. Nature, 2002. **420**(6911): p. 98-102.
27. Altounian, N., et al., *Thermodynamics of ion pairing in lead nitrate solutions as determined with Pb-207 NMR spectroscopy*. Journal of Physical Chemistry B, 2000. **104**(19): p. 4723-4725.

28. Rheingold, A.L., et al., *Superlattices, polymorphs and solid-state NMR spin-lattice relaxation (T-1) measurements of 2,6-di-tert-butyl-naphthalene*. Chemical Communications, 2000(8): p. 651-652.
29. Grutzner, J.B., et al., *A new mechanism for spin-lattice relaxation of heavy nuclei in the solid state: Pb-207 relaxation in lead nitrate*. Journal of the American Chemical Society, 2001. **123**(29): p. 7094-7100.
30. Beckmann, P.A., et al., *Pb-207 spin-lattice relaxation in solid PbMoO₄ and PbCl₂*. Physical Review B, 2006. **74**(21): p. 214421.
31. Vega, A.J., et al., *Spin-lattice relaxation of heavy spin-1/2 nuclei in diamagnetic solids: A Raman process mediated by spin-rotation interaction*. Physical Review B, 2006. **74**(21): p. 214420.
32. Taylor, R.E., et al., *A Combined NMR and DFT Study of Narrow Gap Semiconductors: The Case of PbTe*. The Journal of Physical Chemistry C, 2013. **117**(17): p. 8959-8967.
33. Bakhmutov, V.I., *Strategies for Solid-State NMR Studies of Materials: From Diamagnetic to Paramagnetic Porous Solids*. Chemical Reviews. **111**(2): p. 530-562.
34. Vaughan, R.W., *High-Resolution, Solid-State Nmr*. Annual Review of Physical Chemistry, 1978. **29**: p. 397-419.
35. Fyfe, C.A., et al., *One-Dimensional and 2-Dimensional High-Resolution Solid-State Nmr-Studies of Zeolite Lattice Structures*. Chemical Reviews, 1991. **91**(7): p. 1525-1543.
36. Laws, D.D., H.M.L. Bitter, and A. Jerschow, *Solid-state NMR spectroscopic methods in chemistry*. Angewandte Chemie-International Edition, 2002. **41**(17): p. 3096-3129.
37. Ramsey, N.F., *Magnetic Shielding of Nuclei in Molecules*. Physical Review, 1950. **78**(6): p. 699-703.
38. Fukui, H., *Theory and calculation of nuclear shielding constants*. Progress in Nuclear Magnetic Resonance Spectroscopy, 1997. **31**(4): p. 317-342.
39. Beeler, A.J., et al., *Low-Temperature C-13 Magnetic-Resonance in Solids .3. Linear and Pseudolinear Molecules*. Journal of the American Chemical Society, 1984. **106**(25): p. 7672-7676.
40. Mason, J., *Conventions for the Reporting of Nuclear Magnetic Shielding (or Shift) Tensors Suggested by Participants in the Nato Arw on Nmr Shielding Constants at the University-of-Maryland, College-Park, July 1992*. Solid State Nuclear Magnetic Resonance, 1993. **2**(5): p. 285-288.
41. Hinton, J.F., K.R. Metz, and R.W. Briggs, *Thallium Nmr-Spectroscopy*. Progress in Nuclear Magnetic Resonance Spectroscopy, 1988. **20**: p. 423-513.
42. Bowmaker, G.A., R.K. Harris, and S.W. Oh, *Solid-state NMR spectroscopy of mercury compounds*. Coordination Chemistry Reviews, 1997. **167**: p. 49-94.
43. Dybowski, C. and G. Neue, *Solid state Pb-207 NMR spectroscopy*. Progress in Nuclear Magnetic Resonance Spectroscopy, 2002. **41**(3-4): p. 153-170.

44. Herzfeld, J. and A.E. Berger, *Sideband Intensities in Nmr-Spectra of Samples Spinning at the Magic Angle*. Journal of Chemical Physics, 1980. **73**(12): p. 6021-6030.
45. Zhao, P.D., et al., *Lead-207 NMR spectroscopic study of lead-based electronic materials and related lead oxides*. Journal of Physical Chemistry B, 1999. **103**(48): p. 10617-10626.
46. Taylor, R.E., et al., *Revisiting HgCl₂: A solution- and solid-state Hg-199 NMR and ZORA-DFT computational study*. Journal of Molecular Structure, 2009. **930**(1-3): p. 99-109.
47. Taylor, R.E., S. Bai, and C. Dybowski, *A solid-state Hg-199 NMR study of mercury halides*. Journal of Molecular Structure, 2011. **987**(1-3): p. 193-198.
48. Hahn, E.L., *Spin Echoes*. Physical Review, 1950. **80**(4): p. 580-594.
49. Carr, H.Y. and E.M. Purcell, *Effects of Diffusion on Free Precession in Nuclear Magnetic Resonance Experiments*. Physical Review, 1954. **94**(3): p. 630-638.
50. Meiboom, S. and D. Gill, *Modified Spin-Echo Method for Measuring Nuclear Relaxation Times*. Review of Scientific Instruments, 1958. **29**(8): p. 688-691.
51. Hung, I., A.J. Rossini, and R.W. Schurko, *Application of the Carr-Purcell Meiboom-Gill pulse sequence for the acquisition of solid-state NMR spectra of spin-(1)/(2) nuclei*. Journal of Physical Chemistry A, 2004. **108**(34): p. 7112-7120.
52. Siegel, R., T.T. Nakashima, and R.E. Wasylshen, *Signal-to-noise enhancement of NMR spectra of solids using multiple-pulse spin-echo experiments*. Concepts in Magnetic Resonance Part A, 2005. **26A**(2): p. 62-77.
53. Briand, G.G., et al., *Probing lead(II) bonding environments in 4-substituted pyridine adducts of (2,6-Me₂C₆H₃S)(2)Pb: An X-ray structural and solid-state Pb-207 NMR study*. Inorganic Chemistry, 2007. **46**(21): p. 8625-8637.
54. O'Dell, L.A. and R.W. Schurko, *QCPMG using adiabatic pulses for faster acquisition of ultra-wideline NMR spectra*. Chemical Physics Letters, 2008. **464**(1-3): p. 97-102.
55. Kupce, E. and R. Freeman, *Optimized adiabatic pulses for wideband spin inversion*. Journal of Magnetic Resonance Series A, 1996. **118**(2): p. 299-303.
56. Bhattacharyya, R. and L. Frydman, *Quadrupolar nuclear magnetic resonance spectroscopy in solids using frequency-swept echoing pulses*. Journal of Chemical Physics, 2007. **127**(19): p. 8.
57. MacGregor, A.W., L.A. O'Dell, and R.W. Schurko, *New methods for the acquisition of ultra-wideline solid-state NMR spectra of spin-1/2 nuclides*. Journal of Magnetic Resonance, 2011. **208**(1): p. 103-113.
58. O'Dell, L.A., *The WURST kind of pulses in solid-state NMR*. Solid State Nuclear Magnetic Resonance. **55-56**: p. 28-41.
59. Schurko, R.W., *Ultra-Wideline Solid-State NMR Spectroscopy*. Accounts of Chemical Research. **46**(9): p. 1985-1995.

60. Lucier, B.E.G., et al., *Unravelling the Structure of Magnus' Pink Salt*. Journal of the American Chemical Society, 2014. **136**(4): p. 1333-1351.
61. Lucier, B.E.G., A.R. Reidel, and R.W. Schurko, *Multinuclear solid-state NMR of square-planar platinum complexes - Cisplatin and related systems*. Canadian Journal of Chemistry-Revue Canadienne De Chimie. **89**(7): p. 919-937.
62. Catalano, J., et al., *Pb-207 and Sn-119 Solid-State NMR and Relativistic Density Functional Theory Studies of the Historic Pigment Lead-Tin Yellow Type I and Its Reactivity in Oil Paintings*. Journal of Physical Chemistry A, 2014. **118**(36): p. 7952-7958.
63. Fayon, F., et al., *Empirical correlations between Pb-207 NMR chemical shifts and structure in solids*. Journal of the American Chemical Society, 1997. **119**(29): p. 6837-6843.
64. Gabuda, S.P., et al., *Pb-207 NMR study of novel Pb-Pb chemical bonding in lead monoxides, alpha-PbO and beta-PbO*. Chemical Physics Letters, 1999. **305**(5-6): p. 353-358.
65. Mitchell, M.R., et al., *Sn-119 MAS NMR and first-principles calculations for the investigation of disorder in stannate pyrochlores*. Physical Chemistry Chemical Physics, 2011. **13**(2): p. 488-497.
66. Nizam, M., et al., *Nmr Chemical-Shifts and the Electronic-Structure of Lead in Lead Halides*. Journal of Magnetic Resonance, 1989. **82**(3): p. 441-453.
67. Dybowski, C., et al., *Pb-207 NMR chemical-shift tensors of the lead (II) halides and the lead (II) hydroxyhalides*. Applied Spectroscopy, 1998. **52**(3): p. 426-429.
68. Van Bramer, S.E., et al., *Solid-state Pb-207 NMR studies of lead-group 16 and mixed transition-metal/lead-group 16 element-containing materials*. Magnetic Resonance in Chemistry, 2006. **44**(3): p. 357-365.
69. Shimoni-Livny, L., J.P. Glusker, and C.W. Bock, *Lone pair functionality in divalent lead compounds*. Inorganic Chemistry, 1998. **37**(8): p. 1853-1867.
70. Neue, G., et al., *Determination of Pb-207(2+) chemical shift tensors from precise powder lineshape analysis*. Solid State Nuclear Magnetic Resonance, 1996. **6**(3): p. 241-250.
71. Gabuda, S.P., et al., *Pb-207 NMR of minium, Pb3O4: evidence for the [Pb-2](4+) ion and possible relativistic effects in the Pb-Pb bond*. Solid State Nuclear Magnetic Resonance, 1999. **15**(2): p. 103-107.
72. Dmitrenko, O., et al., *The relationship between Pb-207 NMR chemical shift and solid-state structure in Pb(II) compounds*. Journal of Physical Chemistry A, 2008. **112**(14): p. 3046-3052.
73. Greer, B.J., et al., *Characterising Lone-Pair Activity of Lead(II) by Pb-207 Solid-State NMR Spectroscopy: Coordination Polymers of [N(CN)(2)](-) and [Au(CN)(2)](-) with Terpyridine Ancillary Ligands*. Chemistry-a European Journal, 2011. **17**(13): p. 3609-3618.

74. Catalano, J., et al., *Coordination geometry of lead carboxylates - spectroscopic and crystallographic evidence*. Dalton Transactions, 2015. **44**(5): p. 2340-2347.
75. Sebald, A. and R.K. Harris, *Pb-207 Cp Mas Nmr-Study of Hexaorganyldiplumbanes*. Organometallics, 1990. **9**(7): p. 2096-2100.
76. Buston, J.E.H., et al., *Pb-207 NMR chemical shifts of lead tetracarboxylates*. Magnetic Resonance in Chemistry, 2001. **39**(2): p. 68-76.
77. Cossement, C., et al., *Chemical-Shift Anisotropy and Indirect Coupling in Sno2 and Sno*. Magnetic Resonance in Chemistry, 1992. **30**(3): p. 263-270.
78. Amornsakchai, P., et al., *Solid-state NMR studies of some tin(II) compounds*. Solid State Nuclear Magnetic Resonance, 2004. **26**(3-4): p. 160-171.
79. Clayden, N.J., C.M. Dobson, and A. Fern, *High-Resolution Solid-State Sn-119 Nuclear Magnetic-Resonance Spectroscopy of Ternary Tin Oxides*. Journal of the Chemical Society-Dalton Transactions, 1989(5): p. 843-847.
80. Harris, R.K., et al., *Sn-119 Nmr Shielding Anisotropy and Molecular-Structure*. Journal of Molecular Structure, 1995. **347**: p. 309-319.
81. Mundus, C., et al., *A Sn-119 solid-state nuclear magnetic resonance study of crystalline tin sulphides*. Solid State Nuclear Magnetic Resonance, 1996. **7**(2): p. 141-146.
82. Bowmaker, G.A., et al., *Solid-state Hg-199 MAS NMR studies of mercury(II) thiocyanate complexes and related compounds. Crystal structure of Hg(SeCN)(2)*. Inorganic Chemistry, 1998. **37**(8): p. 1734-1743.
83. Bowmaker, G.A., R.K. Harris, and D.C. Apperley, *Solid-state Hg-199 MAS NMR and vibrational spectroscopic studies of dimercury(I) compounds*. Inorganic Chemistry, 1999. **38**(22): p. 4956-4962.
84. Gabuda, S.P., S.G. Kozlova, and R.L. Davidovich, *Novel-type chemical bonding in TlF due to 6s(2) inert pair activation*. Chemical Physics Letters, 1996. **263**(1-2): p. 253-258.

Chapter 2

QUANTUM CHEMICAL CALCULATIONS OF NMR PARAMETERS

2.1 Theoretical Framework of Density Functional Theory

The primary objective of most state-of-the-art quantum chemical methods is to obtain approximate solutions to the non-relativistic many-body Schrodinger's equation. Under the Born-Oppenheimer approximation, the many-body Schrodinger's equation for an N -electron system is given in atomic units as:

$$\left(-\sum_i^N \frac{1}{2} \nabla_i^2 - \sum_i^N \sum_k^M \frac{Z_k}{r_{ik}} + \sum_i^N \sum_{j>i}^N \frac{1}{r_{ij}} \right) \Psi = E\Psi \quad (2.1)$$

In eq. 2.1, Ψ is the **electronic** wave function and E is the total **electronic** energy. The first term describes the kinetic energy of the N -electron system. The second term gives the potential energy of interaction between the electrons and nuclei, and the third term provides the potential energy of the electron-electron interactions. The presence of the electron-electron interaction term means that the many-body Schrodinger's equation cannot be solved exactly. Hence, approximate quantum chemical methods have been developed to solve Schrodinger-like equations to define complex quantum systems. These approximate methods include Hartree-Fock theory, Moller-Plesset perturbation theory (MP_N), and coupled-cluster methods.[1]

The central quantity of equation 2.1 is the electronic wave function, Ψ . It is a complex quantity that depends on $4N$ variables ($3N$ spatial variables and N spin variables). As mentioned, solution of Eq. 2.1 to obtain the wave function can only be

approximate. One may choose to focus not on the electronic wave function, but rather on a related quantity, the electron density, $\rho(\mathbf{r})$, defined in Eq. 2.2.

$$\rho(\mathbf{r}) = N \int \dots \int |\Psi(\mathbf{x}_1 \mathbf{x}_2 \dots \mathbf{x}_N)|^2 d\mathbf{s}_1 \mathbf{x}_2 \dots \mathbf{x}_N \quad (2.2)$$

The motivation behind density functional theory (DFT) is to solve for the electronic density function, from which one may calculate properties that depend on the electronic state of a system. In particular, focusing on the electron density reduces this complexity of solving for the wave function because $\rho(\mathbf{r})$ depends only on the 3 spatial co-ordinates.

Using electron density rather than a wave function to obtain information about the many-electron systems dates back to early work by Thomas and Fermi in 1927. In this model, the electronic kinetic energy is derived from the quantum statistical theory of a uniform electron gas, whereas the electron-electron and electron-nuclear interactions are treated in a classical manner.

The Thomas-Fermi model is a very crude approximation to the total energy of a many-electron system; however, it illustrates how the energy of a system can be determined purely from the electron density, instead of from the electronic wave function. Although crude, it serves as a theoretical starting point for what is now known as density functional theory (DFT).[2, 3]

2.1.1 Kohn-Sham Formalism of Density Functional Theory

Although the Thomas-Fermi model gives a recipe to approximate the energy from the electron density of a system containing many electrons, modern DFT originated with papers by Hohenberg and Kohn in 1964,[4] and Kohn and Sham in

1965.[5] In the first paper, Hohenberg and Kohn proved two key theorems of DFT, known as Hohenberg-Kohn (HK) theorems. The first HK theorem shows that there is a one-to-one mapping of external potential to ground state density, up to an arbitrary additive constant. The second HK theorem shows the existence of a variational principle for the energy functional of the electron density, thus allowing one to find the best functional possible for describing a system.

Although the HK theorems provide the formal proof of the central importance of the electron density in determining the ground-state energy of a system, the paper by Kohn and Sham in 1965 provides the practical equations to calculate the ground-state energy. In the Kohn-Sham (KS) formalism, the energy functional, $E[\rho(\mathbf{r})]$, is given by eq. 2.3. [2]

$$E[\rho(\mathbf{r})] = T[\rho(\mathbf{r})] + J[\rho(\mathbf{r})] + \int V(\mathbf{r})_{\text{ext}} \rho(\mathbf{r}) d\mathbf{r} + E_{\text{xc}}[\rho(\mathbf{r})] \quad (2.3)$$

The right hand side of eq. 2.3 collects the kinetic energy (T), classical coulomb energy (J), and non-classical exchange-correlation energy (E_{xc}) as functionals of the density. In this expression, the explicit forms of $T[\rho(\mathbf{r})]$ and $E_{\text{xc}}[\rho(\mathbf{r})]$ are not known and must be approximated. In fact, the errors in the Thomas-Fermi model mainly result from the description of the kinetic energy functional by using the uniform electron gas model. In the KS formalism, the kinetic energy functional is expressed in a similar fashion to Hartree-Fock theory, as indicated in eq. 2.4.

$$T[\rho(\mathbf{r})] = -\frac{1}{2} \sum_i^N \int \langle \phi_i | \nabla_i^2 | \phi_i \rangle d\mathbf{r} \quad (2.4)$$

In this equation, ϕ_i is a one-electron orbital of a non-interacting fictitious system. These orbitals are known as KS orbitals. The relation between KS orbitals and the real interacting system is given by eq. 2.5.

$$\rho_o(\mathbf{r}) = \sum_i^N |\phi_i|^2 \quad (2.5)$$

where $\rho_o(\mathbf{r})$ is the exact electron density of the interacting system obtained from the one-electron orbitals of the artificial non-interacting system. This relation is provided in the KS formalism by choosing an effective potential (dependent on the exchange-correlation functional) such that the resulting one-electron orbitals satisfy the relation given in eq. 2.4.

The introduction of orbitals leads to the central equation of KS-DFT, which is obtained by combining eq. 2.3, 2.4 and 2.5. After some rearrangement, the one-electron KS equation is expressed as:

$$\left(-\frac{1}{2}\nabla_i^2 + v(\mathbf{r})_{\text{ext}} + \int \frac{\rho(\mathbf{r}')}{|\mathbf{r} - \mathbf{r}'|} d\mathbf{r}' + v_{\text{XC}}(\mathbf{r}) \right) \phi_i = \varepsilon \phi_i \quad (2.6)$$

Here, the exchange-correlation potential is formally defined as the following functional derivative expression:

$$v_{\text{XC}}(\mathbf{r}) = \frac{\delta E_{\text{xc}}[\rho(\mathbf{r})]}{\delta \rho(\mathbf{r})} \quad (2.7)$$

In eq. 2.6, the coulomb potential and the exchange-correlation potential depend on the electron-density. As a result, the KS equations can only be solved using self-consistent-field (SCF) methods. The general procedure starts with the introduction of an auxiliary basis-set expansion for the one-electron orbitals:[1]

$$\phi_i = \sum_v^M c_{iv} \psi_v \quad (2.8)$$

The basis-set expansion of one-electron orbitals reduces the integro-differential form of eq. 2.6 to a computationally easier matrix equation form. To solve this equation, an initial guess for the expansion coefficients (Eq. 2.8) must be specified. This is usually done by using the symmetry properties of the system at hand. From this initial guess, matrix form of eq. 2.6 can be solved iteratively until a convergence threshold is achieved. Finally, the total energy and other desired properties of the system can be evaluated from this final density of the SCF cycle.

2.1.2 Exchange-Correlation Functionals

The KS formalism of DFT described briefly in the previous section is exact, in theory. However, this is far from the reality of practice, because the exactness of this formalism requires complete knowledge of the form of $E_{xc}[\rho(\mathbf{r})]$ (or the potential form of the functional, $v_{xc}(\mathbf{r})$), which then yields all non-classical interactions of the many-electron system.

The main goal of modern DFT is to find a good approximation for the $E_{xc}[\rho(\mathbf{r})]$. In general, modern DFT formalisms differ only with respect to $E_{xc}[\rho(\mathbf{r})]$. As a result, DFT formalisms are named in the literature and textbooks using acronyms which refer to $E_{xc}[\rho(\mathbf{r})]$. For example, the famous hybrid functional named B3LYP is an acronym for Becke 3-parameter exchange[6] and Lee, Yang and Parr correlation.[7] Today, there is a large selection of exchange-correlation functionals which have been implemented in various program packages. In this section, some of the most common exchange-correlation functionals are discussed briefly.

2.1.2.1 Local Density Approximation (LDA)

Local density (or local spin density) approximation (LDA) is the first step in the quest for the universal $E_{xc}[\rho(\mathbf{r})]$. The very first LDA approach was employed by Kohn and Sham in the original DFT paper.[5] In this approximation, exchange and correlation energies of a given system are approximated by the energy of the homogenous electron gas. The exchange-correlation functional in LDA is expressed by the following relation:

$$E_{XC}^{LDA}[\rho(\mathbf{r})] = \int \rho(\mathbf{r})\epsilon_{XC}(\rho(\mathbf{r}))d\mathbf{r} \quad (2.9)$$

In this expression, $\epsilon_{XC}(\rho(\mathbf{r}))$ is the exchange-correlation energy of the homogenous electron gas per electron. The exchange part of ϵ_{XC} is known analytically, whereas the correlation part can be obtained by employing accurate Monte-Carlo simulations. The LDA functional is local in the sense that the functional depends only on the local values of $\rho(\mathbf{r})$. Despite this drastic approximation at its core, LDA can predict molecular properties of certain systems successfully. However the accuracy of LDA is still insufficient for most chemical systems.

2.1.2.2 Generalized Gradient Approximation (GGA)

The generalized gradient approximation (GGA) produces the next generation of exchange-correlation functionals for the DFT formalism. In GGA, $E_{xc}[\rho(\mathbf{r})]$ depends on density, as well as the gradient of density at each point in space. The exchange-correlation functional within GGA is expressed generically as:

$$E_{XC}^{GGA}[\rho(\mathbf{r})] = \int \rho(\mathbf{r})\epsilon_{XC}(\rho(\mathbf{r}), \nabla\rho(\mathbf{r}))d\mathbf{r} \quad (2.10)$$

GGA functionals are still local, in a mathematical sense. However, they include corrections beyond LDA (homogenous electron density) via the gradient of the

electron density, to account for inhomogeneity in the system. For many chemical systems, the GGA functionals yield much better results than LDA with a comparable scaling factor. As a result, GGA serves as the basic machinery of DFT today for most chemical applications. Some famous GGA functionals include BP86, Becke's exchange functional[8] and Perdew's correlation functional,[9] and PBE, the Perdew-Burke-Ernzerhof exchange-correlation functional. [10]

2.1.2.3 Hybrid Functionals

Hybrid functionals are the next successful alternative to calculate $E_{xc}[\rho(\mathbf{r})]$. The idea behind the introduction of hybrid functionals is to include the exact exchange term from HF theory. Hybrid functionals are generally composed of linear combination of different terms, where the contributions of those terms are fitted by comparison to experiment or post-ab initio methods. For example, the $E_{xc}[\rho(\mathbf{r})]$ for the B3LYP [3, 6] functional is expressed as:

$$E_{XC}^{B3LYP}[\rho(\mathbf{r})] = E_{XC}^{LDA} + a_0(E_X^{HF} - E_X^{LDA}) + a_X(E_X^{GGA} - E_X^{LDA}) + a_C(E_C^{GGA} - E_C^{LDA}) \quad (2.11)$$

Here, the fitted parameters are $a_0 = 0.20$, $a_X = 0.72$ and $a_C = 0.81$. The other widely used hybrid functionals include PBE0[11, 12], B1LYP[13], and B1PW91[14]. In general, hybrid functionals show improvement over GGA functionals for chemical applications.[2, 15]

In this dissertation, some applications of hybrid functionals to the prediction of magnetic shielding of heavy nuclei are discussed in the following chapters. However, the calculation of $E_{xc}[\rho(\mathbf{r})]$ in hybrid functionals requires the calculation of exchange energy from HF theory using one-electron orbitals. This procedure involves numerical determination of two-electron integrals, which is the bottleneck in quantum chemistry

methods. Thus, the computational time in use of hybrid functionals is considerably greater than that for their GGA counterparts.

2.1.3 On the Accuracy of DFT

The KS-DFT is, by no means, a flawless theory. Despite its popularity among computational chemists, there are still some areas where the errors in DFT results in failures to accurately predict the physicochemical properties. A large number of problems in DFT are caused by self-interaction error. The self-interaction error refers to the non-physical interaction of an electron by itself.[2, 16-18] The self-interaction is cancelled via construction of the exchange contribution in the HF formalism. However, since the exchange is only approximated in DFT by the exchange-correlation functional, a residual self-interaction remains. An important example of self-interaction error in DFT is the application to stretched H_2^+ , the simplest molecule in chemistry. In this example, DFT predicts a total energy that is significantly lower than the exact total energy from HF theory at longer bond lengths. This failure of DFT is caused by the non-physical delocalization of the electron density as a result of self-interaction of the electron.[18]

Another important issue in approximate DFT is the meaning of KS orbitals and their eigenvalues. In KS-DFT, orbitals are only introduced as a mathematical trick to obtain a better approximation for the kinetic energy by using eq. 2.4 and 2.5. For this reason, it is often claimed that KS orbitals have no physical meaning, in a strict sense. Additionally, there is no equivalence of Koopmans' theorem in DFT, which would relate the KS eigenvalues to the ionization potentials of a given system in the frozen-orbital approximation. However, the relation between the energy of the highest occupied level and first ionization potential was shown by Janak for exact DFT.[19]

The physical meaning of KS orbitals is still an issue for debate among theoretical chemists and physicists.[20-22] In practice, KS orbitals and their eigenvalues have been used successfully in many qualitative and quantitative descriptions of chemical properties.

2.2 Introducing Relativity in Quantum Chemistry Methods

The impact of relativistic effects in chemistry is a broad and active research area. Some famous textbook examples of the relativistic effects include the yellow color of gold, why mercury is liquid at room temperature, the observed lanthanide contractions, and the inert-pair effect of the 6s orbital in thallium(I) and lead(II).[23-25] Recently, it was shown by Ahuja et al.[26] that 1.7-1.8 V of the standard voltage in car batteries (2.13 eV) arise from relativistic effects in PbO_2 . In another striking example, Hrobarik et al.[27] showed that about 30 ppm deshielding of ^1H chemical shifts are the result of spin-orbit (SO) relativistic effects.

In the preceding section, we have briefly introduced the many-body Schrodinger equation and KS-DFT. However, our discussion was strictly within the non-relativistic limit, which means that all the effects arising from the finite speed of light ($c \approx 137.03599$ au) are ignored. According the Einstein's theory of special relativity, all physical laws and equations must be invariant under Lorentz transformation. Eq. 2.1 is not invariant under such a transformation. Therefore, one needs another set of equations to account the relativistic effects in chemical applications.[28]

2.2.1 Dirac Equation

The starting point for relativistic quantum chemistry is the equation proposed by Dirac in 1928.[29] The relativistic Hamiltonian for a free particle is expressed in eq. 2.12.

$$H = \sqrt{m^2c^4 + p^2c^2} \quad (2.12)$$

From eq. 2.12, one may obtain a wave equation upon the canonical substitution of momentum with its operator form. However, the resulting equation is still not Lorentz invariant because the orders of the derivatives for space and time co-ordinates are different. At this point, Dirac realized that eq. 2.12 could be linearized by introducing matrices, as shown in eq. 2.13.

$$H = \sqrt{m^2c^4 + p^2c^2} = c\boldsymbol{\alpha} \cdot \mathbf{p} + \boldsymbol{\beta}mc^2 \quad (2.13)$$

In this equation, $\boldsymbol{\alpha}$ and $\boldsymbol{\beta}$ are the 4×4 Dirac matrices which are expressed in the block matrix form by the following expression;

$$\boldsymbol{\alpha} = \begin{pmatrix} 0_2 & \boldsymbol{\sigma} \\ \boldsymbol{\sigma} & 0_2 \end{pmatrix}; \boldsymbol{\beta} = \begin{pmatrix} I_2 & 0_2 \\ 0_2 & -I_2 \end{pmatrix} \quad (2.14)$$

where $\boldsymbol{\sigma}$ ($\boldsymbol{\sigma} = \sigma_x, \sigma_y, \sigma_z$) are 2×2 **Pauli spin matrices** and I_2 is the 2×2 identity matrix and 0_2 is the 2×2 zero matrix. In this form, Dirac's equation can be written, after some rearrangements, in atomic units as

$$H^D \Psi^D = \begin{pmatrix} V & c\boldsymbol{\sigma} \cdot \mathbf{p} \\ c\boldsymbol{\sigma} \cdot \mathbf{p} & V - 2c^2 \end{pmatrix} = E \Psi^D \quad (2.15)$$

There are two important aspects of Eq. 2.15. Firstly, the **spin** of the electron is incorporated in Dirac's equation explicitly through the introduction of Pauli matrices in the linearization of the Hamiltonian in eq. 2.13. In contrast, electron spin can be introduced into the non-relativistic quantum mechanics only by an ad-hoc assumption. The other important aspect of eq. 2.15 is the fact that it has both positive

and negative energy solutions. The negative energy solutions of Dirac's equation eventually led to the idea of the existence of anti-particle states of electrons, called positrons. Nowadays, we consider this the birth of quantum field theory, although Dirac initially dismissed the negative-energy solutions of the problem when it was first published.

In quantum chemistry, we generally seek the solutions of eq. 2.15 that correspond to the positive-energy spectrum. As we see below, the solutions may be grouped into two components, the so-called large and small components. As an approximation, it is often typical that one seeks the positive-energy solutions only with the large components.

2.2.2 Four-Component and Two-Component Relativistic Methods

Due to the 4×4 matrix form of eq. 2.15, the eigenvector solutions of this equation are composed of four components:

$$\Psi^D = \begin{pmatrix} \psi_1 \\ \psi_2 \\ \psi_3 \\ \psi_4 \end{pmatrix} = \begin{pmatrix} \psi_L \\ \psi_S \end{pmatrix}; \psi_L = \begin{pmatrix} \psi_1 \\ \psi_2 \end{pmatrix}, \psi_S = \begin{pmatrix} \psi_3 \\ \psi_4 \end{pmatrix} \quad (2.16)$$

In eq. 2.16, the eigenvector solution is grouped into the large component, (ψ_L) and the small component (ψ_S) of the Dirac wave function. For the positive-energy spectrum, the contribution of the small component is much smaller than that of the large component. If eq. 2.15 and 2.16 are combined, the following expressions are obtained.

$$V\psi_L + c\boldsymbol{\sigma} \cdot \mathbf{p}\psi_S = E\psi_L \quad (2.17a)$$

$$c\boldsymbol{\sigma} \cdot \mathbf{p}\psi_L + (V - 2c^2)\psi_S = E\psi_S \quad (2.17b)$$

In eq. 2.17, the small and large components of the Dirac wave function are coupled by the following relation.

$$\psi_S = \frac{1}{2c} k \boldsymbol{\sigma} \cdot \mathbf{p} \psi_L \quad (2.18a)$$

$$k = \left(1 - \frac{V - E}{2c^2} \right)^{-1} \quad (2.18b)$$

In the four-component relativistic formalism, one seeks solutions to both small and large components via simultaneous solutions of the equations in 2.17. However, early attempts with an auxiliary basis set suffered from the so called ‘variational collapse’ [30, 31] when small and large components were varied independently. This problem can be overcome by relating the basis sets for small and large components via eq. 2.18a, which is referred as the kinetic balance approximation.[32] Using eq. 2.18a, one eliminates the small component of the Dirac wave function and sees solutions for only the large component. This approach yields the following eigenvalue equation for the large component only:

$$\left[V + \frac{1}{2} \boldsymbol{\sigma} \cdot \mathbf{p} k \boldsymbol{\sigma} \cdot \mathbf{p} \right] \psi_L = E \psi_L \quad (2.19)$$

This equation is not practical since the Hamiltonian operator depends on k (and E). At this point, one may decouple the small and large components completely by employing Foldy-Wouthuysen transformations,[33] which leads to **exact two-component** relativistic methods. Another approach is to construct approximate decoupling schemes by expanding k in a power series. This formalism leads to **quasi-relativistic two-component** methods. A famous example of such a method is called the zeroth order regular approximation (ZORA),[34-36] which is discussed in the following sub-section.

2.2.3 Zeroth Order Regular Approximation

It is possible to obtain a more practical expression for the Hamiltonian in Eq. 2.19 by employing a power series expansion for k .

$$k = \left(1 - \frac{V - E}{2c^2}\right)^{-1} = 1 + \sum_{n=1}^{\infty} \left(\frac{V - E}{2c^2}\right)^n \quad (2.20)$$

At the first order of this expansion, one gets the Pauli Hamiltonian after some manipulation.

$$H^{Pauli} = V + \frac{p^2}{2} - \frac{p^4}{8c^2} + \frac{Vp^2}{8c^2} + \frac{i}{4c^2} \boldsymbol{\sigma} \cdot (\nabla V \times \mathbf{p}) \quad (2.21)$$

In eq. 2.21, first two terms on the right hand side recover the non-relativistic Hamiltonian. The third term is called the mass-velocity operator, which yields relativistic corrections to the kinetic energy due to the mass-increase effect in special relativity. The fourth term is the Darwin term, which gives a correction to the potential near the nucleus. The last term is the spin-orbit coupling term. It should be noted that the Pauli Hamiltonian transforms to the non-relativistic Hamiltonian at the limit ($c \rightarrow \infty$).

Another expansion[34] can be made for k by the following relation:

$$\begin{aligned} k &= \frac{c^2}{2c^2 - V} \left(1 + \frac{E}{2c^2 - V}\right)^{-1} \\ &= \frac{c^2}{2c^2 - V} + \left(\frac{c^2}{2c^2 - V}\right) \sum_{n=1}^{\infty} -1^n \left(\frac{E}{2c^2 - V}\right)^n \end{aligned} \quad (2.22)$$

At the zeroth order of this expansion series, one can get the ZORA Hamiltonian after some arrangements, which is expressed by eq. 2.23.

$$\begin{aligned}
H^{ZORA} &= V + \frac{1}{2} \boldsymbol{\sigma} \cdot \mathbf{p} \left(\frac{c^2}{2c^2 - V} \right) \boldsymbol{\sigma} \cdot \mathbf{p} \\
&= V + \frac{1}{2} \mathbf{p} \left(\frac{c^2}{2c^2 - V} \right) \mathbf{p} + \frac{i}{2} \left(\frac{c}{2c^2 - V} \right)^2 \boldsymbol{\sigma} \cdot (\nabla V \times \mathbf{p})
\end{aligned} \tag{2.23}$$

The ZORA Hamiltonian includes the familiar spin-orbit coupling term even at the zeroth order of expansion. The complete Hamiltonian in Eq. 2.23 is referred as the ZORA/spin-orbit Hamiltonian. If the spin-orbit coupling term is neglected, one gets the ZORA/scalar Hamiltonian.

The ZORA Hamiltonian gives valence-shell properties and orbital energies of heavy elements, as can four-component relativistic methods.[36] However, the core levels of systems modeled by the ZORA Hamiltonian generally have substantial errors,[37] as a result of the truncation at zeroth order of the expansion of the k in Eq. 2.22. In this expansion, the terms with the constant E are neglected. This neglect is justified for the valence shell orbitals where E is relatively small. However, this approximation carries inherent errors for the core levels where E is large.

2.3 Theory of Magnetic Shielding

Magnetic shielding is the **electronic** contribution to the interaction between the magnetic moment of the nucleus ($\boldsymbol{\mu}_n$) and the external magnetic field (\mathbf{B}_0). This interaction can be expressed by the following Hamiltonian;

$$H^{\text{Spin}} = \boldsymbol{\mu}_n \boldsymbol{\alpha} (1 - \sigma_{\alpha\beta}) \mathbf{B}_{0\beta}; \quad \boldsymbol{\sigma} = \begin{bmatrix} \sigma_{xx} & \sigma_{xy} & \sigma_{xz} \\ \sigma_{yx} & \sigma_{yy} & \sigma_{yz} \\ \sigma_{zx} & \sigma_{zy} & \sigma_{zz} \end{bmatrix} \tag{2.24}$$

In this equation, $\boldsymbol{\sigma}$ is the magnetic-shielding tensor, a rank-2 tensor. It is specified by nine independent components. However, the point symmetry at the nuclear site may reduce the number of independent components. The earliest attempt

at a theory of magnetic shielding was given by Lamb in 1941.[38] His theory considered an explicitly spherically symmetric charge distribution around the nucleus. A more general nonrelativistic quantum-mechanical formalism of magnetic shielding was developed by Ramsey in 1950, which gave expressions for the magnetic shielding in terms of perturbation corrections to the energy caused by the coupling of the spins to the external field mediated by the electrons.[39]

2.3.1 Formulation of Magnetic Shielding from Double Perturbation Theory

The formal definition of the magnetic-shielding tensor is given as the second-order mixed derivative of the **total energy** with respect to the component of the magnetic moment of the nucleus and the component of the external magnetic field, as shown in eq. 2.25.

$$\sigma_{\alpha\beta} = \left. \frac{\partial^2 E}{\partial \mu_\alpha \partial B_\beta} \right|_{\mu_\alpha=0, B_\beta=0} \quad (2.25)$$

For such mixed properties expressed as a second-order energy derivative, one can apply double (or multiple) perturbation theory and the sum over states formula to obtain an explicit expression for the property.[39-43] In the generic formulation of double perturbation theory, the Hamiltonian is expanded in Taylor series using the arbitrary perturbation parameters λ and κ .

$$H = H_0 + \kappa H_{10} + \lambda H_{01} + \kappa\lambda H_{11} + \kappa^2 H_{20} + \dots \quad (2.26a)$$

$$E = E_0 + \kappa E_{10} + \lambda E_{01} + \kappa\lambda E_{11} + \kappa^2 E_{20} + \dots \quad (2.26b)$$

At this point in the derivation, one defines the second-order mixed property E_{11} , by employing a perturbation approach, as shown in eq. 2.27.

$$\begin{aligned}
E_{11} &= \left. \frac{\partial^2 E}{\partial \lambda \partial \kappa} \right|_{\lambda=0, \kappa=0} \\
&= \langle \Psi_0 | H_{11} | \Psi_0 \rangle + 2 \sum_{n \neq 0} \frac{\langle \Psi_0 | H_{10} | \Psi_n \rangle \langle \Psi_n | H_{01} | \Psi_0 \rangle}{E_n - E_0} \quad (2.27)
\end{aligned}$$

To relate the perturbation energy of eq. 2.27 to the magnetic-shielding tensor, one defines the Hamiltonian in the presence of an external magnetic field and a nuclear magnetic moment. This Hamiltonian (**in the non-relativistic limit**) reads, for an N electron system, as

$$H = - \sum_i^N \frac{1}{2} [\nabla_i + \mathbf{A}_0(i) + \mathbf{A}_n(i)]^2 - \sum_i^N \sum_k^M \frac{Z_i}{r_{ik}} + \sum_i^N \sum_{j>i}^N \frac{1}{r_{ij}} \quad (2.28)$$

where \mathbf{A}_0 and \mathbf{A}_n are the vector potentials for the external magnetic field and nuclear magnetic moment, given in eq. 2.29.

$$\mathbf{A}_0(i) = \frac{1}{2} \mathbf{B}_0 \times \mathbf{r}_{i0}, \mathbf{r}_{i0} = \mathbf{r}_i - \mathbf{R}_0 \quad (2.29a)$$

$$\mathbf{A}_n(i) = \frac{\boldsymbol{\mu}_n \times \mathbf{r}_{in}}{r_{in}^3}, \mathbf{r}_{in} = \mathbf{r}_i - \mathbf{R}_n \quad (2.29b)$$

In eq. 2.29, \mathbf{R}_0 is the position of the gauge origin and \mathbf{R}_n is the position of the nuclear magnetic moment. The expansion of the Hamiltonian in eq. 2.28 around $\boldsymbol{\mu}_n$ and \mathbf{B}_0 beyond zero order yields the relevant terms to define the magnetic-shielding tensor.

$$H_{11} = \frac{1}{2c^2} \sum_i^N \frac{(\mathbf{r}_{i0} \cdot \mathbf{r}_{in} - r_{i0} r_{in})}{r_{in}^3} \quad (2.30a)$$

$$H_{10} = \frac{1}{c^2} \sum_i^N \frac{\mathbf{L}_{in}}{r_{in}^3} \quad (2.30b)$$

$$H_{01} = \frac{1}{2} \sum_i^N \mathbf{L}_{i0} \quad (2.30c)$$

where \mathbf{L}_{i0} and \mathbf{L}_{in} are angular momentum operators for electron i with respect to the gauge origin and to the nucleus respectively. Insertion of the equations in 2.30 into Eq. 27 gives the expression for the magnetic shielding in atomic units:

$$\sigma = \langle \Psi_0 | H_{11} | \Psi_0 \rangle + 2 \sum_{m \neq 0} \frac{\langle \Psi_0 | H_{10} | \Psi_m \rangle \langle \Psi_m | H_{01} | \Psi_0 \rangle}{E_m - E_0} \quad (2.31)$$

There are certain aspects of eq. 2.31 that are quite important for quantum chemical calculations of the magnetic-shielding tensor. The expression for the magnetic-shielding tensor (eq. 2.31) shows that there are two contributions. The first term in eq. 2.31 is called the **diamagnetic** term. It depends solely on the ground-state wave function. The second term is called the **paramagnetic** term, which involves both ground- and excited-state wave functions. However, the physical meaning of this separation into two terms for practical calculations in chemical systems is subject to debate due to gauge dependence.[44, 45] Different choices of gauge origin, \mathbf{R}_0 , of the origin of the vector field, result in different parsing of the magnetic-shielding into to the two terms. The gauge dependence in these terms cancels each other out completely, if the **exact wave function** or a variational approximation of the wave function using a **complete basis set** is employed.

Eq. 2.31 is theoretically exact in the **non-relativistic** limit, because all the terms relevant to magnetic shielding are collected in the perturbation expansion. In practical applications, however, this is not true, as the exact form of the ground state wave-function is generally not available for use in this expression, and approximations to the form of the wave function must be used.

Eq. 2.28 is not appropriate for calculation of magnetic shielding when one must include the effects of **relativity**. [24, 46, 47] Inclusion of relativistic effects requires modification of the form of eq. 2.31. For example, in the ZORA formalism for inclusion of the relativistic effects, the expression for the magnetic shielding involves the familiar diamagnetic and paramagnetic terms in eq. 2.31. But, the formalism produces additional terms in the expression, which arise from spin-orbit coupling that occur naturally in the application of the ZORA Hamiltonian.[48, 49]

2.3.2 Gauge Origin Dependence

As mentioned in the previous subsection, the paramagnetic and diamagnetic components of the shielding expression depend on the choice of gauge for the vector potential. The gauge-dependent terms cancel out perfectly in the limit of an infinite basis set. However, in practical calculations where a finite basis set is employed, the calculated magnetic shielding depends on the choice of gauge origin (or choice of the co-ordinate system for the molecule). This dependence is called the **gauge-origin problem**, or lack of gauge invariance. For some examples of gauge dependence in common magnetic shielding calculations, readers are referred to references [44, 45, 47].

There have been various methods proposed to solve the gauge-origin problem in magnetic shielding calculations. One commonly employed method is through the use of gauge-including atomic orbitals (GIAO). This approach was first employed by London in 1937[50] for calculations of electronic energies in an external magnetic field. Later, the method was adapted for magnetic shielding calculations by Pople[51, 52] and by Ditchfield.[41] In the GIAO method, the atomic orbitals (or basis

functions) are modified to include a phase factor that depends on the gauge origin, as expressed in eq. 2.32.

$$\phi_v^{GIAO}(\mathbf{B}_0) = e^{i\mathbf{A}_v \cdot \mathbf{r}} \chi_v \quad (2.32)$$

The GIAO method has been implemented in various *ab initio* methods, including DFT methods for magnetic shielding calculations that include relativistic effects.[53, 54] The convergence of calculated magnetic shielding with respect to basis set size is much faster with GIAOs when compared to other common-origin methods. Other than GIAO, additional methods to account for the gauge dependence in magnetic-shielding calculations include the methods called individual gauge for localized orbitals (IGLO), localized orbital/local origin method (LORG), and the polarization propagator approximation (PPA).[47, 55]

2.3.3 Magnetic Shielding Calculations for Many-Electron Systems

To calculate the magnetic shielding within the framework of DFT, the first step is to solve the KS equations (Eq. 2.6) for the ground-state density without the presence of a perturbing magnetic field. Subsequently, the contributions to eq. 2.31 are obtained as a sum over one-electron states. In this formalism, the ground-state wave function is replaced by products of one-electron KS orbitals, from which one obtains the ground-state energy. For the excited states, virtual KS orbitals are used in a similar manner. The transformed DFT equation of the magnetic shielding for N occupied and M virtual KS orbitals is shown in eq. 2.33.

$$\sigma = \sum_i^N \langle \phi_i^{occ} | h_{11} | \phi_i^{occ} \rangle + 2 \sum_i^N \sum_j^M \frac{\langle \phi_i^{occ} | h_{01} + V'_{xc}(\mathbf{B}_0) | \phi_j^{vir} \rangle \langle \phi_j^{vir} | h_{10} | \phi_i^{occ} \rangle}{\varepsilon_i^{occ} - \varepsilon_j^{vir}} \quad (2.33)$$

In equation 2.33, h_{ab} represents the one-electron form of the perturbation operators given in eq. 2.30. $V'_{xc}(\mathbf{B}_0)$ refers to the response of the exchange-correlation potential to the external magnetic field. For functionals that depend on the **density, or the gradient of the density** (such as LDA or GGAs), the response of the exchange-correlation functional vanishes because of the neglect of current-density terms. This neglect leads to **uncoupled** DFT equations. The uncoupled DFT formalism allows calculation of the magnetic shielding by eq. 2.33 in one step, once the SCF solution is obtained for the many-electron system. For hybrid functionals that include the HF exchange term, the response of the functional depends on how the orbitals are perturbed by the external field. This mixing leads to **coupled DFT equations**, which are solved iteratively. For this reason, using hybrid functionals in magnetic-shielding calculations increases the computational time significantly, compared to GGA functionals. For a relativistic Hamiltonian that includes spin-orbit coupling such as the Hamiltonian in the ZORA formalism, the response of the exchange-correlation functional does not vanish even in the case of GGAs.[56] For heavy nuclei, the inclusion of the response term increases the magnetic shielding by around 500 ppm.

2.4 Literature Review of Magnetic Shielding Calculations for Spin-1/2 Heavy Nuclei

Calculations of magnetic shielding for heavy nuclei such as ^{119}Sn , ^{199}Hg , ^{205}Tl and ^{207}Pb generally require some level of relativistic theory in the model Hamiltonian

and a sufficiently large basis set, due to large number of electrons. Over the last two decades, the implementation of various relativistic methods in quantum chemistry and the rapid increase in computing power have allowed significant developments in the calculation of magnetic shielding for such heavy nuclei. There still remain some areas such as the accurate prediction of the absolute shielding scale, the inclusion of electron correlation effects, and the modelling of solution and solid-state effects that hamper accurate calculation of magnetic shielding for heavy nuclei.

Among the various NMR-active heavy nuclei, ^{199}Hg has been addressed more thoroughly by computational chemists in benchmark calculations than other nuclei. For example, Wolff et al.[49] have shown the importance of relativistic effects to predict experimental trends for ^{199}Hg magnetic shielding in the HgX_2 series (X=CN, Cl, Br etc.). For similar systems, calculations with ZORA and Douglas-Kroll-Hess (DKH) Hamiltonian show the particular importance of spin-orbit coupling terms for accurate predictions of experimental chemical shifts and anisotropies for ^{199}Hg -containing systems.[57, 58] Recently, benchmark calculations which employ four-component methods were applied to ^{199}Hg magnetic-shielding calculations. These investigations have particular importance for establishing an accurate absolute-shielding scale for ^{199}Hg .[59, 60] The comparison of ^{199}Hg magnetic-shielding constants obtained using the ZORA formalism and four-component methods shows that calculations with the ZORA formalism **underestimate** the shielding constants by more than 2000 ppm compared to the four-component methods. However, both methods predict similar trends for the **chemical shifts**. This result is due to the large systematic errors introduced by the ZORA approximation that affects mostly the core levels. These errors cancel out by the definition of chemical shifts via referencing, as

ZORA has been shown to produce valence level integrals with comparable accuracy to four-component theories.[37]

Relativistic benchmark calculations have been applied to other heavy nuclei, as well. In these studies, large spin-orbit-induced contributions to the absolute magnetic shielding and the chemical shift were observed, as was seen for ^{199}Hg . Some selected examples include studies of ^{183}W , ^{195}Pt , and ^{207}Pb . [48, 61-65] In the benchmark studies of ^{119}Sn and ^{125}Te , [66, 67] the authors have concluded that spin-orbit effects are not significant for the predictions of **chemical shifts** whereas they have non-negligible contributions to the **absolute magnetic shielding**.

Calculations of magnetic-shielding tensors of heavy nuclei in solid materials are rather limited in the literature. This scarcity of examples is partially due to the lack of periodic boundary condition (PBC) methods to incorporate relativistic spin-orbit effects. Another challenge for PBC methods is the large number of electrons in the heavy-nucleus-containing systems. As a result, such studies generally involve a cluster *ansatz* to model the solid-state system. The cluster approach has only been applied to produce **qualitative** predictions of experimental trends for chemical shifts and spans of heavy nuclei. [68-73]

REFERENCES

1. Szabo, A. and N.S. Ostlund, *Modern Quantum Chemistry: Introduction to Advanced Electronic Structure Theory*. 1989, Mineola, New York: Dover Publications, Inc.
2. Koch, W. and M.C. Holthausen, *A Chemist's Guide to Density Functional Theory*. 2001, Weinheim: WILEY-VCH Verlag GmbH.
3. Parr, R.G. and W. Yang, *Density-functional theory of atoms and molecules*. 1989, New York: Oxford University Press.
4. Hohenberg, P. and W. Kohn, *Inhomogeneous Electron Gas*. Physical Review B, 1964. **136**(3B): p. 864-871.
5. Kohn, W. and L.J. Sham, *Self-Consistent Equations Including Exchange and Correlation Effects*. Physical Review, 1965. **140**(4A): p. 1133-1138.
6. Becke, A.D., *Density-Functional Thermochemistry .3. The Role of Exact Exchange*. Journal of Chemical Physics, 1993. **98**(7): p. 5648-5652.
7. Lee, C.T., W.T. Yang, and R.G. Parr, *Development of the Colle-Salvetti Correlation-Energy Formula into a Functional of the Electron-Density*. Physical Review B, 1988. **37**(2): p. 785-789.
8. Becke, A.D., *Density-Functional Exchange-Energy Approximation with Correct Asymptotic-Behavior*. Physical Review A, 1988. **38**(6): p. 3098-3100.
9. Perdew, J.P., *Density-Functional Approximation for the Correlation-Energy of the Inhomogeneous Electron-Gas*. Physical Review B, 1986. **33**(12): p. 8822-8824.
10. Perdew, J.P., K. Burke, and M. Ernzerhof, *Generalized gradient approximation made simple*. Physical Review Letters, 1996. **77**(18): p. 3865-3868.
11. Perdew, J.P., M. Ernzerhof, and K. Burke, *Rationale for mixing exact exchange with density functional approximations*. Journal of Chemical Physics, 1996. **105**(22): p. 9982-9985.
12. Adamo, C. and V. Barone, *Toward reliable density functional methods without adjustable parameters: The PBE0 model*. Journal of Chemical Physics, 1999. **110**(13): p. 6158-6170.
13. Becke, A.D., *Density-functional thermochemistry .4. A new dynamical correlation functional and implications for exact-exchange mixing*. Journal of Chemical Physics, 1996. **104**(3): p. 1040-1046.
14. Adamo, C. and V. Barone, *Toward reliable adiabatic connection models free from adjustable parameters*. Chemical Physics Letters, 1997. **274**(1-3): p. 242-250.

15. Geerlings, P., F. De Proft, and W. Langenaeker, *Conceptual density functional theory*. Chemical Reviews, 2003. **103**(5): p. 1793-1873.
16. Jochen, A., *Analyzing NMR shielding tensors calculated with two-component relativistic methods using spin-free localized molecular orbitals*. 2008, AIP. p. 164112.
17. Baer, R., E. Livshits, and U. Salzner, *Tuned Range-Separated Hybrids in Density Functional Theory*, in *Annual Review of Physical Chemistry, Vol 61*. p. 85-109.
18. Cohen, A.J., P. Mori-Sanchez, and W.T. Yang, *Challenges for Density Functional Theory*. Chemical Reviews. **112**(1): p. 289-320.
19. Janak, J.F., *Proof That $\Delta E = \Delta \epsilon_1$ in Density-Functional Theory*. Physical Review B, 1978. **18**(12): p. 7165-7168.
20. Stowasser, R. and R. Hoffmann, *What do the Kohn-Sham orbitals and eigenvalues mean?* Journal of the American Chemical Society, 1999. **121**(14): p. 3414-3420.
21. Bickelhaupt, F.M. and E.J. Baerends, *Kohn-Sham density functional theory: Predicting and understanding chemistry*, in *Reviews in Computational Chemistry, Vol 15*. 2000, Wiley-Vch, Inc: New York. p. 1-86.
22. Chong, D.P., O.V. Gritsenko, and E.J. Baerends, *Interpretation of the Kohn-Sham orbital energies as approximate vertical ionization potentials*. Journal of Chemical Physics, 2002. **116**(5): p. 1760-1772.
23. Ziegler, T., J.G. Snijders, and E.J. Baerends, *Relativistic Effects on Bonding*. Journal of Chemical Physics, 1981. **74**(2): p. 1271-1284.
24. Pyykko, P., *Relativistic Effects in Structural Chemistry*. Chemical Reviews, 1988. **88**(3): p. 563-594.
25. Autschbach, J., *Perspective: Relativistic effects*. Journal of Chemical Physics, 2012. **136**(15): p. 15.
26. Ahuja, R., et al., *Relativity and the Lead-Acid Battery*. Physical Review Letters. **106**(1): p. 018301.
27. Hrobarik, P., et al., *Giant Spin-Orbit Effects on NMR Shifts in Diamagnetic Actinide Complexes: Guiding the Search of Uranium(VI) Hydride Complexes in the Correct Spectral Range*. Angewandte Chemie-International Edition. **51**(43): p. 10884-10888.
28. Reiher, M. and A. Wolf, *Relativistic Quantum Chemistry: The Fundamental Theory of Molecular Science*: Wiley-VCH.
29. Dirac, P.A.M., *The quantum theory of the electron*. Proceedings of the Royal Society of London Series a-Containing Papers of a Mathematical and Physical Character, 1928. **117**(778): p. 610-624.
30. Schwarz, W.H.E. and H. Wallmeier, *Basis Set Expansions of Relativistic Molecular Wave-Equations*. Molecular Physics, 1982. **46**(5): p. 1045-1061.
31. Schwarz, W.H.E. and E. Wechseltrakowski, *The 2 Problems Connected with Dirac-Breit-Roothaan Calculations*. Chemical Physics Letters, 1982. **85**(1): p. 94-97.

32. Stanton, R.E. and S. Havriliak, *Kinetic Balance - a Partial Solution to the Problem of Variational Safety in Dirac Calculations*. Journal of Chemical Physics, 1984. **81**(4): p. 1910-1918.
33. Foldy, L.L. and S.A. Wouthuysen, *On the Dirac Theory of Spin 1/2 Particles and Its Non-Relativistic Limit*. Physical Review, 1950. **78**(1): p. 29-36.
34. Van lenthe, E., E.J. Baerends, and J.G. Snijders, *Relativistic Regular 2-Component Hamiltonians*. Journal of Chemical Physics, 1993. **99**(6): p. 4597-4610.
35. Lenthe, E.v., E.J. Baerends, and J.G. Snijders, *Relativistic total energy using regular approximations*. 1994. **101**(11): p. 9783-9792.
36. Lenthe, E.v., J.G. Snijders, and E.J. Baerends, *The zero-order regular approximation for relativistic effects: The effect of spin-orbit coupling in closed shell molecules*. 1996. **105**(15): p. 6505-6516.
37. Autschbach, J., *The accuracy of hyperfine integrals in relativistic NMR computations based on the zeroth-order regular approximation*. Theoretical Chemistry Accounts, 2004. **112**(1): p. 52-57.
38. Lamb, W.E., *Internal diamagnetic fields*. Physical Review, 1941. **60**(11): p. 817-819.
39. Ramsey, N.F., *Magnetic Shielding of Nuclei in Molecules*. Physical Review, 1950. **78**(6): p. 699-703.
40. Stevens, R.M., W.N. Lipscomb, and R.M. Pitzer, *Perturbed Hartree-Fock Calculations .1. Magnetic Susceptibility and Shielding in LiH Molecule*. Journal of Chemical Physics, 1963. **38**(2): p. 550-560.
41. Ditchfield, R., *Self-Consistent Perturbation-Theory of Diamagnetism .1. Gauge-Invariant Lcao Method for Nmr Chemical-Shifts*. Molecular Physics, 1974. **27**(4): p. 789-807.
42. Wolinski, K., J.F. Hinton, and P. Pulay, *Efficient Implementation of the Gauge-Independent Atomic Orbital Method for NMR Chemical-Shift Calculations*. Journal of the American Chemical Society, 1990. **112**(23): p. 8251-8260.
43. Malkin, V.G., et al., *Nuclear-Magnetic-Resonance Shielding Tensors Calculated with a Sum-over-States Density-Functional Perturbation-Theory*. Journal of the American Chemical Society, 1994. **116**(13): p. 5898-5908.
44. deDios, A.C., *Ab initio calculations of the NMR chemical shift*. Progress in Nuclear Magnetic Resonance Spectroscopy, 1996. **29**: p. 229-278.
45. Fukui, H., *Theory and calculation of nuclear shielding constants*. Progress in Nuclear Magnetic Resonance Spectroscopy, 1997. **31**(4): p. 317-342.
46. Pyykko, P., *On the Relativistic Theory of NMR Chemical-Shifts*. Chemical Physics, 1983. **74**(1): p. 1-7.
47. Kaupp, M., M. Buhl, and V.G. Malkin, *Calculation of NMR and EPR Parameters: Theory and Applications*. 2004, Weinheim: WILEY-VCH Verlag GmbH & Co. KGaA.

48. Rodriguez-Fortea, A., P. Alemany, and T. Ziegler, *Density Functional Calculations of NMR Chemical Shifts with the Inclusion of Spin Orbit Coupling in Tungsten and Lead Compounds*. The Journal of Physical Chemistry A, 1999. **103**(41): p. 8288-8294.
49. Wolff, S.K., et al., *Density functional calculations of nuclear magnetic shieldings using the zeroth-order regular approximation (ZORA) for relativistic effects: ZORA nuclear magnetic resonance*. Journal of Chemical Physics, 1999. **110**(16): p. 7689-7698.
50. London, F., *The quantic theory of inter-atomic currents in aromatic combinations*. Journal De Physique Et Le Radium, 1937. **8**: p. 397-409.
51. Pople, J.A., *Nuclear Magnetic Resonance in Diamagnetic Materials - Theory of Chemical Shifts*. Discussions of the Faraday Society, 1962(34): p. 7-14.
52. Pople, J.A., *Molecular-Orbital Theory of Diamagnetism .I. an Approximate Lcao Scheme*. Journal of Chemical Physics, 1962. **37**(1): p. 53-59.
53. Schreckenbach, G. and T. Ziegler, *Calculation of NMR Shielding Tensors Using Gauge-Including Atomic Orbitals and Modern Density-Functional Theory*. Journal of Physical Chemistry, 1995. **99**(2): p. 606-611.
54. Cheeseman, J.R., et al., *A comparison of models for calculating nuclear magnetic resonance shielding tensors*. Journal of Chemical Physics, 1996. **104**(14): p. 5497-5509.
55. Facelli, J.C., *Chemical shift tensors: Theory and application to molecular structural problems*. Progress in Nuclear Magnetic Resonance Spectroscopy, 2010. **58**(3-4): p. 176-201.
56. Autschbach, J., *The role of the exchange-correlation response kernel and scaling corrections in relativistic density functional nuclear magnetic shielding calculations with the zeroth-order regular approximation*. Molecular Physics, 2013. **111**(16-17): p. 2544-2554.
57. Vaara, J., et al., *Study of relativistic effects on nuclear shieldings using density-functional theory and spin-orbit pseudopotentials*. Journal of Chemical Physics, 2001. **114**(1): p. 61-71.
58. Jokisaari, J., et al., *Hg-199 shielding tensor in methylmercury halides: NMR experiments and ZORA DFT calculations*. Journal of Physical Chemistry A, 2002. **106**(40): p. 9313-9318.
59. Roukala, J., et al., *Relativistic effects on group-12 metal nuclear shieldings*. Physical Chemistry Chemical Physics, 2011. **13**(47): p. 21016-21025.
60. Wodzynski, A., M. Repisky, and M. Pecul, *A comparison of two-component and four-component approaches for calculations of spin-spin coupling constants and NMR shielding constants of transition metal cyanides*. Journal of Chemical Physics, 2012. **137**(1): p. 11.
61. Autschbach, J., *The calculation of NMR parameters in transition metal complexes*, in *Principles and Applications of Density Functional Theory in Inorganic Chemistry I*. 2004. p. 1-48.

62. Autschbach, J. and S. Zheng, *Relativistic Computations of NMR Parameters from First Principles: Theory and Applications*. Annual Reports on NMR Spectroscopy, 2009. **67**: p. 1-95.
63. Truflandier, L.A. and J. Autschbach, *Probing the Solvent Shell with Pt-195 Chemical Shifts: Density Functional Theory Molecular Dynamics Study of Pt-II and Pt-IV Anionic Complexes in Aqueous Solution*. Journal of the American Chemical Society, 2010. **132**(10): p. 3472-3483.
64. Vicha, J., M. Patzschke, and R. Marek, *A relativistic DFT methodology for calculating the structures and NMR chemical shifts of octahedral platinum and iridium complexes*. Physical Chemistry Chemical Physics, 2013. **15**(20): p. 7740-7754.
65. Autschbach, J., *Relativistic calculations of magnetic resonance parameters: background and some recent developments*. Philosophical Transactions of the Royal Society a-Mathematical Physical and Engineering Sciences, 2014. **372**(2011): p. 20120489.
66. Fukuda, R. and H. Nakatsuji, *Quasirelativistic theory for the magnetic shielding constant. III. Quasirelativistic second-order Moller-Plesset perturbation theory and its application to tellurium compounds*. Journal of Chemical Physics, 2005. **123**(4): p. 10.
67. Bagno, A., M. Bonchio, and J. Autschbach, *Computational modeling of polyoxotungstates by relativistic DFT calculations of W-183 NMR chemical shifts*. Chemistry-a European Journal, 2006. **12**(33): p. 8460-8471.
68. Briand, G.G., et al., *Probing lead(II) bonding environments in 4-substituted pyridine adducts of (2,6-Me₂C₆H₃S)(2)Pb: An X-ray structural and solid-state Pb-207 NMR study*. Inorganic Chemistry, 2007. **46**(21): p. 8625-8637.
69. Gerken, M., et al., *Solid-state NMR spectroscopic study of coordination compounds of XeF₂ with metal cations and the crystal structure of [Ba(XeF₂)(5)][AsF₆](2)*. Inorganic Chemistry, 2007. **46**(15): p. 6069-6077.
70. Dmitrenko, O., et al., *The relationship between Pb-207 NMR chemical shift and solid-state structure in Pb(II) compounds*. Journal of Physical Chemistry A, 2008. **112**(14): p. 3046-3052.
71. Dmitrenko, O., S. Bai, and C. Dybowski, *Prediction of (207)Pb NMR parameters for the solid ionic lead(II) halides using the relativistic ZORA-DFT formalism: Comparison with the lead-containing molecular systems*. Solid State Nuclear Magnetic Resonance, 2008. **34**(3): p. 186-190.
72. Taylor, R.E., et al., *Revisiting HgCl₂: A solution- and solid-state Hg-199 NMR and ZORA-DFT computational study*. Journal of Molecular Structure, 2009. **930**(1-3): p. 99-109.
73. Greer, B.J., et al., *Characterising Lone-Pair Activity of Lead(II) by Pb-207 Solid-State NMR Spectroscopy: Coordination Polymers of [N(CN)(2)](-) and [Au(CN)(2)](-) with Terpyridine Ancillary Ligands*. Chemistry-A European Journal, 2011. **17**(13): p. 3609-3618.

Chapter 3

COMPUTATIONAL METHODS

3.1 Magnetic Shielding Calculations in Solid State

Calculations of magnetic-shielding tensor for heavy nuclei in solids require the treatment of two additional dimensions that are not generally encountered in "standard" quantum chemical calculations on molecules in solution or in the gas phase. First, the electrons must be treated as relativistic particles, in part because of the high nuclear charge.[1, 2] Second, unlike solution state, the periodic structure of the solid has effects that are not averaged by rapid motion.[3] To address the latter, two methods have been proposed to predict NMR parameters of nuclei in solids: use of periodic boundary conditions based on the full crystal symmetry,[4-6] and the treatment of model molecular clusters that define the local environment of the NMR nucleus.[6-8] This section provides a general description of these two methodologies.

3.2 Periodic Boundary Calculations and the GIPAW Approach

Periodic boundary calculations generally employ a plane-wave basis and the pseudopotential approximation.[6] The generic formula for wave functions described in terms of the plane-wave basis sets is given in Eq. 3.1,

$$\Psi_{n\mathbf{k}}(\mathbf{r}) = \sum_{\mathbf{G}} c_{n\mathbf{k}}(\mathbf{G}) e^{i(\mathbf{k}+\mathbf{G})\mathbf{r}} \quad (3.1)$$

where the sum is over the reciprocal lattice vectors \mathbf{G} . The basis set is truncated by defining a cut-off energy, E_{cut} , which is given by Eq. 3.2.

$$E_{cut} = \frac{\hbar^2(\mathbf{k} + \mathbf{G})^2}{2m} \quad (3.2)$$

In this truncation scheme, the reciprocal lattice vectors with lower kinetic energy than the predefined maximum cut-off energy are kept in the basis-set expansion of the wave function. One advantage of this scheme is that it allows systematic control of convergence of the calculated property.

An important drawback of the plane-wave basis is representation of the wave function in the region near the nucleus. The true oscillatory behavior of the core and valence states that are close to the core region requires a large number of planewave functions to model the actual wave function. This problem is not encountered in atomic-basis sets (Slater type or Gaussian type) and is solely due to the mathematical form of the plane-wave functions in the Eq. 3.1.

It is convenient to replace the coulomb potential and potential due to the core electrons by a smoother effective potential to address the effect of electrons in this region. This formalism is known as the pseudopotential method. There are several schemes proposed for the construction of the effective potential.[6] Some common choices include the norm-conserving pseudopotential [9] and the ultrasoft pseudopotential.[10]

In the last ten years, periodic-boundary calculations have become popular for the predictions of NMR parameters in solids of known structure.[6] An important method which employs periodic-boundary conditions was developed by Sebastiani et al. with the use of localized Wannier orbitals, as implemented in the program CPMD.[5, 11] Another popular formalism is the Gauge Included Projected Augmented Wave (GIPAW) method of Pickard and Mauri,[4] which extends the PAW formalism introduced by van de Walle and Blöchl.[12] For many cases,

impressive correlations have been obtained by the GIPAW approach between experimental and calculated SSNMR parameters. For nuclei such as ^{13}C [13-15], ^{29}Si [16, 17] and ^{31}P [18], the GIPAW approach has achieved sufficient accuracy for practical applications. However, there are still cases where GIPAW predictions, within the current implementation, deviate from experiment significantly. Some known problematic cases include ^{19}F , ^{43}Ca , [19-21] and heavy nuclei such as ^{119}Sn , ^{207}Pb and ^{209}Bi . [22-24] For a more detailed explanation of the GIPAW method, readers are referred to a recent review by Bonhomme et al. [6]

3.2.1 Approximate Cluster Models

Magnetic-shielding calculations using model clusters that simulate the local solid-state environment are an alternative to period-boundary calculations. Essentially, the cluster approximation involves defining a region within the crystal structure, which is extended around the **NMR nuclei**. At this point, one can perform a non-periodic molecular calculation with atomic-basis sets on the cluster input. The cluster approximation is particularly suitable for magnetic-shielding calculations since the $1/r^3$ dependence of the shielding tensor (Eq. 2.30) [25] can be exploited for fast convergence of calculated parameters with increasing cluster size. In early studies, Tossell [7, 26, 27] investigated the effects of next-nearest neighbors on magnetic shielding for ^{15}N and ^{23}Na by employing molecular clusters to mimic the solid-state structure. Similarly, Valerio et al. [28] employed molecular-cluster-based calculations for magnetic shielding of ^{29}Si and ^{27}Al in zeolite structures. In these cases, it was shown that more accurate chemical-shift and quadrupolar parameters result when the cluster size is sufficiently large to reflect the nature of local electronic structure around the NMR nuclei.

3.2.2 Comparison of GIPAW and Cluster Models for Magnetic Shielding Calculations in Solids

Ideally, both periodic-boundary methods employing the GIPAW formalism and cluster methods should yield the same results, provided that the clusters are sufficiently large, and the same level of theory is employed in the computation. In practice, these methods have certain qualities and deficiencies when applied to magnetic-shielding calculations of solid materials. A comparison of the main aspects of these two methods is given as: [29]

- Periodic-boundary calculations, by definition, include the translational symmetry and the local point group symmetry of the NMR nuclei. In the cluster approximation, the translational symmetry is neglected. The local point group symmetry, however, can be conserved if the cluster is extended symmetrically around the nuclei of interest.
- Periodic-boundary calculations do not involve any parametrization prior to the computational setup. On the other hand, a large number of parameters such as size, charge, termination method, and symmetry constraints must be set for cluster models.
- Termination of the clusters from the extended structure of the solid can result in dangling bonds and uncompensated charge. Quantum chemical modelling of such systems usually yields either non-convergence during the self-consistent-field (SCF) cycle or a difficult convergence, which signals an unphysically small HOMO-LUMO gap for the system. In comparison, periodic-boundary calculations do not have this problem.
- In general, periodic-boundary calculations are computationally more

expensive than cluster methods. Current limitations of GIPAW in terms of electrons per unit cell can be reached rather quickly for solids containing heavy nuclei.

- There is a larger selection of quantum chemistry methods in terms of density functionals (hybrids and meta-hybrids), correlation methods (coupled cluster, MP₂), and relativistic methods (ZORA/Spin-orbit, four-component relativistic) as well as basis sets available for cluster calculations. In comparison, GIPAW calculations can be employed only with DFT at LDA and GGA levels.
- The availability of quantum chemistry program packages which can perform magnetic-shielding calculations is considerably limited for periodic-boundary calculations.

Despite certain disadvantages, cluster modelling has the potential to become a valuable tool for accurate predictions of magnetic-shielding tensors in solids. Cluster models are particularly more suitable for heavy-metal-containing systems, as the inclusion of relativistic effects is crucial for such nuclei.[1, 2] Additionally, magnetic-shielding calculations with spin-orbit effects and exchange-correlation effects beyond GGA can become important for further development and benchmarking of GIPAW methods.

3.3 Definition of Cluster Models for Solids

For the calculations of magnetic-shielding tensors using cluster models, the quality of the predicted properties depends critically on the cluster setup.[29] In this section, the formulation of cluster models for different types of solids is discussed in detail. It is often necessary to define cluster models for molecular solids and covalent

or ionic-network solids separately, since major differences exist in the cluster modelling, in terms of termination scheme and computational treatment of the clusters.

3.3.1 Definition of the Cluster Models for Molecular Solids

Molecular solids are characterized by the relatively strong intramolecular interactions between atoms of the molecule, and by weaker intermolecular interactions. In Figure 3.1, extended solid-state structures of two molecular solids, HgCl_2 [30] and lead(IV) acetate [31] are illustrated.

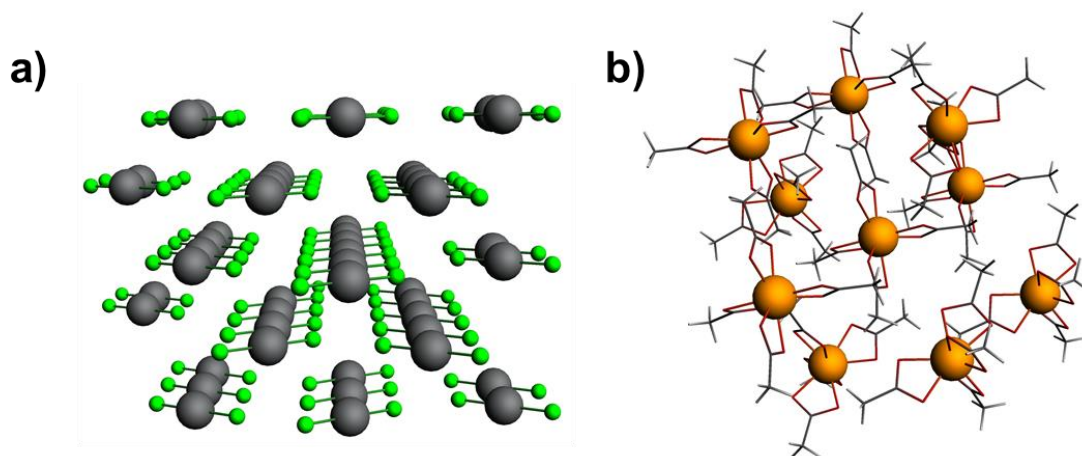


Figure 3.1 Extended solid state structures of a) HgCl_2 and b) lead(IV) acetate, which are illustrated in the ball-and-stick model.

For modelling of a molecular solid with a cluster, there is a natural choice for the termination scheme of the cluster, in which the clusters are defined without breaking any intramolecular bonds. Therefore, the resulting **molecular clusters** do not suffer from dangling bonds or uncompensated charge. In general, SCF convergence

for such clusters can be achieved without further approximations, similar to the case of isolated molecules.[15, 32]

In this study, three types of molecular clusters are defined with respect to their sizes: **a) small clusters b) large clusters and c) extended clusters**. A pictorial representation of small, large, and extended clusters for the case of HgCl_2 are shown in Figure 3.2. Small clusters consist of only the atoms with NMR nuclei (^{199}Hg) and the nearest neighbors (Cl). A large cluster includes the central Cl-Hg-Cl molecule and the next-nearest neighbors of NMR nuclei and Cl atoms in the central molecule. For the proper termination of the cluster, the remainder of the molecules, of which the next-nearest neighbor atoms are a part, are included. The total charge on the cluster becomes zero with this treatment. Extended clusters include the next-nearest neighbors to the large cluster and the atoms to complete the molecules.

There are certain aspects of this cluster definition which require more attention. First, the assignment of the region which designates the **next-nearest** neighbors can be difficult to assess. In the case of HgCl_2 , the nearest neighbors of the Hg atom are **two** covalently bonded Cl atoms. However, the number of atoms in the **next-nearest-neighbor region** of the Hg center depends on a user-defined cut-off radius. This radius is set as 4.0 Å in our definition of the large cluster shown in Figure 3.2 and the resulting next-nearest region of Hg includes six Cl atoms. The quality of predicted properties and the length of computational time depend on the definition of next-nearest region critically. For some cases, it is necessary to perform a series of calculations to see the effect of the cut-off radius on the predicted magnetic-shielding tensor.

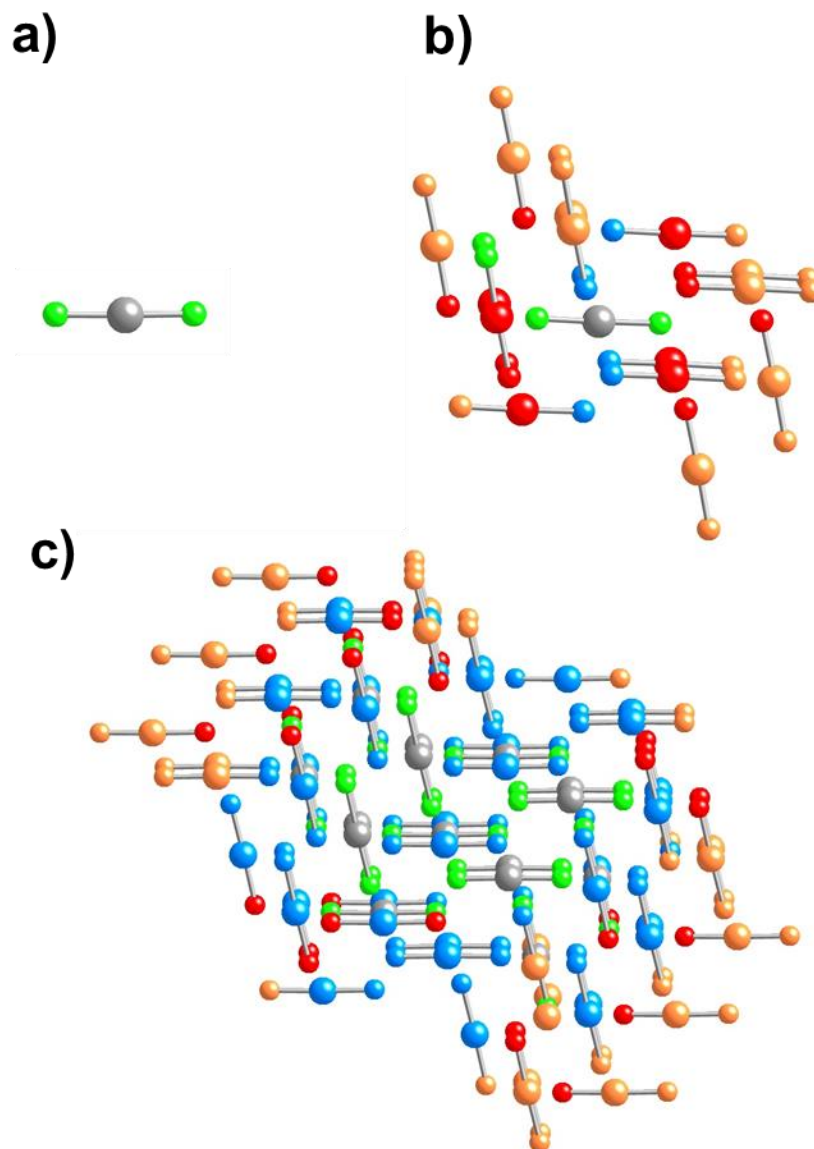


Figure 3.2 Comparison of a) small, b) large, and c) extended clusters of HgCl_2 . The small cluster consists of the NMR-active nucleus and the nearest neighbors to the NMR-active nucleus. A large cluster consists of the central molecule with its NMR-active nuclei and its nearest neighbors, as well as next-nearest neighbors to NMR nuclei (blue) and the ligands (red), and the atoms to complete the molecules (orange). An extended cluster includes the next-nearest neighbors of the large cluster and atoms to complete the molecules.

Another important issue is to check the convergence of the magnetic-shielding tensor with respect to the size of the clusters. For this reason, extended clusters, which include an additional coordination shell compared to large clusters, are introduced. The test for convergence often requires benchmark calculations and careful approximations in quantum chemistry methods with well-behaved systems, since such calculations can reach the limits of capability of the current computer systems easily.

3.3.2 Definition of Cluster Models for Ionic or Covalent Network Solids

The main disadvantage of the use of cluster models occurs when one attempts to extend these methods to ionic or covalent network solids. In that case, any termination of the periodic nature of the solid yields **dangling bonds** and **uncompensated charge** in the model cluster. Quantum chemical modelling of such systems usually yields either non-convergence during the self-consistent-field (SCF) cycle or a difficult convergence, which signals a very small HOMO-LUMO gap for the system. For both situations, the resulting NMR parameters cannot be trusted, and one must seek alternative ways to model the structure.

Ideally, the local point group symmetry of the NMR nucleus is conserved if the model cluster is generated through increasing numbers of coordination shells around the center. In Figure 3.3, this formalism is illustrated for the case of NaF. The clusters include up to first, third, and fifth coordination shell clusters around Na. In this system, both Na and F atoms occupy O_h sites in its crystal structure.[33] The O_h symmetry is also conserved for the central Na atom (the NMR nucleus) in all clusters shown in Figure 3.3. The total charge on the cluster that contains the first coordination shell is (-5), determined from the formal charges of Na, (+1) and F (-1). In clusters that contains

third and fifth coordination shell, the total charges increase to (-25) and (-61) respectively.

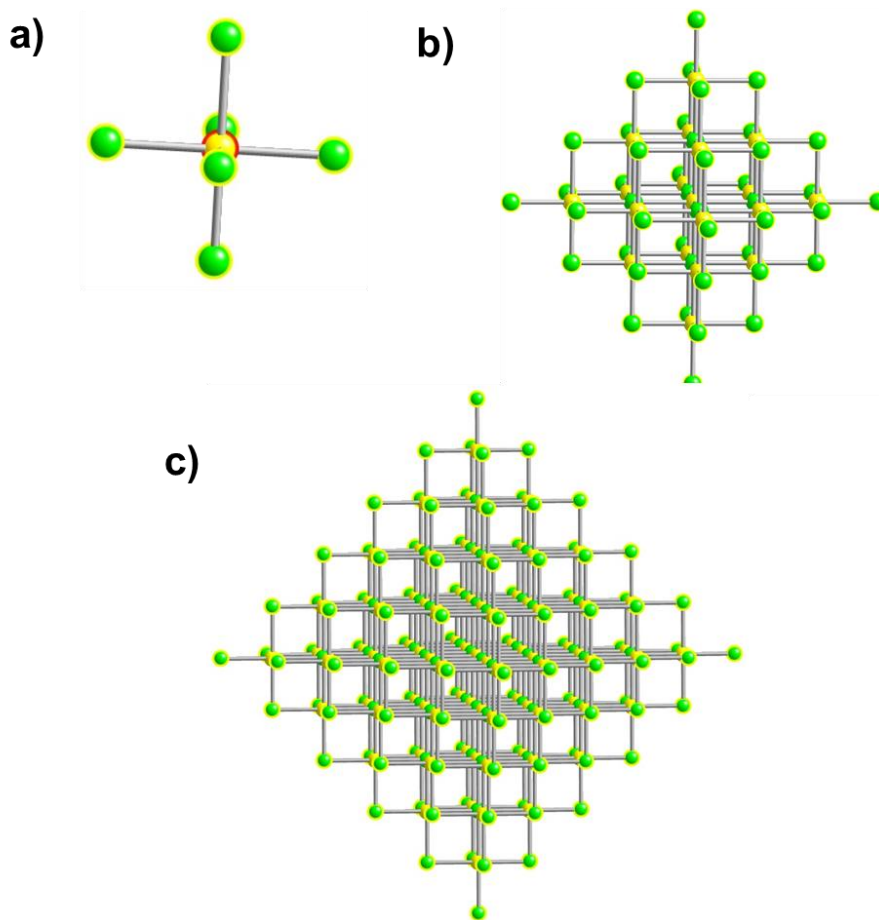


Figure 3.3 Cluster models for NaF that contains a) the first coordination shell, $[\text{NaF}_6]^{5-}$ b) the third coordination shell, $[\text{Na}_{19}\text{F}_{44}]^{25-}$ and c) the fifth coordination shell, $[\text{Na}_{85}\text{F}_{146}]^{61-}$.

It is possible to generate clusters of NaF with zero total charge. However, such clusters still contain dangling bonds (terminal Na and F atoms with coordination

number that is less than six) and the local symmetry of the central atom cannot be preserved since the clusters are not symmetrically extended. Because of the latter, calculations employing such clusters yield non-vanishing magnetic-shielding anisotropy, even though the tensor should be spherically symmetric. [29]

3.3.2.1 Termination of the Cluster for a Network Solid

Using a cluster model of network solids, one often sees oscillatory behavior in the SCF cycle, a result of nearly degenerate energy levels of the frontier orbitals, which are dominated by atomic orbitals of the terminal atoms in the cluster boundaries. Some recipes have been introduced in the literature to achieve reliable SCF convergence in cluster calculations. One solution to this practical problem is to add hydrogens to terminal atoms of the cluster) to stabilize the cluster.[7, 8, 34] This method has been employed to obtain converged solutions with meaningful NMR parameters in solids for a variety of systems. There are, however, some problems with this method. First, the positions of hydrogen atoms are generally determined somewhat arbitrarily, which results in a large range of uncertainty in the calculated magnetic-shielding tensor components. Secondly, this method is not suitable for systems where terminal atoms exhibit a large variety of coordination geometries and addition of hydrogen may cause **overstabilization** or **understabilization** of the frontier orbitals. In this case, the SCF cycle remains oscillatory and further treatment of terminal atoms is generally required.

In other termination schemes, the cluster is embedded in an array of classical point charges to stabilize the terminal atoms and to compensate for long-range coulombic interactions.[29, 35] This approach is known as the **Embedded Ion Method** (EIM). In this formalism, the charge array is usually truncated by performing

an Ewald summation over atomic sites, which allows the exact calculation of the electrostatic potential in ideal **ionic solids**. Various approaches are proposed for the determination of point charge values and the treatment of quantum/classical interface.

The basic machinery and some of the applications of the EIM methods have been reviewed by Weber and Gunne recently.[29] The EIM method has been applied to calculations of magnetic-shielding tensors with some success. However, there are problems associated with the excess charge on the **quantum region** of the cluster.

3.3.2.2 Bond Valence Model Approach in Cluster Models

The problem of SCF convergence may be addressed by a new method applied to cluster models. In this scheme, pseudo-atoms with non-integer nuclear charges (Z_{nuc}) are generated [36-38] to replace the terminal atoms of the cluster. This procedure aims to stabilize the energy levels of frontier orbitals centered on terminal atoms. We refer to this model as 'valence modification of terminal atoms' or VMTA.

In the VMTA model, one must select a range of Z_{nuc} for the pseudo-atom generation. A possible selection can be made such that the residual charge on the cluster is minimized. For example, the charge on the NaF cluster, $[\text{Na}_{19}\text{F}_{44}]^{25-}$, which is shown in Figure 3.3b, can be reduced to 0.08 if the terminal fluorine atoms ($Z_{nuc} = 9.00$) are replaced by pseudo-fluorines ($Z_{nuc} = 9.66$). In this method, the different coordination environments of terminal fluorine atoms are not taken into account since all fluorine atoms are replaced with the same pseudo-atom. Therefore, the SCF problems resulting from overstabilization or understabilization of the frontier orbitals may still exist.

The VMTA method can be further improved by using the bond-valence theory of I. D. Brown and his collaborators to specify appropriate charges on the terminal

atoms.[39-42] This method has been called the bond-valence approach, so that its application to the VMTA method we abbreviate as VMTA/BV. In this method, a set of pseudo atoms with various Z_{nuc} are generated according to the sum of the bond strengths of the terminal atoms. The bond strength (S) for a terminal atom is calculated using the central equation of the bond-valence model:

$$S = \sum_i \exp\left(\frac{R_{i0} - R_i}{b_i}\right) \quad (3.3)$$

In Eq. 3.3, R_i is the bond length between two atoms in a pair containing the terminal atom. R_{i0} and b_i are fitted bond valence parameters tabulated in a recent review of the bond-valence model.[42] In the VMTA/BV scheme, the parameter R_{i0} is slightly modified from the reported values, so that the total bond strength of an atom with a complete coordination sphere corresponds to the oxidation state of that atom in a given cluster. For the terminal atoms, the bond strength, S , is calculated using Eq. 3.3 and the modified Z_{nuc} of the terminal atom (Z_{mod}) is calculated from Eq. 3.4.

$$Z_{mod} = Z_{nuc} + \Delta S \quad (3.4a)$$

$$\Delta S = V_a - S \quad (3.4b)$$

where ΔS is the difference between the valence of the terminal atom, V_a , and the calculated bond strength of the terminal atom in the cluster. In other words, ΔS corresponds to the missing coordination bond strength of the terminal atom.

As an example of the VMTA/BV method, terminal oxygen atoms with different coordination spheres are illustrated in Figures 3.4a and 3.4b for the third coordination shell clusters of α -PbO and β -PbO, respectively. For α -PbO, there is only one unique Pb-O bond length in the crystal structure.[43] Therefore, the bond strength and Z_{mod} of the terminal oxygen atoms only depend on the number of lead atoms

coordinated to the terminal oxygen atom. In Figure 3.4a, there are two distinct terminal oxygen sites. O1 is coordinated to a single lead site, and O2 is coordinated to two lead sites with the same bond length. Calculated bond strengths from the summation in Eq. 3.3 are 0.50 and 1.00 valence units (vu) for O1 and O2 respectively. Because the bond strength of oxygen having complete coordination (i.e., surrounded by four lead atoms) is 2.00 vu, Z_{mod} for each of the two types of terminal oxygen atoms in these clusters is calculated to be 9.50 and 9.00 vu for O1 and O2, respectively.

For β -PbO, calculation of bond strengths is not as simple, due to lower symmetry and multiple Pb-O bond lengths in the structure.[44] As a result, there is more variation in the number of distinct terminal oxygen sites. The calculated bond strengths are 0.37, 0.61, 0.64, 0.99, and 1.01vu for O1 to O5, respectively.

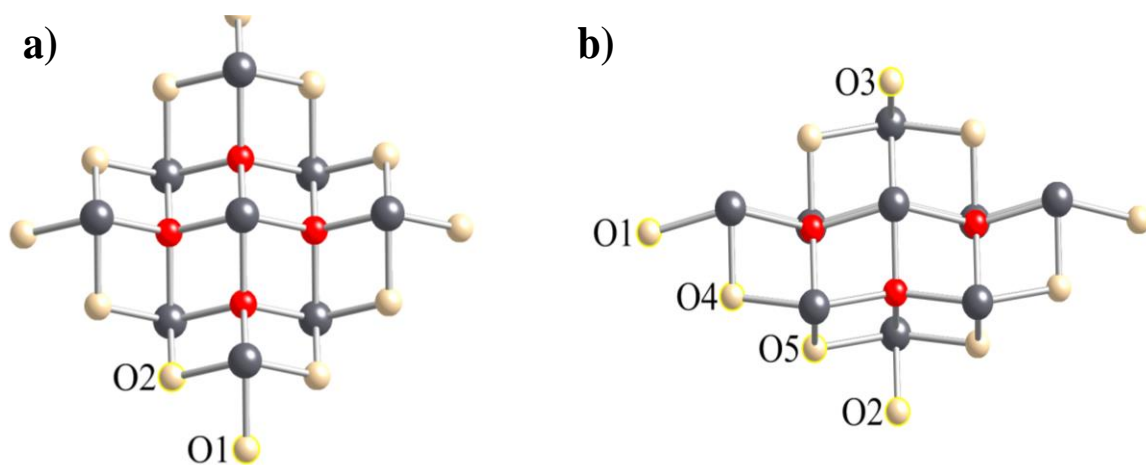


Figure 3.4 Different terminal oxygen sites according to the bond valence model in a) α -PbO and b) β -PbO.

The effect of VMTA/BV on the energy levels of a cluster is illustrated in Figure 3.5 for the third coordination shell geometry of α -PbO.

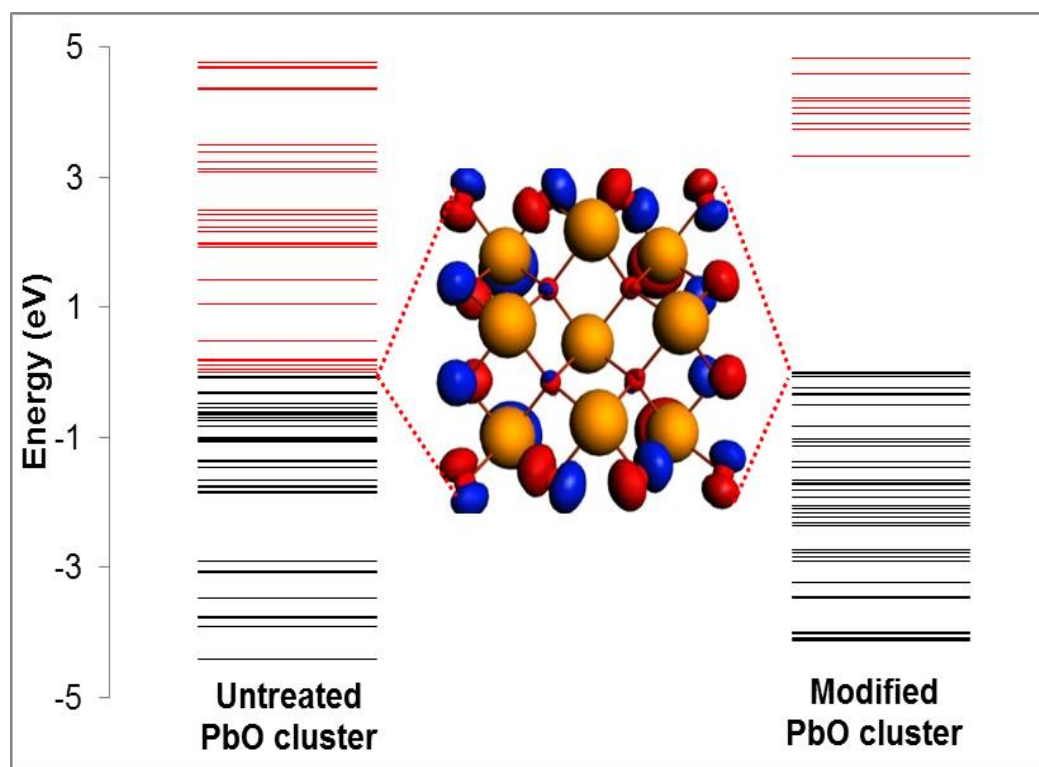


Figure 3.5 Energy levels for the third coordination cluster of α -PbO. The occupied levels are shown in black whereas unoccupied levels are shown in red. These qualitative calculations are carried out with BP86 functionals and the ZORA/spin-orbit Hamiltonian.

For a cluster without any treatment of the terminal atoms, there is no clear difference in energy between the HOMO and LUMO levels. As a result, convergence under SCF is difficult or impossible as the algorithm becomes oscillatory as shown in Figure 3.6. Upon closer inspection, it is seen that the frontier MOs are mostly dominated by the p orbitals of the terminal oxygen atoms. When Z_{nuc} for the atoms is

adjusted as described, these levels are stabilized, due to an additional component of the nuclear potential that creates the energy difference between the HOMO and LUMO levels. As a result, SCF convergence is achieved easily for clusters modified by VMTA/BV. (Figure 3.6)

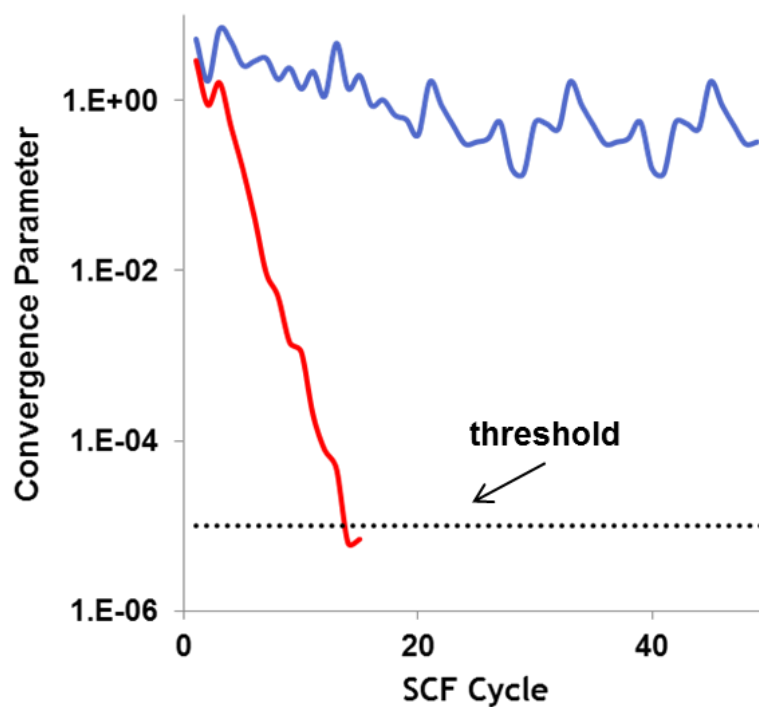


Figure 3.6 Graphical illustration of convergence versus number of SCF cycles for a DFT calculation that employs the α -PbO cluster without VMTA/BV modification (shown by the blue line) and for a DFT calculation using a cluster where the terminal atoms are modified by the VMTA/BV method (shown by the red line).

3.4 Computational Protocols

In this dissertation, computations employing cluster models are performed using the ADF (ADFv2010, ADFv2013 and ADFv2014) suite of programs.[45-47]

The calculations are generally carried out at the DFT level using GGA functionals (BP86 and PBE) [48-50] and hybrid functionals (B3LYP and PBE0), unless otherwise specified.[51-56] Relativistic effects are treated with the ZORA Hamiltonian at the scalar and spin-orbit levels.[57-60] In some cases, non-relativistic DFT is employed for benchmark calculations. All-electron triple zeta double polarization (TZ2P/AE) basis sets are employed for the NMR nuclei and the nearest neighbors. For the rest of the cluster, various types of basis sets (triple zeta single polarization or TZP, and double zeta or DZ) are employed for comparison. For outer shells of the cluster, the frozen core approximation (FCA) is employed to reduce the computational time when GGA density functionals are employed.[61, 62] Finally, the magnetic-shielding tensors are computed with the NMR module by employing the GIAO formalism [63, 64], as implemented in ADF.[2, 65-68]

Some calculations employing periodic-boundary conditions are carried out using the CASTEP program package[69] using DFT at the GGA level and with the GIPAW algorithm.[4] The core-valence interactions are treated by ultrasoft pseudopotentials that are generated on the fly.[10, 70] The wave functions are expanded (using Eq. 3.2) with a cut-off energy of 600 eV, which is generally sufficient to model these systems.

REFERENCES

1. Autschbach, J., *Relativistic calculations of magnetic resonance parameters: background and some recent developments*. Philosophical Transactions of the Royal Society a-Mathematical Physical and Engineering Sciences, 2014. **372**(2011): p. 20120489.
2. Rodriguez-Forteza, A., P. Alemany, and T. Ziegler, *Density Functional Calculations of NMR Chemical Shifts with the Inclusion of Spin Orbit Coupling in Tungsten and Lead Compounds*. The Journal of Physical Chemistry A, 1999. **103**(41): p. 8288-8294.
3. Orendt, A.M. and J.C. Facelli, *Solid-state effects on NMR chemical shifts*. Annual Reports on Nmr Spectroscopy, 2007. **62**: p. 115-178.
4. Pickard, C.J. and F. Mauri, *All-electron magnetic response with pseudopotentials: NMR chemical shifts*. Physical Review B, 2001. **63**(24): p. 13.
5. Sebastiani, D. and M. Parrinello, *A new ab-initio approach for NMR chemical shifts in periodic systems*. Journal of Physical Chemistry A, 2001. **105**(10): p. 1951-1958.
6. Bonhomme, C., et al., *First-Principles Calculation of NMR Parameters Using the Gauge Including Projector Augmented Wave Method: A Chemist's Point of View*. Chemical Reviews, 2012. **112**(11): p. 5733-5779.
7. Tossell, J.A., *Second-nearest-neighbor effects upon N NMR shieldings in models for solid Si₃N₄ and C₃N₄*. Journal of Magnetic Resonance, 1997. **127**(1): p. 49-53.
8. Valerio, G., et al., *Calculation of Si-29 and Al-27 MAS NMR chemical shifts in zeolite-beta using density functional theory: Correlation with lattice structure*. Journal of the American Chemical Society, 1998. **120**(44): p. 11426-11431.
9. Troullier, N. and J.L. Martins, *Efficient Pseudopotentials for Plane-Wave Calculations*. Physical Review B, 1991. **43**(3): p. 1993-2006.
10. Vanderbilt, D., *Soft Self-Consistent Pseudopotentials in a Generalized Eigenvalue Formalism*. Physical Review B, 1990. **41**(11): p. 7892-7895.
11. Sebastiani, D., et al., *NMR chemical shifts in periodic systems from first principles*. Computer Physics Communications, 2002. **147**(1-2): p. 707-710.
12. Van De Walle, C.G. and P.E. Blochl, *1st-Principles Calculations of Hyperfine Parameters*. Physical Review B, 1993. **47**(8): p. 4244-4255.
13. Gervais, C., et al., *Combined first-principles computational and experimental multinuclear solid-state NMR investigation of amino acids*. Journal of Physical Chemistry A, 2005. **109**(31): p. 6960-6969.

14. Johnston, J.C., et al., *Intermolecular shielding contributions studied by modeling the C-13 chemical-shift tensors of organic single crystals with plane waves*. Journal of Chemical Physics, 2009. **131**(14).
15. Holmes, S.T., et al., *Density functional investigation of intermolecular effects on C-13 NMR chemical-shielding tensors modeled with molecular clusters*. Journal of Chemical Physics, 2014. **141**(16): p. 164121.
16. Farnan, I., et al., *The effect of radiation damage on local structure in the crystalline fraction of ZrSiO₄: Investigating the Si-29 NMR response to pressure in zircon and reidite*. American Mineralogist, 2003. **88**(11-12): p. 1663-1667.
17. Profeta, M., F. Mauri, and C.J. Pickard, *Accurate first principles prediction of O-17 NMR parameters in SiO₂: Assignment of the zeolite ferrierite spectrum*. Journal of the American Chemical Society, 2003. **125**(2): p. 541-548.
18. Bonhomme, C., et al., *New perspectives in the PAW/GIPAW approach: J(P-O-Si) coupling constants, antisymmetric parts of shift tensors and NQR predictions*. Magnetic Resonance in Chemistry. **48**: p. S86-S102.
19. Griffin, J.M., et al., *High-Resolution F-19 MAS NMR Spectroscopy: Structural Disorder and Unusual J Couplings in a Fluorinated Hydroxy-Silicate*. Journal of the American Chemical Society. **132**(44): p. 15651-15660.
20. Sadoc, A., et al., *NMR parameters in alkali, alkaline earth and rare earth fluorides from first principle calculations*. Physical Chemistry Chemical Physics. **13**(41): p. 18539-18550.
21. Gervais, C., et al., *New perspectives on calcium environments in inorganic materials containing calcium-oxygen bonds: A combined computational-experimental (43)Ca NMR approach*. Chemical Physics Letters, 2008. **464**(1-3): p. 42-48.
22. Hamaed, H., et al., *Application of Solid-State Bi-209 NMR to the Structural Characterization of Bismuth-Containing Materials*. Journal of the American Chemical Society, 2009. **131**(23): p. 8271-8279.
23. Greer, B.J., et al., *Characterising Lone-Pair Activity of Lead(II) by Pb-207 Solid-State NMR Spectroscopy: Coordination Polymers of [N(CN)(2)](-) and [Au(CN)(2)](-) with Terpyridine Ancillary Ligands*. Chemistry-a European Journal, 2011. **17**(13): p. 3609-3618.
24. Mitchell, M.R., et al., *Sn-119 MAS NMR and first-principles calculations for the investigation of disorder in stannate pyrochlores*. Physical Chemistry Chemical Physics, 2011. **13**(2): p. 488-497.
25. Ramsey, N.F., *Magnetic Shielding of Nuclei in Molecules*. Physical Review, 1950. **78**(6): p. 699-703.
26. Tossell, J.A., *Second-nearest-neighbor effects on the NMR shielding of N in P(3)N(5) and hexagonal BN*. Chemical Physics Letters, 1999. **303**(3-4): p. 435-440.

27. Tossell, J.A., *Quantum mechanical calculation of (23)Na NMR shieldings in silicates and aluminosilicates*. Physics and Chemistry of Minerals, 1999. **27**(1): p. 70-80.
28. Valerio, G. and A. Goursot, *Density functional calculations of the Si-29 and Al-27 MAS NMR spectra of the zeolite mazzite: Analysis of geometrical and electronic effects*. Journal of Physical Chemistry B, 1999. **103**(1): p. 51-58.
29. Weber, J. and J. Gunne, *Calculation of NMR parameters in ionic solids by an improved self-consistent embedded cluster method*. Physical Chemistry Chemical Physics, 2010. **12**(3): p. 583-603.
30. Subramanian, V. and K. Seff, *Mercuric-Chloride, a Redetermination*. Acta Crystallographica Section B-Structural Science, 1980. **36**(SEP): p. 2132-2135.
31. Schurmann, M. and F. Huber, *A Redetermination of Lead(Iv) Acetate*. Acta Crystallographica Section C-Crystal Structure Communications, 1994. **50**: p. 1710-1713.
32. Hartman, J.D., et al., *Fragment-based 13C nuclear magnetic resonance chemical shift predictions in molecular crystals: An alternative to planewave methods*. Journal of Chemical Physics, 2015. **143**(10): p. 102809.
33. Bragg, W.L., *Crystal structure*. Nature, 1920. **105**: p. 646-648.
34. Brouwer, D.H. and G.D. Enright, *Probing local structure in zeolite frameworks: Ultrahigh-field NMR measurements and accurate first-principles calculations of zeolite (29)Si magnetic shielding tensors*. Journal of the American Chemical Society, 2008. **130**(10): p. 3095-3105.
35. Stueber, D., *The embedded ion method: A new approach to the electrostatic description of crystal lattice effects in chemical shielding calculations*. Concepts in Magnetic Resonance Part A, 2006. **28A**(5): p. 347-368.
36. Bermudez, V.M., *Ab Initio Study of the Interaction of Dimethyl Methylphosphonate with Rutile (110) and Anatase (101) TiO2 Surfaces*. Journal of Physical Chemistry C. **114**(7): p. 3063-3074.
37. Casarin, M., C. Maccato, and A. Vittadini, *A comparative study of CO chemisorption on Al2O3 and Ti2O3 nonpolar surfaces*. Journal of Physical Chemistry B, 2002. **106**(4): p. 795-802.
38. Casarin, M., et al., *Experimental and theoretical study of the interaction of CO2 with alpha-Al2O3*. Inorganic Chemistry, 2003. **42**(2): p. 436-445.
39. Brown, I.D. and R.D. Shannon, *Empirical Bond-Strength Bond-Length Curves for Oxides*. Acta Crystallographica Section A, 1973. **A 29**(MAY1): p. 266-282.
40. Brown, I.D. and K.K. Wu, *Empirical Parameters for Calculating Cation-Oxygen Bond Valences*. Acta Crystallographica Section B-Structural Science, 1976. **32**(JUL15): p. 1957-1959.
41. Brown, I.D. and D. Altermatt, *Bond-Valence Parameters Obtained from a Systematic Analysis of the Inorganic Crystal-Structure Database*. Acta Crystallographica Section B-Structural Science, 1985. **41**(AUG): p. 244-247.
42. Brown, I.D., *Recent Developments in the Methods and Applications of the Bond Valence Model*. Chemical Reviews, 2009. **109**(12): p. 6858-6919.

43. Leciejewicz, J., *On Crystal Structure of Tetragonal (Red) Pbo*. Acta Crystallographica, 1961. **14**(12): p. 1304.
44. Garnier, P., J. Moreau, and J.R. Gavarrri, *Rietveld Analysis of the Structure of $Pb(1-X)Ti(X)O(1+X)$ by Neutron-Diffraction*. Materials Research Bulletin, 1990. **25**(8): p. 979-986.
45. ADF2014, SCM, Theoretical Chemistry, Vrije Universiteit, Amsterdam, The Netherlands, <http://www.scm.com>.
46. Guerra, C.F., et al., *Towards an order-N DFT method*. Theoretical Chemistry Accounts, 1998. **99**(6): p. 391-403.
47. te Velde, G., et al., *Chemistry with ADF*. Journal of Computational Chemistry, 2001. **22**(9): p. 931-967.
48. Perdew, J.P., *Density-Functional Approximation for the Correlation-Energy of the Inhomogeneous Electron-Gas*. Physical Review B, 1986. **33**(12): p. 8822-8824.
49. Becke, A.D., *Density-Functional Exchange-Energy Approximation with Correct Asymptotic-Behavior*. Physical Review A, 1988. **38**(6): p. 3098-3100.
50. Perdew, J.P., K. Burke, and M. Ernzerhof, *Generalized gradient approximation made simple*. Physical Review Letters, 1996. **77**(18): p. 3865-3868.
51. Lee, C.T., W.T. Yang, and R.G. Parr, *Development of the Colle-Salvetti Correlation-Energy Formula into a Functional of the Electron-Density*. Physical Review B, 1988. **37**(2): p. 785-789.
52. Becke, A.D., *Density-Functional Thermochemistry .3. the Role of Exact Exchange*. Journal of Chemical Physics, 1993. **98**(7): p. 5648-5652.
53. Becke, A.D., *Density-functional thermochemistry .4. A new dynamical correlation functional and implications for exact-exchange mixing*. Journal of Chemical Physics, 1996. **104**(3): p. 1040-1046.
54. Perdew, J.P., M. Ernzerhof, and K. Burke, *Rationale for mixing exact exchange with density functional approximations*. Journal of Chemical Physics, 1996. **105**(22): p. 9982-9985.
55. Adamo, C. and V. Barone, *Toward reliable adiabatic connection models free from adjustable parameters*. Chemical Physics Letters, 1997. **274**(1-3): p. 242-250.
56. Adamo, C. and V. Barone, *Toward reliable density functional methods without adjustable parameters: The PBE0 model*. Journal of Chemical Physics, 1999. **110**(13): p. 6158-6170.
57. Vanlenthe, E., E.J. Baerends, and J.G. Snijders, *Relativistic Regular 2-Component Hamiltonians*. Journal of Chemical Physics, 1993. **99**(6): p. 4597-4610.
58. Lenthe, E.v., E.J. Baerends, and J.G. Snijders, *Relativistic total energy using regular approximations*. 1994, AIP. p. 9783-9792.

59. Lenthe, E.v., J.G. Snijders, and E.J. Baerends, *The zero-order regular approximation for relativistic effects: The effect of spin-orbit coupling in closed shell molecules*. 1996, AIP. p. 6505-6516.
60. van Lenthe, E., et al., *Relativistic regular two-component Hamiltonians*. International Journal of Quantum Chemistry, 1996. **57**(3): p. 281-293.
61. Schreckenbach, G. and T. Ziegler, *The calculation of NMR shielding tensors based on density functional theory and the frozen-core approximation*. International Journal of Quantum Chemistry, 1996. **60**(3): p. 753-766.
62. Autschbach, J. and E. Zurek, *Relativistic density-functional computations of the chemical shift of Xe-129 in Xe@C-60*. Journal of Physical Chemistry A, 2003. **107**(24): p. 4967-4972.
63. Ditchfield, R., *Self-Consistent Perturbation-Theory of Diamagnetism .1. Gauge-Invariant Lcao Method for Nmr Chemical-Shifts*. Molecular Physics, 1974. **27**(4): p. 789-807.
64. Wolinski, K., J.F. Hinton, and P. Pulay, *Efficient Implementation of the Gauge-Independent Atomic Orbital Method for Nmr Chemical-Shift Calculations*. Journal of the American Chemical Society, 1990. **112**(23): p. 8251-8260.
65. Schreckenbach, G. and T. Ziegler, *Calculation of Nmr Shielding Tensors Using Gauge-Including Atomic Orbitals and Modern Density-Functional Theory*. Journal of Physical Chemistry, 1995. **99**(2): p. 606-611.
66. Wolff, S.K. and T. Ziegler, *Calculation of DFT-GIAO NMR shifts with the inclusion of spin-orbit coupling*. Journal of Chemical Physics, 1998. **109**(3): p. 895-905.
67. Wolff, S.K., et al., *Density functional calculations of nuclear magnetic shieldings using the zeroth-order regular approximation (ZORA) for relativistic effects: ZORA nuclear magnetic resonance*. Journal of Chemical Physics, 1999. **110**(16): p. 7689-7698.
68. Autschbach, J., *The role of the exchange-correlation response kernel and scaling corrections in relativistic density functional nuclear magnetic shielding calculations with the zeroth-order regular approximation*. Molecular Physics, 2013. **111**(16-17): p. 2544-2554.
69. Clark, S.J., et al., *First principles methods using CASTEP*. Z. Kristallogr., 2005. **220**(5-6): p. 567-570.
70. Yates, J.R., et al., *Relativistic nuclear magnetic resonance chemical shifts of heavy nuclei with pseudopotentials and the zeroth-order regular approximation*. Journal of Chemical Physics, 2003. **118**(13): p. 5746-5753.

Chapter 4

MAGNETIC SHIELDING CALCULATIONS FOR MOLECULAR SOLIDS CONTAINING ^{199}Hg NUCLEI

4.1 Introduction

In this chapter, I present calculations of magnetic-shielding tensors for ^{199}Hg nuclei in molecular solids. The calculations are carried out by employing the cluster approach for molecular solids described in chapter 3. The effect of molecular-cluster size on the calculated magnetic-shielding tensors of a suite of mercury-containing materials is systematically evaluated. I also examine the effect of application of the frozen core approximation (FCA) in calculating the magnetic-shielding tensor. I examine the effect of neglect of various parts of the relativistic Hamiltonian in NMR calculations by treating molecular clusters at different levels of theory. The aim is to provide examples of how various approximations affect the prediction of NMR parameters in solids.

All clusters discussed herein are formed from experimental X-ray geometries found in the literature.[1-8] The set includes materials with relatively small first-coordination shells, and does not contain examples of large mercury-containing complexes. For solid systems with hydrogen atoms, e.g. $\text{Hg}(\text{acetate})_2$ and $\text{Hg}_2(\text{NO}_3)_2 \cdot 2\text{H}_2\text{O}$, [3, 4] an optimization of hydrogen positions was carried out on small clusters at the ZORA/scalar level with the BP86 density functional and the TZ2P/AE basis set. The mercury-containing molecular solids (and their crystallographic data) covered in this survey are given in Table 4.1. For some selected

systems (Hg_2Cl_2 and HgBr_2), the co-ordinates of the atomic positions are given in Appendix A.

Table 4.1 Reference Codes and Space Groups for the Investigated Mercury-containing Solids.

Crystal System	Reference Code^a	Space Group
$\text{Hg}(\text{SCN})_2$	10304	C12/m1
$\text{Hg}(\text{CN})_2$	412315	I42d
$\text{Hg}(\text{SeCN})_2$	Bowmaker et al.[7]	P21/c
$\text{Hg}(\text{CO}_2\text{CH}_3)_2$	Allmann et al.[3]	P21/a
HgCl_2	23277	Pnma
HgBr_2	39319	Cmc21
Hg_2Cl_2	23720	I4/mmm
$\text{K}[\text{Hg}(\text{SeCN})_3]$	Bowmaker et al.[7]	P21/n
$\text{Hg}_2(\text{NO}_3)_2 \cdot 2\text{H}_2\text{O}$	1958	P121/n1

a) Codes from the Inorganic Crystal Structure Database[9], or structures are from literature where references are given.

4.2 The Effect of Cluster Size and Charge on Magnetic Shielding

4.2.1 Model Clusters of Hg_2Cl_2

I have investigated the effect of cluster size on the magnetic shielding of Hg_2Cl_2 in clusters formed from the X-ray crystal structure (Figure 4.1). All calculations were performed within the ZORA/Spin-Orbit framework while employing a TZ2P/All-Electron (TZ2P/AE) basis set. For convenience, the predicted NMR chemical-shift principal components are calculated by comparison to the

calculated absolute shielding of the isolated dimethylmercury (DMM) molecule at the same level of theory, **7965** ppm. The calculated NMR parameters are tabulated in Table 4.2, along with the experimental results.

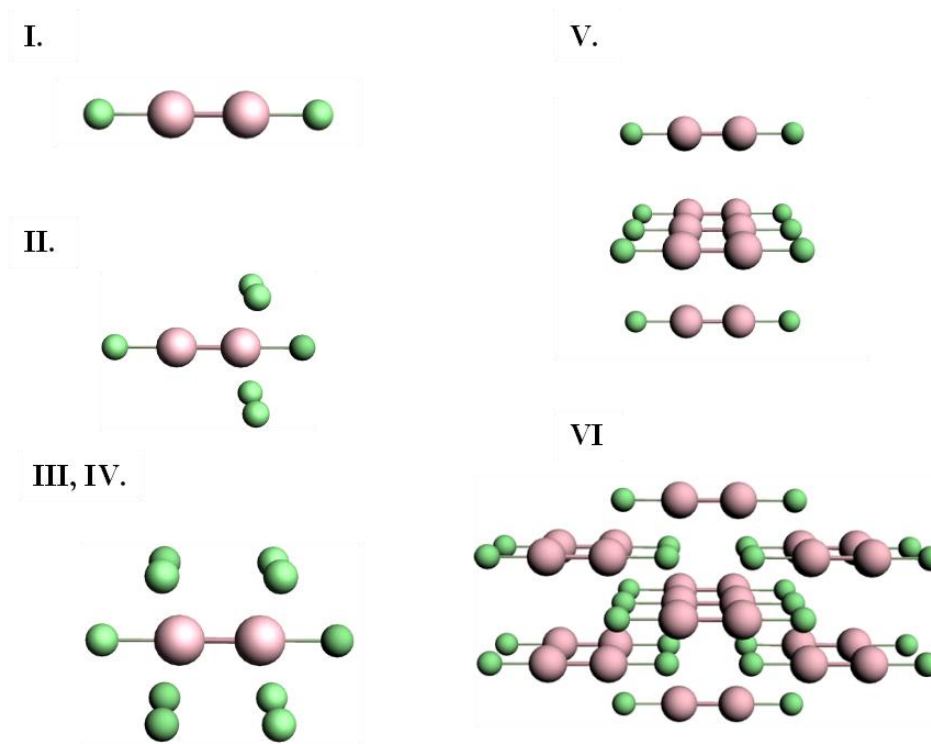


Figure 4.1 Various molecular clusters of Hg_2Cl_2 , as discussed in the text.

For cluster I, which consists of the isolated Hg_2Cl_2 unit, the calculated isotropic shift is about 580 ppm more negative than the experimental value, whereas the span is in error by almost 2000 ppm. This error in the span mostly arises from an error in the δ_{33} component of the chemical-shielding tensor, whereas the other two components are within 100 ppm of the respective experimental values.

Cluster II includes the extended coordination shell of the ^{199}Hg nucleus of interest. The added atoms (compared to cluster I) are the four Cl⁻ ions. The distance from the mercury nucleus to these additional chlorine centers is 3.21 Å, compared to the Hg-Cl bond distance of 2.43 Å.[5] The addition of these four chlorine centers significantly improves the calculated value of δ_{33} relative to the neglect of these centers in cluster I. The introduction of these centers, however, causes significant errors in the values of δ_{11} and δ_{22} that were not seen for cluster I. The calculated span is much smaller than the experimental span. Cluster II does not have certain symmetry elements that cluster I does, in particular the mirror plane between the two Hg centers. It appears that this lack of symmetry is one possible cause of the difference between the values of these two components for cluster I and cluster II.

Table 4.2 Calculated ^{199}Hg NMR Chemical Shifts for Model Clusters of Hg_2Cl_2 .

Model cluster	δ_{11} (ppm)	δ_{22} (ppm)	δ_{33} (ppm)	δ_{iso} (ppm)	Ω (ppm)	Residual^a
Experiment	<u>236</u>	<u>236</u>	<u>-3452</u>	<u>-993</u>	<u>3688</u>	-----
Cluster I	285	285	-5280	-1570	5520	1056
Cluster II	-1588	-1588	-3541	-2239	1937	1490
Cluster III	-803	-804	-3859	-1822	3031	881
Cluster IV	-1	-1	-4063	-1355	4030	402
Cluster V	598	598	-5113	-1306	5665	1003
Cluster VI	-66	-66	-3676	-1269	3582	278

$$\text{a) Residual} = \sqrt{\frac{1}{3} \sum_{i=1}^3 (\delta_{ii}^{\text{calc}} - \delta_{ii}^{\text{exp}})^2}$$

Cluster III adds elements to include the mirror symmetry that was lost in the definition of cluster II. Compared to cluster II, cluster III has four additional chlorine centers present. Calculations on cluster III give an isotropic shift that is 800 ppm more negative than the experimental value, whereas the span is underestimated by about 700 ppm. In general, all the calculated principal components of cluster III are more shielded than the experimental values. This observation is often the fingerprint of excess charge on the molecular cluster, which is the case for both cluster II and cluster III, having charges of -4 and -8, respectively.

Cluster IV is designed to compensate charge by termination with hydrogen atoms. These hydrogen atoms are inserted along the mercury-chlorine bond axis at 0.127 nm from the chlorine. This position maintains the symmetry at the mercury site whose NMR parameters we calculate. The compensation of charge, while maintaining the symmetry, decreases the isotropic shielding of the Hg center compared to that of cluster III. Additionally, residuals of the principal components are much smaller than those of cluster III. Saturation of the dangling bonds to decrease charge on the cluster is important in using clusters to model the local structure in solids for calculating NMR parameters, as these calculations show. However, in such treatments, the calculated chemical-shift tensor is usually dependent on the positions of the hydrogen atoms.

In cluster V, we include only the Hg_2Cl_2 units which contain the four next-nearest Hg atoms to the NMR nucleus of interest. The Hg-Hg distances between the Hg_2Cl_2 units are 0.448 nm. As expected, inclusion of next-nearest Hg centers has a smaller effect on NMR parameters than inclusion of the next-nearest Cl centers, since the Hg-Hg distance is larger than the Hg-Cl distance. Moreover, since the next-nearest

chlorines are missing in this cluster, the agreement between experiment and calculation is not good. Compared to cluster I, there is a considerable difference between the principal components, which indicates that next-nearest Hg atoms should be included in the extended coordination shell in designing the cluster.

In cluster VI, not only is the first coordination shell present, but the extended coordination shell and next-nearest neighbors are also included. Additionally, the structure is completed by adding atoms to produce uncharged Hg_2Cl_2 units, as shown in Figure 4.1. Inclusion of these additional centers improves the calculated values of the chemical-shift tensor components, so that the residual is the smallest of any of the clusters examined. We have found that, with available computational resources, a residual of 200 ppm or less for these kinds of heavy atoms indicates a reasonable model cluster. With this accuracy and the known wide ranges of shifts for ^{199}Hg , calculation with these cluster models allows assignment of shifts to nuclei in unique structural motifs.

4.2.2 Isolated Molecule versus Large Cluster

In this section, NMR parameters for the mercury compounds, using large-cluster models and small-cluster models, are reported. The model clusters are shown in Figure 4.2. The calculated NMR chemical-shift parameters are tabulated in Table 4.3, along with reported experimental values. The σ_{ref} for determining chemical shifts is taken as the intersection of the best-fit linear correlation for each type of cluster (Figure 4.3a and 4.3b). These values are 7853 ppm and 8043 ppm for small and large clusters, respectively.

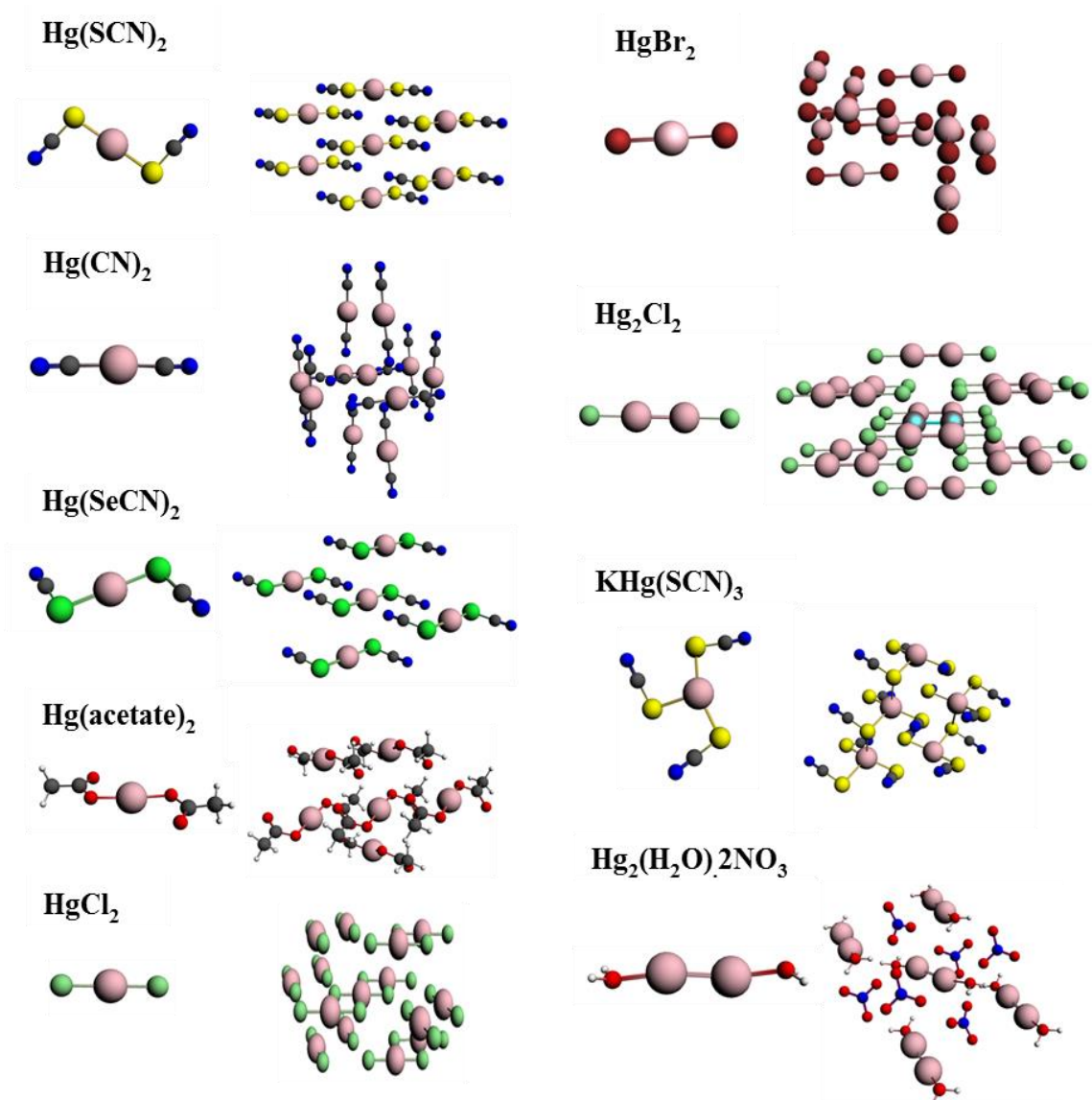


Figure 4.2 Small (left) and large (right) cluster models for the mercury-containing molecular solids.

Table 4.3 NMR Chemical-Shift Parameters for Small and Large Model Clusters of ^{199}Hg -Containing Solids.

Model clusters	δ_{11} (ppm)	δ_{22} (ppm)	δ_{33} (ppm)	δ_{iso} (ppm)	Ω (ppm)	Residual
Hg(SCN)₂						
Experiment[10]	<u>-81</u>	<u>-328</u>	<u>-3390</u>	<u>-1300</u>	<u>3309</u>	-----
Small Cluster	351	-1154	-4694	-1832	5006	926
Large Cluster	198	-501	-3663	-1322	3830	246
Hg(CN)₂						
Experiment[11]	<u>-33</u>	<u>-381</u>	<u>-3773</u>	<u>-1396</u>	<u>3740</u>	-----
Small Cluster	-101	-106	-5490	-1899	5347	1005
Large Cluster	51	-3	-4081	-1344	4099	286
Hg(SeCN)₂						
Experiment[7]	<u>-503</u>	<u>-1337</u>	<u>-3440</u>	<u>-1760</u>	<u>2937</u>	-----
Small Cluster	-617	-1176	-4601	-2131	3953	680
Large Cluster	-503	-1339	-3434	-1759	2908	4
Hg(Acetate)₂						
Experiment[10]	<u>-1859</u>	<u>-1947</u>	<u>-3685</u>	<u>-2497</u>	<u>1826</u>	-----
Small Cluster	-1757	-2052	-4688	-2832	2908	585
Large Cluster	-1948	-2076	-3639	-2554	1678	94
HgCl₂						
Experiment[10]	<u>-282</u>	<u>-573</u>	<u>-4019</u>	<u>-1625</u>	<u>3737</u>	-----
Small Cluster	-134	-135	-5369	-1598	5194	765
Large Cluster	-242	-299	-4311	-1617	4036	232
HgBr₂						
Experiment[12]	<u>-1945</u>	<u>-1945</u>	<u>-3293</u>	<u>-2394</u>	<u>1348</u>	-----
Small Cluster	-2128	-2128	-5331	-3195	3178	1186

Large Cluster	-1898	-1930	-3383	-2403	1473	59
<hr/> Hg_2Cl_2						
Experiment[12]	<u>236</u>	<u>236</u>	<u>-3452</u>	<u>-993</u>	<u>3688</u>	-----
Small Cluster <u>Hg(1)</u>	172	172	-5392	-1683	5520	1121
Small Cluster <u>Hg(2)</u>	172	172	-5392	-1683	5520	1121
Large Cluster <u>Hg(1)</u>	13	12	-3598	-1191	3582	201
Large Cluster <u>Hg(2)</u>	42	42	-3598	-1172	3611	180
<hr/> $\text{K}[\text{Hg}(\text{SCN})_3]$						
Experiment [7]	<u>49</u>	<u>-323</u>	<u>-1941</u>	<u>-738</u>	<u>1990</u>	-----
Small Cluster	-169	-710	-2373	-1084	2187	358
Large Cluster	161	-201	-1808	-616	1953	123
<hr/> $\text{Hg}_2(\text{NO}_3)_2 \cdot 2\text{H}_2\text{O}$						
Experiment[10]	<u>-435</u>	<u>-497</u>	<u>-3669</u>	<u>-1534</u>	<u>3234</u>	-----
Small Cluster <u>Hg(1)</u>	-1614	-1676	-5215	-2835	3572	1312
Small Cluster <u>Hg(2)</u>	-1551	-1656	-5214	-2807	3635	1288
Large Cluster <u>Hg(1)</u>	-988	-1078	-4058	-2042	3045	515
Large Cluster <u>Hg(2)</u>	-813	-1092	-4056	-1987	3217	464

In general, calculations on small clusters predict isotropic chemical shifts (δ_{iso}) to within 300 – 1000 ppm of the experimental values. As seen in Table 4.3, the deviations of the principal components of the chemical-shift tensor calculated for small clusters are often more severely in error (relative to experimental data) than the isotropic shifts. The differences between computed spans (which do not depend on errors in referencing) and experimental spans often exceed 1000 ppm. For this reason, conclusions about the quality of models based on the near agreement of a calculated isotropic chemical shift with an experimental chemical shift can be misleading. More

importantly, the principal components of a chemical-shift tensor reflect important properties of the electronic structure that cannot be discerned by concentrating on the isotropic chemical shift alone. [13, 14] For example, the isotropic chemical shift of HgCl_2 calculated with a small cluster is only 27 ppm from the experimental value, but the calculated span deviates by 1457 ppm from the experimental value.

The spans calculated for large clusters are closer to the experimental values for all cases examined. Additionally, there is better agreement between experimental and predicted isotropic chemical shifts, as well as better agreement between calculated and experimental principal components of the shift tensor, as can be discerned from the smaller residuals for the large clusters. With the exception of the hydrated mercurous nitrate, the residuals of all the large-cluster-model calculations are near or below 200 ppm, which seems to be some limit for clusters of this size for these systems. But, even for the hydrated mercurous nitrate, the large-cluster model gives better agreement with experiment than the small-cluster model.

The performance of small- and large-cluster models is shown graphically in Figures 4.3 and 4.4. In Figure 4.3, the correlation between calculated chemical-shielding tensor components and experimental chemical-shift tensor components is shown for small clusters. In Figure 4.4, the same correlation is shown for large clusters. The correlation for the large clusters has a slope that deviates by only 3% from the ideal slope of -1, whereas the linear correlation for the small clusters deviates by 35% from this ideal value.

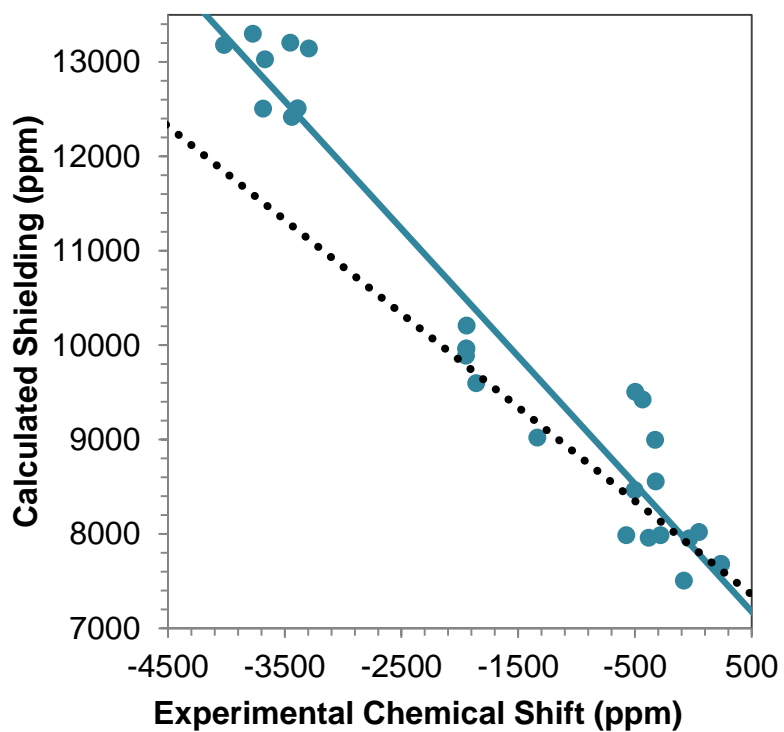


Figure 4.3 Correlation diagram for the calculated principal components of the magnetic-shielding tensor and the principal components of the experimental chemical-shift tensor for the ^{199}Hg -containing systems modelled using **small clusters**. The blue line is the best-fit linear correlation. For the small clusters, $\sigma_{\text{calc}} = -1.3518 \delta_{\text{exp}} + 7854$ and the R^2 value of the correlation is 0.934. The dashed line shows the ideal behavior. ($\sigma_{\text{calc}} = -\delta_{\text{exp}} + 7854$)

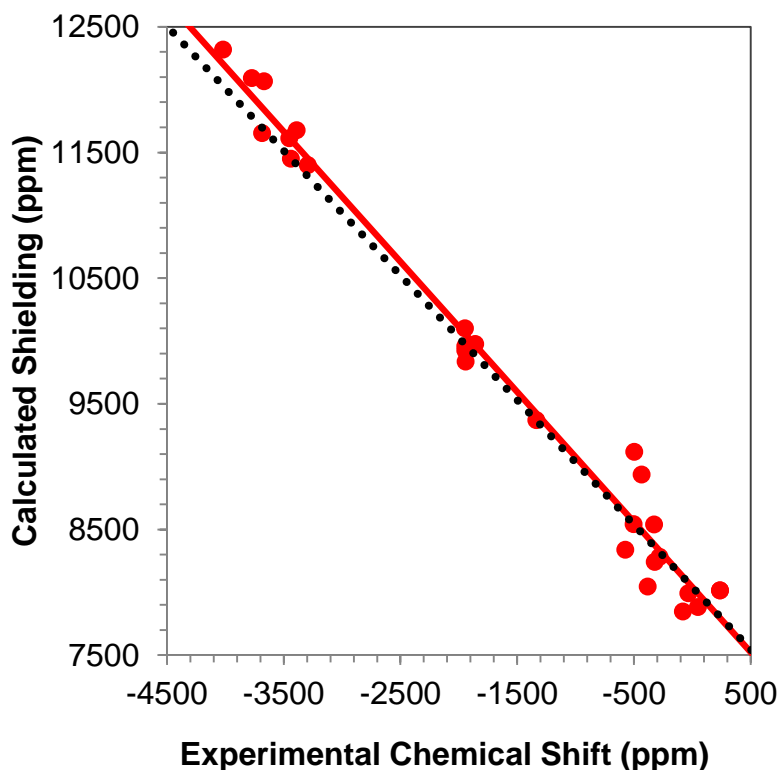


Figure 4.4 Correlation diagram for the calculated principal components of the magnetic-shielding tensor and the principal components of the experimental chemical-shift tensor for the ^{199}Hg -containing systems modelled using **large clusters**. The red line is the best-fit linear correlation. For the large clusters, $\sigma_{\text{calc}} = -1.0352 \delta_{\text{exp}} + 8042$ and the R^2 value of the correlation is 0.981. The dashed line shows the ideal behavior. ($\sigma_{\text{calc}} = -\delta_{\text{exp}} + 8042$)

From the intercept of the best-fit linear correlation lines in Figures 4.3 and 4.4, the absolute shielding of DMM can be estimated within the approximate two-component ZORA/spin-orbit framework for large and small clusters. Within this framework, the absolute shielding of DMM is predicted to be 7854 ppm by the small clusters and 8042 ppm by the large clusters. In separate calculations on an isolated DMM molecule at the same level of theory and with either (a) a fully optimized geometry or (b) the experimental geometry [15] with optimized hydrogen positions,

the predicted isotropic shielding in case (a) is 8120 ppm, and in case (b) it is 7965 ppm. In a previous study, Taylor et al.[16] showed (with the same level of theory that the absolute shielding of DMM is between 7929 and 8095 ppm.

The shielding constant of DMM has also been calculated by means of four-component relativistic methods.[17, 18] Within the four-component DFT theory, the absolute shielding of DMM is found to be 10299 ppm, whereas the Dirac-Hartree-Fock (DHF) formalism gives a value of 12417 ppm. Wodynski et al.[19] report that ZORA reproduces only 75-79% of the shielding values of the four-component results for the heavy metals of the sixth row of the periodic table. Despite the underestimation of the shielding constants, Arcisauskaite et al.[17] showed that ^{199}Hg shielding constants calculated with ZORA/spin-orbit and with four-component DFT follow a similar trend, and the chemical shifts calculated with these two methods are in agreement within 60 ppm. Autschbach shows that the valence-shell properties such as chemical shift and J coupling are well described in the ZORA formalism.[20-22] This observation is supported by our findings that calculations using ZORA produce results in agreement with experiment.

In Ramsey's formulation [23], the shielding is evaluated as an integral of operators which vary as $1/r^3$, where r is the distance from the electron to the nucleus of interest. One expects that major contributions to NMR shielding are predominantly from orbitals that place the electron near the nucleus. For solids, the positions of nearby atoms are exceedingly important in determining the general structure of orbitals. Comparison of the results for small and large clusters shows that medium-to-long-range effects must be taken into account to determine meaningful NMR tensor parameters.

There are two factors that contribute to the difference between the results for small clusters and for large clusters. First, missing atoms in the near region in the small cluster for a ^{199}Hg -containing system may affect the magnetic shielding. A secondary effect results from the fact that the nearest neighbors of the ligands are not included in the small clusters. As a result, the molecular orbitals (MOs) forming Hg-L bonds are largely localized, which would not adequately represent the structural effects on magnetic shielding. Both effects depend on the crystal structure, and they contribute differently to the ^{199}Hg shielding in the two models.

4.3 The Effect of Basis Set and Frozen Core Approximation

The frozen core approximation (FCA) is commonly used in many applications to trim the computational time.[24] It is generally thought that the deep core electrons are not strongly influenced by changes that may influence the valence electrons. I have investigated whether use of the FCA for these clusters yields reliable NMR parameters by the following procedure. For the large clusters of Figure 4.2, the electrons of the first coordination shell near the nucleus of interest were treated with an all-electron (AE) basis set, whereas the rest of the cluster was treated with the FCA. TZP and DZ basis sets with a frozen large core are used in the part of the cluster treated with the FCA. (The details of the frozen core basis sets are given in Table B1 in Appendix B)

4.3.1 Correlation of Experimental and Calculated ^{199}Hg principal components

Figure 4.5 shows the correlation between the calculated magnetic-shielding principal components with FCA(DZ)/AE basis set versus the experimental chemical-shift principal components. The same correlation is shown for the FCA(TZP)/AE basis set in Figure 4.6. In Table 4.4, the results of the calculations employing the FCA are

given for various mercury-containing solids. The σ_{ref} values are taken as the intersections of the best-fit linear correlation (Figure 4.5 and 4.6) for each type of basis set.

Table 4.4 Comparison of Calculated ^{199}Hg NMR Parameters Using the Frozen Core Approximation (FCA) for Remote Regions with Calculations Using the All-Electron (AE) Method for All Regions of the Cluster.

Model clusters	δ_{11} (ppm)	δ_{22} (ppm)	δ_{33} (ppm)	δ_{iso} (ppm)	Ω (ppm)	Residual
Hg(SCN) ₂	<u>-81</u>	<u>-328</u>	<u>-3390</u>	<u>-1300</u>	<u>3309</u>	
FCA(DZ)/AE	209	-557	-3588	-1312	3766	242
FCA(TZP)/AE	197	-503	-3644	-1316	3810	240
All-electron	198	-501	-3663	-1322	3830	246
Hg(CN) ₂	<u>-33</u>	<u>-381</u>	<u>-3773</u>	<u>-1396</u>	<u>3740</u>	
FCA(DZ)/AE	29	-13	-4072	-1352	4068	276
FCA(TZP)/AE	53	12	-4080	-1339	4099	292
All-electron	51	-3	-4081	-1344	4099	286
Hg(SeCN) ₂	<u>-503</u>	<u>-1337</u>	<u>-3440</u>	<u>-1760</u>	<u>2937</u>	
FCA(DZ)/AE	-516	-1256	-3516	-1763	2975	64
FCA(TZP)/AE	-484	-1332	-3436	-1751	2928	12
All-electron	-503	-1339	-3434	-1759	2908	4
Hg(Acetate) ₂	<u>-1859</u>	<u>-1947</u>	<u>-3685</u>	<u>-2497</u>	<u>1826</u>	
FCA(DZ)/AE	-1908	-2030	-3691	-2543	1768	38
FCA(TZP)/AE	-1935	-2061	-3629	-2542	1681	85
All-electron	-1948	-2076	-3639	-2554	1678	94
HgCl ₂	<u>-282</u>	<u>-573</u>	<u>-4019</u>	<u>-1625</u>	<u>3737</u>	
FCA(DZ)/AE	-249	-316	-4303	-1622	4021	222

FCA(TZP)/AE	-232	-309	-4305	-1615	4040	226
All-electron	-242	-299	-4311	-1617	4036	232
HgBr ₂	<u>-1945</u>	<u>-1945</u>	<u>-3293</u>	<u>-2394</u>	<u>1348</u>	
FCA(DZ)/AE	-1867	-1895	-3395	-2386	1516	80
FCA(TZP)/AE	-1894	-1922	-3324	-2380	1418	37
All-electron	-1898	-1930	-3383	-2403	1473	59
Hg ₂ Cl ₂	<u>236</u>	<u>236</u>	<u>-3452</u>	<u>-993</u>	<u>3688</u>	
FCA(DZ)/AE <u>Hg(1)</u>	-21	-21	-3687	-1243	3636	250
FCA(DZ)/AE <u>Hg(2)</u>	-5	-5	-3687	-1232	3652	239
FCA(TZP)/AE <u>Hg(1)</u>	-2	-3	-3582	-1196	3551	209
FCA(TZP)/AE <u>Hg(2)</u>	28	28	-3582	-1176	3581	186
All-electron <u>Hg(1)</u>	13	12	-3598	-1191	3582	201
All-electron <u>Hg(2)</u>	42	42	-3598	-1172	3611	180
K[Hg(SCN) ₃]	<u>49</u>	<u>-323</u>	<u>-1941</u>	<u>-738</u>	<u>1990</u>	
FCA(DZ)/AE	214	-221	-1772	-593	1970	148
FCA(TZP)/AE	164	-210	-1807	-617	1955	121
All-electron	161	-201	-1808	-616	1953	123
Hg ₂ (NO ₃) ₂ ·2H ₂ O	<u>-435</u>	<u>-497</u>	<u>-3669</u>	<u>-1534</u>	<u>3234</u>	
FCA(DZ)/AE <u>Hg(1)</u>	-990	-1014	-4047	-2017	3032	489
FCA(DZ)/AE <u>Hg(2)</u>	-820	-1084	-4048	-1984	3201	461
FCA(TZP)/AE <u>Hg(1)</u>	-993	-1069	-4070	-2044	3053	516
FCA(TZP)/AE <u>Hg(2)</u>	-820	-1090	-4066	-1992	3220	468
All-electron <u>Hg(1)</u>	-988	-1078	-4058	-2042	3045	515
All-electron <u>Hg(2)</u>	-813	-1092	-4056	-1987	3217	464

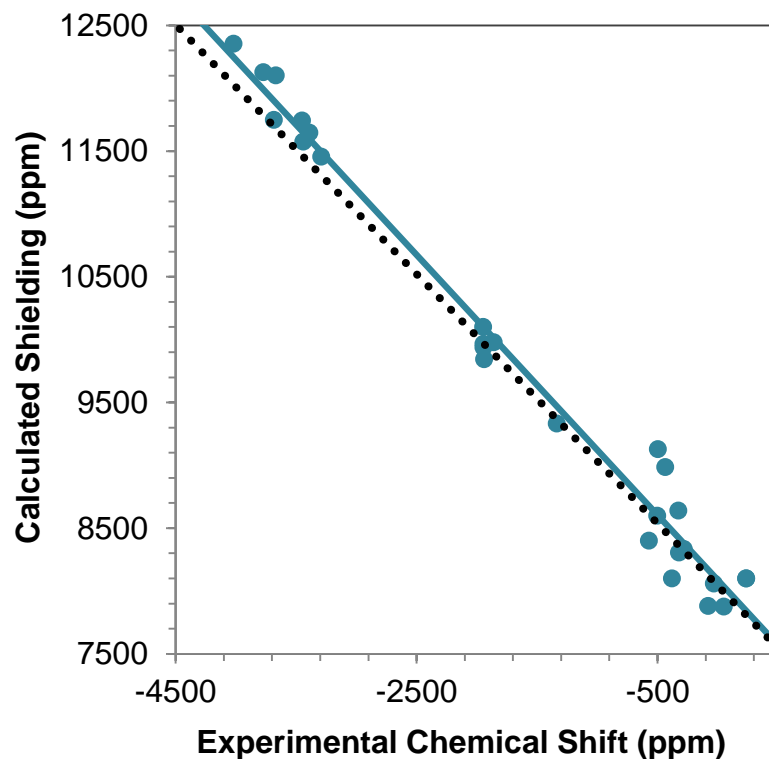


Figure 4.5 Correlation diagram for the calculated principal components of the magnetic-shielding tensor determined with the **FCA(DZ)/AE** basis set, and the principal components of the experimental chemical-shift tensor for the ^{199}Hg -containing molecular solids. For this correlation, $\sigma_{\text{calc}} = -1.0354 \delta_{\text{exp}} + 8085$ and the R^2 value of the correlation is 0.980. The dashed line shows the ideal behavior. ($\sigma_{\text{calc}} = -\delta_{\text{exp}} + 8085$)

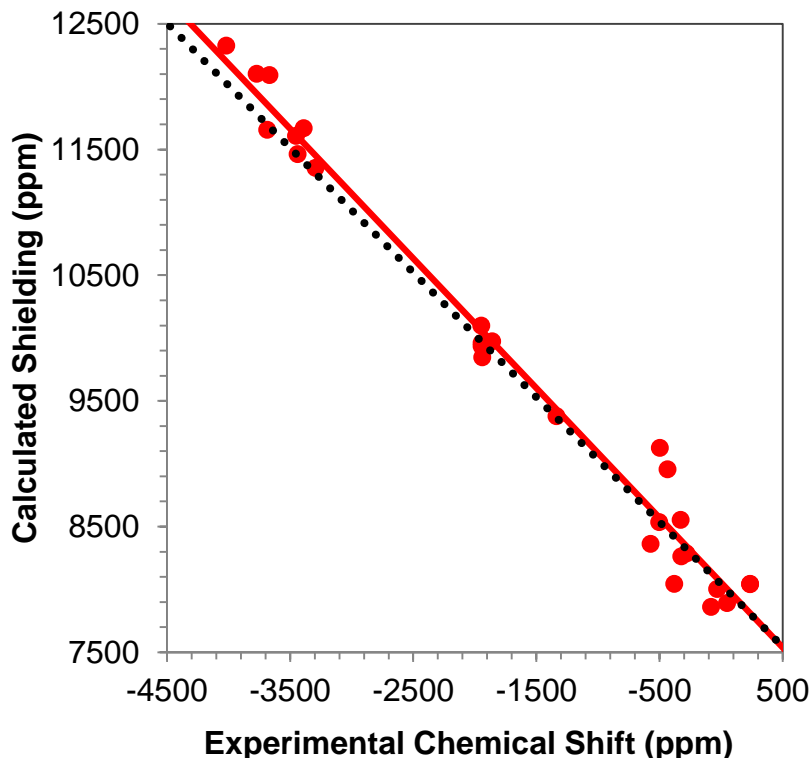


Figure 4.6 Correlation diagram for the calculated principal components of the magnetic-shielding tensor determined with the **FCA(TZP)/AE** basis set, and the principal components of the experimental chemical-shift tensor for the ^{199}Hg -containing molecular solids. For this correlation, $\sigma_{\text{calc}} = -1.0316 \delta_{\text{exp}} + 8055$ and the R^2 value of the correlation is 0.980. The dashed line shows the ideal behavior. ($\sigma_{\text{calc}} = -\delta_{\text{exp}} + 8055$)

From the correlation, σ_{ref} is found to be 8055 ppm or 8085 ppm, respectively, for FCA(TZP)/AE and FCA(DZ)/AE basis sets. The results determined with FCA(TZP)/AE are closer to the all-electron results, as expected. The difference between principal components calculated with the FCA(TZP)/AE and the AE basis sets does not exceed 25 ppm for most cases. The largest difference is 59 ppm for δ_{33} of HgBr_2 . The differences between principal components determined with FCA(DZ)/AE compared to the all-electron basis set are slightly larger. Nevertheless, given the

accuracy of the NMR calculations on heavy nuclei, calculations using the FCA for the remote atoms and calculations with the full all-electron basis set produce almost the same NMR parameters. In fact, Figures 4.5 and 4.6 show that the correlation for results using the FCA with TZP basis set is slightly closer to the ideal case than for results using the full all-electron basis set for the large clusters. This difference is within the uncertainty of the experimental measurements. The two calculations essentially give the same results within experimental error.

4.3.2 Comparison of Computational Time; All Electron vs. Frozen Core

Although there are very small differences in the computed NMR parameters, there is a substantial difference in computational time that favors using the FCA. In Table 4.5, we compare the computational time and number of Cartesian functions employed for selected calculations, when using the all-electron basis set versus the FCA(TZP)/AE and FCA(DZ)/AE basis sets.

Table 4.5 Computational Time (CT) and Number of Cartesian Functions (cf) for Selected AE and FCA Large Cluster Calculations.

Model clusters	AE		FCA(TZP)/AE		FCA(DZ)/AE	
	# of cf	CT (s)	# of cf	CT (s)	# of cf	CT (s)
Hg ₂ Cl ₂	4264	209040	2584	13020	2080	1037
HgCl ₂	3030	20160	1840	2940	1406	1260
Hg(CN) ₂	2706	15240	1716	3540	1206	1200
HgBr ₂	2409	14460	1822	2460	1432	600

The calculations with the triple-zeta basis set generally take longer than those with the double-zeta basis set, but they are both substantially shorter than a calculation on the same cluster using the all-electron wave function. For example, the all-electron calculation for a large cluster of Hg_2Cl_2 took nearly 2.5 days, whereas the FCA(TZP)/AE treatment of the same cluster required 3.6 hours and the FCA(DZ)/AE treatment took only 35 minutes. These results indicate that the FCA can be applied to the peripheral portions of large clusters in solid-state NMR calculations with minimal introduction of significant errors.

4.3.3 Convergence of Magnetic Shielding with Cluster Size

An important criterion in the cluster-based approach is the convergence of NMR parameters with increasing cluster size. Since the computational requirements are considerably low with FCA basis sets, it is possible to investigate whether calculated parameters are converged with these larger clusters. For this reason, the principal components of the magnetic-shielding tensor are calculated for $\text{Hg}(\text{SCN})_2$ and Hg_2Cl_2 at the BP86/ZORA/Spin-Orbit level of theory with the FCA/TZP/AE basis set. The molecular clusters are extended another coordination shell from the 'large clusters (extended clusters) as explained in Chapter 3. The resulting extended clusters for $\text{Hg}(\text{SCN})_2$ and Hg_2Cl_2 are displayed in Figure 4.7. Table 4.6 shows the comparison of chemical-shielding components for large clusters and extended clusters of $\text{Hg}(\text{SCN})_2$ and Hg_2Cl_2 .

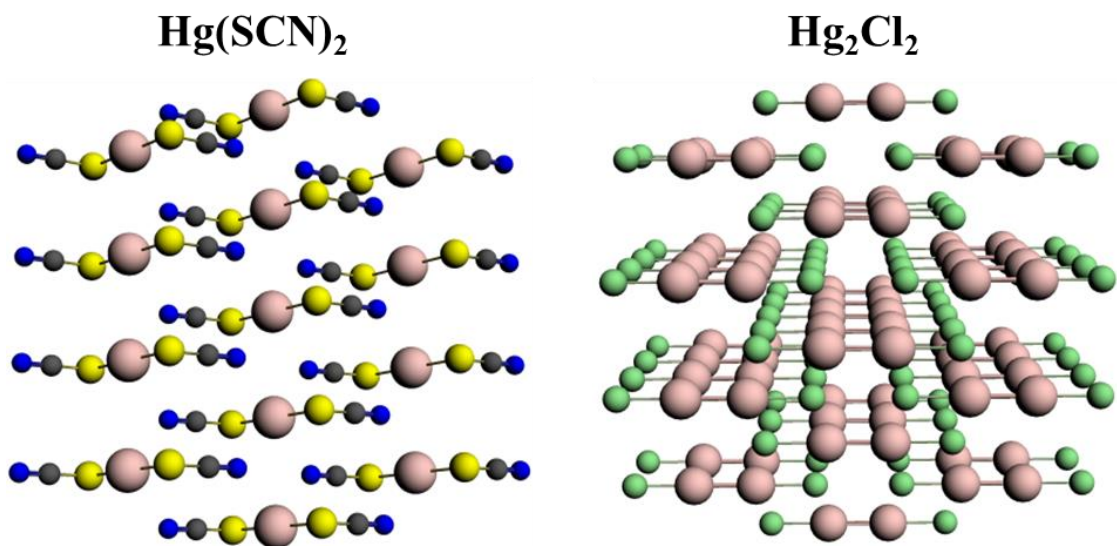


Figure 4.7 Extended cluster models for Hg(SCN)₂ and Hg₂Cl₂.

For Hg(SCN)₂, the large cluster and the extended cluster produce similar results. The differences between σ_{33} and σ_{11} are 22 ppm and 9 ppm, whereas σ_{22} is the same for the large cluster and the extended cluster. The difference in σ_{iso} is only 4 ppm. For Hg₂Cl₂, the differences are slightly larger than those of Hg(SCN)₂. The largest difference is for σ_{33} (79 ppm). On the other hand, the differences for σ_{iso} are 5 ppm and 13 ppm for Hg(1) and Hg(2) respectively. For all calculated principal components, the variation between the two clusters is less than 1%, which would be a valid convergence criterion for heavy-nucleus shieldings.

Table 4.6 Comparison of ^{199}Hg NMR Parameters of Large Clusters and Extended Clusters of $\text{Hg}(\text{SCN})_2$ and Hg_2Cl_2 Using the Frozen Core Approximation

Model clusters	σ_{11} (ppm)	σ_{22} (ppm)	σ_{33} (ppm)	σ_{iso} (ppm)
$\text{Hg}(\text{SCN})_2$				
Large cluster	7860	8554	11670	9361
Extended cluster	7869	8554	11648	9357
Hg_2Cl_2				
Large cluster <u>Hg(1)</u>	8058	8058	11609	9242
Large cluster <u>Hg(2)</u>	8028	8028	11609	9222
Extended cluster <u>Hg(1)</u>	8089	8090	11531	9237
Extended cluster <u>Hg(2)</u>	8088	8088	11530	9235

4.4 Relativistic Effects on ^{199}Hg Magnetic Shielding

An important consideration in the calculation of magnetic shielding of heavy nuclei such as ^{199}Hg , ^{207}Pb , and ^{119}Sn is the inclusion of relativistic effects.[25-28] Including relativistic terms in the Hamiltonian increases the computational time, which makes it of some practical importance to determine how significantly these affect the calculated magnetic shielding. These effects are investigated by comparing results of calculations that (a) neglect all relativistic terms (nonrelativistic results) with (b) results of calculations that include only scalar relativistic corrections, and with (c) results of calculations that include the full spin-orbit interaction for large clusters.

Figure 4.8 shows the correlation between calculated magnetic shieldings and experimental chemical shifts for all tensor components of the large clusters, when the

system is treated with only nonrelativistic terms. The linear correlation has a slope of -0.667 and an intercept of 6221 ppm.

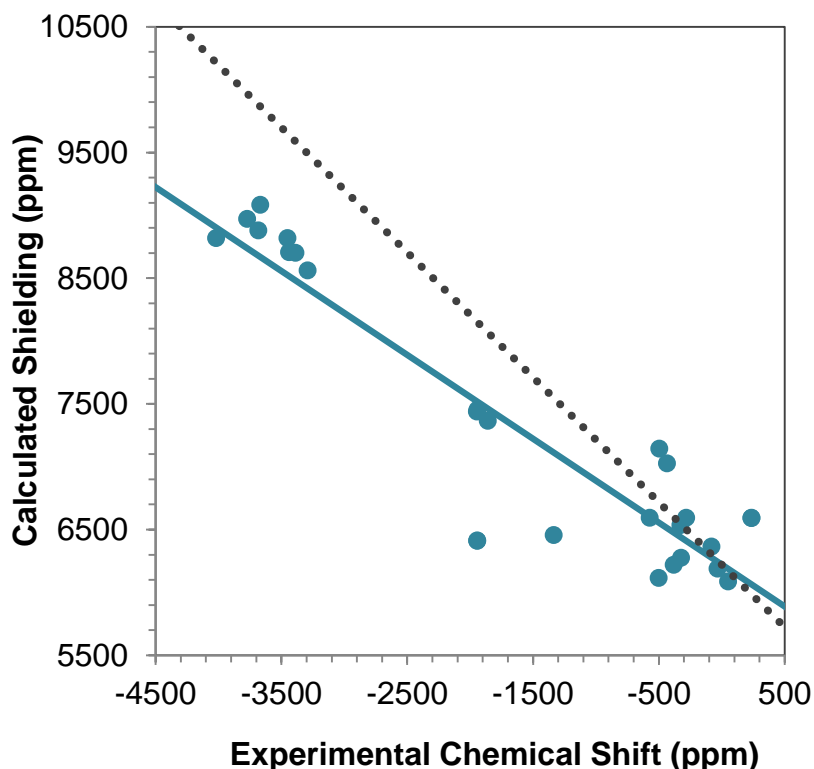


Figure 4.8 Correlation diagram for the calculated principal components of the magnetic-shielding tensor at the **nonrelativistic** level of theory (BP86/AE), and the principal components of the experimental chemical-shift tensor for the ^{199}Hg -containing molecular solids. For this correlation, $\sigma_{\text{calc}} = -0.667\delta_{\text{exp}} + 6221$ and R^2 is 0.841. The dashed line shows the ideal behavior.

Figure 4.9 shows a similar correlation for the same systems when only **scalar relativistic corrections** are considered at ZORA level. The slope of the linear correlation is -0.695 for this system and the intercept is 5976 ppm. The inclusion of

the scalar relativistic terms improves agreement with the experimental data marginally over the nonrelativistic results.

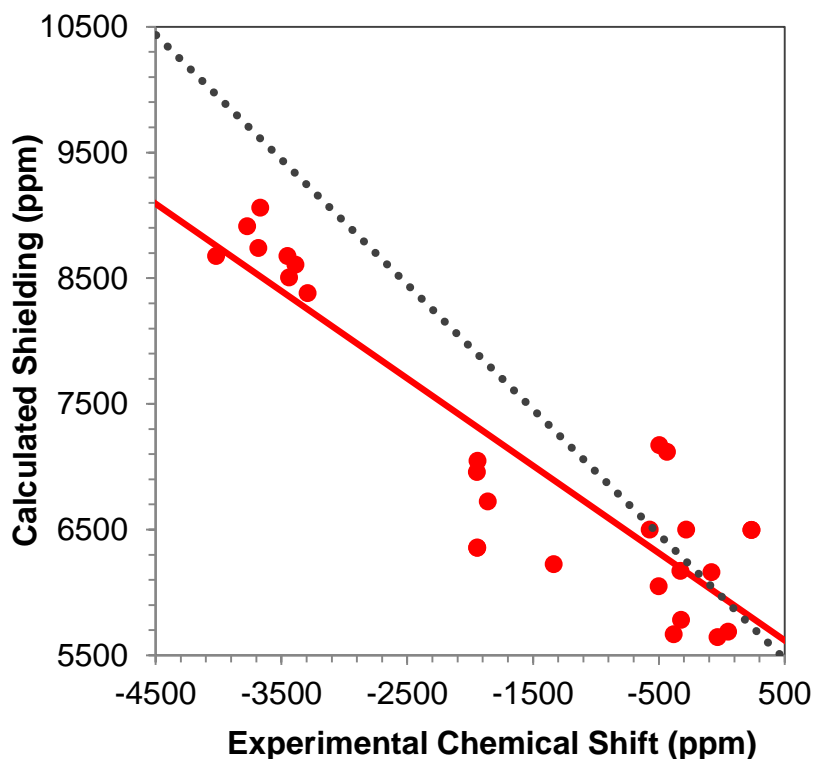


Figure 4.9 Correlation diagram for the calculated principal components of the magnetic-shielding tensor at **ZORA/scalar level of theory**, and the principal components of the experimental chemical-shift tensor for the ^{199}Hg -containing molecular solids. For this correlation, $\sigma_{\text{calc}} = -0.695\delta_{\text{exp}} + 5965$ and the R^2 value of the correlation is 0.806. The dashed line shows the ideal behavior.

The data of Figure 4.4 show the result of inclusion of **relativistic effects at the spin-orbit level**. The slope of the linear correlation line is -1.035 and the intercept is 8042 ppm. Thus, within 3.5%, the slope of this linear trend is correct. In addition, comparison of Figures 4.4, 4.8 and 4.9 shows that scatter about the ideal line is much

smaller when the ZORA spin-orbit Hamiltonian is used. Significantly, there is a systematic error of approximately 2000 ppm in the predicted value of the magnetic shielding of DMM when the spin-orbit terms are neglected. From these calculations, it is clear that one must include spin-orbit relativistic terms in the Hamiltonian when calculating magnetic shieldings of mercury-containing solids.

REFERENCES

1. Dorm, E., *Studies on the crystal chemistry of the mercurous ion and of mercurous salts*. Chemical Communications, University of Stockholm, 1970(3): p. 1-25.
2. Beaucham, A.I. and D. Goutier, *Crystal and Molecular Structure of Mercuric Thiocyanate*. Canadian Journal of Chemistry, 1972. **50**(7): p. 977-981.
3. Allmann, R., *Structure of Mercuric Acetate*. Zeitschrift Fur Kristallographie, 1973. **138**: p. 366-373.
4. Grdenic, D., M. Sikirica, and I. Vickovic, *Redetermination of Crystal-Structure of Mercury(I) Nitrate Dihydrate*. Acta Crystallographica Section B-Structural Science, 1975. **31**(AUG15): p. 2174-2175.
5. Subramanian, V. and K. Seff, *Mercuric-Chloride, a Redetermination*. Acta Crystallographica Section B-Structural Science, 1980. **36**(SEP): p. 2132-2135.
6. Pakhomov, V.I., et al., *Better Accuracy of HgBr₂ Structure*. Zhurnal Neorganicheskoi Khimii, 1990. **35**(10): p. 2476-2478.
7. Bowmaker, G.A., et al., *Solid-state Hg-199 MAS NMR studies of mercury(II) thiocyanate complexes and related compounds. Crystal structure of Hg(SeCN)₂*. Inorganic Chemistry, 1998. **37**(8): p. 1734-1743.
8. Reckeweg, O. and A. Simon, *X-ray and Raman investigations on cyanides of mono- and divalent metals and synthesis, crystal structure and Raman spectrum of Tl-5(CO₃)₂(CN)*. Zeitschrift Fur Naturforschung Section B-a Journal of Chemical Sciences, 2002. **57**(8): p. 895-900.
9. *The Inorganic Crystal Structure Database is copyrighted by the Fachinformationszentrum Karlsruhe and the National Institute of Standards and Technology.* <http://icsd.fiz-karlsruhe.de>.
10. Bowmaker, G.A., R.K. Harris, and D.C. Apperley, *Solid-state Hg-199 MAS NMR and vibrational spectroscopic studies of dimercury(I) compounds*. Inorganic Chemistry, 1999. **38**(22): p. 4956-4962.
11. Bowmaker, G.A., R.K. Harris, and S.W. Oh, *Solid-state NMR spectroscopy of mercury compounds*. Coordination Chemistry Reviews, 1997. **167**: p. 49-94.
12. Taylor, R.E., S. Bai, and C. Dybowski, *A solid-state Hg-199 NMR study of mercury halides*. Journal of Molecular Structure, 2011. **987**(1-3): p. 193-198.
13. Orendt, A.M. and J.C. Facelli, *Solid-state effects on NMR chemical shifts*. Annual Reports on Nmr Spectroscopy, 2007. **62**: p. 115-178.

14. Bonhomme, C., et al., *First-Principles Calculation of NMR Parameters Using the Gauge Including Projector Augmented Wave Method: A Chemist's Point of View*. Chemical Reviews, 2012. **112**(11): p. 5733-5779.
15. Kashiwabara, K., et al., *Electron Diffraction Study of Dimethylmercury*. Bulletin of the Chemical Society of Japan, 1973. **46**(2): p. 407-409.
16. Taylor, R.E., et al., *Revisiting HgCl₂: A solution- and solid-state Hg-199 NMR and ZORA-DFT computational study*. Journal of Molecular Structure, 2009. **930**(1-3): p. 99-109.
17. Arcisauskaite, V., et al., *Nuclear magnetic resonance shielding constants and chemical shifts in linear Hg-199 compounds: A comparison of three relativistic computational methods*. Journal of Chemical Physics, 2011. **135**(4): p. 11.
18. Roukala, J., et al., *Relativistic effects on group-12 metal nuclear shieldings*. Physical Chemistry Chemical Physics, 2011. **13**(47): p. 21016-21025.
19. Wodynski, A., M. Repisky, and M. Pecul, *A comparison of two-component and four-component approaches for calculations of spin-spin coupling constants and NMR shielding constants of transition metal cyanides*. Journal of Chemical Physics, 2012. **137**(1): p. 11.
20. Autschbach, J., *The accuracy of hyperfine integrals in relativistic NMR computations based on the zeroth-order regular approximation*. Theoretical Chemistry Accounts, 2004. **112**(1): p. 52-57.
21. Autschbach, J., *The calculation of NMR parameters in transition metal complexes*, in *Principles and Applications of Density Functional Theory in Inorganic Chemistry I*. 2004. p. 1-48.
22. Autschbach, J., *Relativistic calculations of magnetic resonance parameters: background and some recent developments*. Philosophical Transactions of the Royal Society a-Mathematical Physical and Engineering Sciences, 2014. **372**(2011): p. 20120489.
23. Ramsey, N.F., *Magnetic Shielding of Nuclei in Molecules*. Physical Review, 1950. **78**(6): p. 699-703.
24. Autschbach, J. and E. Zurek, *Relativistic density-functional computations of the chemical shift of Xe-129 in Xe@C-60*. Journal of Physical Chemistry A, 2003. **107**(24): p. 4967-4972.
25. Pyykko, P., *On the Relativistic Theory of Nmr Chemical-Shifts*. Chemical Physics, 1983. **74**(1): p. 1-7.
26. Fukuda, R., M. Hada, and H. Nakatsuji, *Quasirelativistic theory for magnetic shielding constants. II. Gauge-including atomic orbitals and applications to molecules*. Journal of Chemical Physics, 2003. **118**(3): p. 1027-1035.
27. Bagno, A., G. Casella, and G. Saielli, *Relativistic DFT calculation of Sn-119 chemical shifts and coupling constants in tin compounds*. Journal of Chemical Theory and Computation, 2006. **2**(1): p. 37-46.
28. Autschbach, J. and S. Zheng, *Relativistic Computations of NMR Parameters from First Principles: Theory and Applications*. Annual Reports on NMR Spectroscopy, 2009. **67**: p. 1-95.

Chapter 5

MAGNETIC SHIELDING CALCULATIONS FOR NETWORK SOLIDS EMPLOYING CLUSTERS ADAPTED FROM BOND VALENCE THEORY

5.1 Introduction

In this chapter, magnetic-shielding calculations employing cluster models are presented for covalent- or ionic-network solids containing nuclei ^{207}Pb , ^{31}P and ^{29}Si . The calculations are carried out with the method of valence modification of terminal atoms using bond valence (VMTA/BV), the details of which are introduced in Chapter 3. This chapter consists of three parts. The first part is devoted to test calculations with different cluster models on $\alpha\text{-PbO}$ and $\beta\text{-PbO}$. Some arguments regarding the symmetry and charge of the clusters are given in this section. In the second part, the application of the VMTA/BV model is shown for magnetic-shielding calculations of ^{207}Pb -containing solids. Finally, calculated magnetic-shielding tensors of lighter nuclei such as ^{31}P and ^{29}Si by the GIPAW procedure with periodic boundary conditions (PBC) and the VMTA/BV cluster-based approach are compared for benchmark purposes.

The materials investigated in this study are selected by the following criteria: a) the solid state structures of the systems must have been resolved with high-quality diffraction studies; b) the principal components of the chemical-shift tensors for the NMR nuclei of interest must have been measured by SSNMR techniques with a high degree of accuracy. In Tables 5.1, the investigated lead-containing solids [1-10] and their crystallographic information are tabulated. The same type of information is given

in Tables 5.2 and 5.3 for silicon-containing solids [11-19] and phosphorus-containing solids [20-25], respectively. For some selected systems (α -PbO and Pb₃O₄), the coordinates of the atomic positions used in model clusters are given in Appendix A.

Table 5.1 Reference Codes and Crystallographic Data for Lead-Containing Solids

Crystal System	Reference Code ^a	Space Group	Unique Pb(II) Sites by Symmetry
α -PbO	15466	<i>P4/nmm</i>	1
β -PbO	40180	<i>Pbcm</i>	1
Pb ₃ O ₄	4106	<i>P4₂/mbc</i>	1 ^b
Pb ₂ SnO ₄	31482	<i>Pbam</i>	2
PbF ₂	154994	<i>Pnma</i>	1
PbCl ₂	27736	<i>Pnma</i>	1
PbBr ₂	202134	<i>Pnma</i>	1
PbClOH	404572	<i>Pnma</i>	1
PbBrOH	404573	<i>Pnma</i>	1
PbIOH	Lutz et al	<i>Pnma</i>	1
PbSiO ₃	26812	<i>P2/n</i>	3
Pb ₃ (PO ₄) ₂	14247	<i>C2/c</i>	2

a) Codes are from the Inorganic Crystal Structure Database, or the structures are from the literature if no code is given.

b) There is also a unique Pb(IV) site for this system.

Table 5.2 Reference Codes and Crystallographic Data for Silicon-Containing Solids

Crystal System	Reference Code	Space Group	Unique Si Sites by Symmetry
α -quartz	162490	<i>P3₂21</i>	1
Li ₂ Si ₂ O ₅	67110	<i>Pbcn</i>	1

Na ₂ SiO ₃	15388	<i>Cmc2₁</i>	1
Na ₂ Si ₂ O ₅	34669	<i>Pcnb</i>	1
Mg ₂ SiO ₄	12124	<i>Pbnm</i>	1
MgSiO ₃	64629	<i>Pbca</i>	2
CaSiO ₃	201537	<i>P-1</i>	3
Ca ₃ Si ₂ O ₇	2282	<i>P12₁/a1</i>	2
CaMgSiO ₅	202280	<i>Pbnm</i>	1

Table 5.3 Reference Codes and Crystallographic Data for Phosphorus-Containing Solids

Crystal System	Reference Code ^a	Space Group	Unique P Sites by Symmetry
Mg ₃ (PO ₄) ₂	31005	<i>P12₁/n1</i>	1
Mg ₂ P ₄ O ₁₂	4280	<i>C12/c1</i>	2
Mg ₂ P ₂ O ₇	15326	<i>B12₁/c1</i>	2
MgP ₄ O ₁₁	300214	<i>P12₁/c1</i>	4
Li ₆ O ₆ P ₁₈ ·3H ₂ O	85734	<i>R-3mH</i>	1
Ca ₄ P ₂ O ₉	160461	<i>P12₁1</i>	4
SnHPO ₄	25033	<i>P12₁/c1</i>	1

5.2 Magnetic Shielding Calculations on α -PbO and β -PbO

This section presents the effects of size, charge and point group symmetry of model clusters on calculated magnetic-shielding tensors in network solids. All calculations in the section were carried out at the BP86/TZ2P level of theory with the ZORA/spin-orbit Hamiltonian.

5.2.1 Effect of Termination Method and Cluster Size on the ^{207}Pb Magnetic Shielding Tensor

Clusters of α -PbO and β -PbO with different sizes, as well as the effects of cluster size on predicted principal components of the shielding tensor, were investigated by the HA, VMTA and VMTA/BV methods. Clusters up to the first, third, and fifth atomic coordination shells around the NMR nucleus are shown in Figure 5.1. Only the odd-numbered coordination shells are considered, because clusters terminated with lead atoms are inherently difficult to handle computationally.

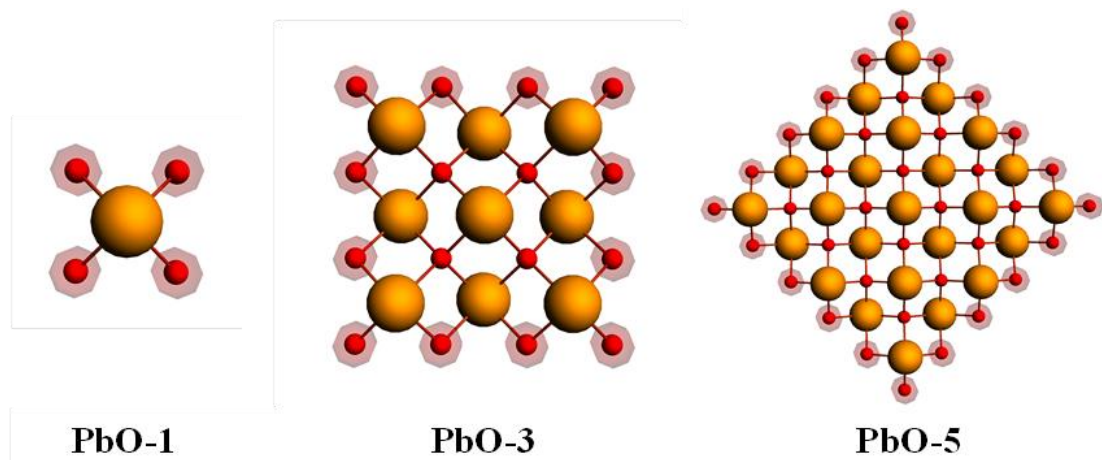


Figure 5.1 First, third and fifth coordination shell geometries of α -PbO. The terminal oxygen atoms are shown in red circles. The corresponding β -PbO clusters have the same bonding network with differences in bond lengths and angles.

The calculated NMR parameters for clusters of the two different forms of PbO (α -PbO and β -PbO) using the HA, VMTA, and VMTA/BV methods are given in Table 5.4. The method used in each case is given by its abbreviation and the prefix gives the maximum coordination shell in the cluster.

Table 5.4 Principal Components of the ^{207}Pb Magnetic-Shielding Tensor, Reduced Chemical Shifts and Residuals (R) for Various Cluster Models of $\alpha\text{-PbO}$ and $\beta\text{-PbO}$.

$\alpha\text{-PbO}$	σ_{11} (ppm)	σ_{22} (ppm)	σ_{33} (ppm)	$\Delta\delta_{11}$ (ppm)	$\Delta\delta_{22}$ (ppm)	$\Delta\delta_{33}$ (ppm)	R^a
Experiment[26]				<u>1100</u>	<u>1100</u>	<u>-2200</u>	_____
1-HA	9400	9400	10645	415	415	-830	969
1-VMTA	7385	7385	9681	765	765	-1531	473
1-VMTA/BV	9451	9451	11269	606	606	-1212	699
3-HA	6204	6204	8918	905	905	-1809	276
3-VMTA	5861	5861	8870	1003	1003	-2006	137
3-VMTA/BV	5887	5889	8827	981	979	-1960	170
5-HA	5935	5935	8922	995	995	-1991	148
5-VMTA	5936	5936	8906	990	990	-1980	156
5-VMTA/BV	5914	5915	8900	996	994	-1990	148
$\beta\text{-PbO}$	σ_{11} (ppm)	σ_{22} (ppm)	σ_{33} (ppm)	$\Delta\delta_{11}$ (ppm)	$\Delta\delta_{22}$ (ppm)	$\Delta\delta_{33}$ (ppm)	R
Experiment[26]				<u>1293</u>	<u>1233</u>	<u>-2527</u>	_____
1-HA	9125	9533	10871	718	310	-1028	1069
1-VMTA	7109	7525	9537	948	532	-1480	754
1-VMTA/BV	8630	9283	11516	1180	527	-1706	629
3-HA	5956	6406	9270	1255	805	-2059	367
3-VMTA	5747	6228	9273	1335	855	-2190	294
3-VMTA/BV	5655	6197	9352	1413	871	158	261
5-HA	6136	6150	9630	1169	1155	-2324	144
5-VMTA	6098	6172	9593	1190	1115	-2305	157
5-VMTA/BV	6100	6150	9581	1177	1127	-2304	158
$a) \text{ Residual} = \sqrt{\frac{1}{3} \sum_{i=1}^3 (\Delta\delta_{ii}^{calc} - \Delta\delta_{ii}^{exp})^2}$							

In Table 5.4, the **reduced chemical shifts** are defined by the following relation:

$$\Delta\delta_{ii} = \delta_{ii} - \delta_{iso} = \sigma_{iso} - \sigma_{ii} \quad (5.1)$$

For α -PbO and β -PbO, the predicted principal shielding components for a model cluster terminated at the first coordination sphere strongly depend on the termination method, with values that can be different from one another by more than 2000 ppm. On the other hand, for clusters of α -PbO and β -PbO including atoms up to the third coordination shell, the predicted principal shielding components are significantly less dependent on the termination method. For example, the largest difference between values found with different methods (in this case, VMTA and HA) is only 343 ppm, the difference for σ_{11} ($= \sigma_{22}$) of α -PbO. There are only small differences in the principal components calculated by the VMTA or the VMTA/BV method, showing that these two methods are similar. The maximum difference for calculated components by these two methods is no greater than 100 ppm.

For clusters that include the fifth coordination shell of α -PbO or β -PbO, the principal components calculated using the three termination methods agree with each other to within 50 ppm. This agreement reflects the fact that the various termination methods have little effect on the shielding values calculated for fifth-coordination-sphere clusters chosen to represent these network solids.

A comparison of the calculated values to experimental results is illustrated with the residuals of the components of the reduced chemical-shift tensor. (Table 5.4) These residuals are generally smaller for larger clusters. For clusters containing only the first coordination shell, the residuals range from 473 ppm to 1069 ppm. For clusters containing up to the third coordination shell, the residuals range from 137

ppm to 367 ppm. For clusters containing up to the fifth coordination shell, the residuals range only from 144 to 158 ppm. The larger the clusters, regardless of termination method, the closer the calculated components are to the experimental components.

5.2.2 Symmetry Requirements for Calculated Principal Components

The local symmetry of the electronic environment surrounding the NMR-active nucleus affects the values of the principal components of the magnetic-shielding tensor. We have deliberately perturbed the symmetry of cluster models of α -PbO to determine the extent of this effect. In Figure 5.2 is shown an example, in which a fifth-coordination-shell cluster model is perturbed by adding up to the seventh coordination shell along the + x axis.

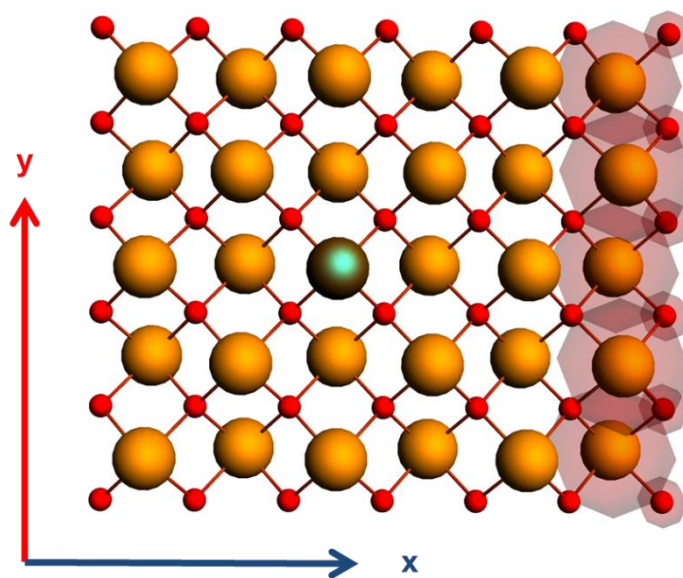


Figure 5.2 Distorted fifth coordination-shell cluster of α -PbO. The added coordination in the x-direction is shown in red circles, and the central ^{207}Pb nucleus is highlighted in green.

For the calculated magnetic-shielding parameters in Table 5.5, I have used models extended by two coordination shells in the + x direction for the first-, third-, and fifth-coordination-shell cluster models to lower the symmetry at the site of the NMR-active nucleus.

From the X-ray crystal structure, the Pb sites in α -PbO have C_{4v} site symmetry. [1] By symmetry constraints, the skew (κ) is either -1.00 ($\sigma_{11} < \sigma_{22} = \sigma_{33}$) or +1.00 ($\sigma_{11} = \sigma_{22} < \sigma_{33}$). Experimentally, α -PbO has a skew of +1.00. [26-28] Calculated NMR parameters for the symmetric and perturbed clusters are presented in Table 5.5.

Table 5.5 Principal Components of the ^{207}Pb Magnetic-shielding Tensors of Symmetric and Perturbed Clusters of α -PbO

α -PbO	σ_{11} (ppm)	σ_{22} (ppm)	σ_{33} (ppm)	σ_{iso} (ppm)	Ω (ppm)	κ
1sym^a	9451	9451	11269	10057	1818	1.00
1pert^b	8183	8578	10964	9241	2781	0.72
Difference	1268	873	305	816	-963	0.28
3sym^a	5887	5889	8827	6868	2940	1.00
3pert^b	5734	5875	8737	6782	3004	0.91
Difference	153	14	90	86	-64	0.09
5sym^a	5914	5915	8900	6910	2986	1.00
5pert^b	5906	5909	8888	6901	2982	1.00
Difference	8	6	2	9	4	0.00

^aSymmetric cluster
^bPerturbed cluster

For a cluster that contains the first coordination shell, the differences between principal components of symmetric and perturbed clusters are 1268, 873 and 305 ppm for σ_{11} , σ_{22} and σ_{33} , respectively, with a predicted κ of 0.72 for the perturbed structure. For a cluster that includes the third coordination shell, κ is 0.91, only 0.09 from the ideal value. For this cluster model, the differences range only between 14 and 153 ppm for the principal components. For a model containing coordination shells through the fifth coordination shell, the differences between the calculated principal components of the perturbed and symmetric models are very small. The calculated κ for both clusters are +1.00, within 1%. These results, along with the results in Table 5.4, indicate that the principal values of the magnetic-shielding tensor converge to a limit for a cluster that contains up to the fifth coordination shell of ^{207}Pb . Deviations from symmetry occurring at the edges of a cluster **of sufficient size** seem to have minimal effects on the derived magnetic-shielding tensor and its symmetry at this level of precision.

5.2.3 Effects of the Charge on the Terminal Atoms

For $\alpha\text{-PbO}$, the VMTA/BV method predicts 9.50 and 9.00 for Z_{mod} of the two types of terminal oxygen atoms. I investigate how the value of Z_{mod} in the range of 9.30 to 9.70 and 8.80 to 9.20 for these two sites, respectively, affects the predicted NMR magnetic-shielding parameters. For these models, the total charge on a cluster depends on the size of the cluster as well as Z_{mod} of the two terminal oxygen sites, as indicated in Table 5.6. As seen in Figure 5.3 and 5.4 respectively, σ_{iso} and Ω are linearly correlated with the deviation, ΔZ_{mod} , of Z_{mod} from the optimal values (9.50 and 9.00). For the cluster containing only the first coordination sphere, the variation of the isotropic shielding and the span with Z_{mod} is large. In changing Z_{mod} by 0.4, the

isotropic magnetic shielding varies by over 2000 ppm and the span varies by over 1000 ppm. On the other hand, for the largest cluster (through the fifth coordination sphere), the isotropic shielding differs by 157 ppm and the span varies by 55 ppm, at most, showing the lack of sensitivity to Z_{mod} in large clusters.

Table 5.6 Dependence of the Predicted Magnetic-shielding Tensor of α -PbO on the Total Charge on a Cluster Extending to the Fifth Coordination Shell

Z_{mod} on O1 and O2	Charge of the Cluster	Mulliken Charge on Pb	σ_{11} (ppm)	σ_{22} (ppm)	σ_{33} (ppm)	σ_{iso} (ppm)	Ω (ppm)
9.30, 8.80	-4.0	1.344	6005	6006	8959	6990	2954
9.40, 8.90	-2.0	1.364	5957	5959	8928	6948	2971
9.50, 9.00	0.0	1.381	5914	5915	8900	6910	2986
9.60, 9.10	2.0	1.395	5874	5876	8873	6874	2999
9.70, 9.20	4.0	1.408	5839	5841	8848	6843	3009

The overall charge on the cluster is partially delocalized onto other atoms in the cluster. As an example, from Table 5.6, there is a small, but strong, positive correlation between the Mulliken charge on the central lead atom and Z_{mod} of the terminal oxygen sites in this fifth-coordination-shell model. In addition, the magnetic-shielding components are correlated with the Mulliken charge on the central lead atom, showing that magnetic shielding reflects the delocalization of charge. The change in the principal components of magnetic shielding with the Mulliken charge demonstrates that there is a somewhat stronger effect on the two degenerate components (σ_{11} and σ_{22}) than on the unique component (σ_{33}). This difference between the unique component and the non-unique components in their dependence

on delocalization of charge suggests that more electron density from delocalization ends up in orbitals the principal direction of which is in the 1-2 plane, rather than in orbitals whose orientation is perpendicular to that plane. This change is also reflected in the gradual change of Ω with total charge on the cluster. These variations of magnetic-shielding parameters with charge on the cluster are even stronger for smaller clusters, as shown in Figure 5.3 and 5.4.

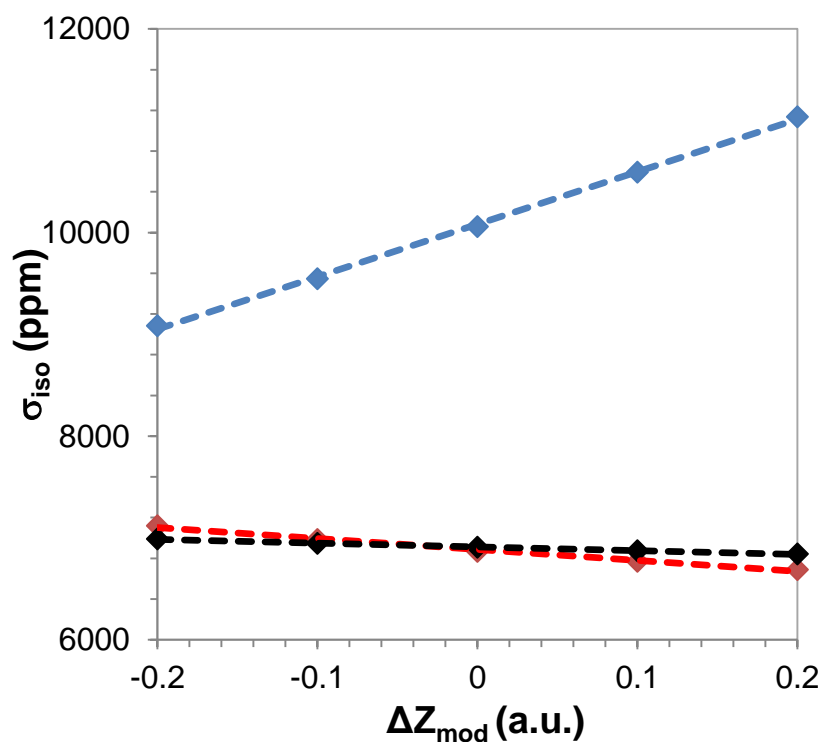


Figure 5.3 The effect of Z_{mod} on isotropic shielding for models that extend through the first (blue), third (red), and fifth (black) coordination shells for α -PbO. ΔZ_{mod} is the deviation of Z_{mod} from the optimal values determined by the VMTA/BV method.

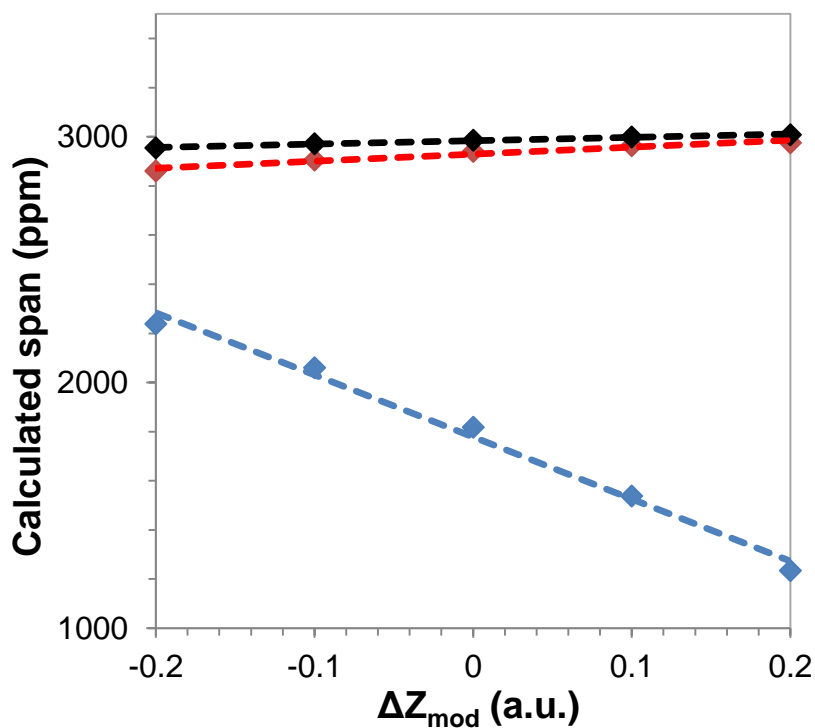


Figure 5.4 The effect of Z_{mod} on calculated span for models that extend through the first (blue), third (red), and fifth (black) coordination shell for α -PbO. ΔZ_{mod} is the deviation of Z_{mod} from the optimal values determined by the VM TA/BV method.

5.3 VM TA/BV Model for ^{207}Pb Magnetic Shielding Calculations for Various Lead-Containing Solids

Comparisons between experimental and calculated principal components of the ^{207}Pb magnetic shielding tensors are presented for a variety of lead-containing materials in Table 5.1. The calculations are carried out with cluster models that are terminated using the VM TA/BV model. In this model, the bond strengths are calculated using equations 3.3 and 3.4, with parameters, R_{i0} and b_i , tabulated in the Table B2 in Appendix B. The calculations were carried out with BP86 density functional, unless indicated otherwise. The relativistic effects were treated with the ZORA Hamiltonian at the scalar or spin-orbit level. For the basis set, TZ2P/AE is used

for the NMR nuclei and the first coordination shell, whereas DZ/FCA is employed for the rest of the cluster. The cluster models for some selected systems are shown in Figure 5.5.

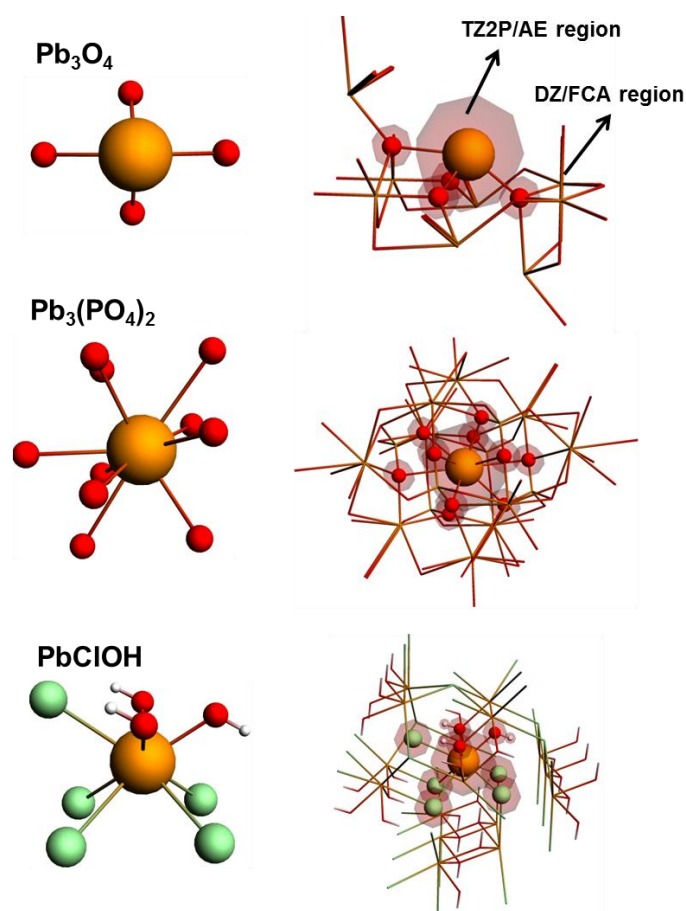


Figure 5.5 First and third coordination-shell clusters for selected systems investigated in this work. The TZ2P/AE (all-electron) region is shown in the ball-and-stick model, whereas the region where FCA/DZ is used is shown by a stick model.

5.3.1 Effect of Cluster Size

The relationship between experimental and calculated principal components of the ^{207}Pb shielding tensors of these various materials is displayed in Figure 5.6 for the first-coordination-shell model and in Figure 5.7 for the third-coordination-shell model. The calculated magnetic-shielding tensor data of these correlations are tabulated in Table B3 in Appendix B. Results for the first-coordination-shell model show a strong scatter of the data, with R^2 of only 0.608 for a linear correlation. Even for qualitative predictions, NMR parameters obtained using the first-coordination-shell model to represent the structure cannot be trusted for these kinds of network solids, as compared to the situation for molecular solids in the previous chapter, and calculations with this model are not reported in subsequent analyses.

Use of a model that includes structure through the third coordination shell greatly improves the correlation between experimental and calculated principal components, as can be seen in Figure 5.7. For the linear correlation, $R^2 = 0.983$ and the slope of the best-fit linear correlation line is -0.869, with an intercept of 8643 ppm. The slope of the correlation line deviates by 13% from the ideal case, which has a slope of -1.

The predicted absolute magnetic shielding of the reference material, tetramethyllead (TML), from a linear correlation is 9990 ppm for the model that includes only up to the first coordination shell. A similar linear correlation of the third-coordination-shell model gives a value of 8653 ppm. The absolute shielding of TML calculated from a model of the molecular solid based on the reported X-ray structure [29] with optimized hydrogen atom positions gives a value of the isotropic

shift of TML of 8136 ppm. There is a significant difference between this estimated shielding of TML and that extracted from the linear correlation of Figure 5.6. On the other hand, the value extracted from Figure 5.7 is much closer to the predicted shielding of TML based on its solid-state structure.

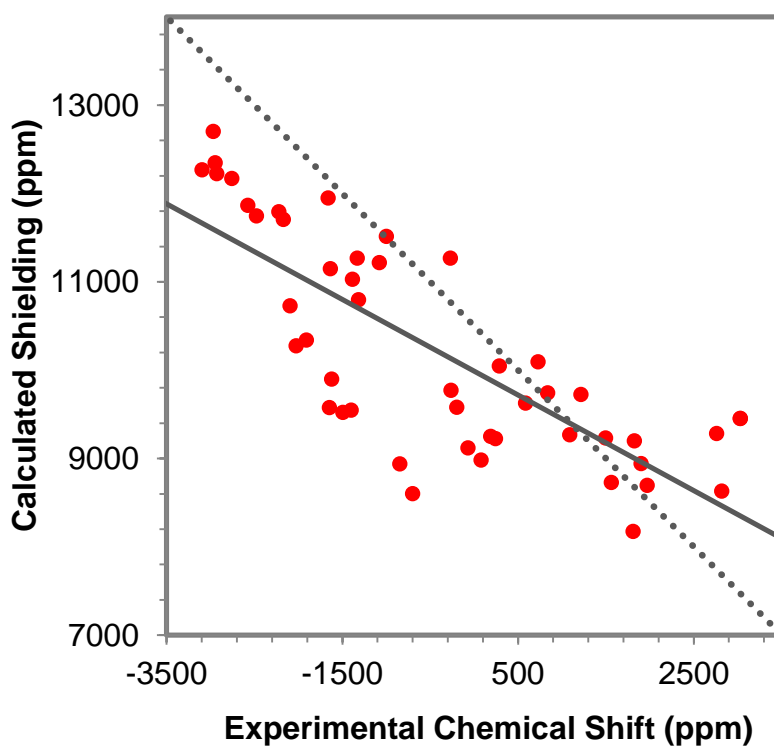


Figure 5.6 The correlation between experimental and calculated principal components for the first coordination-shell model (\bullet). The equation of the linear correlation line for the first-coordination-shell model is: $\sigma_{\text{cal}} = -0.541\delta_{\text{exp}} + 9990$ with $R^2 = 0.608$. The dotted line shows ideal behavior (with a slope of -1).

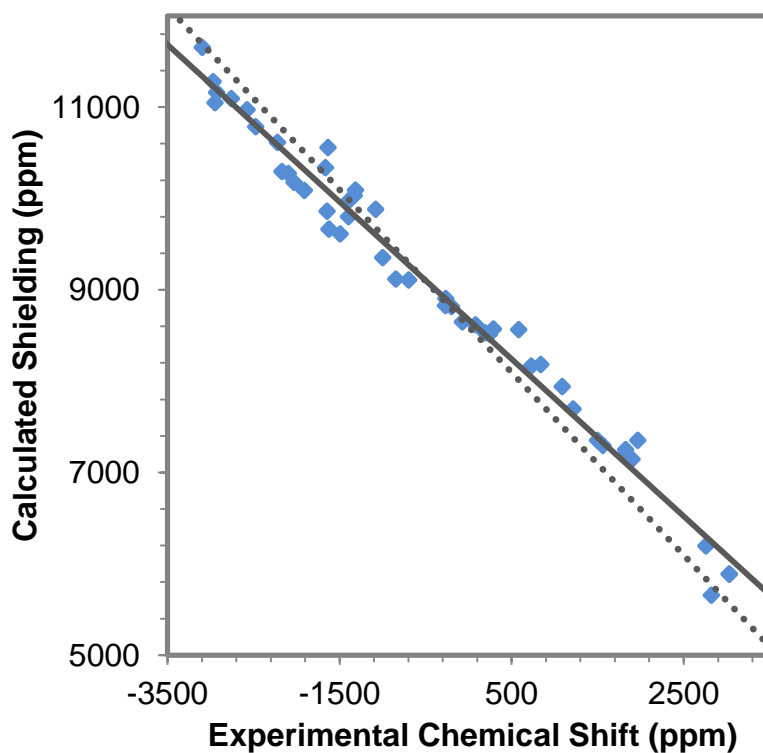


Figure 5.7 The correlation between experimental and calculated principal components for the third coordination-shell model (\blacklozenge). The equation of the linear correlation line for the first-coordination-shell model is: $\sigma_{\text{cal}} = -0.869\delta_{\text{exp}} + 8643$ with $R^2 = 0.983$. The dotted line shows ideal behavior (with a slope of -1).

5.3.2 Relativistic Effects

In general, for heavy atoms, the contributions to the shielding due to the relativistic nature of the electrons are significant. [30-33] For the third-coordination-shell model, we compare magnetic-shielding tensors of the suite of materials in Table 5.1 determined with inclusion of only scalar relativistic corrections to the magnetic-shielding tensors determined using the full spin-orbit relativistic Hamiltonian. The treatment is at the ZORA/DFT level of theory. The correlation of experimental and theoretical principal components and spans is shown in Figure 5.8 and 5.9, respectively.

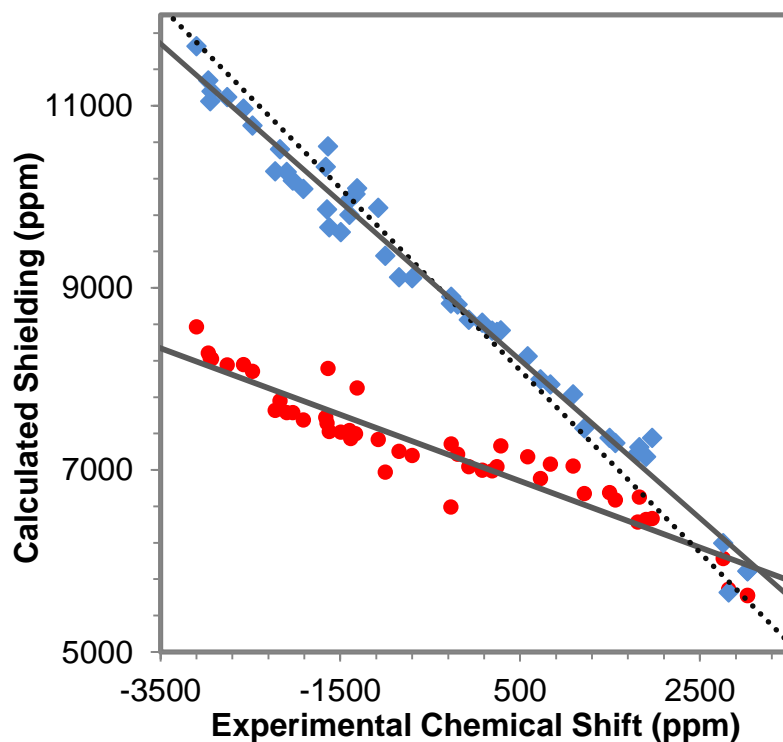


Figure 5.8 The correlation between principal components of the magnetic shielding and experimental chemical shift of various lead-containing solids: (●) with inclusion of only scalar relativistic terms; (◆) with inclusion of all relativistic corrections through spin-orbit effects. The calculations were carried out on a third-coordination-shell model at the ZORA/DFT level. The equation of the correlation line for the principal components is: $\sigma_{\text{cal}} = -0.365\delta_{\text{exp}} + 7060$ with $R^2 = 0.887$ for ZORA/scalar calculations, and $\sigma_{\text{cal}} = -0.869\delta_{\text{exp}} + 8643$ with $R^2 = 0.983$ for ZORA/spin-orbit calculations. The dotted line shows ideal behavior.

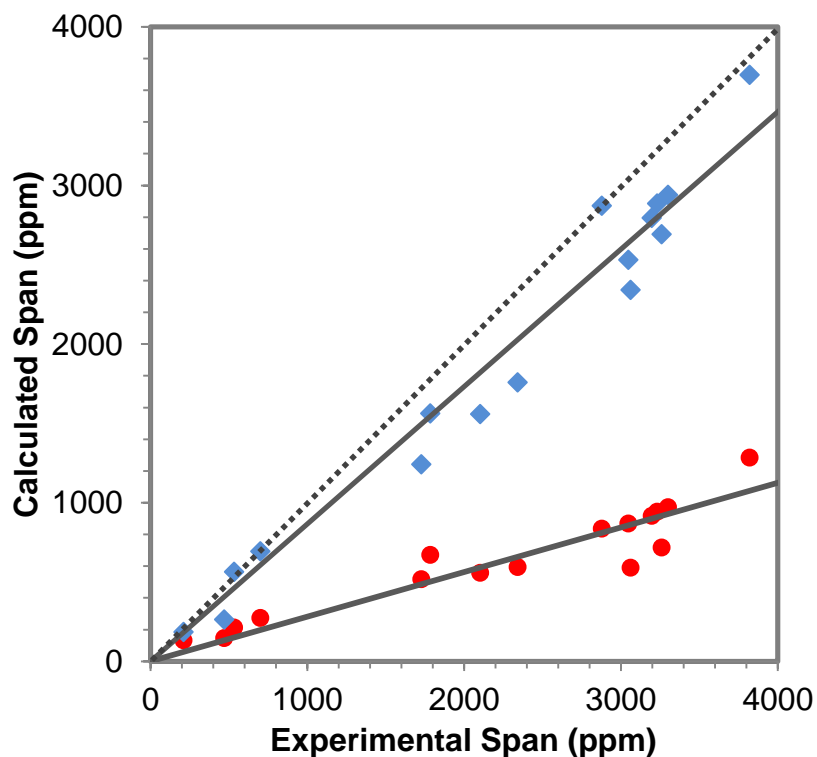


Figure 5.9 The correlation of magnetic-shielding span with experimental span of the various lead-containing solids: (•) with inclusion of only scalar relativistic terms; (♦) with inclusion of all relativistic corrections through spin-orbit effects. For the span, the correlation is: $\Omega_{\text{cal}} = 0.281\Omega_{\text{exp}}$ with $R^2 = 0.871$ for ZORA/scalar calculations and $\Omega_{\text{cal}} = 0.866\Omega_{\text{exp}}$ with $R^2 = 0.962$ for ZORA/spin-orbit calculations. The dotted line shows ideal behavior.

The slope of the correlation line for shielding principal components with experimental chemical- shift components is -0.365 when only scalar relativistic effects are included, whereas the slope of the correlation line for magnetic-shielding principal components when the full relativistic Hamiltonian is used is -0.869. Neither is the ideal value of -1, but the inclusion of spin-orbit relativistic terms gives a correlation much closer to the ideal than does the inclusion of only scalar relativistic effects in the ZORA Hamiltonian, showing that spin-orbit terms cannot be neglected in calculations

of magnetic shieldings of ^{207}Pb . A similar result for the ^{199}Hg magnetic shielding of solids was observed in the previous chapter.

The predicted magnetic shielding of TML from the correlation at the scalar relativistic level is 7060 ppm, whereas a calculation for an isolated TML molecule at this scalar relativistic level gives a shielding of 5171 ppm, a difference of 1889 ppm. At ZORA/spin-orbit level, this difference is calculated as 507 ppm which indicates that inclusion of the spin-orbit correction is essential to achieve better agreement with the calculated reference shielding from calculation on the reference molecule.

The span of a tensor is independent of the reference. In Figure 5.9, the correlation of the predicted and experimental spans is shown for these lead-containing solids. At the ZORA/scalar level of theory, the slope of the best-fit linear correlation of 0.281 deviates significantly from the ideal value of +1. At the ZORA/spin-orbit level of theory, the slope of the best-fit linear correlation is 0.866, much closer to the ideal value. This disparity again demonstrates that spin-orbit terms must be included in calculations of magnetic shielding of ^{207}Pb solids.

One striking feature of Figure 5.9 is that the predicted NMR parameters obtained by use of the scalar relativistic terms systematically underestimate the span of the shielding tensor ($\sigma_{33}-\sigma_{11}$), as compared to values calculated at the spin-orbit level. The spin-orbit calculation also underestimates the span as compared to the experiment, but by a substantially smaller difference. Similar results have been shown for ^{207}Pb previously, [34, 35] and for ^{199}Hg in this study.

5.3.3 Accuracy of Calculated Principal Components of the ^{207}Pb Shielding Tensor

It is shown in the sections above that it is possible to achieve a good correlation between experimental and theoretical principal components of a wide array of lead-containing materials, provided one uses the full spin-orbit-including Hamiltonian at the ZORA level and creates clusters using the VMTA/BV model with inclusion of structure at least to the third coordination shell. Even at this level of approximation, the correlation between predicted and experimental results may deviate from the ideal case (in which the slope of the correlation line is exactly -1). In this section, some remarks and results on the accuracy of theoretically and experimentally determined ^{207}Pb magnetic-shielding tensor are given in order to understand the possible source of the deviations between experiment and theory.

5.3.3.1 Clusters and the VMTA/BV Model

In sections 5.2 and 5.3, it is seen that one must include extended solid-state effects by using structural models that account for contributions to the magnetic shielding from atoms in at least the third coordination shell about the nucleus of interest. Inclusion of effects through the fifth coordination shell demonstrates that agreement slightly improves by the addition of further atoms as shown in Figure 5.10 for selected lead-containing materials. However, the slope of the correlation lines approaches the ideal case by only about 2%, and the improvement in fit is negligible, suggesting that extending the cluster further is likely to give no substantial improvement in agreement between theory and experiment.

Cluster models, without the use of VMTA/BV theory, have been applied to calculations of ^{207}Pb principal components in other solid systems. [34-36] In those examples, the ZORA/spin-orbit Hamiltonian was applied at the BP86 level of density

functional theory, and no additional treatment was applied to the terminal atoms. For all investigated systems, the span, Ω , is consistently underestimated by the model, whether in molecular or network solids. This underestimation cannot therefore be attributed to the use of VMTA/BV for termination of the cluster.

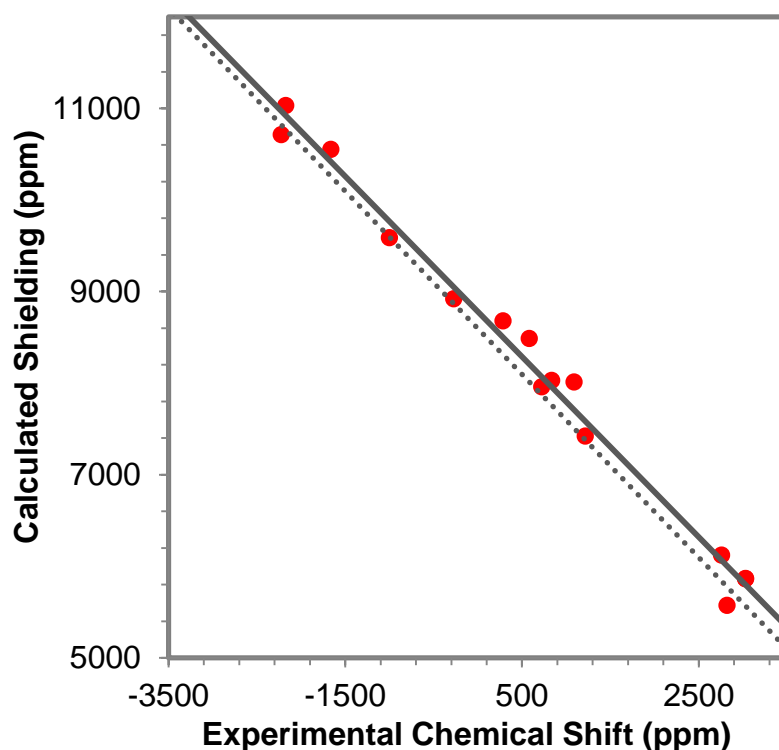


Figure 5.10 The correlation of the principal components of the experimental chemical-shift tensor and the predicted shielding tensor for α -PbO, β -PbO, Pb₂SnO₄, Pb₃O₄ and PbSiO₃ using fifth-coordination-shell cluster models. For the fifth-coordination-shell model, the correlation line is $\sigma_{\text{cal}} = -0.910\delta_{\text{exp}} + 8690$ with $R^2 = 0.986$. The dotted line shows ideal behavior. The equation of the correlation line for the third-coordination-shell model for the same data set is: $\sigma_{\text{cal}} = -0.891\delta_{\text{exp}} + 8689$ with $R^2 = 0.983$.

5.3.3.2 Relativistic Effects at the ZORA/Spin-Orbit Level

The importance of relativistic effects on shielding of heavy nuclei such as ^{207}Pb has been investigated previously.[30] The present results also indicate the necessity of inclusion of spin-orbit effects for calculation of magnetic shielding for these heavy nuclei. It has been shown that the absolute shielding constants for heavy nuclei calculated with ZORA at the spin-orbit level differ considerably from results that are carried out by four-component relativistic methods. [37-39] Autschbach [40] has shown that this difference mainly results from hyperfine integrals involving the core levels. He has also shown that the hyperfine integrals over the valence shells may be evaluated at the ZORA level with accuracy close to that achievable by calculation with four-component relativistic methods. [40] As a result, the heavy-nucleus chemical shifts determined at the ZORA level of approximation agree well with those calculated with the four-component formalism. For molecular solids like some Hg-containing materials, the principal components of chemical-shift tensors have been shown to be predicted with good accuracy using the ZORA Hamiltonian. The present results show that ^{207}Pb chemical shifts of network solids calculated at the ZORA level of approximation also agree reasonably well with experiment. To the author's knowledge, there are no reported calculations of ^{207}Pb chemical shifts with the four-component formalism, but the present results obtained with the ZORA approximation suggest that they would also be in agreement.

5.3.3.3 Effect of the Density Functional by Introducing Exact Exchange

GGA functionals are the common choice for relativistic magnetic-shielding calculations due to efficient scaling of the methods in both SCF and NMR routines.

For light nuclei such as ^{13}C and ^{29}Si , introducing exact exchange (via hybrid functionals) improves the correlation between experimental and calculated chemical shifts. [41] Recently, hybrid density functionals have been introduced for relativistic calculations of magnetic shielding and spin-spin coupling constants. [42-44] In Table 5.7, the principal components and spans of ^{207}Pb magnetic-shielding tensors for five materials, which are evaluated with the BP86 or B3LYP functionals, are compared.

Table 5.7 Predicted Principal Components of ^{207}Pb Magnetic-Shielding Tensors, Determined at Either the ZORA/BP86 Level of Theory or the ZORA/B3LYP Level of Theory on a Cluster Extending to the Third Coordination Shell.

BP86	σ_{11} (ppm)	σ_{22} (ppm)	σ_{33} (ppm)	σ_{iso} (ppm)	Ω (ppm)
α -PbO	5887	5889	8827	6868	2940
β -PbO	5655	6197	9352	7068	3697
PbSiO ₃ (site 1)	7459	7995	10331	8595	2872
PbSiO ₃ (site 2)	7829	8249	10522	8867	2693
PbSiO ₃ (site 3)	7940	8532	10281	8918	2341
B3LYP	σ_{11} (ppm)	σ_{22} (ppm)	σ_{33} (ppm)	σ_{iso} (ppm)	Ω (ppm)
α -PbO	5862	5865	8919	6882	3058
β -PbO	5572	6119	9587	7092	4015
PbSiO ₃ (site 1)	7419	7960	10551	8643	3133
PbSiO ₃ (site 2)	8009	8484	11030	9174	3021
PbSiO ₃ (site 3)	8027	8679	10710	9139	2683

There are two characteristics of the shielding parameters determined by the calculations with B3LYP and with BP86. Firstly, the difference of the B3LYP and

BP86 values of σ_{33} for a particular material is always larger than the difference of either σ_{11} or σ_{22} . Secondly, the spans, Ω , calculated with B3LYP are always larger than those calculated with BP86. In comparing to experiment, the predicted span determined with B3LYP is always closer to the experiment than spans calculated with BP86.

In Figure 5.11, the correlation between experimental and calculated principal components of ^{207}Pb shielding tensors at the BP86 and B3LYP levels of theory are shown. As expected from the comparison of spans, Ω , the slope of the correlation line determined with the hybrid functional (B3LYP) is -0.985, much closer to the ideal value than the correlation line for the same parameters determined at the BP86 level of theory (-0.895), demonstrating that the use of hybrid functionals accounts for contributions to the magnetic shielding more completely than the use of GGA functionals like BP86. The effects of exchange and hybrid functionals are investigated in more detail for ^{207}Pb magnetic-shielding tensor and the results are discussed in Chapter 6.

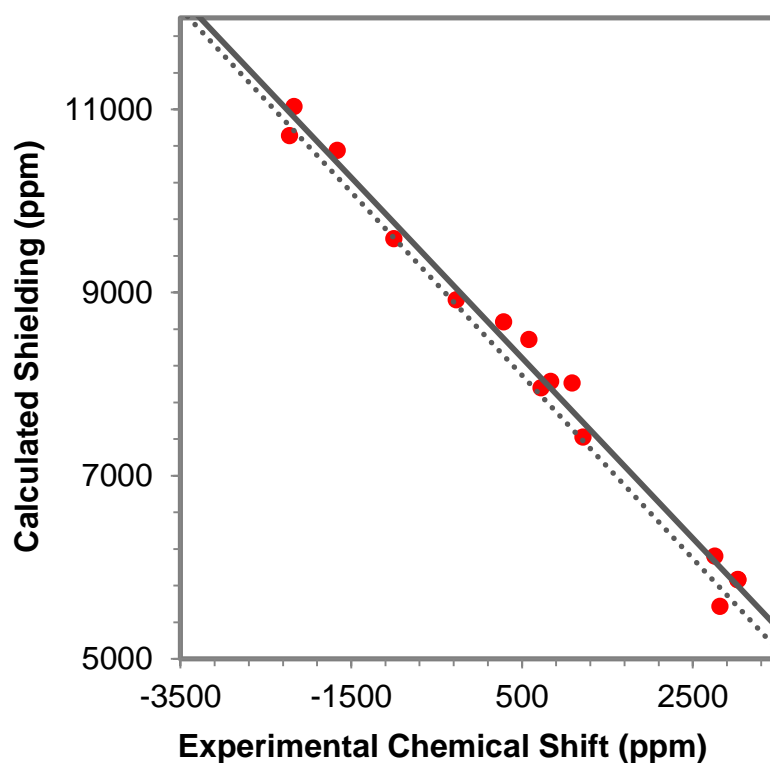


Figure 5.11 The effect of B3LYP on the calculated principal components of sites in α -PbO, β -PbO and PbSiO₃ for the third-coordination-shell model. The equation of the correlation line is: $\sigma_{\text{cal}} = -0.985\delta_{\text{exp}} + 8781$ with $R^2 = 0.987$. The equation of the correlation line for the model using BP86 for the same data set is: $\sigma_{\text{cal}} = -0.898\delta_{\text{exp}} + 8605$ with $R^2 = 0.987$. The dotted line shows ideal behavior. The values of the slope show how use of B3LYP approaches the ideal behavior.

5.3.3.4 Experimental Uncertainty

Due to the challenging nature of the spectroscopy of nuclei like ^{207}Pb having wide powder patterns, there are uncertainties associated with the experimental data. This uncertainty affects the quality of comparisons like those in Figure 5.11. In addition, uncertainty about structural parameters derived from X-ray or neutron diffraction measurements contribute to uncertainty in the predicted values. In Table 5.8 are the results of several reports of experimental chemical-shift parameters of α -

PbO and β -PbO. The measured principal components may vary by as much as 200 ppm, depending on the report. Averaging these three independent measurements, one obtains average values with uncertainties of up to 200 ppm, as given in Table 5.8. The uncertainty in principal components ranges from about 50 to 170 ppm. The uncertainties in the span, which is independent of the reference, are 190 ppm and 146 ppm (about 5-6%), implying that we cannot distinguish the experimental values differing by less than about 100 ppm.

Table 5.8 Experimental ^{207}Pb Chemical-Shift Tensors of the Two Forms of PbO.

α -PbO	δ_{11} (ppm)	δ_{22} (ppm)	δ_{33} (ppm)	δ_{iso} (ppm)	Ω (ppm)
Gabuda et al. [26]	3030	3030	-270	1930	3300
Fayon et al. [27]	2977	2977	-137	1939	3114
Zhao et al. [28]	2984	2984	-334	1878	3318
Average	2997 \pm 48	2997 \pm 48	-247 \pm 169	1916 \pm 55	3244 \pm 190
β -PbO	δ_{11} (ppm)	δ_{22} (ppm)	δ_{33} (ppm)	δ_{iso} (ppm)	Ω (ppm)
Gabuda et al. [26]	2820	2760	-1000	1527	3820
Fayon et al. [27]	2945	2573	-972	1515	3917
Zhao et al. [28]	2953	2695	-1040	1536	3993
Average	2906 \pm 126	2676 \pm 160	-1004 \pm 58	1526 \pm 18	3910 \pm 146

Apart from approximations in the computational formalism that may contribute to the uncertainty in predicted values of the principal components, the uncertainty may also reflect uncertainty in X-ray and neutron diffraction structural parameters used in the definition of the cluster. Dmitrenko et al. [36, 45] showed that calculated ^{207}Pb

chemical-shift parameters can vary significantly for small changes in bond length and bond angle. They also show that calculated NMR parameters may vary by as much as 200 ppm, depending on the X-ray geometry used to define the system. For these reasons, we conclude that agreement between experiment and theory for the ^{207}Pb principal components of a chemical-shift tensor of $\pm 5\%$ is agreement within the current levels of combined uncertainty.

5.4 Performance of PBC and VM TA/BV Models on Magnetic Shielding Calculations for Non-Relativistic Systems: the Case of ^{29}Si and ^{31}P

In this section, ^{29}Si and ^{31}P magnetic-shielding tensors in covalent-network solids (Tables 5.2 and 5.3) are investigated using periodic and cluster-based calculations. The PBC are carried out using the GIPAW approach with the PBE density functional and the planewave basis set with cut-off energy of 600 eV. The core orbitals are replaced by ultrasoft pseudopotentials (USPPs) generated *on the fly* (OTF).

In the cluster-based calculations of magnetic shielding, two all-electron (AE) basis sets were employed for different regions of the cluster. The central region of the cluster, which consisted of the central Si or P site and the four directly-adjacent oxygen sites, was given the larger AE TZ2P basis set. The atomic sites located further from the center were given the smaller AE TZP basis set. Charge compensation on the outermost atomic shells was accomplished through the VM TA/BV method. Calculations on clusters were performed using the GGA-PBE functional and the hybrid functional PBE0. The PBE0 functional results from the admixture of 25% Hartree-Fock (HF) exchange with the GGA-PBE functional. Two example clusters are shown in Figure 5.12.

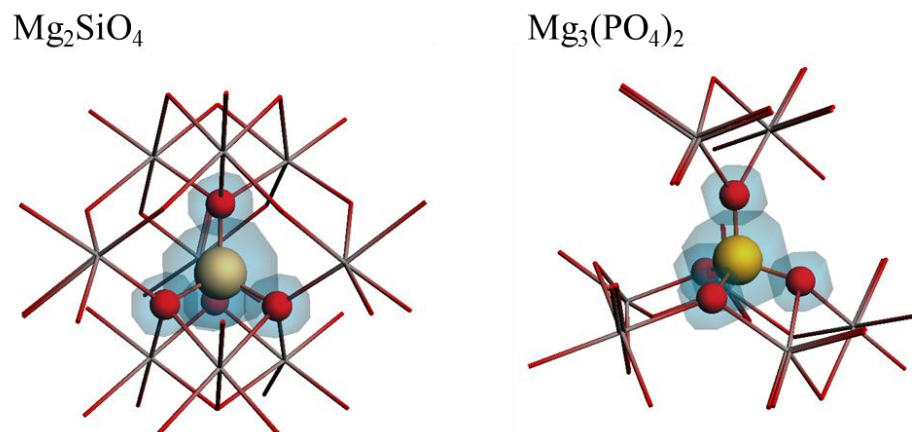


Figure 5.12 Illustration of third-coordination-shell clusters for Mg_2SiO_4 and $\text{Mg}_3(\text{PO}_4)_2$. The TZ2P region is shown in ball-and-stick model and the TZP region is shown as a wireframe model.

5.4.1 Cluster Size and Magnetic Shielding in ^{29}Si - and ^{31}P -Containing Solids

A series of test magnetic-shielding calculations using model clusters of various sizes is summarized in Table 5.9 for α -quartz, Na_2SiO_3 , $\text{Mg}_2\text{P}_4\text{O}_{12}$, and $\text{Mg}_3(\text{PO}_4)_2$. The clusters are expanded around the NMR-active nucleus up to the first, third, and fifth coordination shells.

Experimental chemical shifts (relative to a reference compound) have been converted to the magnetic-shielding scale using proposed empirical conversions. The reference shielding constants are 368.5 ppm (tetramethylsilane) [46] for ^{29}Si and 328.4 ppm (85% H_3PO_4) [47] for ^{31}P nuclei. As can be seen in Table 5.9, the residuals between calculated and experimental magnetic shielding for the third and fifth coordination shells differ from each other in the range of 1 – 2 ppm. However, differences in computed residuals between first- and third-coordination-shell clusters are significantly larger, with the highest deviation being around 50 ppm.

Table 5.9 Principal Components of Experimental and Computed Magnetic-Shielding Tensors, Isotropic Magnetic Shielding, and Span for First, Third, and Fifth Coordination-Shell Clusters of α -quartz, Na_2SiO_3 , $\text{Mg}_2\text{P}_4\text{O}_{12}$, and $\text{Mg}_3(\text{PO}_4)_2$ Determined with VMTA/BV Model.

Model Cluster	σ_{11} (ppm)	σ_{22} (ppm)	σ_{33} (ppm)	σ_{iso} (ppm)	Ω (ppm)	Residual (ppm)
α -quartz						
Experiment	<u>471.1</u>	<u>475.5</u>	<u>477.6</u>	<u>474.7</u>	<u>6.5</u>	---
First shell	440.7	441.5	442.5	441.6	1.8	33.2
Third shell	447.0	450.3	456.4	451.2	9.4	23.6
Fifth shell	447.5	449.9	459.2	452.2	11.7	22.7
Na_2SiO_3						
Experiment	<u>388.2</u>	<u>429.4</u>	<u>519.1</u>	<u>445.6</u>	<u>130.9</u>	---
First shell	401.4	432.8	483.8	439.3	82.4	21.8
Third shell	357.9	395.9	499.0	417.6	141.1	28.5
Fifth shell	363.9	398.1	495.0	419.0	131.2	26.8
$\text{Mg}_2\text{P}_4\text{O}_{12}$ (P1 site)						
Experiment	<u>272.5</u>	<u>329.4</u>	<u>487.0</u>	<u>363.0</u>	<u>214.5</u>	---
First shell	240.8	280.6	403.6	303.8	162.9	58.7
Third shell	262.6	317.3	479.4	353.1	216.8	10.0
Fifth shell	258.7	316.8	489.9	355.1	231.2	10.9
$\text{Mg}_3(\text{PO}_4)_2$						
Experiment	<u>315.7</u>	<u>325.7</u>	<u>344.2</u>	<u>328.5</u>	<u>28.5</u>	---
First shell	293.7	303.7	327.1	308.2	33.4	20.5
Third shell	303.4	317.5	331.3	317.4	27.9	11.3
Fifth shell	305.4	313.5	336.0	318.3	30.6	10.4

The similarity in residuals computed for the third and fifth coordination shells suggests that third-coordination-shell clusters are sufficiently large to model the magnetic shielding.

The lowest residuals between calculation and experiment for the three sizes of model clusters examined are generally seen for the third- and fifth-coordination-shell clusters. For Na_2SiO_3 , the lowest value of R is found for the first coordination shell. However, this deviation from the general trend appears to be the result of accidental cancellation of errors, as indicated by the calculated spans. The experimental span of 130.9 ppm is more in line with the values calculated for the third- and fifth-coordination-shell clusters (141.1 ppm and 131.2 ppm, respectively) than with the span for the first-coordination shell cluster (82.4 ppm).

5.4.2 Effect of Basis Set in Cluster-based and Period Boundary Calculations

Calculated magnetic-shielding tensors depend strongly on basis sets and electronic-state approximations such as pseudopotentials used in the calculation. Results obtained near the basis-set limit can be used to compare computational methodologies because finite-basis-set effects are minimized.[48] To test the convergence of computed NMR parameters with respect to the basis-set size, plane-wave pseudopotential calculations were run on α -quartz and $\text{Mg}_3(\text{PO}_4)_2$ with cutoff energies of 200 eV, 400 eV, 600 eV, and 800 eV. Similarly, all-electron cluster-based calculations were run on the same systems, for which the Slater-type all-electron basis set on the central SiO_4 or PO_4 tetrahedra was DZ, DZP, TZP, and TZ2P, in increasing order of degrees of freedom. The results of these calculations are presented in Table 5.10.

Table 5.10 Calculated ^{29}Si and ^{31}P Principal Components of Magnetic-Shielding Tensors for Various All-Electron Slater-Type and Pseudopotential Plane-Wave Basis Sets.

Basis Set	σ_{11} (ppm)	σ_{22} (ppm)	σ_{33} (ppm)	σ_{iso} (ppm)	Ω (ppm)
α -quartz					
DZ	451.9	463.0	471.8	462.2	19.8
DZP	451.7	454.5	464.4	456.9	12.6
TZP	448.1	451.7	457.7	452.5	9.5
TZ2P	447.0	450.3	456.4	451.2	9.4
200 eV	413.2	424.0	426.7	421.3	13.5
400 eV	427.6	431.4	435.1	431.4	7.5
600 eV	426.8	430.6	434.5	430.6	7.7
800 eV	426.7	430.2	434.2	430.4	7.5
$\text{Mg}_3(\text{PO}_4)_2$					
DZ	304.9	321.0	335.3	320.4	30.4
DZP	300.8	316.6	330.9	316.1	30.1
TZP	304.2	319.1	332.8	318.7	28.6
TZ2P	303.4	317.5	331.3	317.4	27.9
200 eV	258.3	262.7	284.7	268.6	26.4
400 eV	267.8	273.8	297.2	279.6	29.4
600 eV	268.6	274.4	297.9	280.3	29.3
800 eV	268.6	274.4	297.9	280.3	29.3

The difference in the calculated principal components of the magnetic-shielding tensor derived with the TZP basis set, as compared to those determined with the TZ2P basis set (or in going from a cutoff energy of 600 eV to a cutoff energy of

800 eV for the GIPAW calculations) is negligible. In GIPAW calculations, individual principal components of the computed magnetic-shielding tensor differ by no more than 0.4 ppm between cutoff energies of 600 eV and 800 eV. In the cluster calculations, the largest difference in computed magnetic shielding between TZP and TZ2P is 1.6 ppm. Similarly, the largest difference in calculated spans between 600 eV and 800 eV is 0.2 ppm and the largest difference in spans between TZP and TZ2P is 0.7 ppm.

The periodic and cluster-based computational methodologies yield NMR parameters that differ significantly. At the basis-set limit (600 eV or TZ2P), the magnetic shielding is predicted to be larger when using Slater-type basis functions than when using plane waves. For α -quartz, the difference in computed isotropic shielding is about 21 ppm; for $\text{Mg}_3(\text{PO}_4)_2$, the difference in isotropic shielding is about 37 ppm. However, both methods predict similar values of the span, indicating that the two methods predict similar differences between nuclei in different chemical environments, but different absolute shieldings, even with sufficiently large basis set.

5.4.3 Comparison of Periodic and Cluster Models for ^{29}Si and ^{31}P -Containing Solids

In Figure 5.13 and 5.14, the correlation plots between experimental and calculated principal components are shown for ^{29}Si - and ^{31}P -containing solids (Table 5.2 and 5.3) respectively. Experimental chemical shifts are converted to the magnetic-shielding scale using the reference shielding values given in section 5.4.1. As suggested in the previous section, magnetic-shielding constants obtained using the AE cluster-based methods are substantially more shielded than those obtained with the GIPAW method.

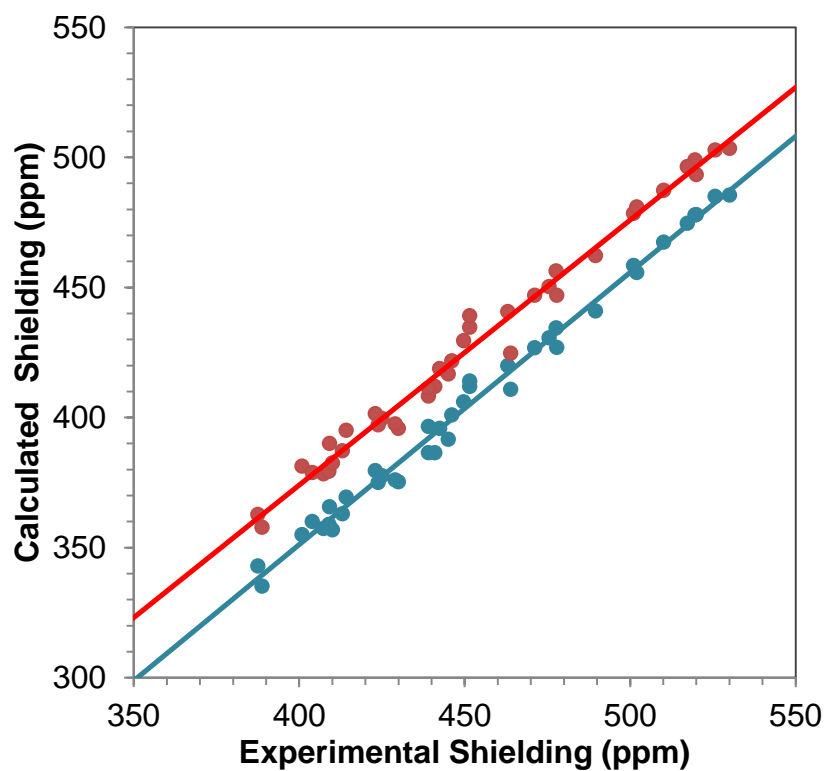


Figure 5.13 Correlation between calculated and experimental principal components of magnetic-shielding tensors for ^{29}Si -containing materials. Values obtained using the GIPAW approach are shown in blue, and results obtained using the VMTA/BV cluster approach are shown in red. Results were computed at the PBE level of theory. The best-fit correlations are given as solid lines.

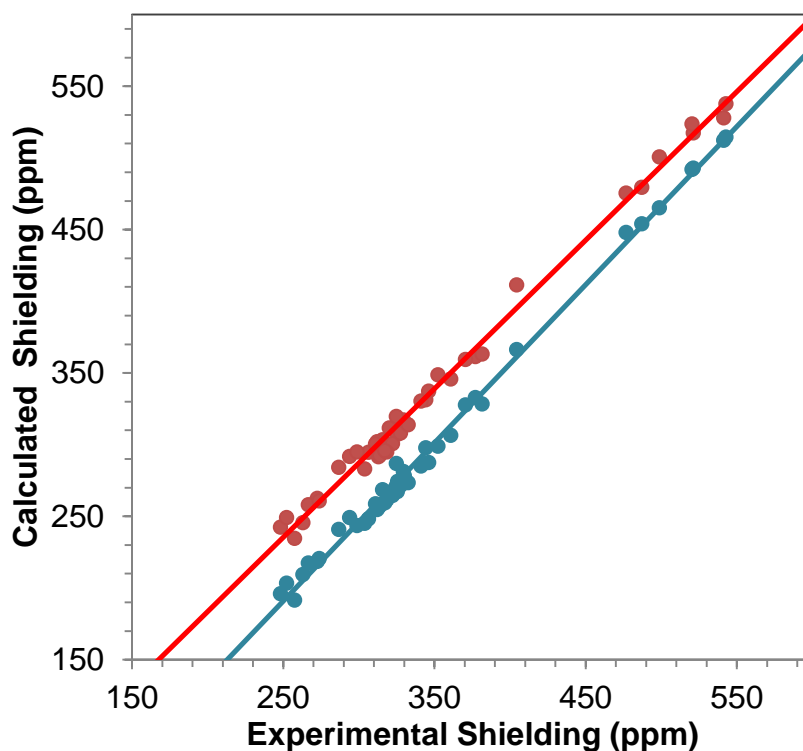


Figure 5.14 Correlation between calculated and experimental principal components of magnetic-shielding tensors for ^{31}P -containing materials. Values obtained using the GIPAW approach are shown in blue, and results obtained using the VMTA/BV cluster approach are shown in red. Results were computed at the PBE level of theory. The best-fit correlations are given as solid lines.

For ^{29}Si -containing solids, linear regressions on the GIPAW and VMTA/BV cluster datasets yield the following best-fit relations;

$$\sigma_{ii}^{GIPAW} = (1.05 \pm 0.02) \sigma_{ii}^{exp} - (67 \pm 7) \text{ ppm}, R^2 = 0.991 \quad (5.2)$$

$$\sigma_{ii}^{VMTA/BV} = (1.02 \pm 0.02) \sigma_{ii}^{exp} - (33 \pm 9) \text{ ppm}, R^2 = 0.986 \quad (5.3)$$

For ^{31}P -containing solids, the following relations are obtained.

$$\sigma_{ii}^{GIPAW} = (1.10 \pm 0.01) \sigma_{ii}^{exp} - (85 \pm 4) \text{ ppm}, R^2 = 0.996 \quad (5.4)$$

$$\sigma_{ii}^{VMTA/BV} = (1.04 \pm 0.01) \sigma_{ii}^{exp} - (24 \pm 5) \text{ ppm}, R^2 = 0.993 \quad (5.5)$$

The largest differences between the correlations obtained from GIPAW calculations and the cluster calculations are in the intercept of the correlation lines. The calculated principal components with cluster models are generally more shielded than those calculated with GIPAW method. This result is probably due to the pseudopotential approximation [49] employed in GIPAW calculations. In comparison, the slope of the correlation lines and the quality of the linear fit are quite similar between two methods. This comparison shows that cluster models with intermediate sizes can reach or extend the accuracy of PBCs in magnetic-shielding calculations.

One advantage of using cluster models is the ability to employ density functionals beyond GGAs in NMR calculations. In this aspect, the hybrid functional PBE0 (25% HF exchange) is employed for calculations of magnetic-shielding tensors of the same set of ^{29}Si and ^{31}P -containing solids. The correlation plots of this analysis are given in the Figure B1 and Figure B2 in Appendix B. Comparison of the experimental and calculated principal components yields the following best-fit relations;

$$^{29}\text{Si} : \quad \sigma_{ii}^{VMTA/BV} = (1.00 \pm 0.02) \sigma_{ii}^{exp} - (10 \pm 10) \text{ ppm}, R^2 = 0.983 \quad (5.6)$$

$$^{31}\text{P} : \quad \sigma_{ii}^{VMTA/BV} = (1.00 \pm 0.01) \sigma_{ii}^{exp} - (1 \pm 4) \text{ ppm}, R^2 = 0.994 \quad (5.7)$$

It should be noted that the slopes of the correlation lines obtained at the PBE0/TZ2P level do not differ from unity to within experimental error, whereas the results obtained with the pure GGA-PBE method do, and the intercepts of the correlation lines for PBE0/TZ2P are much closer to zero than those observed with the GGA-PBE

method. The latter indicates that it is possible to calculate **absolute magnetic shieldings** using the PBE0 functional.

REFERENCES

1. Leciejewicz, J., *On Crystal Structure of Tetragonal (Red) Pbo*. Acta Crystallographica, 1961. **14**(12): p. 1304.
2. Boucher, M.L. and D.R. Peacor, *Crystal Structure of Alamosite Pbsio₃*. Zeitschrift Fur Kristallographie Kristallgeometrie Kristallphysik Kristallchemie, 1968. **126**(1-3): p. 98.
3. Keppler, U., *Structure of Low-Temperature Form of Lead Phosphate Pb₃(Po₄)₂*. Zeitschrift Fur Kristallographie Kristallgeometrie Kristallphysik Kristallchemie, 1970. **132**(3): p. 228.
4. Gavarrì, J.R. and D. Weigel, *Lead Oxides .I. Crystal-Structure of PbO₄ Minimum at Ambient Temperature (293 K)*. Journal of Solid State Chemistry, 1975. **13**(3): p. 252-257.
5. Nozik, Y.Z., L.E. Fykin, and L.A. Muradyan, *Refinement of Crystal-Structure of Cotunnite, Pbcl₂, by Neutron-Diffraction Method*. Kristallografiya, 1976. **21**(1): p. 76-79.
6. Gavarrì, J.R., et al., *Structure of Snpb₂o₄ at 4 Temperatures - the Relation between Thermal-Expansion and Thermal Agitation*. Journal of Solid State Chemistry, 1981. **36**(1): p. 81-90.
7. Lumbreras, M., et al., *Structure and Ionic-Conductivity of Mixed Lead Halides Pbcl₂xbr₂(1-X)*. Solid State Ionics, 1986. **20**(4): p. 295-304.
8. Garnier, P., J. Moreau, and J.R. Gavarrì, *Rietveld Analysis of the Structure of Pb(1-X)Ti(X)O(1+X) by Neutron-Diffraction*. Materials Research Bulletin, 1990. **25**(8): p. 979-986.
9. Lutz, H.D., et al., *Neutron and x-ray structure determination of laurionite-type Pb{O(H,D)}X, with X=Cl,Br, and I, hydrogen bonds to lead(II) ions as a hydrogen-bond acceptor*. Journal of Solid State Chemistry, 1996. **124**(1): p. 155-161.
10. Ehm, L., et al., *High-pressure X-ray diffraction study on alpha-PbF₂*. Journal of Physics and Chemistry of Solids, 2003. **64**(6): p. 919-925.
11. Pant, A.K. and D.W.J. Cruickshank, *Crystal structure of α-Na₂Si₂O₅*. Acta Crystallogr., Sect. B, 1968. **B 24**: p. 13.
12. Hazen, R.M., *Effects of temperature and pressure on the crystal structure of forsterite*. Am. Mineral., 1976. **61**(11-1): p. 1280-1293.
13. Saburi, S., et al., *Refinement of the structure of rankinite*. Mineral. J., 1976. **8**(4): p. 240-246.
14. Ohashi, Y., *Polysynthetically-twinned structures of enstatite and wollastonite*. Phys. Chem. Miner., 1984. **10**(5): p. 217-229.

15. Ghose, S., V. Schomaker, and R.K. McMullan, *Enstatite, Mg₂Si₂O₆: a neutron diffraction refinement of the crystal structure and a rigid-body analysis of the thermal vibration*. Z. Kristallogr., 1986. **176**(3-4): p. 159-175.
16. Sharp, Z.D., R.M. Hazen, and L.W. Finger, *High-pressure crystal chemistry of monticellite, CaMgSiO₄*. Am. Mineral., 1987. **72**(7-8): p. 748-755.
17. Smith, R.I., et al., *The structure of metastable lithium disilicate, Li₂Si₂O₅*. Acta Crystallogr., Sect. C, 1990. **46**: p. 363-365.
18. Liu, F., et al., *Structural and electronic properties of seldium metasilicate*. Chem. Phys. Lett., 1993. **215**(4): p. 401-404.
19. Antao, S.M., et al., *State-of-the-art high-resolution powder X-ray diffraction (HRXRPD) illustrated with rietveld structure refinement of quartz, sodalite, tremolite, and meionite*. Canadian Mineralogist, 2008. **46**: p. 1501-1509.
20. Calvo, C., *Crystal structure of α-Mg₂P₂O₇*. Acta Crystallogr., 1967. **23**: p. 289.
21. Nord, A.G. and Kierkega.P, *Crystal structure of Mg₃(PO₄)₃*. Acta Chemica Scandinavica, 1968. **22**(5): p. 1466.
22. Nord, A.G. and K.B. Lindberg, *Crystal structure of magnesium tetrametaphosphate, Mg₂P₄O₁₂*. Acta Chemica Scandinavica, 1975. **A 29**(1): p. 1-6.
23. McDonald, R.C. and K. Eriks, *Crystallographic studies of tin(II) compounds. 2. structures of tin(II) hydrogen phosphate and tin(II) phosphite, SnHPO₄ AND SnHPO₃*. Inorganic Chemistry, 1980. **19**(5): p. 1237-1241.
24. Stachel, D., et al., *Crystal structure of magnesium ultraphosphate, MgP₄O₁₁*. Z. Kristallogr., 1992. **199**(3-4): p. 275-276.
25. Toumi, M., et al., *X-Ray powder structure determination of Li₆P₆O₁₈·3H₂O*. European Journal of Solid State and Inorganic Chemistry, 1998. **35**(10-11): p. 689-697.
26. Gabuda, S.P., et al., *Pb-207 NMR study of novel Pb-Pb chemical bonding in lead monoxides, alpha-PbO and beta-PbO*. Chemical Physics Letters, 1999. **305**(5-6): p. 353-358.
27. Fayon, F., et al., *Empirical correlations between Pb-207 NMR chemical shifts and structure in solids*. Journal of the American Chemical Society, 1997. **119**(29): p. 6837-6843.
28. Zhao, P.D., et al., *Lead-207 NMR spectroscopic study of lead-based electronic materials and related lead oxides*. Journal of Physical Chemistry B, 1999. **103**(48): p. 10617-10626.
29. Fleischer, H., S. Parsons, and C.R. Pulham, *Tetramethyllead(IV) at 150 K*. Acta Crystallographica Section E-Structure Reports Online, 2003. **59**: p. M11-M13.
30. Rodriguez-Fortea, A., P. Alemany, and T. Ziegler, *Density Functional Calculations of NMR Chemical Shifts with the Inclusion of Spin Orbit Coupling in Tungsten and Lead Compounds*. The Journal of Physical Chemistry A, 1999. **103**(41): p. 8288-8294.

31. Autschbach, J., *The calculation of NMR parameters in transition metal complexes*. Principles and Applications of Density Functional Theory in Inorganic Chemistry I, 2004. **112**: p. 1-48.
32. Autschbach, J. and S. Zheng, *Relativistic Computations of NMR Parameters from First Principles: Theory and Applications*. Annual Reports on NMR Spectroscopy, 2009. **67**: p. 1-95.
33. Autschbach, J., *Relativistic calculations of magnetic resonance parameters: background and some recent developments*. Philosophical Transactions of the Royal Society a-Mathematical Physical and Engineering Sciences, 2014. **372**(2011): p. 20120489.
34. Briand, G.G., et al., *Probing lead(II) bonding environments in 4-substituted pyridine adducts of (2,6-Me₂C₆H₃S)(2)Pb: An X-ray structural and solid-state Pb-207 NMR study*. Inorganic Chemistry, 2007. **46**(21): p. 8625-8637.
35. Greer, B.J., et al., *Characterising Lone-Pair Activity of Lead(II) by Pb-207 Solid-State NMR Spectroscopy: Coordination Polymers of [N(CN)(2)](-) and [Au(CN)(2)](-) with Terpyridine Ancillary Ligands*. Chemistry-a European Journal, 2011. **17**(13): p. 3609-3618.
36. Dmitrenko, O., et al., *The relationship between Pb-207 NMR chemical shift and solid-state structure in Pb(II) compounds*. Journal of Physical Chemistry A, 2008. **112**(14): p. 3046-3052.
37. Roukala, J., et al., *Relativistic effects on group-12 metal nuclear shieldings*. Physical Chemistry Chemical Physics, 2011. **13**(47): p. 21016-21025.
38. Arcisauskaite, V., et al., *Nuclear magnetic resonance shielding constants and chemical shifts in linear 199Hg compounds: A comparison of three relativistic computational methods*. 2011. **135**(4): p. 044306.
39. Wodynski, A., M. Repisky, and M. Pecul, *A comparison of two-component and four-component approaches for calculations of spin-spin coupling constants and NMR shielding constants of transition metal cyanides*. Journal of Chemical Physics, 2012. **137**(1): p. 014311.
40. Autschbach, J., *The accuracy of hyperfine integrals in relativistic NMR computations based on the zeroth-order regular approximation*. Theoretical Chemistry Accounts, 2004. **112**(1): p. 52-57.
41. Holmes, S.T., et al., *Density functional investigation of intermolecular effects on C-13 NMR chemical-shielding tensors modeled with molecular clusters*. Journal of Chemical Physics, 2014. **141**(16): p. 164121.
42. Krykunov, M., T. Ziegler, and E. van Lenthe, *Implementation of a Hybrid DFT Method for Calculating NMR Shieldings Using Slater-Type Orbitals with Spin-Orbital Coupling Included. Applications to (OS)-O-187, Pt-195, and C-13 in Heavy-Metal Complexes*. Journal of Physical Chemistry A, 2009. **113**(43): p. 11495-11500.
43. Krykunov, M., T. Ziegler, and E. Van Lenthe, *Hybrid Density Functional Calculations of Nuclear Magnetic Shieldings Using Slater-Type Orbitals and*

- the Zeroth-Order Regular Approximation*. International Journal of Quantum Chemistry, 2009. **109**(8): p. 1676-1683.
44. Autschbach, J., *The role of the exchange-correlation response kernel and scaling corrections in relativistic density functional nuclear magnetic shielding calculations with the zeroth-order regular approximation*. Molecular Physics, 2013. **111**(16-17): p. 2544-2554.
 45. Dmitrenko, O., S. Bai, and C. Dybowski, *Prediction of (207)Pb NMR parameters for the solid ionic lead(II) halides using the relativistic ZORA-DFT formalism: Comparison with the lead-containing molecular systems*. Solid State Nuclear Magnetic Resonance, 2008. **34**(3): p. 186-190.
 46. Jameson, C.J. and A.K. Jameson, *Absolute shielding scale for ²⁹Si*. Chem. Phys. Lett., 1988. **149**(3): p. 300-305.
 47. Jameson, C.J., A. De Dios, and A.K. Jameson, *Absolute shielding scale for ³¹P from gas-phase NMR studies*. Chem. Phys. Lett., 1990. **167**(6): p. 575-582.
 48. Holmes, S.T., et al., *Critical analysis of cluster models and exchange-correlation functionals for calculating magnetic shielding in molecular solids*. Journal of Chemical Theory and Computation, 2015. **11**(11): p. 5227-5241.
 49. Pickard, C.J. and F. Mauri, *All-electron magnetic response with pseudopotentials: NMR chemical shifts*. Phys. Rev. B, 2001. **63**(24): p. 245101.

Chapter 6

EFFECT OF COORDINATION CHEMISTRY AND OXIDATION STATE ON MAGNETIC SHIELDING TENSOR

6.1 Introduction

In this chapter, calculations of principal components of the magnetic-shielding tensor for a variety of ^{207}Pb -, ^{119}Sn -, and ^{125}Te -containing solids are presented. The investigated systems exhibit a variety of coordination environments and oxidation states. Some remarks on the inclusion of spin-orbit effects in ZORA Hamiltonian are made, based on the observed results of the calculations. For ^{119}Sn and ^{125}Te nuclei, the arguments in the literature regarding the importance of the relativistic effects are re-evaluated. Additionally, the effect of exact Hartree-Fock (HF) exchange via hybrid functionals on the calculated magnetic-shielding tensors are investigated for ^{207}Pb -, ^{119}Sn -, and ^{125}Te -containing solids. The motivation of this study is to provide the link between level of theory, electronic and coordination structure of NMR nuclei, and the accuracy of calculated NMR parameters.

6.2 The Relation between Coordination Chemistry and Magnetic Shielding of ^{207}Pb nuclei

Lead has a versatile coordination chemistry due to its ability to adopt different geometries.[1-3] The solid-state structures of lead compounds reflect these different geometries, often because of the presence of a lone pair.[4] Electronic structures generally fall into one of three categories: (a) lead(II) centers with a stereochemically

active lone pair, (b) lead(II) centers with a stereochemically inactive lone pair, and (c) lead(IV) centers without the lone pair. (Figure 6.1a.)

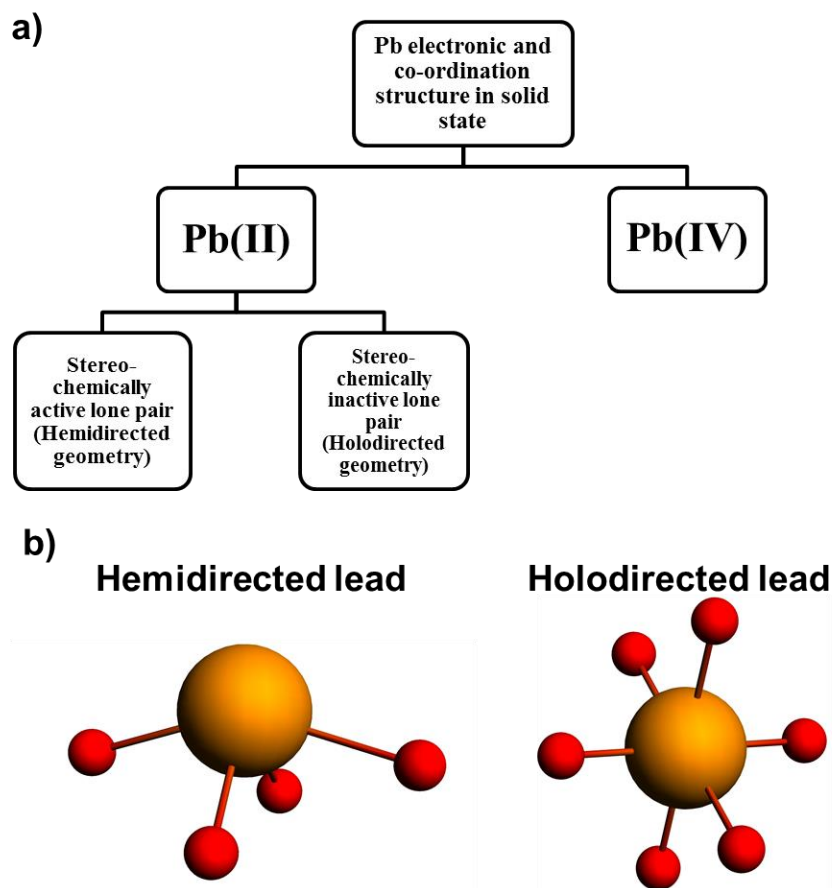


Figure 6.1 (a) Classification scheme of lead coordination in the solid state; (b) schematic structures of hemidirected and holodirected Pb centers. The orange ball represents the lead atom and red balls represent, bonding ligands. In the holodirected geometry, ligands are approximately uniformly distributed about the lead center, whereas in the hemidirected geometry, ligands tend to be non-uniformly distributed.

The effects of the lone pair are readily observable in the X-ray diffraction structures of lead-containing compounds (Figure 6.1b). For groups (b) and (c), the coordination geometry of lead is holodirected [5-10] and for group (a), it is hemidirected.[5, 11-14] Other structural parameters such as coordination number and Pb-ligand bond length are also correlated with the lone-pair activity, suggesting that lone-pair activity is a strong determinant of electronic state in lead(II) compounds.[4, 15]

The various classes of lead coordination compounds have solid-state nuclear magnetic (SSNMR) fingerprints.[16] In general, ^{207}Pb SSNMR spectra of hemidirected lead(II) coordination systems show chemical-shift tensors with large spans (Ω) due to the asymmetric electron density distribution around the lead site.[17-19] For such materials, the skew (κ) of the ^{207}Pb shielding tensor tends to be positive and close to 1.00, indicating the existence of a significantly shielded unique principal component of the chemical-shift tensor. By comparison, ^{207}Pb SSNMR measurements of holodirected lead(II) systems exhibit a tensor that has a smaller span than for hemidirected sites.[17-19] The ^{207}Pb SSNMR literature for lead(IV) systems is sparser than for lead(II), but reports suggest that these sites generally have small chemical-shift spans, similar to holodirected lead(II) sites.[20-23] In addition, the range of isotropic ^{207}Pb chemical shifts of lead(IV) sites is, in general, smaller than that of either hemidirected or holodirected lead(II) sites. Table 6.1 gives experimental structural [5-13, 24, 25] and ^{207}Pb NMR chemical-shift parameters [17-21, 23, 26] for fourteen lead-containing solids, which are investigated in this study.

Table 6.1 Experimental Crystallographic Data and ^{207}Pb Chemical Shifts of Lead-Containing Materials

Compounds	Space Group	Lead C.N. ^a	δ_{11} (ppm)	δ_{22} (ppm)	δ_{33} (ppm)	δ_{iso} (ppm)	Ω (ppm)
Hemidirected Lead(II) Systems							
1. α -PbO	<i>P4/nmm</i>	4	3030	3030	-270	1930	3300
2. β -PbO	<i>Pbcm</i>	4	2820	2760	-1000	1527	3820
3. Pb ₃ O ₄ , lead(II)	<i>P4₂/mbc</i>	4	1968	1496	-1079	795	3047
4. Pb ₂ SnO ₄ , site I	<i>Pbam</i>	4	1900	1825	-1330	798	3230
5. Pb ₂ SnO ₄ , site II		4	1810	1560	-1385	662	3195
6. PbSiO ₃ , site I	<i>P2/n</i>	3-6	1215	726	-1663	93	2878
7. PbSiO ₃ , site II		4-6	1089	584	-2170	-166	3259
8. PbSiO ₃ , site III			838	287	-2223	-366	3061
Holodirected Lead(II) and Lead(IV) Systems							
9. Pb ₃ (PO ₄) ₂ , site I	<i>C2/c</i>	8	-2759	-2931	-2969	-2886	210
10. PbCO ₃	<i>Pbnm</i>	9	-2311	-2481	-3075	-2622	764
11. Pb ₃ O ₄ , lead(IV)	<i>P4₂/mbc</i>	6	-1008	-1141	-1166	-1105	158
12. Ca ₂ PbO ₄	<i>Pbam</i>	6	-910	-1041	-1314	-1088	404
13. Pb(OAc ^b) ₄	<i>P2₁/n</i>	8	-1692	-1938	-1988	-1873	296
14. Pb(BB ^c) ₄	<i>I4₁/a</i>	8	-1722	-1972	-1972	-1889	250
The chemical shift tensor is given, in the Maryland convention, by frequency-ordered principal components ($\delta_{11} \geq \delta_{22} \geq \delta_{33}$) and by $\delta_{iso} = (\delta_{11} + \delta_{22} + \delta_{33})/3$, $\Omega = \delta_{33} - \delta_{11}$ and $\kappa = 3(\delta_{22} - \delta_{iso})/\Omega$.							
a) C.N. = coordination number							
b) OAc = acetate							
c) BB = o-benzylbenzoate							

The computations, in this part, were carried out using either the BP86 or B3LYP density functional. An all-electron TZ2P basis set was used for the first-

coordination sphere of the cluster. The remainder of the cluster was treated with the all-electron DZ basis set. Relativistic effects were incorporated at the ZORA/scalar or ZORA/spin-orbit level.

The input geometries of the clusters were created from X-ray or neutron diffraction structures of the solids. For network solids, the bond valence model for modification of terminal atoms (VMTA/BV) was employed for the termination of clusters, as described in Chapter 3. For lead(IV) tetraacetate ($\text{Pb}(\text{OAc})_4$) and lead(IV) tetra(*o*-benzylbenzoate) ($\text{Pb}(\text{BB})_4$), no modification of the terminal atoms was necessary due to the molecular nature of these solids.[7, 8] For their cluster models, hydrogen positions were optimized at the ZORA/scalar/BP86/TZ2P level of theory. All clusters included atoms up to the third coordination shell, with the NMR-active nucleus at the center of the cluster. Examples of the clusters for two selected systems are given in Figure 6.2.

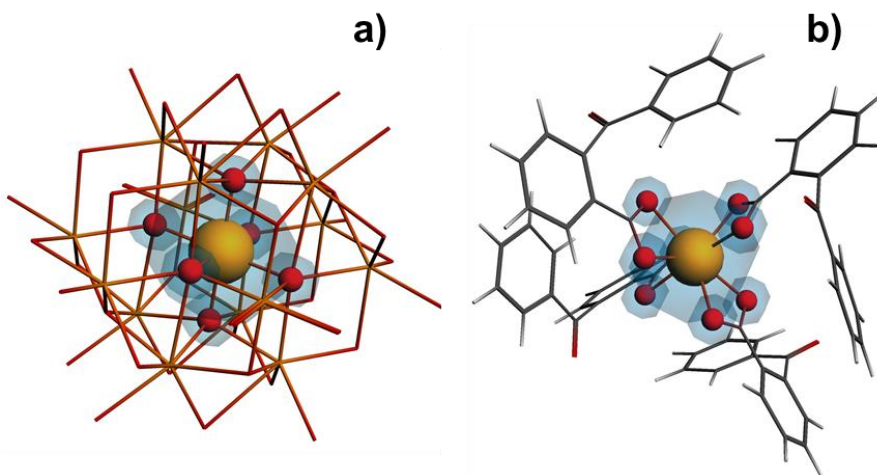


Figure 6.2 Cluster models for (a) Ca_2PbO_4 and (b) $\text{Pb}(\text{BB})_4$. The highlighted regions (shown in ball-and-stick models) represent the first coordination shell for the lead center. These atoms are treated with the TZ2P basis set. The higher coordination shells (shown with stick models) are treated with the DZ basis set.

6.2.1 Relativistic Effects on Principal Components: ZORA/Scalar vs. ZORA/Spin-Orbit

A plot of experimental tensor principal components versus principal components calculated with the ZORA/scalar Hamiltonian is given in Figure 6.3. A similar plot of experimental principal components versus principal components calculated using the ZORA/spin-orbit Hamiltonian is given in Figure 6.4. Table 6.2 gives the best-fit linear correlations between experimental and calculated data. In this table, the correlations of the holodirected and the hemidirected systems are considered separately, as well as the overall correlation of the complete set for each calculational protocol.

At the ZORA/scalar relativistic level, the correlation between calculated and experimental data deviates significantly from the ideal case (slope = -1), as seen in Figure 6.3. R^2 for the correlation (Table 6.2) for the complete data set is only 0.479, a poor linear correlation between theory and experiment. However, the correlations of principal components for only the hemi-directed sites (blue symbols) and the correlation of principal components for only the holodirected sites (red symbols) are substantially stronger, evidence that the groups correspond to two distinct subpopulations at this level of theory. The distinction between the hemidirected and the holodirected groups is the principal reason for the poor correlation when all components are considered as a single group. The correlation line for the holodirected systems at the ZORA/scalar level of theory has a slope of -1.22, much closer to the expected ideal dependence than that of the hemidirected systems, which has a slope of -0.33. (Table 6.2)

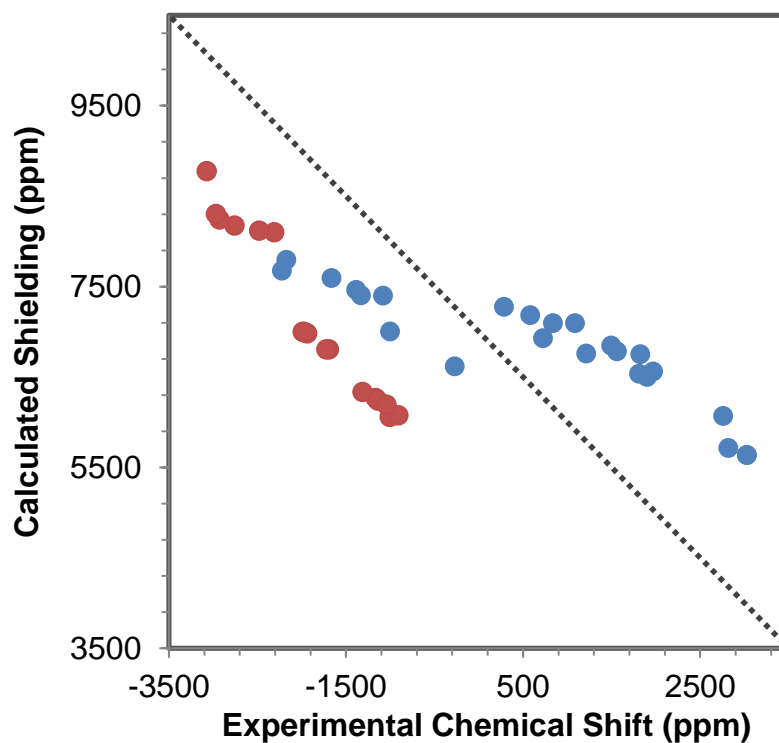


Figure 6.3 The correlation between experimental and calculated principal components for calculations at the **BP86/ZORA/scalar** relativistic level of theory. Data for hemidirected geometries are indicated by blue symbols, whereas data for holo-directed lead centers are indicated by red symbols. The dotted line in each graph shows the ideal behavior (a relation with a slope of -1). The best-fit linear correlations are given in Table 6.2.

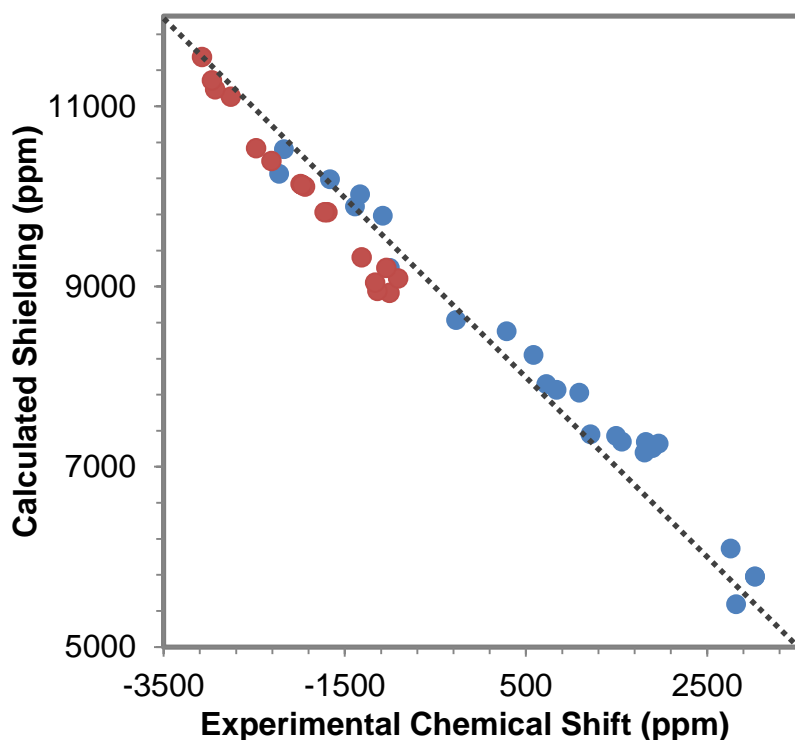


Figure 6.4 The correlation between experimental and calculated principal components for at the **BP86/ZORA/spin-orbit** relativistic level of theory. The dotted line in each graph shows the ideal behavior. The best-fit linear correlations are given in Table 6.2.

A similar correlation of experimental components and principal components calculated with the ZORA/spin-orbit Hamiltonian shows much closer agreement with the ideal behavior for both holodirected and hemidirected subgroups, with R^2 being greater than 0.97 for both. (Table 6.2.) The complete group has a similarly high correlation coefficient. Figure 6.4 shows that the two subsets (holodirected and hemidirected) have similar trends. In each case, the slope of the correlation line is not exactly -1, but it is consistently closer to -1 than one obtains in the ZORA/scalar-relativistic case. The conclusion of this comparison is that it is essential, in the case

of ^{207}Pb NMR spectroscopy, to utilize the full spin-orbit relativistic Hamiltonian in making predictions of magnetic shielding. A similar relation was observed for the ^{207}Pb -containing solids investigated in the previous chapter as well.

Table 6.2 Linear Regression Correlations of Experimental ^{207}Pb Chemical-Shift Tensor Principal Components with Calculated ^{207}Pb Magnetic-Shielding Tensor Principal Components, Using the BP86 Functional and the ZORA/Scalar Relativistic Hamiltonian or the ZORA/Spin-Orbit Relativistic Hamiltonian.

Compounds	Best-fit correlation line	R²
BP86/ZORA/scalar		
Hemidirected only	$\sigma_{\text{calc}} = -0.33\delta_{\text{exp}} + 7063$	0.804
Holodirected only	$\sigma_{\text{calc}} = -1.22\delta_{\text{exp}} + 4803$	0.954
All results	$\sigma_{\text{calc}} = -0.28\delta_{\text{exp}} + 6846$	0.479
BP86/ZORA/spin-orbit		
Hemidirected only	$\sigma_{\text{calc}} = -0.89\delta_{\text{exp}} + 8621$	0.976
Holodirected only	$\sigma_{\text{calc}} = -1.17\delta_{\text{exp}} + 7814$	0.983
All results	$\sigma_{\text{calc}} = -0.86\delta_{\text{exp}} + 8516$	0.974

The intercepts of the best-fit equations in Table 6.2 (σ at $\delta = 0$) predict the absolute shielding of the reference material, tetramethyllead (TML). One may also calculate this quantity directly. The calculated absolute shielding of TML (determined from calculation on an isolated TML molecule with the ZORA/scalar relativistic Hamiltonian) is 5171 ppm, in reasonable agreement (within 400 ppm) with the intercept (4803 ppm) found for the holodirected materials. On the other hand, the ZORA/scalar value of the intercept (7063 ppm) for the hemidirected materials is

approximately 2000 ppm larger. The structure of TML shows that it is a lead(IV) site with holodirected geometry. One expects that TML should evidence NMR shielding that is correlated with other holodirected materials, and that is what is observed.

The shielding of an isolated TML molecule calculated with the ZORA/spin-orbit Hamiltonian is 8136 ppm. This value can be compared to the extrapolated intercept of the set of holodirected materials (7814 ppm), and is within 350 ppm of that value. The intercept of the complete set (8516 ppm) is ~400 ppm larger than the calculated shielding of isolated TML, at this level of theory. In general, inclusion of spin-orbit terms provides closer agreement between the predicted absolute shielding of TML and the intercepts obtained from correlation of the different subgroups.

To make the point more clearly, Figure 6.5 shows the differences between ^{207}Pb shielding components calculated with the ZORA/spin-orbit Hamiltonian and the shielding components calculated with the ZORA/scalar Hamiltonian.

For all cases except σ_{11} of $\beta\text{-PbO}$, the components obtained with the ZORA/spin-orbit Hamiltonian are more shielded than components obtained with the ZORA/scalar Hamiltonian. The differences in principal components show a distinct dependence on the coordination and oxidation state of lead. (Figure 6.5.) Compounds 1-8 contain hemidirected sites, whereas compounds 9-14 contain either holodirected sites or lead(IV) sites. $\Delta\sigma_{33}$ (the difference between ZORA/spin-orbit and ZORA/scalar in the most shielded calculated component) is significantly larger than $\Delta\sigma_{11}$ or $\Delta\sigma_{22}$ for hemidirected sites. In fact, $\Delta\sigma_{33}$ is larger than 2000 ppm for all systems we have examined. For compounds 9-14, the change in the principal components obtained from the two relativistic methods is more uniform and ranges between 2200 and 3139 ppm. In all cases, the use of the full spin-orbit Hamiltonian

makes every principal component more shielded. For hemidirected sites, the most shielded direction (σ_{33}) is affected most; in the case of holodirected sites or lead(IV) sites, all three components are affected roughly equally by the inclusion of spin-orbit terms.

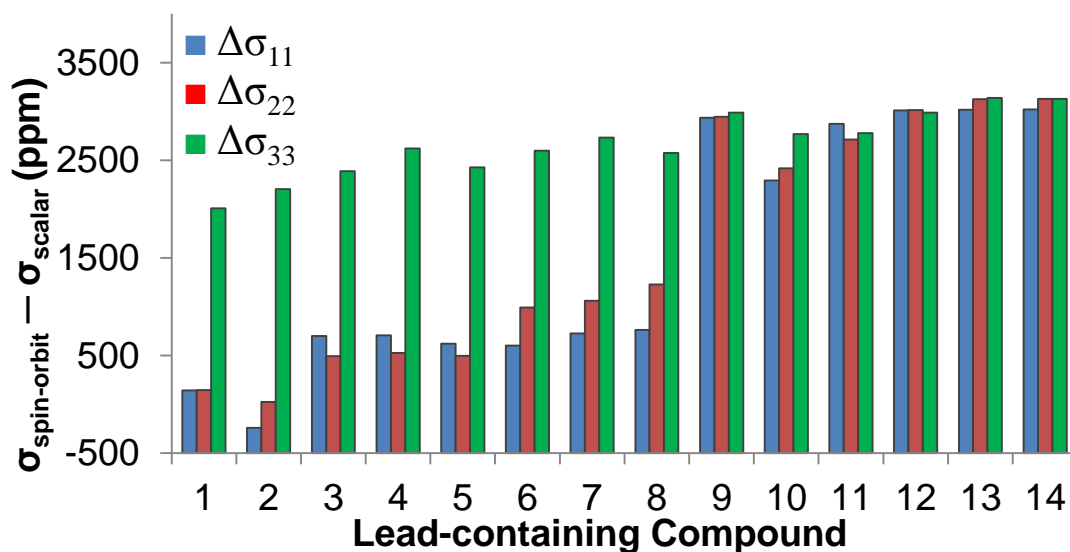


Figure 6.5 The difference ($\Delta\sigma$) between ^{207}Pb components calculated using the full ZORA/spin-orbit Hamiltonian and components calculated using the ZORA/scalar Hamiltonian. The numbering scheme for labeling lead-containing compounds is given in Table 6.1.

In Figure 6.6 are shown the orientations of the ^{207}Pb magnetic-shielding tensors' axes of α -PbO and lead(IV) acetate in the local frames. For α -PbO, the 33 principal axis of the tensor is parallel to the axis of the molecular orbital that primarily results from linear combination of the Pb 6s and 6p atomic orbitals. (Figure 6.6a.) For the same system, the 11 and 22 axes are in the plane formed by the lead atoms in the crystal. As seen in Figure 6.5, the spin-orbit effects in α -PbO (and in other hemi-

directed systems) are substantially larger for σ_{33} than for σ_{11} and σ_{22} . On the other hand, for lead(IV) acetate, the 33 axis of the tensor is nearly aligned with the longest Pb-O bond (2.31 Å), as shown in Figure 6.6b. In this system, the 6s orbital makes contributions mainly to the bonding orbitals. For lead(IV) acetate, all three components of the tensor are more uniformly affected by the spin-orbit interaction, as seen in Figure 6.5.

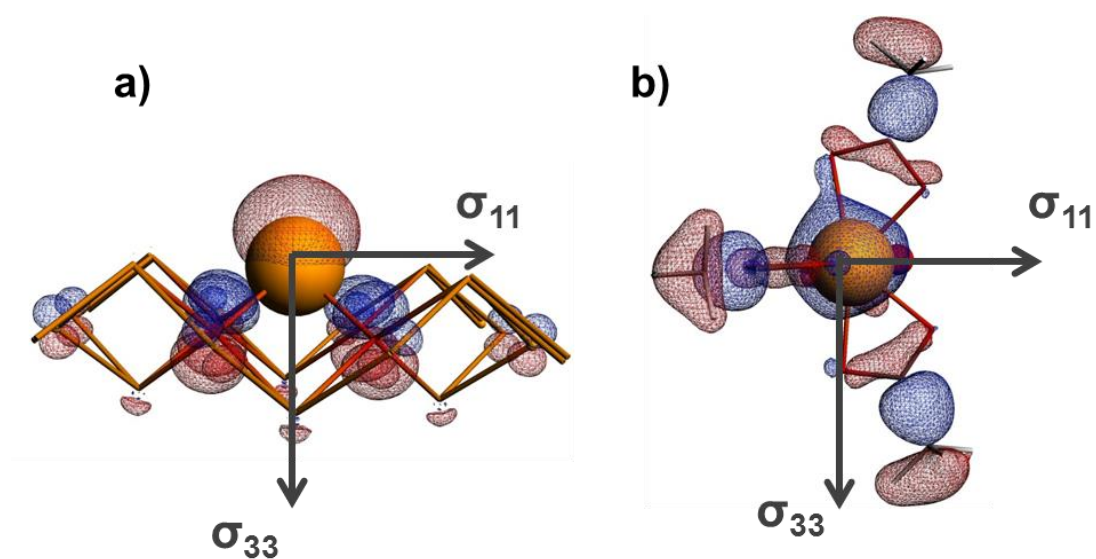


Figure 6.6 The orientation of shielding tensors and the MOs with significant 6s (Pb-centered) contributions are shown for (a) α -PbO and (b) Pb(OAc)₄. The σ_{22} component is perpendicular to the page for both systems.

In Chapter 5, calculations of magnetic shielding for hemidirected systems show that the use of a nonrelativistic Hamiltonian or a scalar relativistic Hamiltonian results in a significant underestimation of the span (Ω), by up to 2500 ppm. The

present results (Figure 6.5) suggest that this underestimation results from the absence of the contributions of the spin-orbit terms to σ_{33} .

To the author's knowledge, calculations of lead (IV) magnetic-shielding tensors have not been reported. Mitchell et al.[27] have investigated ^{119}Sn isotropic chemical shifts using the GIPAW approach with scalar relativistic pseudopotentials for a mixture of tin(II)- and tin(IV)-containing systems. Their results indicate that the calculated tin(II) isotropic shieldings deviate from experiment more strongly than do calculated isotropic shieldings for tin(IV) sites.[27] These findings are consistent with the current results for ^{207}Pb shielding, suggesting that inclusion of spin-orbit effects are probably crucial for the calculation of ^{119}Sn magnetic-shielding tensors, as well. The impact of spin-orbit coupling on the calculated ^{119}Sn magnetic shielding tensors is discussed in section 6.3.

6.2.2 The Effect of Density Functional on Calculated ^{207}Pb Principal Components: BP86 vs. B3LYP

An algorithm for the calculation of exact Hartree-Fock (HF) exchange has recently allowed hybrid DFT calculations of NMR parameters with ZORA.[28, 29] Inclusion of HF exchange generally improves the agreement between experimental chemical shifts and calculated magnetic shieldings, as compared to calculations with GGA functionals such as BP86.[30-33] In this section, I discuss the performance of a hybrid functional (B3LYP with 20% HF exchange) for the calculations of ^{207}Pb magnetic-shielding tensors. In Figure 6.7, a plot of experimental and calculated tensor principal components is shown for calculations at B3LYP/ZORA/spin-orbit levels of theory. Table 6.3 shows equations for the best-fit linear correlations of the data in

Figure 6.7, and the previously obtained best-fit linear correlations at BP86/ZORA/spin-orbit level for comparison.

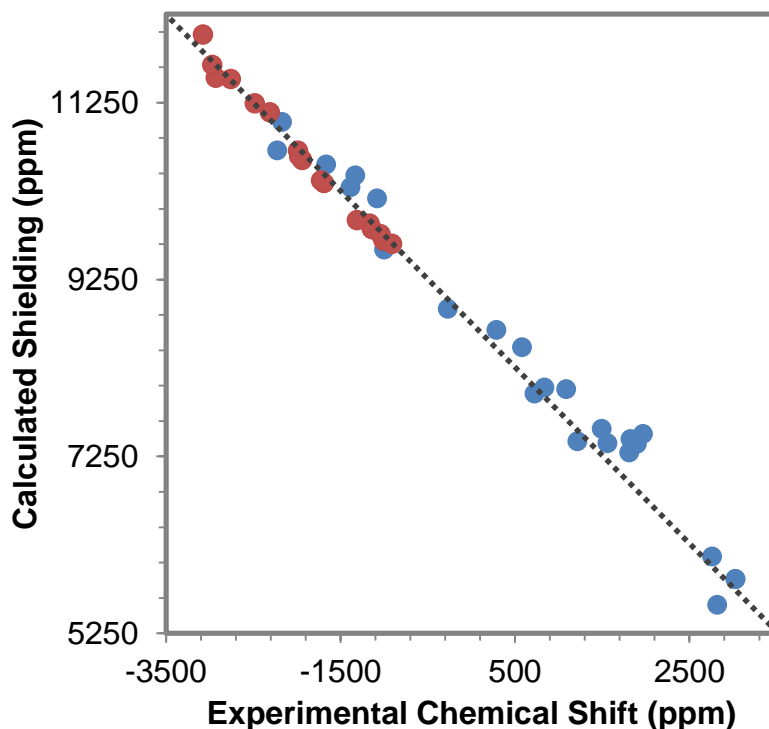


Figure 6.7 The correlation between principal components of the experimental ^{207}Pb chemical-shift tensor and the principal components of the calculated ^{207}Pb magnetic-shielding tensor determined at the B3LYP(20% XC)/ZORA/spin-orbit level of theory. Holodirected lead centers are represented by blue symbols; hemidirected lead centers are represented by red symbols. The dotted lines show the expected ideal behavior.

For the complete data set (hemidirected plus holodirected lead sites), the correlation obtained with the B3LYP functional is better than the correlation when the BP86 functional is used. The slope of the correlation line (-0.95) for data determined

with the B3LYP functional is within 5% of the ideal case, and the data are not as scattered about the best-fit correlation line. Even when the holodirected and hemidirected subgroups are analyzed separately, the calculation with a B3LYP functional is better than a calculation with the BP86 functional, as seen by comparing the slopes of the correlation lines. Use of the B3LYP functional also gives consistent values of the reference shielding, to within about 250 ppm. The predicted reference shieldings of the subgroups calculated with the BP86 functional differ by ~800 ppm. These results demonstrate the importance of inclusion of HF exchange in magnetic-shielding calculations for ^{207}Pb sites with different coordination chemistries and oxidation states.

Table 6.3 Linear Regression Correlations of Experimental ^{207}Pb Chemical-Shift Tensor Principal Components with Calculated ^{207}Pb Magnetic-Shielding Tensor Principal Components, Using the BP86 and B3LYP Functionals and the ZORA/Spin-Orbit Hamiltonian.

Compounds	Equation of the best-fit correlation line	R ²
BP86/ZORA/spin-orbit		
Hemidirected	$\sigma_{\text{calc}} = -0.89\delta_{\text{exp}} + 8621$	0.976
Holodirected	$\sigma_{\text{calc}} = -1.17\delta_{\text{exp}} + 7814$	0.983
All	$\sigma_{\text{calc}} = -0.86\delta_{\text{exp}} + 8516$	0.974
B3LYP/ZORA/spin-orbit		
Hemidirected	$\sigma_{\text{calc}} = -0.97\delta_{\text{exp}} + 8898$	0.976
Holodirected	$\sigma_{\text{calc}} = -1.04\delta_{\text{exp}} + 8633$	0.990
All	$\sigma_{\text{calc}} = -0.95\delta_{\text{exp}} + 8853$	0.987

In Figure 6.8, the difference between principal components calculated with a B3LYP functional and a BP86 functional.

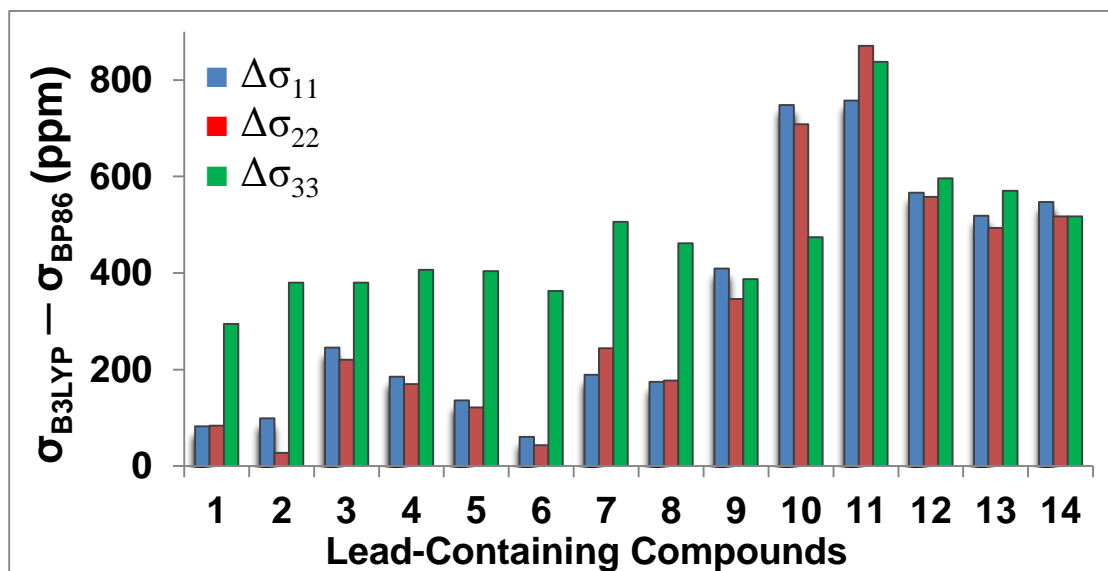


Figure 6.8 The difference between ^{207}Pb components ($\Delta\sigma_{ii}$) calculated using the B3LYP, and BP86 density functionals. Both sets of calculations are carried out using the ZORA/spin-orbit Hamiltonian.

For the hemidirected lead sites (1-8), the difference in σ_{33} or $\Delta\sigma_{33}$ is larger for each system than the change in σ_{11} or σ_{22} . In this subset, $\Delta\sigma_{33}$ ranges between 295-506 ppm. In comparison, $\Delta\sigma_{11}$ and $\Delta\sigma_{22}$ are 245-84 ppm. This non-uniform effect of HF exchange on the calculated principal components alters the slope of the correlation line from -0.89 (BP86) to -0.97, indicating a better agreement between theory and experiment when hybrid functionals are employed. For systems 9-14 (holodirected sites), the differences between shielding components are generally larger than those for systems 1-8 (hemidirected sites). In this subset, $\Delta\sigma_{ii}$ range between 387-871 ppm.

The largest change in the principal components is observed for the lead(IV) site in Pb₃O₄. For all systems, the calculated principal components are more shielded when the B3LYP functional is employed.

To understand the effect of HF exchange on principal components, magnetic-shielding tensors are calculated using the B3LYP functional, with variable amounts of HF exchange, for two systems: α -PbO (hemidirected) and lead(IV) acetate (holodirected). The results are shown in Table 6.4.

Table 6.4 Effect of HF Exchange on ²⁰⁷Pb Magnetic-Shielding Tensors in α -PbO and Lead(IV) Acetate, Determined at the B3LYP Level of Theory.

HF Exchange (%)	σ_{11} (ppm)	σ_{22} (ppm)	σ_{33} (ppm)
α -PbO			
10	5831	5834	8752
15	5846	5849	8834
20	5862	5865	8919
25	5877	5879	9007
30	5891	5894	9096
35	5905	5907	9187
Lead(IV) Acetate			
10	10064	10347	10442
15	10204	10475	10576
20	10342	10602	10708
25	10479	10728	10838
30	10615	10853	10966
35	10748	10976	11091

In both cases, inclusion of more HF exchange in the functional leads to more shielded principal components. For α -PbO, there is a somewhat stronger effect of HF exchange on σ_{33} than on σ_{11} and σ_{22} . The change in σ_{33} over the range of 10%-35% HF exchange is 435 ppm. Over the same range, σ_{11} and σ_{22} change by less than 75 ppm. In the case of lead(IV) acetate, the change in principal components is more uniform than for α -PbO, with changes in principal components of 684, 629 and 648 ppm for σ_{11} , σ_{22} and σ_{33} , respectively.

Figure 6.9 shows the correlation of the calculated span ($\Omega = \sigma_{33} - \sigma_{11}$) of α -PbO as a function of the amount of HF exchange in the functional. A similar plot is shown for lead(IV) acetate in Figure 6.10. For both systems, there is a strong linear relation between calculated span and the fraction of HF exchange. In the case of α -PbO, the span increases as the fraction of HF exchange increases, from 2921 ppm at 10% HF exchange to 3282 ppm at 35% HF exchange. On the other hand, for lead(IV) acetate, the span decreases with increasing HF exchange, from 378 ppm at 10% HF exchange to 343 ppm at 35% HF exchange. For the holodirected lead(IV) acetate, the span is approximately 10% of the span for the hemidirected α -PbO. For both cases, the calculated span is closer to the experimental value (Table 6.1) when including a higher percentage of HF exchange. This observation suggests that inclusion of more HF exchange in the B3LYP functional from the default 20% improves the calculated ^{207}Pb NMR span.

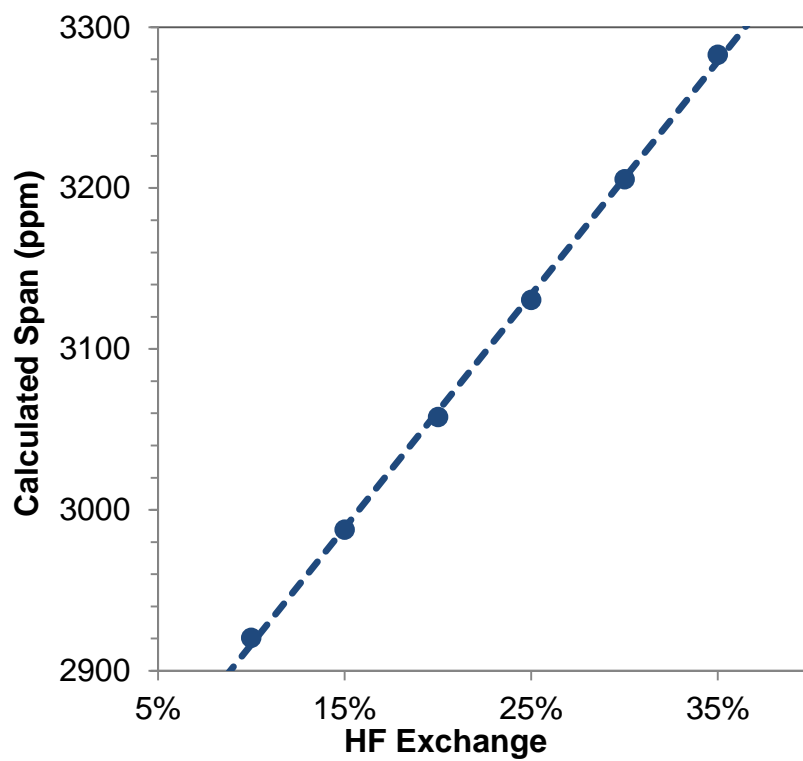


Figure 6.9 The correlation between calculated span and fraction of HF exchange in the B3LYP functional for α -PbO.

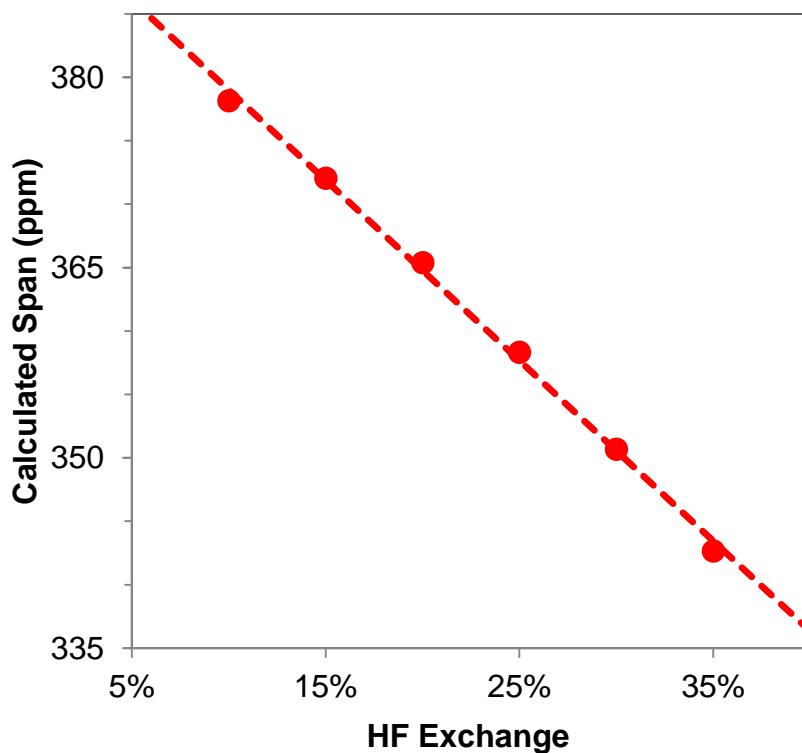


Figure 6.10 The correlation between calculated span and fraction of HF exchange in the B3LYP functional for lead(IV) acetate.

6.3 The Relation between Coordination Chemistry, Oxidation State and Magnetic Shielding of ^{119}Sn nuclei

Experimental ^{119}Sn NMR parameters depend on the local coordination geometry and share important similarities with those of ^{207}Pb as discussed in the previous section.[2, 34] For instance, tin(II) species generally exhibit hemidirected coordination chemistry [35-39] with characteristically wide chemical-shift spans of 600–1200 ppm.[40-42] In contrast, tin(IV) species generally exhibit holodirected coordination chemistry [13, 43-47] with spans under 400 ppm. The differences in magnetic-shielding parameters between the two structural motifs reflect the fact that crystal structures of tin(II) compounds usually have large void spaces to accommodate

the lone pair of electrons, whereas the coordination geometry around tin(IV) sites is more nearly spherically symmetric. In the previous section, it is shown that ^{207}Pb NMR parameters illustrate the differences among NMR parameters of lead nuclei at sites of different stereochemistry and how these differences are enhanced by relativistic effects, particularly by spin-orbit coupling. A similar result might be expected for ^{119}Sn .

Twelve tin-containing solids with known X-ray or neutron diffraction structures and with known principal components of the chemical-shift tensor determined by solid-state NMR spectroscopy have been investigated. In Table 6.5, the experimental SSNMR parameters [40, 42, 48-52] and some crystallographic information [13, 35-39, 43-47] are given for the investigated systems. The computations, in this section, were carried out using either PBE or PBE0 density functional. The all-electron (AE) TZ2P basis set was employed for the NMR-active nucleus (^{119}Sn) and its first coordination shell, whereas the remainder of the cluster was treated with the smaller AE TZP basis set. Two example clusters, including a schematic of the partitioning of the basis sets, are illustrated in Figure 6.11. All clusters are treated with VMTA/BV model. Relativistic effects were incorporated at the ZORA/scalar or ZORA/spin-orbit level. Linear dependence threshold of 10^{-4} is applied for the cluster calculations employing PBE functional. For calculations employing the PBE0 functional, it was realized that a more stringent threshold parameter is necessary for the numerical problems associated with the linear dependence of the basis functions; therefore the threshold parameter was increased to 5×10^{-3} in these calculations.

Table 6.5 Experimental Crystallographic Data and ^{119}Sn Chemical Shifts of Tin-Containing Materials.

Compound s	Space Group	Tin C.N.	δ_{11} (ppm)	δ_{22} (ppm)	δ_{33} (ppm)	δ_{iso} (ppm)	Ω (ppm)
Tin(II) systems							
SnO	<i>P4/nmm</i>	4	121	121	-867	-208	988
SnHPO ₄	<i>P12₁/c1</i>	5	-606	-712	-1553	-957	947
SnHPO ₃	<i>I1c1</i>	4	-290	-420	-1435	-715	1145
SnC ₂ O ₄	<i>C12/c1</i>	4-6	-523	-639	-1474	-879	951
SnSO ₄	<i>Pnma</i>	4	-1047	-1070	-1679	-1265	632
BaSnF ₄	<i>P4/nmm</i>	5	-596	-596	-1486	-893	890
Tin(IV) systems							
SnO ₂	<i>P4₂/mnm</i>	6	-550	-573	-686	-603	136
Ca ₂ SnO ₄	<i>Pbam</i>	6	-459	-512	-664	-545	205
SnS ₂	<i>P-3m1</i>	6	-730	-730	-835	-765	105
Pb ₂ SnO ₄	<i>Pbam</i>	6	-558	-566	-692	-605	134
Na ₆ Sn ₂ S ₇	<i>C12/c1</i>	4	232	60	-107	62	339
Sr ₂ SnO ₄	<i>Pccn</i>	6	-510	-548	-681	-580	171

In this section, calculations employing model clusters are accompanied with periodic boundary calculations (PBC) which employs the GIPAW method.[53, 54] These calculations were performed at the PBE level with core orbitals replaced by ultrasoft pseudopotentials generated on the fly and with a plane-wave cutoff energy of 600 eV. Relativistic effects were included at the ZORA/scalar level through the pseudopotential approximation of Yates and co-workers.[55]

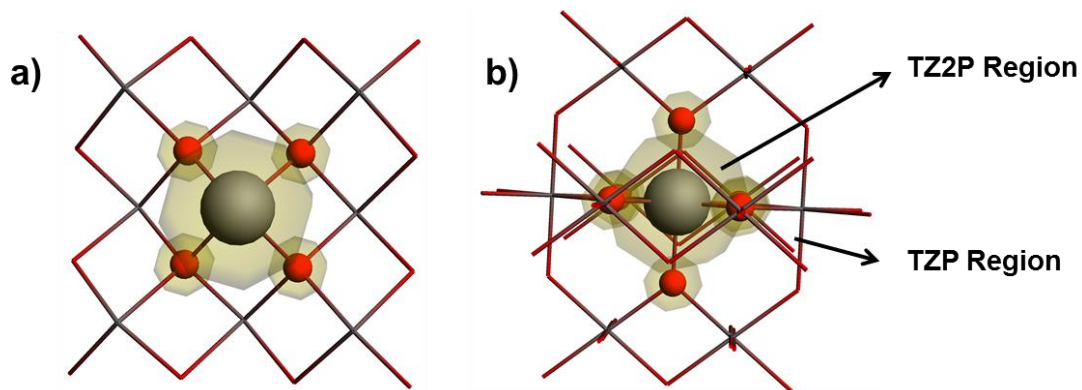


Figure 6.11 Cluster models for a) SnO and b) SnO₂. The central ball-and-stick region, representing the NMR-active ¹¹⁹Sn center and the first-coordination shell, are treated with the TZ2P basis set. The outer coordination shells are treated with the smaller TZP basis set.

6.3.1 Relativistic Effects on Principal Components of ¹¹⁹Sn: ZORA/Scalar vs. ZORA/Spin-Orbit

All calculations discussed in this subsection were performed with the PBE density functional. Figure 6.12 shows the correlations between the principal components of calculated magnetic-shielding tensors determined at PBE/GIPAW level and the principal components of experimental chemical-shift tensors. In comparison, Figure 6.13 and 6.14 shows the similar correlation plots for cluster calculations with PBE/ZORA/scalar and PBE/ZORA/spin-orbit level of theory respectively. Table 6.6 presents the parameters of the linear best-fit lines for tin(II) and tin(IV)-containing solids.

For tin(II)-containing solids analyzed as a separate subset (Table 6.6), the correlation between calculated magnetic shielding and experimental chemical-shift values deviates significantly from ideal agreement at the ZORA/scalar level. The deviation from the ideal case (slope = -1.00) is 29% and 23% for the linear best-fit lines obtained using periodic PBE/GIPAW and PBE/ZORA/scalar methods,

respectively. The extrapolated shielding of the reference compound (tetramethyltin), σ_{ref} , which is given by the intercept of the best-fit line, is 3019 ppm by the PBE/GIPAW method. The PBE/ZORA/scalar value of σ_{ref} is 2745 ppm.

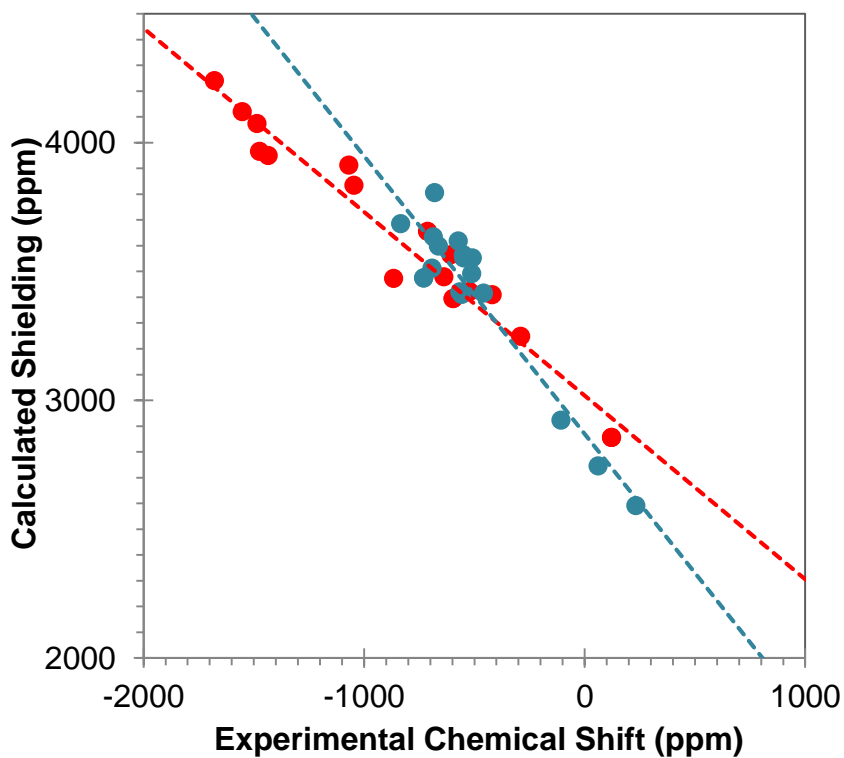


Figure 6.12 Correlations between calculated principal components of ^{119}Sn magnetic-shielding tensors and experimental ^{119}Sn chemical-shift tensors for twelve tin-containing solids, as determined with the **PBE/GIPAW** method. Sn(II) sites are shown in red; Sn(IV) sites are shown in blue.

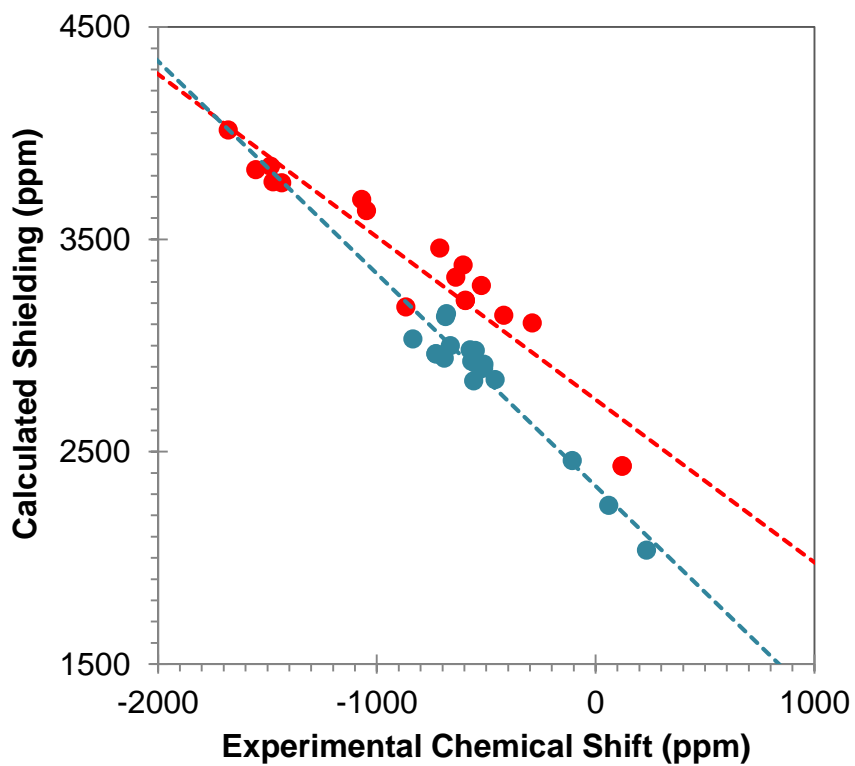


Figure 6.13 Correlations between calculated principal components of ^{119}Sn magnetic-shielding tensors and experimental ^{119}Sn chemical-shift tensors for twelve tin-containing solids, as determined with the **PBE/ZORA/scalar** and cluster method. Sn(II) sites are shown in red; Sn(IV) sites are shown in blue.

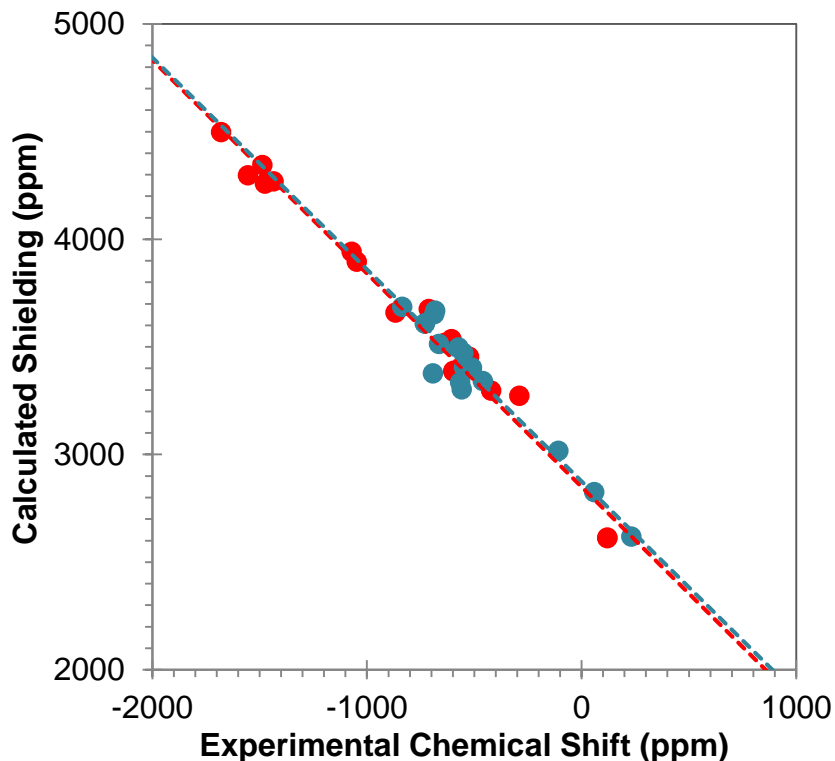


Figure 6.14 Correlations between calculated principal components of ^{119}Sn magnetic-shielding tensors and experimental ^{119}Sn chemical-shift tensors for twelve tin-containing solids, as determined with the **PBE/ZORA/spin-orbit** and cluster method. Sn(II) sites are shown in red; Sn(IV) sites are shown in blue.

For the subset of tin(IV)-containing solids, the PBE/GIPAW and PBE/ZORA/scalar methods are much closer to the ideal value of -1.00. However, the predicted reference shieldings predicted by the two methods differ by 531 ppm. These results indicate that the predicted magnetic shieldings determined either with the cluster model treated with the ZORA/scalar Hamiltonian or with the GIPAW formalism are dependent on the oxidation state and the coordination geometry of the tin atom in the solid system.

When the cluster models are treated with **ZORA/spin-orbit Hamiltonian**, the correlation between calculated principal components of magnetic-shielding tensors and experimental principal components of chemical-shift tensors shows significant improvement. The improvement is particularly striking for tin(II)-containing solids, as shown in Table 6.6. The parameters of the linear correlation lines (slope and σ_{ref}) are more consistent between the subsets of tin(II) and tin(IV)-containing solids, emphasizing the importance of spin-orbit effects on the magnetic-shielding tensor of ^{119}Sn nuclei.

Table 6.6 Linear-Regression Parameters for the Linear Relations Between Calculated Magnetic Shieldings and Experimental Chemical Shifts of ^{119}Sn -Containing Solids

Method	slope	σ_{ref} (ppm)	R^2
<i>Tin(II)-containing solids</i>			
PBE/GIPAW	-0.71 ± 0.04	3019 ± 38	0.95
PBE/ZORA/scalar	-0.77 ± 0.06	2745 ± 60	0.91
PBE/ZORA/spin-orbit	-0.99 ± 0.03	2849 ± 34	0.98
<i>Tin(IV)-containing solids</i>			
PBE/GIPAW	-1.08 ± 0.10	2869 ± 55	0.89
PBE/ZORA/scalar	-1.00 ± 0.07	2338 ± 41	0.92
PBE/ZORA/spin-orbit	-0.99 ± 0.06	2875 ± 37	0.94
<i>All Systems</i>			
PBE/GIPAW	-0.77 ± 0.04	3001 ± 36	0.90
PBE/ZORA/scalar	-0.92 ± 0.07	2499 ± 52	0.85
PBE/ZORA/spin-orbit	-0.98 ± 0.03	2867 ± 22	0.97

In Table 6.7, the predicted chemical-shift parameters resulting from each method, along with reported experimental values are presented for the twelve tin-containing solids. Calculated magnetic-shielding parameters have been converted to the chemical-shift scale using the predicted σ_{ref} from the linear best-fit correlations for **all systems** given in Table 6.6. The residuals between the experimental and calculated principal components of the chemical-shift tensors are given in Table 6.7, which is a measure of the overall quality of performance of each computational methodology.

Table 6.7 Calculated and Experimental NMR Parameters of ^{119}Sn -Containing Solids Determined with Various DFT Methods.

Compounds	δ_{11} (ppm)	δ_{22} (ppm)	δ_{33} (ppm)	δ_{iso} (ppm)	Ω (ppm)	Residual ^a (ppm)
Tin(II)-containing solids						
<u>SnO</u>	<u>121</u>	<u>121</u>	<u>-867</u>	<u>-208</u>	<u>988</u>	-
PBE/GIPAW	145	145	-472	-61	617	229
PBEZORA/scalar	45	45	-677	-196	722	126
PBE/ZORA/spin-orbit	256	253	-793	-94	1049	117
<u>SnHPO₄</u>	<u>-606</u>	<u>-712</u>	<u>-1553</u>	<u>-957</u>	<u>947</u>	-
PBE/GIPAW	-564	-655	-1119	-779	555	254
PBEZORA/scalar	-874	-954	-1323	-1050	449	247
PBE/ZORA/spin-orbit	-669	-808	-1429	-969	760	97
<u>SnHPO₃</u>	<u>-290</u>	<u>-420</u>	<u>-1435</u>	<u>-715</u>	<u>1145</u>	-
PBE/GIPAW	-247	-409	-949	-535	702	282
PBEZORA/scalar	-602	-638	-1262	-834	660	241
PBE/ZORA/spin-orbit	-405	-430	-1402	-745	996	69
<u>SnC₂O₄</u>	<u>-523</u>	<u>-639</u>	<u>-1474</u>	<u>-879</u>	<u>951</u>	-

PBE/GIPAW	-421	-479	-965	-622	544	314
PBEZORA/scalar	-778	-816	-1266	-953	488	216
PBE/ZORA/spin-orbit	-587	-651	-1392	-877	805	61
<u>SnSO₄</u>	<u>-1047</u>	<u>-1070</u>	<u>-1679</u>	<u>-1265</u>	<u>632</u>	-
PBE/GIPAW	-834	-912	-1239	-995	405	297
PBEZORA/scalar	-1130	-1183	-1510	-1274	380	127
PBE/ZORA/spin-orbit	-1028	-1075	-1630	-1245	602	30
<u>BaSnF₄</u>	<u>-596</u>	<u>-596</u>	<u>-1486</u>	<u>-893</u>	<u>890</u>	-
PBE/GIPAW	-394	-394	-1073	-620	679	290
PBEZORA/scalar	-708	-708	-1340	-919	632	124
PBE/ZORA/spin-orbit	-520	-520	-1478	-839	958	62
Tin(IV)-containing solids						
<u>SnO₂</u>	<u>-550</u>	<u>-573</u>	<u>-686</u>	<u>-603</u>	<u>136</u>	-
PBE/GIPAW	-564	-617	-633	-605	69	41
PBEZORA/scalar	-471	-475	-631	-526	160	79
PBE/ZORA/spin-orbit	-605	-630	-785	-673	180	73
<u>Ca₂SnO₄</u>	<u>-459</u>	<u>-512</u>	<u>-664</u>	<u>-545</u>	<u>205</u>	-
PBE/GIPAW	-415	-491	-597	-501	182	48
PBEZORA/scalar	-334	-389	-495	-406	161	141
PBE/ZORA/spin-orbit	-474	-529	-647	-550	173	16
<u>SnS₂</u>	<u>-730</u>	<u>-730</u>	<u>-835</u>	<u>-765</u>	<u>105</u>	-
PBE/GIPAW	-474	-475	-684	-544	211	226
PBEZORA/scalar	-456	-456	-527	-479	71	286
PBE/ZORA/spin-orbit	-741	-742	-819	-767	77	13
<u>Pb₂SnO₄</u>	<u>-558</u>	<u>-566</u>	<u>-692</u>	<u>-605</u>	<u>134</u>	-
PBE/GIPAW	-410	-419	-512	-447	101	159
PBEZORA/scalar	-328	-421	-436	-395	108	216

PBE/ZORA/spin-orbit	-436	-468	-509	-471	73	139
<u>Na₆Sn₂S₇</u>	<u>232</u>	<u>60</u>	<u>-107</u>	<u>62</u>	<u>339</u>	-
PBE/GIPAW	409	255	78	247	331	186
PBEZORA/scalar	468	257	46	257	423	199
PBE/ZORA/spin-orbit	249	41	-150	47	399	29
<u>Sr₂SnO₄</u>	<u>-510</u>	<u>-548</u>	<u>-681</u>	<u>-580</u>	<u>171</u>	-
PBE/GIPAW	-551	-551	-805	-636	253	75
PBEZORA/scalar	-407	-412	-645	-488	238	100
PBE/ZORA/spin-orbit	-536	-539	-801	-625	265	71

For tin(IV)-containing solids, the performance of PBE/GIPAW shows some improvement over its performance in calculations of the chemical shifts in tin(II) systems. For example, the accuracy of calculated principal components for SnO₂, Ca₂SnO₄, Pb₂SnO₄ and Sr₂SnO₄ by the PBE/GIPAW method are comparable to results obtained with PBE/ZORA/spin-orbit methods. The agreement between experiment and PBE/GIPAW predictions are not as good for SnS₂ and Na₆Sn₂S₇. In these latter systems, the first coordination shell around tin consists of sulfur atoms rather than oxygen atoms. The magnitude of spin-orbit effects on ¹¹⁹Sn magnetic shielding is probably increased by the presence of the heavier sulfur atom in the coordination environment. In these two cases, the residuals determined with the PBE/ZORA/spin-orbit calculations are 13 and 29 ppm, respectively, whereas residuals by the PBE/ZORA/scalar are 286 and 199 ppm.

To understand the effect of spin-orbit coupling on the ¹¹⁹Sn magnetic-shielding tensor, we present the differences ($\Delta\sigma_{ii}$) between principal components of magnetic-

shielding tensors calculated at the PBE/ZORA/spin-orbit level and those calculated at the PBE/ZORA/scalar level (Figure 6.15).

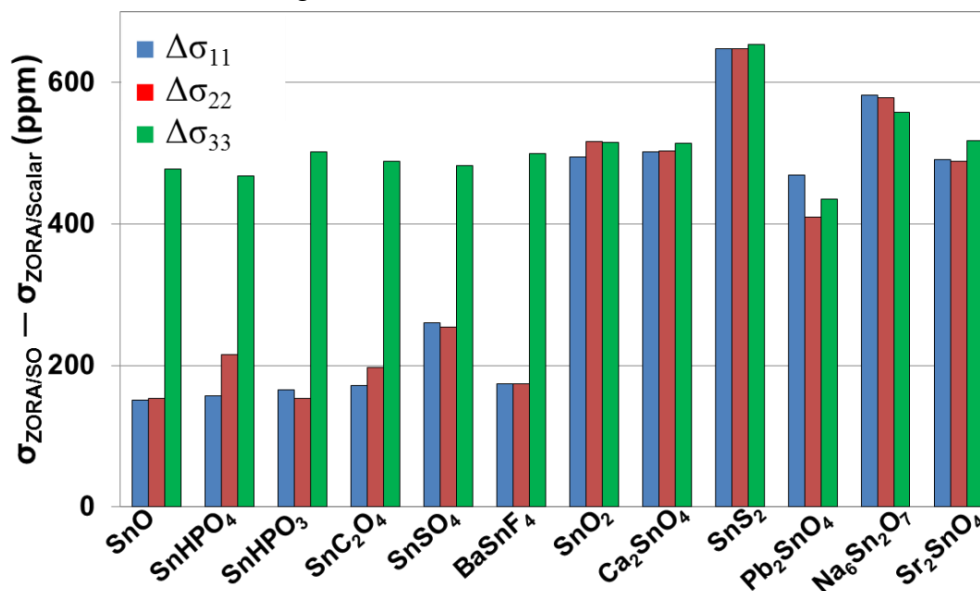


Figure 6.15 The differences ($\Delta\sigma_{ii}$) in principal components of ^{119}Sn magnetic-shielding tensors calculated with the PBE/ZORA/spin-orbit method and the PBE/ZORA/scalar method. All calculations modeled the solid-state environment with the cluster-based VMTA/BV approach.

It is evident that spin-orbit effects on magnetic-shielding tensors exhibit a strong dependence on the oxidation state of tin. For tin(II)-containing systems, the contribution of spin-orbit effects on magnetic shielding is largest for the σ_{33} component where $\Delta\sigma_{33}$ are around 500 ppm. The spin-orbit effects are lesser for σ_{11} and σ_{22} , with $\Delta\sigma_{ii}$ ranging between 154 - 260 ppm. In comparison, the contribution of spin-orbit effects on each principal component of the magnetic-shielding tensor is more uniform for tin(IV)-containing systems, with $\Delta\sigma_{ii}$ varying between 435 - 654 ppm. The largest change in any magnetic-shielding tensor between PBE/ZORA/spin-orbit and PBE/ZORA/scalar results is observed for SnS₂ where $\Delta\sigma_{ii}$ is 654 ppm.

Indeed, among the tin(IV)-containing materials, the residuals of PBE/GIPAW and cluster-based PBE/ZORA/scalar results are highest for this compound, due to only partial cancellation of spin-orbit effects when magnetic shieldings are converted to chemical shifts.

The results in Figure 6.15 for spin-orbit effects on the ^{119}Sn magnetic-shielding tensor show a striking resemblance to the recently-investigated spin-orbit effects on coordination compounds of lead. In the case of ^{207}Pb -containing solids, spin-orbit effects show a similar dependence on the oxidation state (+2 or +4) and coordination geometry (hemidirected or holodirected) around the ^{207}Pb nuclei. The magnitudes of the spin-orbit effects for ^{119}Sn and ^{207}Pb are quite different, as expected. Overall, the magnitude of spin-orbit effects ($\Delta\sigma_{ii}$) for the investigated ^{119}Sn -containing systems varies between 154 - 654 ppm. In comparison, the spin-orbit effects on ^{207}Pb magnetic-shielding tensor are generally 2000 - 3000 ppm. This difference is likely due to the larger nuclear charge on ^{207}Pb , resulting in a more efficient spin-orbit coupling.

The accuracy of calculated NMR parameters for ^{119}Sn nuclei has been systematically investigated for a series of isolated tin(IV) molecules by Bagno et al. [56] using the ZORA/scalar and ZORA/spin-orbit methods. The results indicate that the both ZORA/scalar and ZORA/spin-orbit methods work quite well for predicting chemical shifts when no other heavy atom is bound to tin.[56] In such systems, the predicted spin-orbit effects on the isotropic magnetic shielding vary by around 500 ppm and mostly cancel out when magnetic shieldings are converted to the chemical-shift scale.[56] These findings partially agree with the PBE/GIPAW and PBEZORA/scalar results for tin(IV)-containing solids. However, for tin(II)-

containing solids, the assumption that spin-orbit effects will cancel out when computed magnetic-shielding parameters are converted to the chemical-shift scale is incorrect.

The magnetic shielding (or absolute shielding) of tetramethyltin, or σ_{ref} , can be estimated from the intersection of the best-fit correlation lines in Table 6.6. From the PBE/ZORA/spin-orbit method, σ_{ref} is predicted to be 2867 ppm from the correlation obtained for all tin-containing systems. In comparison, a single calculation on tetramethyltin at the same level of theory gives 2852 ppm for σ_{ref} , which is a discrepancy of only 15 ppm. With the four-component relativistic DFT (with BP86 functional), σ_{ref} is computed as 3199 ppm.[57] It is clear that PBE/ZORA/spin-orbit underestimates σ_{ref} by ~12% compared to the four-component DFT. The underestimation of absolute shieldings predicted by ZORA calculations has been discussed in the previous chapters. Nevertheless, the current results, as well as previous results on other heavy nuclei such as ^{207}Pb and ^{199}Hg , demonstrate that the ZORA/spin-orbit predictions for the **chemical-shift tensor** agree with the experimental values within ~2%, possibly due to the cancellation of higher-order relativistic effects beyond spin-orbit coupling.

In the previous investigations of lighter nuclei such as ^{13}C , ^{19}F or ^{29}Si , the performances of the GIPAW method and cluster models for the predictions of magnetic-shielding tensors in solids are similar, provided that sufficiently large clusters are used for the comparison.[55, 58-61] In contrast, the current results show that, although PBE/GIPAW and cluster-based PBE/ZORA/scalar methods yield similar trends for tin(II) and tin(IV)-containing solids, the two methods yield quite different results for σ_{ref} (Table 6.6).

To compare the two methods in the absence of solid-state effects, calculations are performed on isolated molecules (SnF_2 , $\text{Sn}(\text{CN})_2$, $\text{Sn}(\text{OH})_2$, SnF_4 , $\text{Sn}(\text{CH}_3)_4$, and SnH_4) containing ^{119}Sn in oxidation states of +2 or +4. The results are shown in Table 6.8.

Table 6.8 Comparison of Calculated Magnetic Shieldings (σ_{iso}) for Tin-Containing Molecules using GIPAW^a and ZORA/scalar Methods.

Molecule ^b	σ_{iso} (ppm)	
	PBE/ZORA/scalar	PBE/GIPAW
SnF_2	2854	2880
$\text{Sn}(\text{CN})_2$	2053	2111
$\text{Sn}(\text{OH})_2$	2465	2516
SnF_4	3002	3364
$\text{Sn}(\text{CH}_3)_4$	2370	2829
SnH_4	2982	3354

a) For GIPAW calculations the isolated molecular state is approximated by employing large unit cells. ($a = 20 \text{ \AA}$)

b) Geometries are optimized at PBE/ZORA/scalar level of theory.

For the tin(II) species (SnF_2 , $\text{Sn}(\text{CN})_2$, and $\text{Sn}(\text{OH})_2$), the calculated magnetic shieldings determined by the PBE/ZORA/scalar and PBE/GIPAW methods are quite similar, with the PBE/GIPAW approach yielding results that are more shielded by 26 - 58 ppm. On the other hand, the calculated magnetic shieldings of the tin(IV) species (SnF_4 , $\text{Sn}(\text{CH}_3)_4$, and SnH_4) are predicted by the PBE/GIPAW approach to be 362 - 460 ppm more shielded. Therefore, one should expect that the calculated magnetic

shieldings with the PBE/ZORA/scalar Hamiltonian and the PBE/GIPAW method deviate from one another for ^{119}Sn nuclei. Moreover, the difference in the calculated magnetic shieldings depends on the electronic structure of the system investigated.

6.3.2 The Performance of Hybrid DFT Methods for the Calculated ^{119}Sn Magnetic-Shielding Tensor

In section 6.2, it is shown that introducing exact exchange via hybrid functionals improves the predicted principal components for ^{207}Pb -containing solids. In this section, the performance of PBE0 functional (with 25% HF exchange) and ZORA/spin-orbit Hamiltonian is analyzed in a similar manner for the calculations of ^{119}Sn magnetic-shielding tensor.

In Figure 6.16, the correlation between the principal components of the calculated magnetic-shielding tensor at the PBE0/ZORA/spin-orbit level of theory and the principal components of the experimental chemical-shift tensor is displayed. The slope of the correlation line when all systems are considered is -1.03 ± 0.02 . On the other hand, there is less scatter about the best-fit line ($R^2 = 0.99$) than was obtained at the PBE/ZORA/spin-orbit level. In general, the calculated principal components obtained with the PBE0/ZORA/spin-orbit method are 100-200 ppm more shielded than the calculated principal components obtained with the PBE/ZORA/spin-orbit method. The predicted shielding of the reference compound is found to be 3003 ± 16 ppm, indicating a slightly more shielded value obtained at PBE0/ZORA/spin-orbit level of theory than at the PBE/ZORA/spin-orbit level.

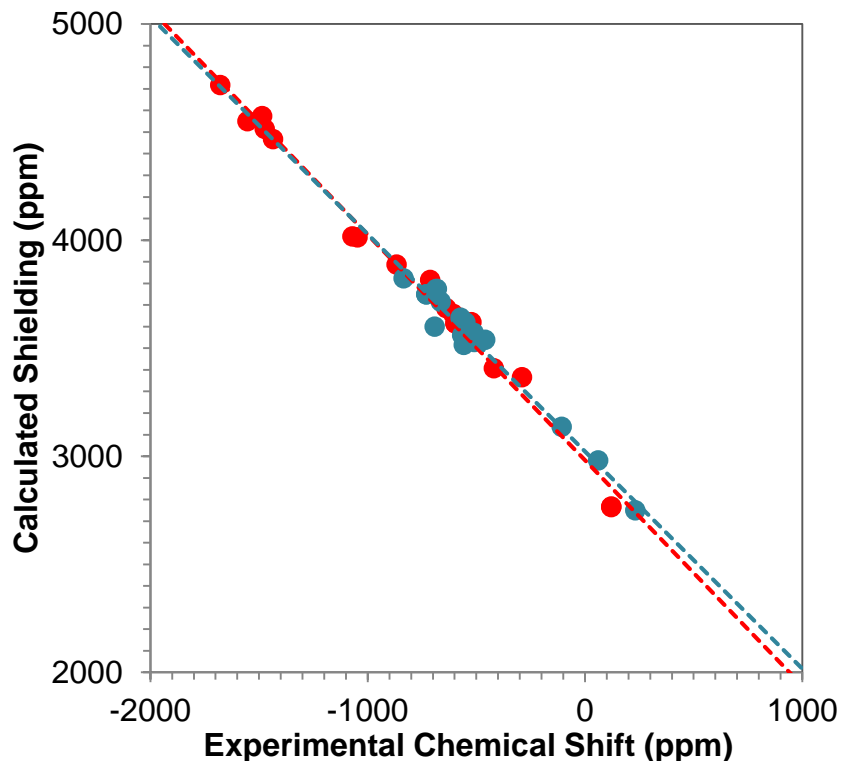


Figure 6.16 Correlation between calculated principal components of ^{119}Sn magnetic-shielding tensors and experimental ^{119}Sn chemical-shift tensors for twelve tin-containing solids. Calculations were performed at the PBE0/ZORA/spin-orbit level of theory. Sn(II) sites are shown in red; Sn(IV) sites are shown in blue.

In Table 6.9, the predicted principal components of the chemical-shift tensors at the PBE0/ZORA/spin-orbit level of theory and the experimental values are tabulated. For all tin-containing solids, the calculated residuals between theory and experiment are below 100 ppm and the largest residual (94 ppm) is seen for SnO. In general, the agreement between experiment and theory improves when PBE0 is employed instead of PBE. However, this improvement, for most of the cases, is quite small. As the NMR calculations employing hybrid functionals are considerably larger than for GGA functionals especially with a relativistic Hamiltonian, the latter may

remain the more cost effective option for the calculations of ^{119}Sn magnetic-shielding tensor in similar systems.

Table 6.9 Experimental and Calculated NMR Parameters of ^{119}Sn -Containing Solids using Model Clusters and PBE0/ZORA/Spin-Orbit Level of Theory.

Compounds	δ_{11} (ppm)	δ_{22} (ppm)	δ_{33} (ppm)	δ_{iso} (ppm)	Ω (ppm)	Residual (ppm)
Tin(II)-containing solids						
<u>SnO</u>	<u>121</u>	<u>121</u>	<u>-867</u>	<u>-208</u>	<u>988</u>	-
PBE0/ZORA/spin-orbit	236	236	-885	-138	1121	94
<u>SnHPO₄</u>	<u>-606</u>	<u>-712</u>	<u>-1553</u>	<u>-957</u>	<u>947</u>	-
PBE0/ZORA/spin-orbit	-657	-813	-1547	-1006	890	66
<u>SnHPO₃</u>	<u>-290</u>	<u>-420</u>	<u>-1435</u>	<u>-715</u>	<u>1145</u>	-
PBE0/ZORA/spin-orbit	-363	-404	-1465	-744	1102	46
<u>SnC₂O₄</u>	<u>-523</u>	<u>-639</u>	<u>-1474</u>	<u>-879</u>	<u>951</u>	-
PBE0/ZORA/spin-orbit	-618	-683	-1512	-938	894	65
<u>SnSO₄</u>	<u>-1047</u>	<u>-1070</u>	<u>-1679</u>	<u>-1265</u>	<u>632</u>	-
PBE0/ZORA/spin-orbit	-1011	-1015	-1715	-1247	704	43
<u>BaSnF₄</u>	<u>-596</u>	<u>-596</u>	<u>-1486</u>	<u>-893</u>	<u>890</u>	-
PBE0/ZORA/spin-orbit	-613	-613	-1571	-932	958	51
Tin(IV)-containing solids						
<u>SnO₂</u>	<u>-550</u>	<u>-573</u>	<u>-686</u>	<u>-603</u>	<u>136</u>	-
PBE0/ZORA/spin-orbit	-617	-639	-770	-675	153	73
<u>Ca₂SnO₄</u>	<u>-459</u>	<u>-512</u>	<u>-664</u>	<u>-545</u>	<u>205</u>	-
PBE0/ZORA/spin-orbit	-536	-569	-713	-606	177	62
<u>SnS₂</u>	<u>-730</u>	<u>-730</u>	<u>-835</u>	<u>-765</u>	<u>105</u>	-
PBE0/ZORA/spin-orbit	-747	-747	-821	-772	75	16

<u>Pb₂SnO₄</u>	<u>-558</u>	<u>-566</u>	<u>-692</u>	<u>-605</u>	<u>134</u>	-
PBE0/ZORA/spin-orbit	-513	-558	-597	-556	85	61
<u>Na₆Sn₂S₇</u>	<u>232</u>	<u>60</u>	<u>-107</u>	<u>62</u>	<u>339</u>	-
PBE0/ZORA/spin-orbit	252	21	-134	46	387	30
<u>Sr₂SnO₄</u>	<u>-510</u>	<u>-548</u>	<u>-681</u>	<u>-580</u>	<u>171</u>	-
PBE0/ZORA/spin-orbit	-526	-531	-772	-610	246	54

6.4 Effects of Relativistic Spin-Orbit Coupling and Hartree-Fock Exchange on Calculated Principal Components of Magnetic-Shielding Tensor for ¹²⁵Te Nuclei

The relativistic effects on the calculated NMR parameters of ¹²⁵Te nuclei have been investigated previously on the isolated ¹²⁵Te-containing molecules.[62-64] In these studies, authors claimed that the spin-orbit contributions to the **chemical shifts** are rather small, due to cancellation between different compounds when the chemical shifts are evaluated.[62-64] It should be noted that these conclusions were based on the correlations between experimental and calculated δ_{iso} of the ¹²⁵Te-containing molecules rather than the principal components. In the previous sections, it is shown that the similar arguments for the ¹¹⁹Sn or ²⁰⁷Pb magnetic-shielding tensors become rather obsolete when the principal components of the magnetic-shielding tensor are investigated instead of the isotropic value. Additionally, the spin-orbit contributions to the magnetic-shielding tensor can depend strongly on the coordination geometry and the oxidation state of the nuclei of interest. Here, a similar study involving ¹²⁵Te-containing solids is presented. In Table 6.10, the experimental SSNMR parameters [65-67] and crystallographic information [67-76] are given for the investigated ¹²⁵Te-containing solids.

Table 6.10 Experimental Crystallographic Data and ^{125}Te Chemical Shifts of Tellurium-Containing Materials.

Compounds	Space Group	Te C.N.	δ_{11} (ppm)	δ_{22} (ppm)	δ_{33} (ppm)	δ_{iso} (ppm)	Ω (ppm)
TeO_2	<i>P4₁2₁2</i>	4-6	2031	1558	736	1442	1295
Te(OH)_6 , site I	<i>P12₁/n1</i>	6	724	659	637	673	87
Te(OH)_6 , site II		6	733	653	613	666	120
TeCl_4 , site I	<i>C12/c1</i>	6	2114	2093	1454	1887	660
TeCl_4 , site II		6	2100	2057	1430	1862	670
Li_2TeO_3	<i>C12/c1</i>	3	1929	1888	1349	1722	580
Na_2TeO_3	<i>P12₁/a1</i>	3-4	2036	1971	1355	1787	681
Ag_2TeO_3	<i>P12₁/a1</i>	3-4	1873	1801	1300	1658	573
SnTe_3O_8	<i>Ia-3</i>	4-6	2164	1631	699	1498	1465
$\beta\text{-TeO}_2$	<i>Pbca</i>	5	2219	1716	710	1548	1509
MgTe_2O_5	<i>Pbcn</i>	4-5	2165	1949	927	1680	1238
(p-MeC ₆ H ₄) ₂ TeCl ₂ , site I	<i>P2₁/n</i>	4	1191	945	679	938	512
(p-MeC ₆ H ₄) ₂ TeCl ₂ , site II		4	1108	1004	743	952	365
{(CH ₃) ₂ SnTe} ₃ , site I	<i>I4₁/a</i>	2	-385	-652	-720	-586	335
{(CH ₃) ₂ SnTe} ₃ , site II		2	-348	-842	-973	-721	625

The computations involving ^{125}Te -containing solids were carried out with cluster models. PBE and PBE0 density functional and ZORA Hamiltonian were employed. The all-electron (AE) TZ2P basis set was employed for the NMR-active nucleus (^{125}Te) and the first coordination shell around the NMR-active nucleus, whereas the remainder of the cluster was treated with the smaller AE TZP basis set.

6.4.1 Relativistic Effects on Principal Components of ^{125}Te : ZORA/Scalar vs. ZORA/Spin-Orbit

In Figures 6.17 and 6.18, the correlations between the principal components of calculated magnetic-shielding tensors are displayed for PBE/ZORA/scalar and PBE/ZORA/spin-orbit level of theories. At PBE/ZORA/scalar level of theory, the correlation between experimental and calculated principal components of ^{125}Te magnetic-shielding tensors yields the following best-fit relation;

$$\sigma_{ii}^{ZORA/SC} = (-0.81 \pm 0.03) \delta_{ii}^{exp} + (2734 \pm 39) \text{ ppm}, R^2 = 0.954 \quad (6.1)$$

At PBE/ZORA/spin-orbit level, the best-fit relation is;

$$\sigma_{ii}^{ZORA/SO} = (-1.02 \pm 0.02) \delta_{ii}^{exp} + (3409 \pm 28) \text{ ppm}, R^2 = 0.985 \quad (6.2)$$

When only scalar effects are included in the ZORA Hamiltonian, the slope of the best-fit line deviates from the ideal case by 19%. The scatter around the correlation line is rather small compared to the correlations obtained for ^{207}Pb and ^{119}Sn -containing solids with ZORA/scalar Hamiltonian, as indicated by the R^2 value (0.954) of the fit. When both scalar and spin-orbit terms are included in ZORA Hamiltonian (ZORA/spin-orbit), the slope of the best-fit line deviates only 2% from the ideal case. Additionally, the scatter around the best-fit line is reduced at ZORA/spin-orbit level compared to ZORA/scalar case. These results show that the inclusion of spin-orbit effects is also important to obtain the best agreement between theory and experiment for ^{125}Te magnetic-shielding tensors.

From the intersection of the best-fit line, the absolute shielding of the reference compound, Me_2Te is predicted as 2734 and 3409 ppm at ZORA/scalar and ZORA/spin-orbit levels respectively. The absolute shielding of Me_2Te , when calculated from the isolated molecule, becomes 2515 ppm for ZORA/scalar and 3237

ppm for ZORA/spin-orbit. In both cases, the predicted absolute shielding becomes larger by ~700 ppm when spin-orbit effects are included in the ZORA Hamiltonian.

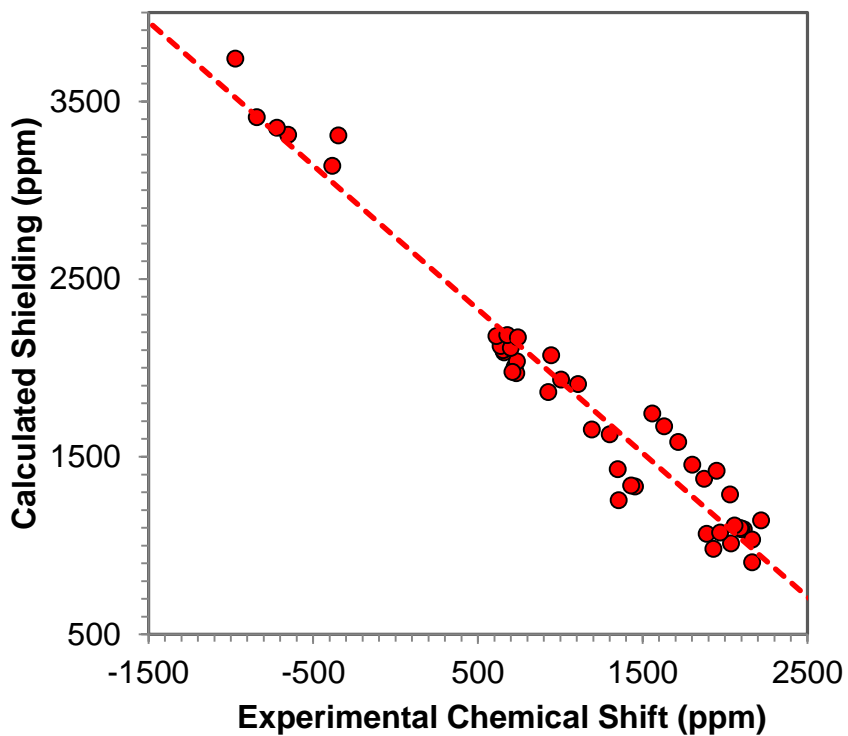


Figure 6.17 Correlations between calculated principal components of ^{125}Te magnetic-shielding tensors at PBE/ZORA/scalar level of theory and experimental ^{125}Te chemical-shift tensors for the tellurium-containing solids tabulated in Table 6.10. The dotted line represents the best-fit line.

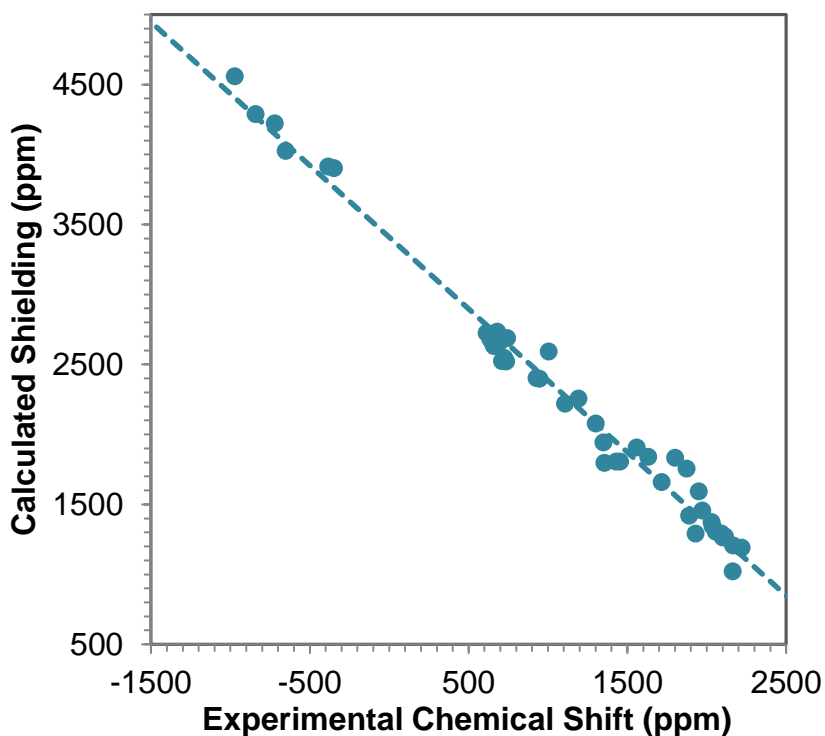


Figure 6.18 Correlations between calculated principal components of ^{125}Te magnetic-shielding tensors at PBE/ZORA/spin-orbit level of theory and experimental ^{125}Te chemical-shift tensors for the tellurium-containing solids. The dotted line represents the best-fit line.

In the previous sections, it is shown that the spin-orbit effects on the principal components depend strongly on the coordination geometry and the oxidation state of the NMR nuclei. In Figure 6.19, the differences between the principal components of ^{125}Te magnetic-shielding tensor calculated with the ZORA/spin-orbit Hamiltonian and the principal components calculated with the ZORA/scalar Hamiltonian are displayed for some selected ^{125}Te -containing solids. As seen from Figure 6.19, the spin-orbit effects on ^{125}Te magnetic-shielding tensors also show a strong dependence on oxidation state and coordination chemistry as well.

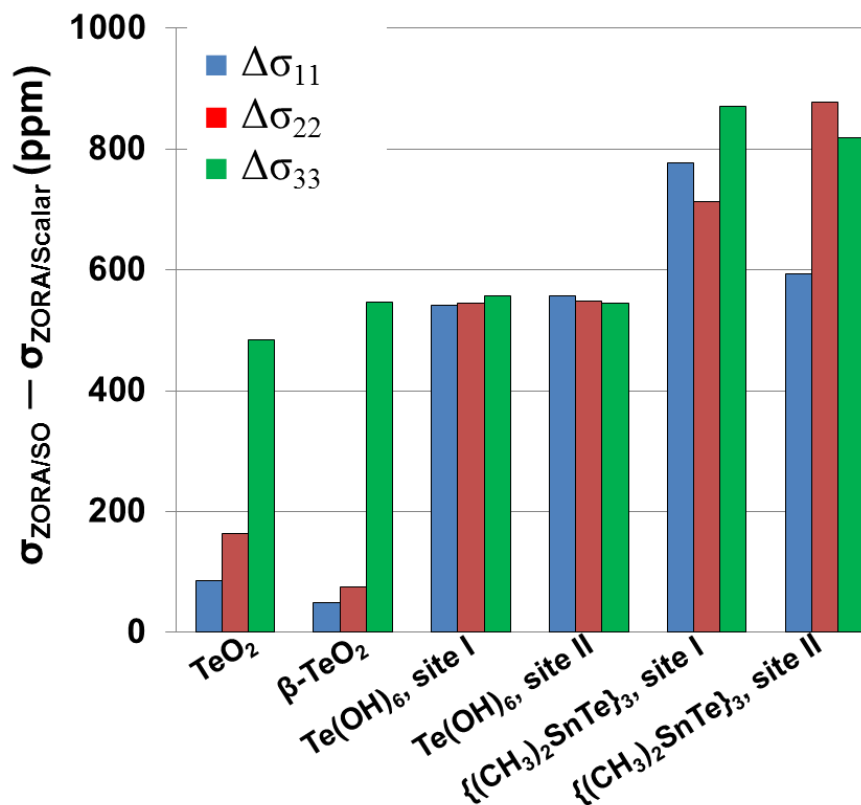


Figure 6.19 The differences ($\Delta\sigma_{ii}$) in principal components of ^{125}Te magnetic-shielding tensors calculated with the ZORA/spin-orbit method and the ZORA/scalar method. All calculations modeled the solid-state environment with the cluster-based VMTA/BV approach. Magnetic-shielding calculations used the PBE functional.

For TeO₂ and β-TeO₂ (tellurium is in +4 oxidation state), the contribution of spin-orbit effects on magnetic shielding is largest for the σ_{33} component (~500 ppm) whereas the spin-orbit effects for σ_{11} and σ_{22} range between 49 - 164 ppm. The spin-orbit contribution to principal components for TeO₂ and β-TeO₂ shows a similar variation which was seen for hemi-directed lead(II) and tin(II) compounds.

Te(OH)₆ has two inequivalent tellurium(VI) sites in its crystal structure. Both sites exhibit holodirected coordination geometry. The spin-orbit contribution on each principal component of ¹²⁵Te magnetic-shielding tensor in Te(OH)₆ shows very little variation with $\Delta\sigma_{ii}$ ranging between 541-557 ppm.

Among all the investigated ¹²⁵Te-containing solids, the largest spin-orbit contributions are observed for the ¹²⁵Te sites in {(CH₃)₂SnTe}₃. The calculated $\Delta\sigma_{ii}$ ranges between 593-871 ppm. In this system, the oxidation state of the tellurium is -2 and each tellurium site is bonded to two tin atoms. The large spin-orbit contributions are probably the result of both oxidation state of tellurium and HAHA relativistic effects between tin and tellurium.

6.4.2 The Performance of Hybrid DFT Methods for the Calculated ¹²⁵Te Magnetic-Shielding Tensor

In Figure 6.20, the correlation between experimental and calculated principal components at PBE0/ZORA/spin-orbit level of theory is shown for the ¹²⁵Te-containing solids. The following best-fit relation is obtained from the correlation;

$$\sigma_{ii}^{PBE0/ZORA/SO} = (-1.10 \pm 0.02) \delta_{ii}^{exp} + (3656 \pm 23) \text{ ppm}, R^2 = 0.991 \quad (6.3)$$

The slope of the correlation obtained with PBE0 functional shows an increasing deviation from the ideal case compared to the slope obtained with PBE functional. On the other hand, there is less scatter around the best-fit line and the R² value of the fit is larger than 0.99. The calculated principal components with PBE0 are more shielded than those calculated with PBE for all ¹²⁵Te-containing solids except Ag₂TeO₃. The predicted absolute shielding of the Me₂Te, in the PBE0 case, is 3656 ppm (Eq. 6.3), which is 247 ppm more shielded compared to the absolute shielding obtained with the PBE functional. Overall, the quality of the linear fit with PBE0

improves slightly compared to the PBE case, a similar result obtained for the ^{119}Sn magnetic-shielding tensors.

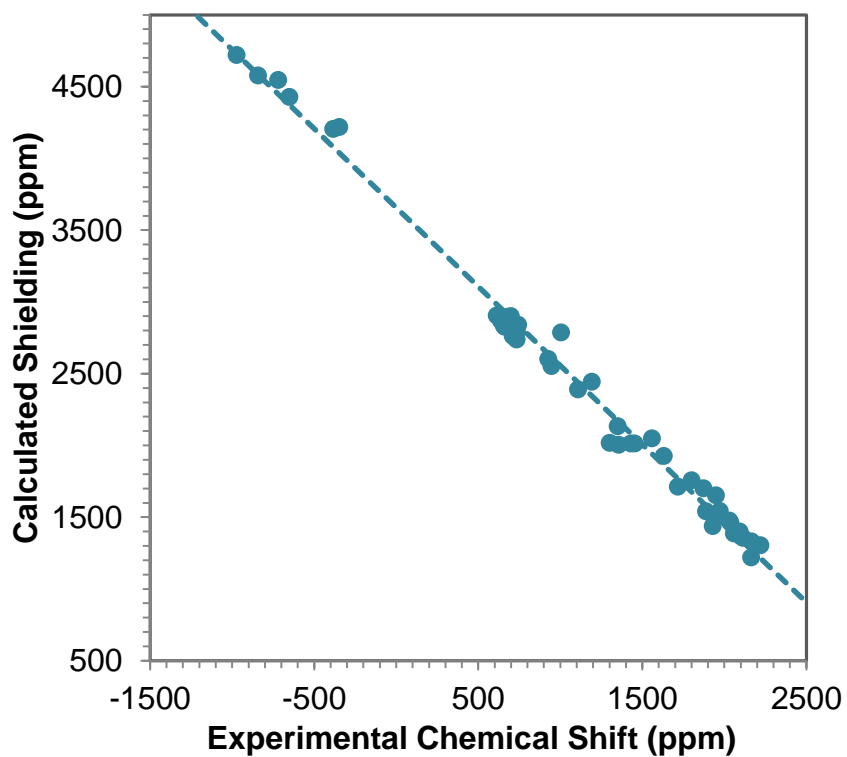


Figure 6.20 Correlation between calculated principal components of ^{125}Te magnetic-shielding tensors at PBE0/ZORA/spin-orbit level of theory and experimental ^{125}Te chemical-shift tensors for the tellurium-containing solids. The dotted line represents the best-fit line.

REFERENCES

1. Claudio, E.S., H.A. Godwin, and J.S. Magyar, *Fundamental coordination chemistry, environmental chemistry, and biochemistry of lead(II)*. Progress in Inorganic Chemistry, Vol 51. Vol. 51. 2003. 1-144.
2. Harrison, P.G., *Orgaometallic Compounds of Germanium, Tin, and Lead*. 1985, London: Chapman and Hall.
3. Wells, A.F., *Structural Inorganic Chemistry*. 5th ed. 1984, Oxford: Oxford University Press.
4. Shimoni-Livny, L., J.P. Glusker, and C.W. Bock, *Lone pair functionality in divalent lead compounds*. Inorganic Chemistry, 1998. **37**(8): p. 1853-1867.
5. Keppler, U., *Structure of Low-Temperature Form of Lead Phosphate $Pb_3(Po_4)_2$* . Zeitschrift Fur Kristallographie Kristallgeometrie Kristallphysik Kristallchemie, 1970. **132**(3): p. 228-235.
6. Gavarrri, J.R. and D. Weigel, *Lead Oxides .I. Crystal-Structure of PbO_4 Minimum at Ambient Temperature (293 K)*. Journal of Solid State Chemistry, 1975. **13**(3): p. 252-257.
7. Schurmann, M. and F. Huber, *A Redetermination of Lead(IV) Acetate*. Acta Crystallographica Section C-Crystal Structure Communications, 1994. **50**: p. 1710-1713.
8. Prout, K., et al., *Tetrakis(o-benzoylbenzoato-O,O')lead(IV) dichloromethane solvate*. Acta Crystallographica Section C-Crystal Structure Communications, 1996. **52**: p. 351-354.
9. Antao, S.M. and I. Hassan, *The orthorhombic structure of $CaCO_3$, $SrCO_3$, $PbCO_3$ AND $BaCO_3$:linear structural trends*. Canadian Mineralogist, 2009. **47**(5): p. 1245-1255.
10. Teichert, A. and H. Mullerbuschbaum, *On the Crystal-Structure of Ca_2PbO_4* . Zeitschrift Fur Anorganische Und Allgemeine Chemie, 1992. **607**(1): p. 128-130.
11. Leciejewicz, J., *On Crystal Structure of Tetragonal (Red) PbO* . Acta Crystallographica, 1961. **14**(12): p. 1304.
12. Boucher, M.L. and D.R. Peacor, *Crystal Structure of Alamosite $PbSiO_3$* . Zeitschrift Fur Kristallographie Kristallgeometrie Kristallphysik Kristallchemie, 1968. **126**(1-3): p. 98-111.
13. Gavarrri, J.R., et al., *Structure of $SnPb_2O_4$ at 4 Temperatures - the Relation between Thermal-Expansion and Thermal Agitation*. Journal of Solid State Chemistry, 1981. **36**(1): p. 81-90.

14. Lutz, H.D., et al., *Neutron and x-ray structure determination of laurionite-type $Pb\{O(H,D)\}X$, with $X=Cl, Br$, and I , hydrogen bonds to lead(II) ions as a hydrogen-bond acceptor.* Journal of Solid State Chemistry, 1996. **124**(1): p. 155-161.
15. Catalano, J., et al., *Coordination geometry of lead carboxylates - spectroscopic and crystallographic evidence.* Dalton Transactions, 2015. **44**(5): p. 2340-2347.
16. MacKenzie, K.J.D. and M.E. Smith, *Multinuclear Solid-State NMR of Inorganic Materials.* Pergamon Materials Series ed. R.W. Cahn. 2002, Amsterdam: Pergamon.
17. Neue, G., et al., *Determination of $Pb-207(2+)$ chemical shift tensors from precise powder lineshape analysis.* Solid State Nuclear Magnetic Resonance, 1996. **6**(3): p. 241-250.
18. Fayon, F., et al., *Empirical correlations between $Pb-207$ NMR chemical shifts and structure in solids.* Journal of the American Chemical Society, 1997. **119**(29): p. 6837-6843.
19. Zhao, P.D., et al., *Lead-207 NMR spectroscopic study of lead-based electronic materials and related lead oxides.* Journal of Physical Chemistry B, 1999. **103**(48): p. 10617-10626.
20. Gabuda, S.P., et al., *$Pb-207$ NMR of minium, Pb_3O_4 : evidence for the $[Pb-2](4+)$ ion and possible relativistic effects in the $Pb-Pb$ bond.* Solid State Nuclear Magnetic Resonance, 1999. **15**(2): p. 103-107.
21. Buston, J.E.H., et al., *$Pb-207$ NMR chemical shifts of lead tetracarboxylates.* Magnetic Resonance in Chemistry, 2001. **39**(2): p. 68-76.
22. Buston, J.E.H., et al., *Structural investigations of a lead(IV) tetraacetate-pyridine complex.* Dalton Transactions, 2005(19): p. 3195-3203.
23. Van Bramer, S.E., et al., *Solid-state $Pb-207$ NMR studies of lead-group 16 and mixed transition-metal/lead-group 16 element-containing materials.* Magnetic Resonance in Chemistry, 2006. **44**(3): p. 357-365.
24. Garnier, P., J. Moreau, and J.R. Gavarrri, *Rietveld Analysis of the Structure of $Pb(1-X)Ti(X)O(1+X)$ by Neutron-Diffraction.* Materials Research Bulletin, 1990. **25**(8): p. 979-986.
25. Sebald, A. and R.K. Harris, *$Pb-207$ Cp Mas Nmr-Study of Hexaorganoyldiplumbanes.* Organometallics, 1990. **9**(7): p. 2096-2100.
26. Gabuda, S.P., et al., *$Pb-207$ NMR study of novel $Pb-Pb$ chemical bonding in lead monoxides, $\alpha-PbO$ and $\beta-PbO$.* Chemical Physics Letters, 1999. **305**(5-6): p. 353-358.
27. Mitchell, M.R., et al., *$Sn-119$ MAS NMR and first-principles calculations for the investigation of disorder in stannate pyrochlores.* Physical Chemistry Chemical Physics, 2011. **13**(2): p. 488-497.
28. Krykunov, M., T. Ziegler, and E. van Lenthe, *Implementation of a Hybrid DFT Method for Calculating NMR Shieldings Using Slater-Type Orbitals with Spin-Orbital Coupling Included. Applications to (OS)-O-187, Pt-195, and C-13 in*

- Heavy-Metal Complexes*. Journal of Physical Chemistry A, 2009. **113**(43): p. 11495-11500.
29. Krykunov, M., T. Ziegler, and E. Van Lenthe, *Hybrid Density Functional Calculations of Nuclear Magnetic Shieldings Using Slater-Type Orbitals and the Zeroth-Order Regular Approximation*. International Journal of Quantum Chemistry, 2009. **109**(8): p. 1676-1683.
 30. Aquino, F., N. Govind, and J. Autschbach, *Scalar Relativistic Computations of Nuclear Magnetic Shielding and g-Shifts with the Zeroth-Order Regular Approximation and Range-Separated Hybrid Density Functionals*. Journal of Chemical Theory and Computation. **7**(10): p. 3278-3292.
 31. Hrobarik, P., et al., *Giant Spin-Orbit Effects on NMR Shifts in Diamagnetic Actinide Complexes: Guiding the Search of Uranium(VI) Hydride Complexes in the Correct Spectral Range*. Angewandte Chemie-International Edition. **51**(43): p. 10884-10888.
 32. Saielli, G., R. Bini, and A. Bagno, *Computational F-19 NMR. 1. General features*. Theoretical Chemistry Accounts. **131**(3): p. 11.
 33. Holmes, S.T., et al., *Density functional investigation of intermolecular effects on C-13 NMR chemical-shielding tensors modeled with molecular clusters*. Journal of Chemical Physics, 2014. **141**(16): p. 164121.
 34. Burt, J., W. Levason, and G. Reid, *Coordination chemistry of the main group elements with phosphine, arsine and stibine ligands*. Coordination Chemistry Reviews. **260**: p. 65-115.
 35. Pannetier, J. and G. Denes, *Tin(II) Oxide - Structure Refinement and Thermal-Expansion*. Acta Crystallographica Section B-Structural Science, 1980. **36**(NOV): p. 2763-2765.
 36. Ahmad, M.M., Y. Yamane, and K. Yamada, *Structure, ionic conduction, and giant dielectric properties of mechanochemically synthesized BaSnF4*. Journal of Applied Physics, 2009. **106**(7).
 37. Donaldso.Jd and D.C. Puxley, *Crystal-Structure of Tin(II) Sulfate*. Acta Crystallographica Section B-Structural Crystallography and Crystal Chemistry, 1972. **B 28**(MAR15): p. 864.
 38. McDonald, R.C. and K. Eriks, *Crystallographic Studies of Tin(II) Compounds .2. Structures of Tin(II) Hydrogen Phosphate and Tin(II) Phosphite, Snhpo4 and Snhpo3*. Inorganic Chemistry, 1980. **19**(5): p. 1237-1241.
 39. Gleizes, A. and J. Galy, *Coordination Polyhedron of Tin(II) in Snc2o4 - Structural Relationships between Snc2o4, Na2c2o4 and Na2sn(C2o4)2*. Journal of Solid State Chemistry, 1979. **30**(1): p. 23-33.
 40. Cossement, C., et al., *Chemical-Shift Anisotropy and Indirect Coupling in Sno2 and Sno*. Magnetic Resonance in Chemistry, 1992. **30**(3): p. 263-270.
 41. Wrackmeyer, B., *Application of ¹¹⁹Sn NMR parameters*. Annu. Rep. NMR Spectroscopy, 1999. **38**: p. 203-264.
 42. Amornsakchai, P., et al., *Solid-state NMR studies of some tin(II) compounds*. Solid State Nuclear Magnetic Resonance, 2004. **26**(3-4): p. 160-171.

43. Baur, W.H., *Über Die Verfeinerung Der Kristallstrukturbestimmung Einiger Vertreter Des Rutiltyps - TiO_2 , SnO_2 , GeO_2 Und MgF_2* . Acta Crystallographica, 1956. **9**(5): p. 515-520.
44. Jumas, J.C., et al., *Structural Investigation of Thiocompounds with Anionic Groups of Pyro Type, $\text{Na}_6\text{X}_2\text{S}_7$ ($\text{X}=\text{Ge}, \text{Sn}$) and $\text{Ba}_3\text{Sn}_2\text{S}_7$* . Revue De Chimie Minerale, 1974. **11**(1): p. 13-26.
45. Yamane, H., et al., *Preparation, crystal structure, and photoluminescence of $\text{Ca}_2\text{SnO}_4:\text{Eu}^{3+}$, Y^{3+}* . Journal of Solid State Chemistry, 2008. **181**(10): p. 2559-2564.
46. Fu, W.T., D. Visser, and D.J.W. Ijdo, *High-resolution neutron powder diffraction study on the structure of Sr_2SnO_4* . Journal of Solid State Chemistry, 2002. **169**(2): p. 208-213.
47. Hazen, R.M. and L.W. Finger, *Crystal-Structures and Compressibilities of Layer Minerals at High-Pressure .1. SnS_2 , Berndtite*. American Mineralogist, 1978. **63**(3-4): p. 289-292.
48. Catalano, J., et al., *Pb-207 and Sn-119 Solid-State NMR and Relativistic Density Functional Theory Studies of the Historic Pigment Lead-Tin Yellow Type I and Its Reactivity in Oil Paintings*. Journal of Physical Chemistry A, 2014. **118**(36): p. 7952-7958.
49. Clayden, N.J., C.M. Dobson, and A. Fern, *High-Resolution Solid-State Sn-119 Nuclear Magnetic-Resonance Spectroscopy of Ternary Tin Oxides*. Journal of the Chemical Society-Dalton Transactions, 1989(5): p. 843-847.
50. MacGregor, A.W., L.A. O'Dell, and R.W. Schurko, *New methods for the acquisition of ultra-wideline solid-state NMR spectra of spin-1/2 nuclides*. Journal of Magnetic Resonance, 2011. **208**(1): p. 103-113.
51. Mundus, C., et al., *A Sn-119 solid-state nuclear magnetic resonance study of crystalline tin sulphides*. Solid State Nuclear Magnetic Resonance, 1996. **7**(2): p. 141-146.
52. Pietrass, T. and F. Taulelle, *Sn-119 solid-state NMR of tin sulfides. Evidence of polytypism in SnS_2* . Magnetic Resonance in Chemistry, 1997. **35**(6): p. 363-366.
53. Pickard, C.J. and F. Mauri, *All-electron magnetic response with pseudopotentials: NMR chemical shifts*. Physical Review B, 2001. **63**(24): p. 13.
54. Clark, S.J., et al., *First principles methods using CASTEP*. Z. Kristallogr., 2005. **220**(5-6): p. 567-570.
55. Yates, J.R., C.J. Pickard, and F. Mauri, *Calculation of NMR chemical shifts for extended systems using ultrasoft pseudopotentials*. Physical Review B, 2007. **76**(2).
56. Bagno, A., G. Casella, and G. Saielli, *Relativistic DFT calculation of Sn-119 chemical shifts and coupling constants in tin compounds*. Journal of Chemical Theory and Computation, 2006. **2**(1): p. 37-46.

57. Malkin, E., et al., *The Absolute Shielding Constants of Heavy Nuclei: Resolving the Enigma of the Sn-119 Absolute Shielding*. Journal of Physical Chemistry Letters. **4**(3): p. 459-463.
58. Yates, J.R., et al., *Relativistic nuclear magnetic resonance chemical shifts of heavy nuclei with pseudopotentials and the zeroth-order regular approximation*. J. Chem. Phys., 2003. **118**(13): p. 5746-5753.
59. Sadoc, A., et al., *NMR parameters in alkali, alkaline earth and rare earth fluorides from first principle calculations*. Phys. Chem. Chem. Phys., 2011. **13**(41): p. 18539-18550.
60. Holmes, S.T., et al., *Density functional investigation of intermolecular effects on ¹³C NMR chemical-shielding tensors modeled with molecular clusters*. J. Chem. Phys., 2014. **141**(16): p. 164121.
61. Holmes, S.T., et al., *Critical Analysis of Cluster Models and Exchange-Correlation Functionals for Calculating Magnetic Shielding in Molecular Solids*. Journal of Chemical Theory and Computation, 2015. **11**(11): p. 5229-5241.
62. Hada, M., et al., *Quasirelativistic study of Te-125 nuclear magnetic shielding constants and chemical shifts*. Journal of Computational Chemistry, 2001. **22**(13): p. 1502-1508.
63. Kaupp, M., M. Buhl, and V.G. Malkin, *Calculation of NMR and EPR Parameters: Theory and Applications*. 2004, Weinheim: WILEY-VCH Verlag GmbH & Co. KGaA.
64. Fukuda, R. and H. Nakatsuji, *Quasirelativistic theory for the magnetic shielding constant. III. Quasirelativistic second-order Moller-Plesset perturbation theory and its application to tellurium compounds*. Journal of Chemical Physics, 2005. **123**(4).
65. Gay, I.D., C.H.W. Jones, and R.D. Sharma, *A Multinuclear Solid-State Nmr-Study of the Dimethyltin Chalcogenides ((Ch3)2sns)3, ((Ch3)2snse)3, ((Ch3)2snste)3*. Journal of Magnetic Resonance, 1989. **84**(3): p. 501-514.
66. Sakida, S., S. Hayakawa, and T. Yoko, *Part I. Te-125 NMR study of tellurite crystals*. Journal of Non-Crystalline Solids, 1999. **243**(1): p. 1-12.
67. Beckmann, J., et al., *Secondary bonding in para-substituted diphenyltellurium dichlorides (p-XC6H4)(2)TeCl2 (X = H, Me, MeO) probed by Te-125 MAS NMR spectroscopy. Crystal and molecular structure of (p-MeC6H4)(2)TeCl2*. Journal of Organometallic Chemistry, 2003. **669**(1-2): p. 149-153.
68. Beyer, H., *Verfeinerung Der Kristallstruktur Von Tellurit Dem Rhombischen Teo2*. Zeitschrift Fur Kristallographie Kristallgeometrie Kristallphysik Kristallchemie, 1967. **124**(3): p. 228.
69. Lindqvist, O., *Refinement of Structure of Alpha-Teo2*. Acta Chemica Scandinavica, 1968. **22**(3): p. 977.
70. Buss, B. and B. Krebs, *Crystal Structure of Tellurium Tetrachloride*. Inorganic Chemistry, 1971. **10**(12): p. 2795.

71. Meunier, G. and J. Galy, *Hitherto Unknown Deformation of Fluorine-Type Lattice - Crystal Structure of Phases Mte_{308} ($M=Ti, Sn, Hf, Zr$)*. Acta Crystallographica Section B-Structural Crystallography and Crystal Chemistry, 1971. **B 27**(MAR): p. 602.
72. Lindqvist, O. and M.S. Lehmann, *Neutron-Diffraction Refinement of Crystal-Structure of Telluric Acid, $Te(OH)_6$ (Mon)*. Acta Chemica Scandinavica, 1973. **27**(1): p. 85-95.
73. Folger, F., *Crystal-Structure of Li_2TeO_3* . Zeitschrift Fur Anorganische Und Allgemeine Chemie, 1975. **411**(2): p. 103-110.
74. Masse, R., J.C. Guitel, and I. Tordjman, *Chemical Preparation and Crystalline-Structure of Sodium and Silver Tellurides - Na_2TeO_3, Ag_2TeO_3* . Materials Research Bulletin, 1980. **15**(4): p. 431-436.
75. Batchelor, R.J., F.W.B. Einstein, and C.H.W. Jones, *2 Crystal Modifications of Hexamethylcyclotristannatellurane*. Acta Crystallographica Section C-Crystal Structure Communications, 1989. **45**: p. 1813-1815.
76. Weil, M., *Redetermination of $MgTe_2O_5$* . Acta Crystallographica Section E-Structure Reports Online, 2005. **61**: p. I237-I239.

Chapter 7

CONCLUSION

This dissertation provides a route for accurate prediction of magnetic-shielding tensors of heavy nuclei-containing solids, by employing the cluster approximation for extended systems, relativistic density functional theory (DFT). The performance of cluster models with differing charge, symmetry and size have been examined. Calculations at different level of theory (from periodic-boundary calculations to cluster calculations, from including relativistic properties to neglecting them, from using the frozen-core approximation to the use of all-electron basis sets, and from simple GGA functionals to hybrid functionals) have established a hierarchy of quantum chemical methods for accurate predictions of the magnetic-shielding tensor.

Perhaps the most important result of this dissertation is that it is possible to calculate the magnetic-shielding tensor accurately for nuclei in extended systems using model clusters that represent only a certain region of a solid. From Ramsey's expression for the magnetic-shielding tensor,[1] it is evident that the main contributions are determined by the form of the electronic wave function in a rather small region around NMR nuclei, as a result of the $1/r^3$ dependency in the sum-over-states formula. The results show that one can describe the wave function over that region with good accuracy by using properly built cluster models. The methods presented in this study have only been applied to calculations of magnetic-shielding tensors; however, they may be appropriate for calculation of other NMR observables such as EFG tensors or spin-spin couplings.

It is important to take the nature of the solid into account when modelling extended systems using cluster models. For molecular solids, the task is relatively easy because it is possible to build a cluster with proper symmetry and free of dangling bonds or excess charge. In chapter 4, it is shown that calculated principal components converge smoothly to the experimental values for such systems with increasing cluster size.

For ionic or covalent network solids, one must deal appropriately with termination of the cluster to obtain a reasonable SCF solution to the many-body equation. For solid systems which evince large variations in bond lengths in the structure, modification of terminal-atom nuclear charge by a bond valence model, VMTA/BV, allows one to obtain meaningful SCF solutions for clusters representing a network solid.

Another important result from this study is that the ZORA Hamiltonian, an approximation of the four-component (4c) Dirac Hamiltonian, works quite well for the predictions of **chemical-shift tensors** of heavy nuclei (^{199}Hg , ^{207}Pb , ^{119}Sn and ^{125}Te). On the other hand, the calculated **absolute shieldings** deviate from the results obtained from 4c relativistic DFT computations, which shows that the ZORA approximation can produce large errors for the contributions from the core levels.[2-5]

For all the heavy nuclei investigated, the inclusion of **spin-orbit** terms in the ZORA Hamiltonian is essential to get magnetic shieldings that reflect the experimental chemical-shift data. One may get qualitative agreement in some cases by employing the ZORA Hamiltonian with only scalar relativistic terms, but for the highest accuracy, the spin-orbit components in the Hamiltonian must be included.

Spin-orbit effects are strongly dependent on the atomic number of the NMR nucleus. For ^{199}Hg and ^{207}Pb , the spin-orbit contributions to isotropic shielding are generally a few thousand ppm, whereas for ^{125}Te and ^{119}Sn , the spin-orbit contributions range between 300-800 ppm.

In chapter 4, the comparison of results on small clusters (often a single isolated unit) with large clusters demonstrates that, to predict the NMR magnetic shielding accurately, one must take into account the effects of the surrounding environment, and specifically one must treat the problem with a large cluster that maintains the point symmetry at the site of the nucleus of interest. In some cases, the isotropic shift may be fortuitously predicted for an isolated unit, but the tensor components may be in substantial error. The cluster model must be chosen so that the local site symmetry at the nucleus of interest is maintained, which determines the minimal size of the cluster.

Of concern in calculation of magnetic shielding in these heavy-nuclei-containing materials is the computation time that a large-cluster model may require. I examined the use of the frozen-core approximation (FCA) for atomic centers removed from the locality of the nucleus of interest as a means to shorten this calculation time. The calculations show that using the FCA on more remote centers makes a minimal difference in computed NMR parameters, compared to calculations with models using the full all-electron basis set. The use of the FCA for these more remote centers presents a substantial savings in computational time when compared with the all-electron approach, and I suggest that using the FCA in this manner for computation of NMR parameters may allow one to specify the environment with larger clusters that better define the effects of structure, without sacrificing much accuracy.

In chapter 5, test calculations on various clusters demonstrate that the predicted principal components of the magnetic-shielding tensor are not dependent on the termination scheme when a cluster containing atoms through the fifth coordination shell is employed. For all termination schemes, the agreement between experiment and calculation improves as larger clusters are employed. Most errors due to truncation of the structure are sufficiently minimized if one uses clusters terminated at the third coordination shell or higher. Including only the first coordination sphere in a cluster is usually not sufficient to account for longer-range effects.

Calculations of ^{29}Si and ^{31}P magnetic-shielding constants in network solids obtained using the cluster model with VMTA/BV are compared to values obtained using the GIPAW approach, which treats the materials with periodic boundary conditions. The cluster-based calculations lead to a modest increase in accuracy for relative chemical-shift parameters over those obtained by the GIPAW approach. Furthermore, the cluster-based calculations lead to a significant increase in accuracy for absolute magnetic-shielding parameters. Additionally, use of the hybrid functional PBE0 improves upon the GGA-PBE functional for calculations of the principal components of magnetic-shielding tensors of both ^{29}Si and ^{31}P sites. The extrapolated shieldings of the reference compounds are predicted to be more shielded when using the PBE0 functional than is observed for the pure DFT functionals.

In chapter 6, ^{207}Pb , ^{119}Sn and ^{125}Te magnetic-shielding tensors have been calculated for materials containing NMR nuclei in different coordination geometries and oxidation states. At the ZORA/scalar relativistic level of theory, there is a significant inconsistency in correlations of ^{207}Pb and ^{119}Sn magnetic-shielding and chemical-shift principal components for the set of various chemical environments I

considered. The scatter for the total set of lead and tin compounds is large, and the predicted correlation is far from the ideal case. When spin-orbit (SO) effects are included in the ZORA Hamiltonian, the correlation between theory and experiment is significantly improved. The correlation parameters for both hemidirected and holodirected sites are quite similar, unlike the situation for the ZORA/scalar relativistic case. In the case of hemidirected sites with an oxidation state of +2, the poor performance of the ZORA/scalar relativistic Hamiltonian is largely the result of underestimation of σ_{33} , the component that corresponds to the situation that the axis of the stereochemically active lone-pair orbital points along the magnetic field.

For holodirected systems, the neglect of spin-orbit effects yields quite large differences, but the differences are similar for all three components. The spin-orbit effects on principal components show a similar dependence on oxidation state and coordination geometry for ^{125}Te -containing solids, as well.

As seen by calculations with the hybrid functional, there is a significant effect of inclusion of Hartree-Fock (HF) exchange for ^{207}Pb nuclei than is usually done. The results demonstrate that employing hybrid functionals for ^{207}Pb shielding calculations yields better agreement with experiment for both holodirected and hemidirected lead-containing systems. There is a strong dependence of the magnitude of the principal components on the amount of HF exchange introduced in the calculation. Its effect is particularly noticeable on the span. The results suggest that one should include more HF exchange in the functional than the default value of 20%, to have calculated principal components agree more closely with experiment.

The agreement between calculated and experimental principal components of the magnetic-shielding tensor is improved further by the use of hybrid functionals for

^{119}Sn and ^{125}Te nuclei, as well. However, the improvement is relatively small in these cases, which suggest that the GGA functionals may remain the most cost-effective choice for calculations of ^{119}Sn and ^{125}Te magnetic-shielding tensors in similar systems.

REFERENCES

1. Ramsey, N.F., *Magnetic Shielding of Nuclei in Molecules*. Physical Review, 1950. **78**(6): p. 699-703.
2. Autschbach, J., *The accuracy of hyperfine integrals in relativistic NMR computations based on the zeroth-order regular approximation*. Theoretical Chemistry Accounts, 2004. **112**(1): p. 52-57.
3. Roukala, J., et al., *Relativistic effects on group-12 metal nuclear shieldings*. Physical Chemistry Chemical Physics, 2011. **13**(47): p. 21016-21025.
4. Wodynski, A., M. Repisky, and M. Pecul, *A comparison of two-component and four-component approaches for calculations of spin-spin coupling constants and NMR shielding constants of transition metal cyanides*. Journal of Chemical Physics, 2012. **137**(1): p. 11.
5. Autschbach, J., *Relativistic calculations of magnetic resonance parameters: background and some recent developments*. Philosophical Transactions of the Royal Society a-Mathematical Physical and Engineering Sciences, 2014. **372**(2011): p. 20120489.

Appendix A

CARTESIAN COORDINATES USED IN CLUSTER MODELS

Small Cluster of Hg₂Cl₂

Hg	4.13000000	-2.75300000	1.72500000
Cl	9.08000000	-2.85700000	1.73900000
Hg	6.65600000	-2.80600000	1.73300000
Cl	1.70600000	-2.70200000	1.71900000

Large Cluster of Hg₂Cl₂

Cl	25.16300000	-0.14200000	6.12700000
Cl	24.95800000	8.75800000	7.17700000
Cl	25.34600000	4.83900000	2.21100000
Cl	24.77400000	3.77700000	11.09300000
Cl	25.06000000	4.30800000	6.65200000
Cl	30.69700000	2.43200000	4.52900000
Cl	19.81200000	2.26500000	3.80800000
Cl	30.41100000	1.90100000	8.97100000
Cl	19.52600000	1.73400000	8.25000000
Cl	30.59500000	6.88200000	5.05400000
Cl	19.71000000	6.71500000	4.33400000
Cl	30.30900000	6.35100000	9.49600000
Cl	19.42400000	6.18500000	8.77500000
Cl	17.80500000	-0.25400000	5.64000000
Cl	17.59900000	8.64600000	6.69000000
Cl	17.98800000	4.72600000	1.72300000
Cl	17.41600000	3.66500000	10.60600000
Cl	17.70200000	4.19600000	6.16500000
Cl	23.33900000	2.31900000	4.04200000
Cl	12.45400000	2.15300000	3.32100000
Cl	23.05300000	1.78800000	8.48300000
Cl	12.16800000	1.62200000	7.76200000
Cl	23.23600000	6.76900000	4.56700000
Cl	12.35100000	6.60300000	3.84600000
Cl	22.95000000	6.23800000	9.00900000
Cl	12.06500000	6.07200000	8.28800000

Hg	22.74400000	-0.17900000	5.96700000
Hg	22.53900000	8.72100000	7.01700000
Hg	22.92800000	4.80200000	2.05000000
Hg	22.35500000	3.74000000	10.93300000
Hg	22.64100000	4.27100000	6.49200000
Hg	28.27800000	2.39500000	4.36900000
Hg	17.39300000	2.22800000	3.64800000
Hg	27.99200000	1.86400000	8.81000000
Hg	17.10700000	1.69800000	8.09000000
Hg	28.17600000	6.84500000	4.89400000
Hg	17.29100000	6.67800000	4.17300000
Hg	27.89000000	6.31400000	9.33600000
Hg	17.00500000	6.14800000	8.61500000
Hg	20.22400000	-0.21700000	5.80000000
Hg	20.01800000	8.68300000	6.85000000
Hg	20.40700000	4.76300000	1.88400000
Hg	19.83500000	3.70200000	10.76600000
Hg	20.12100000	4.23300000	6.32500000
Hg	25.75800000	2.35600000	4.20200000
Hg	14.87300000	2.19000000	3.48100000
Hg	25.47200000	1.82500000	8.64400000
Hg	14.58700000	1.65900000	7.92300000
Hg	25.65500000	6.80600000	4.72700000
Hg	14.77000000	6.64000000	4.00600000
Hg	25.36900000	6.27500000	9.16900000
Hg	14.48400000	6.10900000	8.44800000

Small Cluster of HgBr₂

Hg	22.73200000	-13.10600000	-8.37700000
Br	25.07500000	-13.67400000	-7.97100000
Br	20.38800000	-12.54200000	-8.78100000

Large Cluster of HgBr₂

Br	21.81300000	-14.55300000	-5.62400000
Br	17.03200000	-11.04300000	-9.56300000
Br	22.26400000	-15.84700000	-10.04400000
Br	19.84300000	-8.86900000	-7.49000000
Br	27.88600000	-11.50000000	-5.89800000
Br	20.29400000	-10.16400000	-11.91000000
Br	28.33700000	-12.79500000	-10.31900000
Br	25.07500000	-13.67400000	-7.97100000

Br	22.52000000	-21.63200000	-5.90100000
Br	25.33000000	-19.45800000	-3.82800000
Br	25.78200000	-20.75300000	-8.24800000
Br	21.66200000	-4.46700000	-8.59400000
Br	22.11400000	-5.76200000	-13.01400000
Br	18.85200000	-6.64100000	-10.66700000
Br	17.12600000	-13.42100000	-6.43400000
Br	17.57700000	-14.71600000	-10.85500000
Br	20.38800000	-12.54200000	-8.78100000
Br	23.19900000	-10.36900000	-6.70800000
Br	27.15000000	-15.05600000	-4.93200000
Br	23.65000000	-11.66300000	-11.12900000
Br	27.60100000	-16.35100000	-9.35200000
Br	24.33900000	-17.23000000	-7.00500000
Hg	17.94000000	-8.84100000	-10.11600000
Hg	20.75000000	-6.66700000	-8.04300000
Hg	21.20200000	-7.96200000	-12.46300000
Hg	19.47000000	-13.98400000	-6.03000000
Hg	19.92200000	-15.27900000	-10.45000000
Hg	23.42700000	-19.43000000	-6.45300000
Hg	25.54300000	-10.93200000	-6.30400000
Hg	26.23800000	-17.25700000	-4.38000000
Hg	22.73200000	-13.10600000	-8.37700000
Hg	25.99400000	-12.22700000	-10.72400000
Hg	26.68900000	-18.55100000	-8.80100000

First coordination shell cluster of α -PbO

Pb	0.00000000	0.00000000	0.00000000
O	1.40038000	-1.40038000	-1.18676000
O	-1.40038000	1.40038000	-1.18676000
O	1.40038000	1.40038000	-1.18676000
O	-1.40038000	-1.40038000	-1.18676000

Third coordination shell cluster α -PbO

Pb	0.00000000	0.00000000	0.00000000
O	4.20130000	-4.20130000	-1.18671000
O	1.40047000	-4.20117000	-1.18661000
O	-1.40047000	-4.20117000	-1.18661000
O	4.20117000	-1.40047000	-1.18661000
O	1.40038000	-1.40038000	-1.18676000

O	4.20117000	1.40047000	-1.18661000
O	-4.20130000	-4.20130000	-1.18671000
O	-1.40038000	-1.40038000	-1.18676000
O	-4.20117000	-1.40047000	-1.18661000
O	1.40038000	1.40038000	-1.18676000
O	-1.40038000	1.40038000	-1.18676000
O	4.20130000	4.20130000	-1.18671000
O	1.40047000	4.20117000	-1.18661000
O	-4.20117000	1.40047000	-1.18661000
O	-1.40047000	4.20117000	-1.18661000
O	-4.20130000	4.20130000	-1.18671000
Pb	0.00000000	-2.80092000	-2.37349000
Pb	2.80092000	0.00000000	-2.37349000
Pb	-2.80092000	0.00000000	-2.37349000
Pb	0.00000000	2.80092000	-2.37349000
Pb	2.80090000	-2.80090000	0.00024000
Pb	-2.80090000	-2.80090000	0.00024000
Pb	2.80090000	2.80090000	0.00024000
Pb	-2.80090000	2.80090000	0.00024000

Fifth coordination shell cluster α -PbO

Pb	0.00000000	0.00000000	0.00000000
Pb	-5.71567935	-1.72821739	3.03116971
Pb	-3.94554025	0.02877063	0.33666072
Pb	-0.00000938	7.89124755	-0.67448670
Pb	-0.00000256	3.94559772	-0.33721611
O	9.96525954	0.02880240	0.33702816
Pb	-0.00000256	-3.94560281	0.33715653
Pb	-0.00000938	-7.89126622	0.67426826
Pb	7.89112235	-0.05752131	-0.67349801
O	7.99226205	2.01603104	0.33666642
O	6.01954487	4.00309996	0.33652576
O	7.99226205	-1.92966629	0.67387940
O	6.01972185	0.05757833	0.67371857
Pb	6.12097598	2.13116159	1.68389992
O	6.01954487	-3.88794244	1.01092162
Pb	6.12097598	-1.81453731	2.02109451
Pb	-3.94536412	-3.91665478	0.67381699
Pb	-7.89114112	0.05753743	0.67327662
O	4.04678307	5.99027802	0.33629652
O	2.07413165	7.97741221	0.33593234

O	4.04692012	2.04472927	0.67358744
O	2.07405969	4.03200825	0.67333960
O	4.04692012	-1.90078645	1.01076638
O	2.07393351	0.08636727	1.01063075
O	4.04678307	-5.84635372	1.34784062
O	2.07405969	-3.85929094	1.34772036
Pb	2.17546647	6.10550672	1.68340396
O	2.07413165	-7.80473526	1.68465530
Pb	2.17544383	2.15991219	2.02082347
Pb	2.17544383	-1.78570217	2.35801101
O	0.10132373	9.96482787	0.33578912
Pb	2.17546647	-5.73133634	2.69496660
O	0.10132373	6.01922763	0.67297505
O	-1.87150467	8.00618611	0.67263091
O	0.10134080	2.07337661	1.01038285
O	-1.87139345	4.06078083	1.01002272
O	0.10134080	-1.87187139	1.34753908
O	-1.87125191	0.11513791	1.34729119
O	0.10132373	-5.81775634	1.68454973
O	-1.87139345	-3.83051833	1.68440380
O	0.10132373	-9.76335661	2.02173604
O	-1.87150467	-7.77596130	2.02135456
Pb	3.94535900	3.91664972	-0.67387637
Pb	3.94553513	-0.02877570	-0.33672029
Pb	-1.77016985	6.13428062	2.02010288
O	-3.84413731	6.04782325	1.00966407
Pb	-1.77010795	2.18868547	2.35751517
O	-3.84425389	2.10227637	1.34697677
O	-5.81689911	4.08941670	1.34660131
O	-3.84425389	-1.84323934	1.68415590
O	-5.81707439	0.14389608	1.68380599
O	-3.84413731	-5.78880843	2.02120869
O	-5.81689911	-3.80162881	2.02096077
Pb	-1.77010794	-1.75692888	2.69470273
Pb	-1.77016985	-5.70256243	3.03166557
Pb	3.94535900	-3.97419856	0.00046585
O	-7.78963507	2.13112034	1.68341609
Pb	-3.94536411	3.97419347	-0.00052561
O	-7.78963507	-1.81457856	2.02061087
O	-9.76261208	0.17266925	2.02049650
Pb	-5.71567935	2.21748150	2.69397494

First coordination shell cluster of Pb_3O_4

Pb	3.10600000	-7.56700000	-17.64300000
O	2.60700000	-8.06600000	-19.74300000
O	2.27500000	-9.42800000	-16.77600000
O	5.08500000	-8.76600000	-17.97200000
O	0.39800000	-7.58200000	-17.95400000

Third coordination shell cluster of Pb_3O_4

O	6.03100000	-7.16900000	-15.31700000
O	-1.59400000	-8.40700000	-20.37100000
O	-1.92700000	-9.76900000	-17.40400000
O	6.36400000	-5.80700000	-18.28400000
O	6.60100000	-11.03100000	-17.02600000
O	6.93300000	-9.66900000	-19.99300000
O	2.94000000	-6.70400000	-22.71000000
O	-0.37400000	-5.88300000	-15.44600000
O	-0.04100000	-4.52100000	-18.41300000
O	1.94200000	-10.79000000	-13.80900000
O	7.37200000	-12.72900000	-19.53400000
O	-1.88900000	-3.61900000	-16.39100000
O	-0.43800000	-8.98400000	-15.06200000
O	8.28000000	-7.17200000	-20.51100000
O	0.22700000	-6.26000000	-20.99600000
O	7.61500000	-9.89600000	-14.57700000
O	2.60700000	-8.06600000	-19.74300000
O	2.27500000	-9.42800000	-16.77600000
O	5.08500000	-8.76600000	-17.97200000
O	0.39800000	-7.58200000	-17.95400000
O	4.68400000	-9.66500000	-14.80000000
O	5.35000000	-6.94100000	-20.73400000
Pb	6.64900000	-7.73800000	-19.13900000
Pb	6.31600000	-9.10000000	-16.17200000
Pb	0.17400000	-9.59900000	-17.09000000
Pb	0.50700000	-8.23700000	-20.05700000
Pb	3.10600000	-7.56700000	-17.64300000
Pb	5.66900000	-11.21000000	-19.02800000
Pb	3.10100000	-11.15400000	-15.66100000
Pb	-1.30500000	-6.06300000	-17.44700000
Pb	3.76700000	-8.43000000	-21.59500000
O	7.87900000	-8.07100000	-17.33900000

O	0.28200000	-10.25400000	-19.19300000
O	1.11900000	-8.85100000	-22.08500000
O	0.45300000	-11.57500000	-16.15100000

Fifth coordination shell cluster of Pb_3O_4

O	-5.44600000	-31.64300000	-21.59900000
O	-5.48700000	-31.66400000	-18.31700000
O	5.18100000	-28.39500000	-21.44700000
O	5.14100000	-28.41600000	-18.16600000
O	2.62400000	-27.89500000	-26.39800000
O	-5.58800000	-29.03500000	-13.37900000
O	-6.01500000	-20.96400000	-23.17900000
O	-6.09600000	-21.00600000	-16.61700000
O	0.74700000	-35.72900000	-23.18900000
O	0.66600000	-35.77100000	-16.62600000
O	-5.42600000	-28.95200000	-26.50400000
O	2.46200000	-27.97700000	-13.27300000
O	-8.69500000	-21.01400000	-21.57200000
O	-5.52700000	-31.68400000	-15.03600000
O	-8.73500000	-21.03500000	-18.29100000
O	-2.90900000	-27.68800000	-28.10600000
O	-5.40600000	-31.62200000	-24.88000000
O	-4.74100000	-23.45000000	-24.82000000
O	5.22200000	-28.37400000	-24.72800000
O	-4.86300000	-23.51200000	-14.97600000
O	5.10000000	-28.43600000	-14.88400000
O	-3.11200000	-27.79200000	-11.70000000
O	0.47400000	-32.79400000	-23.17400000
O	-0.31100000	-28.16800000	-26.43600000
O	0.39300000	-32.83600000	-16.61100000
O	-0.47300000	-28.25100000	-13.31100000
O	-4.17200000	-33.64000000	-19.95500000
O	-10.46600000	-19.42600000	-19.94300000
O	7.10700000	-27.13100000	-16.49200000
O	-7.02500000	-33.38400000	-23.27000000
O	-7.10600000	-33.42500000	-16.70800000
O	7.18800000	-27.09000000	-23.05500000
O	6.91200000	-30.00500000	-19.79500000
O	-4.43600000	-19.22300000	-21.50800000
O	-1.57400000	-34.12000000	-18.28500000
O	-1.53300000	-34.09900000	-21.56600000

O	-4.47700000	-19.24400000	-18.22700000
O	-4.68100000	-26.10000000	-26.47700000
O	-3.16300000	-21.70900000	-23.14900000
O	-4.84300000	-26.18200000	-13.35200000
O	-3.24400000	-21.75000000	-16.58600000
O	-9.87600000	-26.92500000	-19.98300000
O	1.20800000	-23.28900000	-19.82300000
O	5.31200000	-34.92500000	-19.84600000
O	1.67600000	-23.35100000	-16.53600000
O	-9.95800000	-27.45500000	-16.70500000
O	1.75800000	-23.31000000	-23.09800000
O	-9.87700000	-27.41300000	-23.26800000
O	-7.23800000	-27.38400000	-21.59400000
O	-2.95000000	-27.70900000	-24.82500000
O	-2.99100000	-27.73000000	-21.54400000
O	-4.78200000	-23.47100000	-21.53900000
O	1.26800000	-25.93900000	-21.48000000
O	-3.07200000	-27.77100000	-14.98100000
O	-3.03100000	-27.75000000	-18.26200000
O	0.88200000	-30.20700000	-18.23000000
O	-4.82200000	-23.49200000	-18.25800000
O	0.92300000	-30.18600000	-21.51100000
O	1.22800000	-25.95900000	-18.19900000
O	-7.27800000	-27.40500000	-18.31300000
O	2.54200000	-28.42500000	-23.12100000
O	-6.09700000	-21.49400000	-19.90200000
O	-4.95700000	-29.01400000	-23.21700000
O	-5.03800000	-29.05500000	-16.65400000
O	-0.39200000	-27.72100000	-16.58900000
O	-5.31200000	-26.12000000	-16.63900000
O	-4.76200000	-26.14100000	-19.91500000
O	2.46100000	-28.46600000	-16.55800000
O	2.54300000	-27.93600000	-19.83600000
O	0.94200000	-32.85600000	-19.88600000
O	-5.50700000	-28.99300000	-19.94200000
O	-0.31100000	-27.68000000	-23.15100000
O	-5.23100000	-26.07900000	-23.20200000
O	-0.39200000	-28.21000000	-19.87400000
O	0.84200000	-30.22800000	-14.94800000
O	-7.31900000	-27.42500000	-15.03100000
O	1.30900000	-25.91800000	-24.76100000
O	2.71400000	-34.44500000	-21.51600000
O	1.18700000	-25.98000000	-14.91700000

O	-7.19700000	-27.36300000	-24.87500000
O	2.67300000	-34.46600000	-18.23400000
O	0.96300000	-30.16600000	-24.79200000
Pb	0.59000000	-34.27200000	-21.54100000
Pb	1.09500000	-28.06200000	-21.49500000
Pb	-4.65000000	-21.36800000	-18.24200000
Pb	-5.19500000	-27.59800000	-15.00600000
Pb	-5.15500000	-27.57800000	-18.28800000
Pb	1.05500000	-28.08300000	-18.21400000
Pb	1.01400000	-28.10400000	-14.93300000
Pb	0.55000000	-34.29300000	-18.25900000
Pb	-4.60900000	-21.34700000	-21.52300000
Pb	-5.11400000	-27.55700000	-21.56900000
Pb	-5.07400000	-27.53600000	-24.85000000
Pb	1.13600000	-28.04200000	-24.77700000
Pb	3.63100000	-33.30000000	-19.85600000
Pb	-6.66200000	-30.73600000	-16.68500000
Pb	0.05200000	-25.03200000	-16.56600000
Pb	4.38200000	-27.13500000	-16.52600000
Pb	-3.68800000	-24.44000000	-16.60900000
Pb	-8.03700000	-26.12300000	-16.67300000
Pb	-2.15400000	-26.62600000	-13.32200000
Pb	-1.99200000	-26.54400000	-26.44700000
Pb	2.01700000	-31.15500000	-16.58100000
Pb	-2.31300000	-29.05200000	-16.62100000
Pb	4.22300000	-29.56100000	-19.82500000
Pb	0.13300000	-24.99000000	-23.12900000
Pb	2.53900000	-25.21000000	-19.81900000
Pb	4.46300000	-27.09300000	-23.08900000
Pb	-7.77700000	-19.87000000	-19.91200000
Pb	-8.19600000	-28.54900000	-19.97200000
Pb	-3.60600000	-24.39800000	-23.17100000
Pb	-6.09400000	-24.22000000	-19.91900000
Pb	-7.95600000	-26.08200000	-23.23600000
Pb	-2.07300000	-26.58500000	-19.88400000
Pb	-6.58100000	-30.69500000	-23.24800000
Pb	2.09800000	-31.11400000	-23.14300000
Pb	-0.38900000	-30.93500000	-19.89100000
Pb	-4.17500000	-30.91500000	-19.93700000
Pb	-2.23100000	-29.01100000	-23.18300000
O	0.19800000	-35.70900000	-19.91400000
O	-3.16200000	-21.22100000	-19.86400000

Appendix B

ADDITIONAL TABLES AND FIGURES

Table B1 Frozen Inner Shells in FCA(TZP)/AE and FCA(DZ)/AE Basis Sets for the Elements in Large Clusters of ^{199}Hg -Containing Solids

Elements	Frozen Core Orbitals*
Hg	[...]4f
S, Cl	[...]2p
C, N, O, F	[...]1s
Se, Br	[...]3p
I	[...]4p

*Frozen inner shells are up to and including the listed orbitals for the given elements.

Table B2 R_0 and b Parameters Used in the Bond Valence Modelling of the Clusters of Investigated Systems

Bond type	R_0	b
α -PbO		
Pb-O	1.969	0.49
β -PbO		
Pb-O	1.999	0.49
Pb ₃ O ₄		
Pb(II)-O	1.995	0.49

Pb(IV)-O	2.029	0.37
<hr/>		
Pb ₂ SnO ₄		
Pb-O	1.980	0.49
Sn-O	1.926	0.37
<hr/>		
PbF ₂		
Pb-F	2.022	0.382
<hr/>		
PbCl ₂		
Pb-Cl	2.447	0.40
<hr/>		
PbBr ₂		
Pb-Br	2.597	0.40
<hr/>		
PbClOH		
Pb-Cl	2.583	0.40
Pb-O	1.882	0.49
<hr/>		
PbBrOH		
Pb-Br	2.699	0.40
Pb-O	1.893	0.49
<hr/>		
PbIOH		
Pb-I	2.900	0.386
Pb-O	1.907	0.40
<hr/>		
PbSiO ₃		
Si-O	1.624	0.37
Pb-O	1.997	0.49
<hr/>		
Pb ₃ (PO ₄) ₂		
P-O	1.612	0.37
Pb-O	1.977	0.49
<hr/>		

Table B3 Calculated NMR Chemical Shielding Parameters of First and Third Coordination Shell Clusters of Lead-Containing Systems Determined at ZORA-SO/BP86 Level of Theory

Model clusters	σ_{11} (ppm)	σ_{22} (ppm)	σ_{33} (ppm)	σ_{iso} (ppm)	Ω (ppm)	κ
α-PbO						
1-VMTA/BV	9451	9451	11269	10057	1818	1.00
3-VMTA/BV	5887	5889	8827	6868	2940	1.00
β-PbO						
1-VMTA/BV	8630	9283	11516	9810	2886	0.55
3-VMTA/BV	5655	6197	9352	7068	3697	0.71
Pb₃O₄						
1-VMTA/BV	8696	9233	11218	9716	2522	0.57
3-VMTA/BV	7350	7353	9881	8195	2531	1.00
Pb₂SnO₄ (site 1)						
1-VMTA/BV	8941	9198	11270	9803	2329	0.78
3-VMTA/BV	7146	7251	10032	8143	2885	0.93
Pb₂SnO₄ (site 2)						
1-VMTA/BV	8175	8727	11029	9311	2854	0.61
3-VMTA/BV	7187	7296	9983	8155	2796	0.92
PbF₂						
1-VMTA/BV	11746	11865	12348	11986	603	0.60
3-VMTA/BV	10784	10971	11049	10935	264	0.95
PbCl₂						
1-VMTA/BV	9521	9899	10276	9899	756	0.00
3-VMTA/BV	9612	9664	10177	9818	565	-0.41
PbBr₂						

1-VMTA/BV	8602	8940	9548	9030	946	0.29
3-VMTA/BV	9108	9118	9802	9343	694	0.81
PbClOH						
1-VMTA/BV	9226	9773	10730	9910	1503	0.27
3-VMTA/BV	8516	8903	10275	9231	1759	0.56
PbBrOH						
1-VMTA/BV	9251	9579	10341	9724	1090	0.40
3-VMTA/BV	8530	8817	10088	9145	1558	0.56
PbIOH						
1-VMTA/BV	8983	9121	9575	9227	592	0.53
3-VMTA/BV	8618	8649	9860	9043	1242	0.63
PbSiO₃ (site 1)						
1-VMTA/BV	9725	10093	11950	10589	2225	0.67
3-VMTA/BV	7459	7995	10331	8595	2872	0.97
PbSiO₃ (site 2)						
1-VMTA/BV	9270	9626	11705	10200	2435	0.71
3-VMTA/BV	7829	8249	10522	8867	2693	0.63
PbSiO₃ (site 3)						
1-VMTA/BV	9742	10046	11792	10526	2050	0.70
3-VMTA/BV	7940	8532	10281	8918	2341	0.69
Pb₃(PO₄)₂ (site 1)						
1-VMTA/BV	12169	12225	12702	12365	533	0.79
3-VMTA/BV	11094	11159	11279	11178	185	0.49
Pb₃(PO₄)₂ (site 2)						
1-VMTA/BV	10797	11147	12268	11404	1471	0.52
3-VMTA/BV	10092	10556	11654	10767	1562	0.29

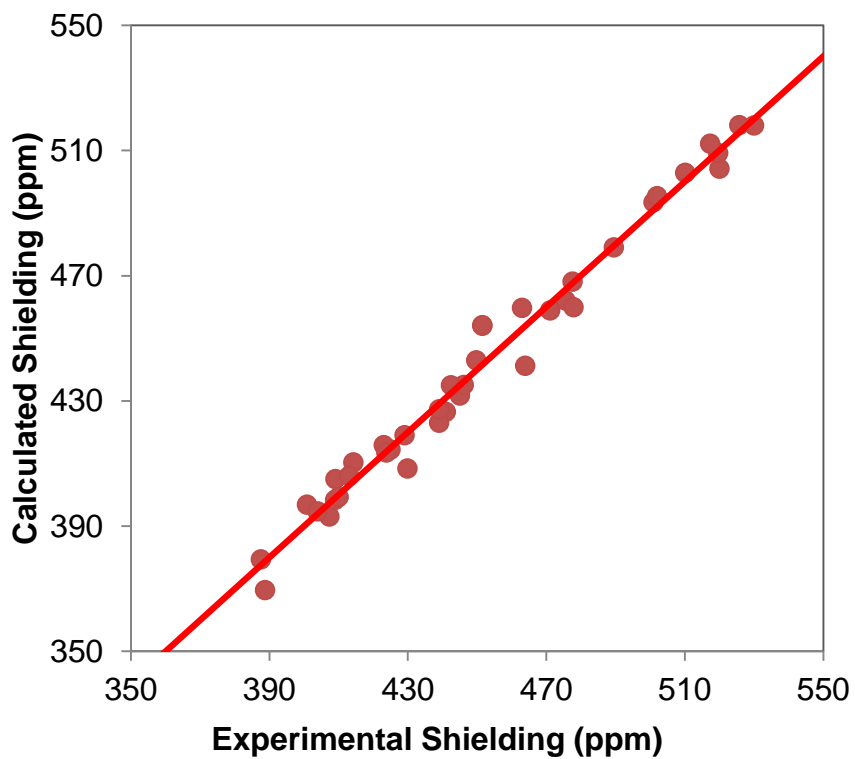


Figure B1 Correlation between calculated and experimental principal components of magnetic-shielding tensors for ^{29}Si -containing materials. Results were computed at the PBE0 level of theory. The best-fit correlation is given as solid line.

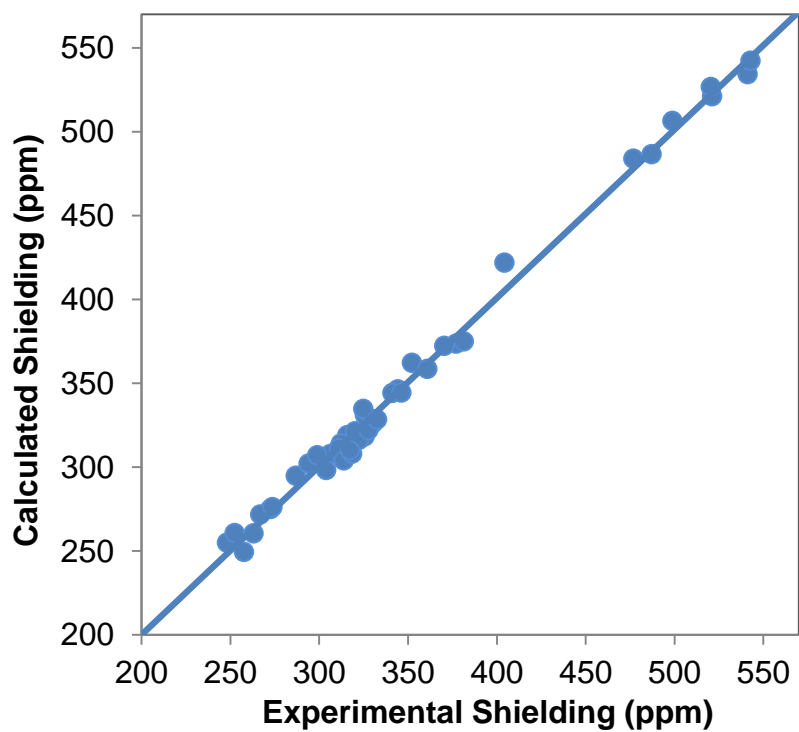


Figure B2 Correlation between calculated and experimental principal components of magnetic-shielding tensors for ^{31}P -containing materials. Results were computed at the PBE0 level of theory. The best-fit correlation is given as solid line.

Appendix C

PERMISSION AND COPYRIGHT

Calculation of chemical-shift tensors of heavy nuclei: a DFT/ZORA investigation of ^{199}Hg chemical-shift tensors in solids, and the effects of cluster size and electronic-state approximations

F. Alkan and C. Dybowski, *Phys. Chem. Chem. Phys.*, 2014, **16**, 14298

DOI: 10.1039/C4CP01682C

This article is licensed under a [Creative Commons Attribution 3.0 Unported Licence](#). Material from this article can be used in other publications provided that the correct acknowledgement is given with the reproduced material.

Reproduced material should be attributed as follows:

- For reproduction of material from NJC:
[Original citation] - Published by The Royal Society of Chemistry (RSC) on behalf of the Centre National de la Recherche Scientifique (CNRS) and the RSC.
- For reproduction of material from PCCP:
[Original citation] - Published by the PCCP Owner Societies.
- For reproduction of material from PPS:
[Original citation] - Published by The Royal Society of Chemistry (RSC) on behalf of the European Society for Photobiology, the European Photochemistry Association, and RSC.
- For reproduction of material from all other RSC journals:
[Original citation] - Published by The Royal Society of Chemistry.

Chemical-shift tensors of heavy nuclei in network solids: a DFT/ZORA investigation of ^{207}Pb chemical-shift tensors using the bond-valence method

F. Alkan and C. Dybowski, *Phys. Chem. Chem. Phys.*, 2015, **17**, 25014

DOI: 10.1039/C5CP03348A

This article is licensed under a [Creative Commons Attribution 3.0 Unported Licence](#). Material from this article can be used in other publications provided that the correct acknowledgement is given with the reproduced material.

Reproduced material should be attributed as follows:

- For reproduction of material from NJC:
[Original citation] - Published by The Royal Society of Chemistry (RSC) on behalf of the Centre National de la Recherche Scientifique (CNRS) and the RSC.
- For reproduction of material from PCCP:
[Original citation] - Published by the PCCP Owner Societies.
- For reproduction of material from PPS:
[Original citation] - Published by The Royal Society of Chemistry (RSC) on behalf of the European Society for Photobiology, the European Photochemistry Association, and RSC.
- For reproduction of material from all other RSC journals:
[Original citation] - Published by The Royal Society of Chemistry.

Spin-orbit effects on the ^{119}Sn magnetic-shielding tensor in solids: a ZORA/DFT investigation

F. Alkan, S. T. Holmes, R. J. Iuliucci, K. T. Mueller and C. Dybowski, *Phys. Chem. Chem. Phys.*, 2016, **18**, 18914

DOI: 10.1039/C6CP03807G

If you are not the author of this article and you wish to reproduce material from it in a third party non-RSC publication you must [formally request permission](#) using RightsLink. Go to our [Instructions for using RightsLink page](#) for details.

Authors contributing to RSC publications (journal articles, books or book chapters) do not need to formally request permission to reproduce material contained in this article provided that the correct acknowledgement is given with the reproduced material.

Reproduced material should be attributed as follows:

- For reproduction of material from NJC:
Reproduced from Ref. XX with permission from the Centre National de la Recherche Scientifique (CNRS) and The Royal Society of Chemistry.
- For reproduction of material from PCCP:
Reproduced from Ref. XX with permission from the PCCP Owner Societies.
- For reproduction of material from PPS:
Reproduced from Ref. XX with permission from the European Society for Photobiology, the European Photochemistry Association, and The Royal Society of Chemistry.
- For reproduction of material from all other RSC journals and books:
Reproduced from Ref. XX with permission from The Royal Society of Chemistry.

If you are the author of this article you still need to obtain permission to reproduce the whole article in a third party publication with the exception of reproduction of the whole article in a thesis or dissertation.

JOHN WILEY AND SONS LICENSE
TERMS AND CONDITIONS

May 20, 2016

This Agreement between Fahri Alkan ("You") and John Wiley and Sons ("John Wiley and Sons") consists of your license details and the terms and conditions provided by John Wiley and Sons and Copyright Clearance Center.

License Number	3873340454224
License date	May 20, 2016
Licensed Content Publisher	John Wiley and Sons
Licensed Content Publication	Journal of Computational Chemistry
Licensed Content Title	Analysis of the bond-valence method for calculating 29Si and 31P magnetic shielding in covalent network solids
Licensed Content Author	Sean T. Holmes, Fahri Alkan, Robbie J. Iulucci, Karl T. Mueller, Cecil Dybowski
Licensed Content Date	Apr 26, 2016
Pages	1
Type of Use	Dissertation/Thesis
Requestor type	Author of this Wiley article
Format	Print and electronic
Portion	Full article
Will you be translating?	No
Title of your thesis / dissertation	RELATIVISTIC DFT CALCULATIONS OF MAGNETIC SHIELDING TENSORS FOR SPIN ½ HEAVY NUCLEI
Expected completion date	Jul 2016
Expected size (number of pages)	220
Requestor Location	Fahri Alkan DEPARTMENT OF CHEMISTRY None None NEWARK, DE 19711 United States Attn: Fahri Alkan



RightsLink®

Home

Account Info

Help



Title: Effect of Co-Ordination Chemistry and Oxidation State on the 207Pb Magnetic-Shielding Tensor: A DFT/ZORA Investigation
Author: Fahri Alkan, C. Dybowski
Publication: The Journal of Physical Chemistry A
Publisher: American Chemical Society
Date: Jan 1, 2016
Copyright © 2016, American Chemical Society

Logged in as:

Fahri Alkan

Account #:

3001030576

LOGOUT

PERMISSION/LICENSE IS GRANTED FOR YOUR ORDER AT NO CHARGE

This type of permission/license, instead of the standard Terms & Conditions, is sent to you because no fee is being charged for your order. Please note the following:

- Permission is granted for your request in both print and electronic formats, and translations.
- If figures and/or tables were requested, they may be adapted or used in part.
- Please print this page for your records and send a copy of it to your publisher/graduate school.
- Appropriate credit for the requested material should be given as follows: "Reprinted (adapted) with permission from (COMPLETE REFERENCE CITATION). Copyright (YEAR) American Chemical Society." Insert appropriate information in place of the capitalized words.
- One-time permission is granted only for the use specified in your request. No additional uses are granted (such as derivative works or other editions). For any other uses, please submit a new request.